Tritium analytics by beta induced X-ray spectrometry

Zur Erlangung des akademischen Grades eines

DOKTORS DER NATURWISSENSCHAFTEN

von der Fakultät für Physik des

Karlsruher Instituts für Technologie

genehmigte

DISSERTATION

von

Diplom-Physiker

Marco Röllig

aus Hermsdorf

<table>
<tr><td>Referent:</td><td>Prof. Dr. G. Drexlin
Institut für Experimentelle Kernphysik
Karlsruher Institut für Technologie</td></tr>
<tr><td>Korreferent:</td><td>Prof. Dr.-Ing. M. Noe
Institut für Technische Physik
Karlsruher Institut für Technologie</td></tr>
<tr><td>Tag der mündlichen Prüfung:</td><td>30.10.2015</td></tr>
</table>

Contents

List of Figures

List of Tables

1. Introduction

Tritium analytics is a prerequisite condition for the safe and reliable operation of tritium handling facilities. It comprises several methods for activity and composition monitoring of tritiated gases, liquids or solids [Dem12]. At the Tritium Laboratory Karlsruhe (TLK) [Doe08] the development of new tritium analytics is an important part of the R&D task [Dem12]. A main trigger for that are the challenging analytical requirements of the next generation neutrino mass experiment KATRIN [KAT04].

The Karlsruhe Tritium Neutrino (KATRIN) experiment is going to measure the electron energy spectrum of the tritium β-decay with an unprecedented sensitivity. This is the basis of a kinematic method for an model-independent determination of the neutrino mass. After three full years of measurement time the designed discovery potential of KATRIN is 0.35 eV/c^2 with a 5σ significance [KAT04]. In case of no signal the new upper limit will be 0.2 eV/c^2 (90 % C.L.).

KATRIN uses a Windowless Gaseous Tritium Source (WGTS) with a source activity of 10^{11} Bq [Bab12]. All tritium related parts of KATRIN including the WGTS are located inside the TLK. For the proper operation of the WGTS a large amount of tritium infrastructure is necessary. The tritium purity inside the source must be retained above $\geqslant$ 95 % over the whole measurement time [Bab12]. The total tritium throughput will be in the range of $\approx$ 40 g/day and is processed in the KATRIN closed tritium cycle [Bor06].

At the TLK, a reference fuel cycle was developed as part of the fusion R&D program for the International Thermonuclear Experimental Reactor (ITER) [Dem12]. It comprises several experimental facilities for tritium storage and tritium removal from exhaust gases and isotope separation. All of these systems are necessary for the operation of KATRIN. An essential part of each of these subsystems are activity monitors for process control and accountancy. A high tritium throughput as it can be found in KATRIN and routine operation over three full years of measurement time create new requirements for these activity monitors. Typical requirements are inline/online ability, short measurement times and high accuracy and precision and many more. An activity monitor based on the Beta Induced X-ray Spectrometry (BIXS) [Wes60], [Mat98] method could be the answer to the increased requirements.

Activity monitoring is also vital for the KATRIN WGTS. To achieve the aimed sensitivity of KATRIN, the activity inside the WGTS must be stabilized and monitored on the 0.1 % level [Bab12]. In-situ tritium activity monitoring of the WGTS on the 0.1 % level is a challenging task and a customized BIXS system was designed to do this [Bab14]. As this system is under construction the potential sensitivity is still unclear and must be studied by Monte Carlo simulations.

One of the major problems for tritium analytics for gaseous tritium are surface contaminations. Tritium accumulates during exposure and causes an increasing background signal called memory effect [Wag11], [Roe13]. This signal is in most cases indistinguishable from tritium in the gas phase. As this is of particular importance for any monitoring system aiming for the 0.1 % level, a specialiced experimental facility for the measurement of surface contamination is urgently needed.

Therefore, the three subtasks which were focused in this work are

1. the development of a tritium process monitor and accountancy tool based on the BIXS method,

2. a benchmark of the designed high stability BIXS activity monitor of the KATRIN tritium source by Monte Carlo simulations and

3. the design of an instrument for the in-situ investigation of surface contaminations of arbitrary solid sample materials.

The thesis is structured as following: In chapter 2 the analytical requirements of the KATRIN closed tritium cycle are discussed. Three open issues are addressed which finally leads to the goals of this work. As the BIXS method is used for these open issues, the fundamentals of BIXS are explained in chapter 3. Also Geant4 simulations of a very basic BIXS system are presented. The actual design and the following characterization of a tritium process monitor based on BIXS is discussed in chapter 4. In chapter 5 the potential performance of the KATRIN BIXS system is studied by Monte Carlo simulations. Tritium surface contaminations and how they affect BIXS systems (especially in case of KATRIN) are studied in chapter 6. This is done by a specialized experimental facility which was designed and built during this work. An outlook and summary in chapter 7 concludes this work.

2. Analytical requirements for the closed tritium cycle at TLK

A closed tritium cycle is a necessity for fusion projects as the **I**nternational **T**hermonuclear **E**xperimental **R**eactor (ITER) with high tritium fuel rates of about $\approx$ 1.1 kg/day[1] [Aym02], [Glu07]. The technical realization of a closed fuel cycle is an ongoing R&D process and one of the tasks of the **T**ritium **L**aboratory **K**arlsruhe (TLK) [Bor06]. A reference process is realized at TLK which will also used for the **Ka**rlsruhe **Tri**tium **N**eutrino Experiment (KATRIN) [KAT04]. KATRIN uses a gaseous tritium source with a tritium throughput of about $\approx$ 40 g/day to measure the neutrino mass. Safe and reliable tritium management in fuel cycles with such a high throughput faces new technological challenges such as the need for improved tritium analytics. Therefore, the development of a variety of analytical tools is an important part of the R&D activities at TLK [Dem12]. Furthermore, KATRIN needs improved tritium analytics to reach its defined sensitivity goals [Bab12].

In section 2.1 the closed tritium cycle realized at TLK is explained using the example of KATRIN. Important subsystems as tritium storage, tritium removal and isotope separation are outlined. General technical requirements of three monitoring tasks in the TLK closed tritium cycle are discussed in section 2.2. Also current open issues are discussed there. Finally, this leads to the goals of this work outlined in section 2.3.

2.1. The closed tritium cycle of KATRIN

Closed loop operation of tritium comprises several tasks as tritium confinement, safe storage, purification and accountancy. Each of these tasks is challenging due to the (radio)chemical properties of tritium.

With a half-life time of 12.3 years tritium decays under emission of a β-electron and an electron-antineutrino to ^{3}He. The maximum energy of the β-electron is 18.6 keV. Chemically, tritium has similar chemical properties as hydrogen or deuterium with some modifications due to the higher mass. Isotopic effects change for example the adsorption behavior and can be utilized for isotope separation as explained later. Further chemical differences can be promoted by the decay energy. Especially radiochemical effects necessitate test experiments when handling tritium compared to hydrogen or deuterium.

Hydrogen usually comes in molecular form and there are six possible isotopologues (H_2, D_2, T_2, HD, DT, HT) which are abbreviated as Q_2. All hydrogen species are chemically

---

[1]   The calculated fuel rate of ITER is based on a tritium consumption of 76 g/day and a burn-up fraction of 0.3 % [Aym02].
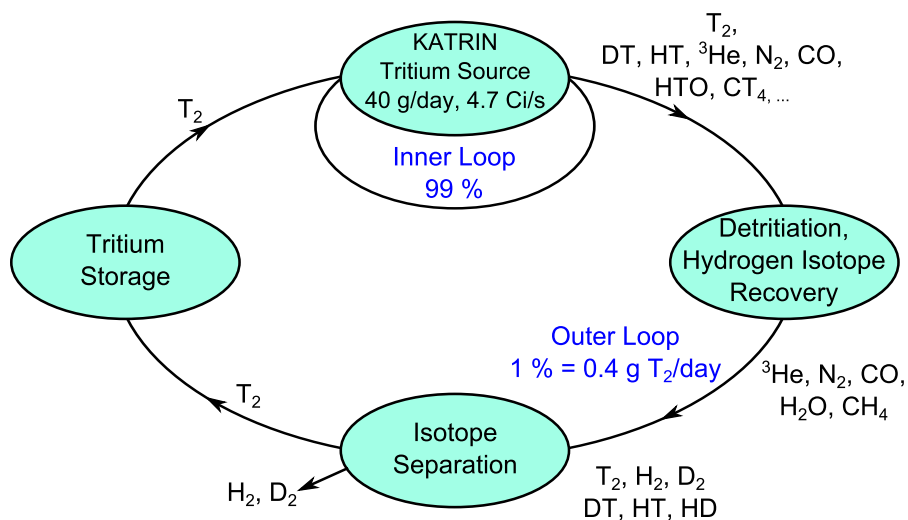
Figure 2.1.: The closed tritium cycle of KATRIN.

very reactive. Therefore, tritium must be continuously processed to preserve purity[2]. Even when stored in stainless steel vessels, gas-wall interactions change tritium purity over time and produce additional tritiated gas species as e.g. tritiated methanes [Pri13], [Fis11].

In figure 2.1 a schematic of the KATRIN closed tritium cycle realized at TLK is shown. Except for the numerous experiments which require tritium there are three important subsystems which shall be explained in more detail.

2.1.1. Tritium storage

A safe way to store tritium is to dissolve it in a solid as a metal hydride. At TLK there are nine uranium and one zirconium/cobalt getter beds installed with a total allowed storage capacity of 40 g [Pen00]. All containers are double-walled as the getter beds must be heated up to 550°C to release the tritium. At these elevated temperatures tritium can permeate in significant amounts through the first stainless steel wall. The second wall housing confines the permeated tritium.

All getter beds are connected to a vacuum manifold and can be loaded or evacuated for tritium release. The inner vessel of the getter bed is designed to withstand pressures of 30 bar. This is more than the pressure which is attained when the getter bed is loaded to the maximum specified loading capacity[3] and heated up to 550°C. Nevertheless, helium from the tritium decay, which can't be gettered, is transferred from each getter bed on a regular basis.

Tritium which is transferred from the tritium storage to another subsystem or vice versa is going through the **T**ritium **T**ransfer **S**ystem (TTS) [Pen00]. In the TTS the accountancy

---

[2]   Due to the tritium decay (≈ 5.5 %/year) there is also a constant decrease of tritium purity.

[3]   The maximum specified loading capacity of $9.3 \cdot 10^{14}$ Bq per getter bed is about 40 % of the total loading capacity.

must be performed by measuring the pressure and temperature in a known volume and performing a composition analysis to determine the tritium purity ϵ_T. From that, the amount of transferred tritium is calculated by the ideal gas law. The composition analysis is done by gas chromatography at TLK. Therefore, a gas sample must be taken from the initial gas mixture and analyzed over several hours.

2.1.2. Tritium clean-up

Tritium is used at TLK in numerous test experiments in the context of fusion and KATRIN R&D. When using tritiated gas mixtures in these test experiments or later in KATRIN, several effects will cause a steady pollution of the initial gas mixture and the formation of new tritiated gas species. Prominent effects are

- pollution with ^{3}He from the β-decay,

- the formation of HT from T_2 due to gas-wall interactions with stainless steel surfaces,

- the formation of tritiated methane species CQ_4 due to gas-wall interactions with stainless steel surfaces,

- the formation of HTO from H_2O due to isotope exchange reactions with residual water in non baked-out systems,

- pollution with typical process gases, purge gases, cryogetter materials or residual gas from atmospheric air such as H_2, D_2, N_2, CO, CO_2, He, Ar and others.

These are typical pollution processes and not at all a comprehensive list. To preserve a certain tritium purity, test gas mixtures must be recycled on a regular basis and the tritium must be removed from unwanted exhaust gases. Tritium removal from exhaust gases is done by the CAPER[4] facility [Bor07] which was designed as a reference process for the **T**okamak **E**xhaust **P**rocessing (TEP) of ITER. The CAPER process is shown in figure 2.2. There are three consecutive steps for Q_2 recovery at highest purity.

In the first step the pure Q_2 fraction of the exhaust gas mixture is separated by a Pd/Ag permeator. In the second step which comprises a catalyst bed and an additional Pd/Ag permeator, hydrocarbons such as tritiated methanes are cracked by the catalyst and the released Q_2 fraction is separated by the permeator. The second step is carried out in a closed loop as long as necessary. Detritiation factors higher than 1000 are possible [Bor07]. The third step comprises a Pd/Ag catalytic membrane reactor which employs isotopic swamping in a counter-current mode for tritium recovery. It is used to achieve very high detritiation factors of about 10^5 [Dem10]. Tritiated gas species are fed into the catalyst side and ^{1}H is fed into the purge gas side in counter-current mode. Both sides are separated by a Pd/Ag membrane which is solely permeable for hydrogen isotopes. ^{1}H from the purge side permeates to the catalyst site where isotope exchange reactions occur and molecular tritium is released. The tritium permeates to the purge side and is recovered from the purge gas stream.

---

[4]   **Cap**rice **per**meator (CAPER)
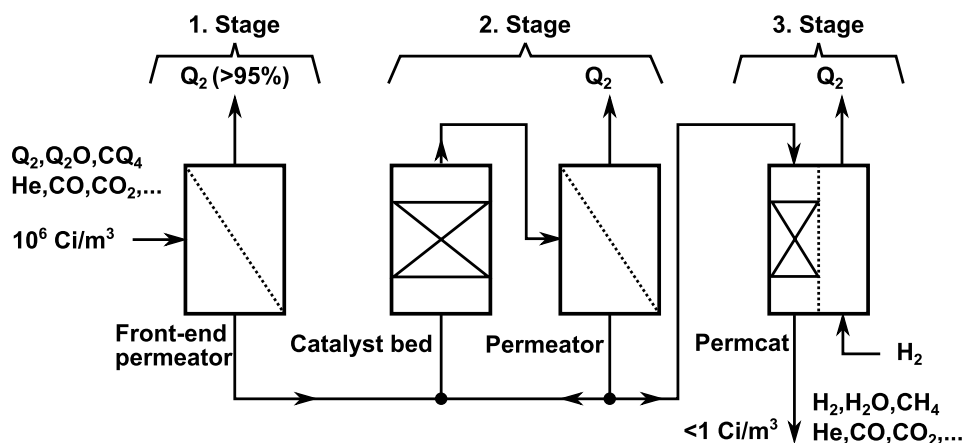
Figure 2.2.: Three step CAPER process for tritium removal from exhaust gases. A description of the process is given in the text.

An exhaust gas mixture is not always processed in all three CAPER steps. It depends on the actual gas mixture, the requirements regarding the detritiation factor and the amount of gas. Also the time needed for processing in each step depends on the actual gas mixture. Therefore, continuous activity monitoring is vital during each processing step. This is done by ionization chambers (IC) in CAPER. As ICs show a strong pressure dependence they must be operated in pressure stabilized mode. Due to their limitations regarding accuracy and precision further gas chromatography measurements are necessary to determine tritium purities. The removed Q_2 can then be transferred to the isotope separation system.

2.1.3. Isotope separation

A schematic of the isotope separation system is shown in figure 2.3. The isotope separation system is based on the displacement gas chromatography principle [Doe02]. A batch of the Q_2 gas mixture is injected from the sample vessel into the sample coil. Then it is fed together with a carrier gas into a 6 m column containing aa-alumina oxide which is coated with 20 weight % palladium. The column is operated at room temperature and ambient pressure.

Hydrogen isotopes are dissolved in the palladium in atomic form. Due to strong isotopic effects in desorption isotherms, they are separated in the column in fractions of H_2, D_2, T_2 and only minor fractions of mixed isotopes. The light hydrogen isotopes transfer preferentially into the palladium and displace the heavier isotopes which remain therefore preferentially in the gas phase. By that, the heavier isotopes are going faster through the column.

The separated isotopes are identified at the outlet by activity monitoring with an ionization chamber and a thermal conductivity detector. Individual isotope fractions are transferred to getter beds by switching the relevant valves. When the separation is finished the column is regenerated by heating it up to 200°C. Depending on the aimed detritiation factor and the initial Q_2 mixture repeated runs may be necessary.
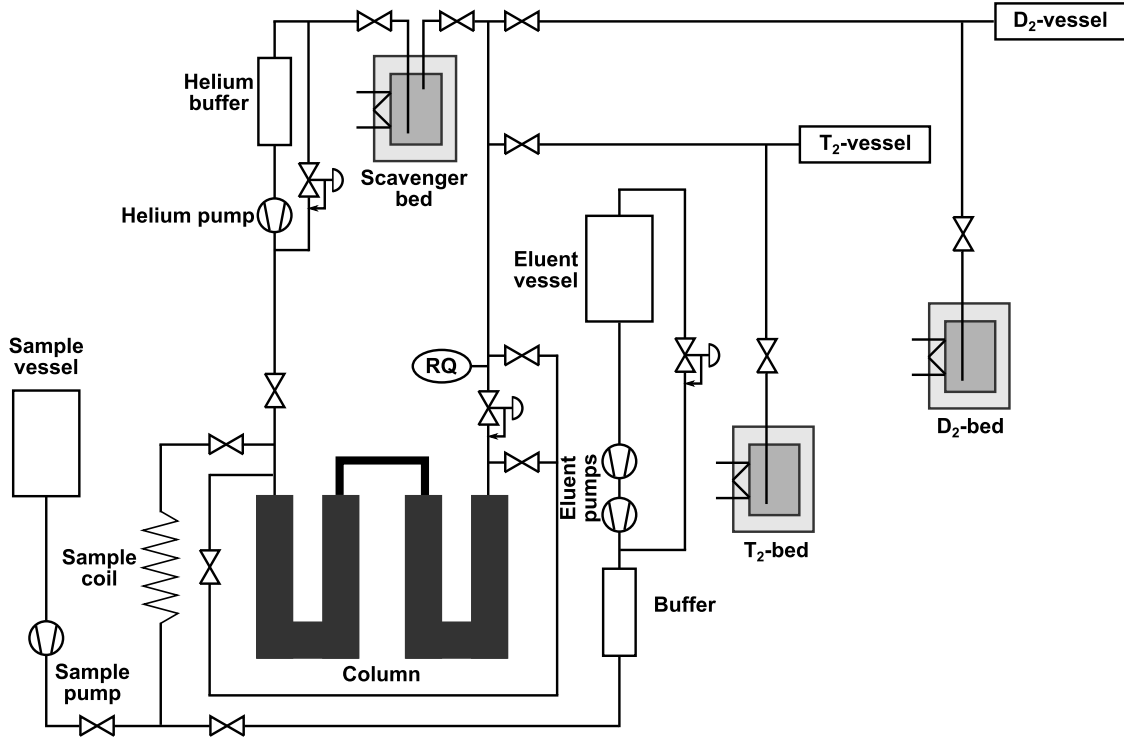
Figure 2.3.: Schematic of the isotope separation system at TLK according to [Doe05].

After separation the tritium can be transferred to the TTS and further to the TLG or it can be transferred to an experiment. This shall be illustrated for the example of the proposed KATRIN operation.

2.1.4. Inner and outer loop of KATRIN

As an example for an experiment which depends on the mentioned TLK infrastructure, the gaseous tritium source of KATRIN is briefly described here. Details about the KATRIN working principle and requirements will follow in chapter 5. Here we will focus on the tritium source and the required tritium process technology. KATRIN uses the β-decay of tritium to measure the neutrino mass with an unprecedented sensitivity [KAT04] and needs therefore a gaseous tritium source.

From the physics point of view the KATRIN source is a cylindrical gas column with a length of 10 m and a diameter of 90 mm. Gaseous tritium is injected in the middle of the source tube through a system of capillaries, freely streams to both ends and is pumped out by 12 turbo molecular pumps. One of the KATRIN requirements which must be fulfilled by the TLK infrastructure, is the stability of the source strength S on the 0.1 % level. The source strength of KATRIN is given by

$$S = A_Q \cdot \rho d \cdot \epsilon_T \tag{2.1}$$
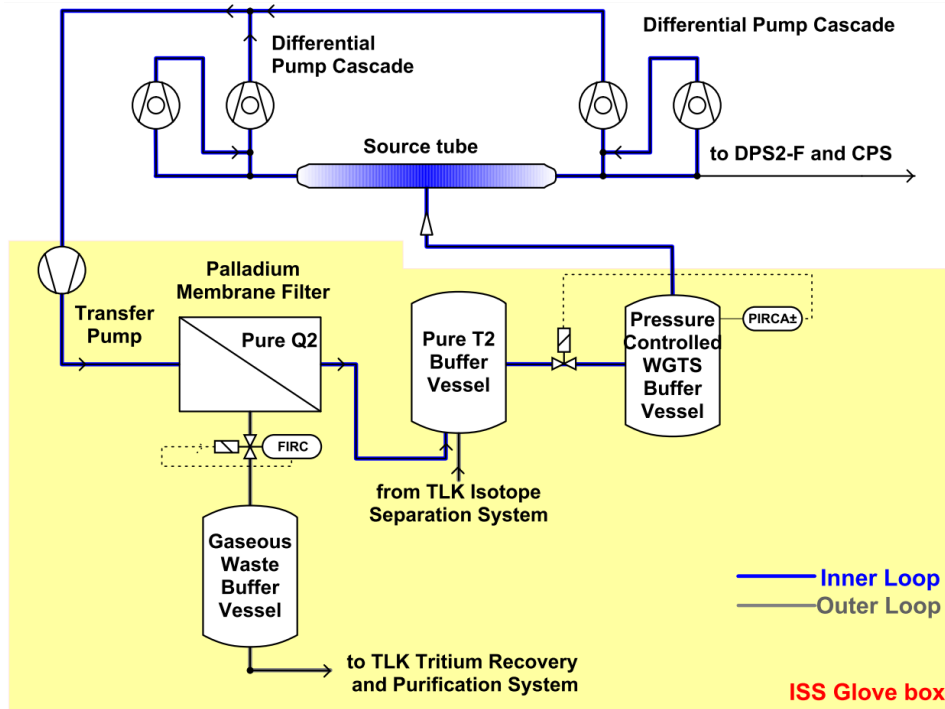
Figure 2.4.: Schematic view of the inner and outer tritium loop of KATRIN [Stu10].

A_Q is the cross sectional area of the source, ρd is the column density and ϵ_T the tritium purity. Key parameters which must be stabilized and monitored to achieve the KATRIN requirements regarding the source strength are

- the beam tube temperature T_{BT} which will be between 27 K and 30 K but stabilized on the ± 30 mK level,

- the adjustable inlet pressure p_{in} of about 10^{-3} mbar,

- the outlet pressure p_{out} of about $0.05 \cdot p_{in}$ and

- the tritium purity ϵ_T of $\geqslant 95$ %.

In [Bab12] the function principle and first measurement results of the temperature stabilization of the KATRIN tritium source are discussed. The stabilization of the other parameters is the main task of the KATRIN tritium cycle which is shown in figure 2.4.

For keeping the tritium purity $\geqslant 95$ %, the gaseous tritium is continuously cycled in the inner loop through a Pd/Ag membrane filter ("permeator") which only let pass Q_2 species. Hydrocarbons from gas-wall interactions or other previously mentioned impurities are channeled to the outer loop (1 % to 5 % of the total gas stream). The exhaust gas is periodically processed by the previously mentioned CAPER facility and the ISS. Tritium is then injected again to the pure T_2 buffer vessel of the inner loop. A pressure controlled buffer vessel is used to stabilize the inlet pressure to the source tube. The outlet pressure is stabilized by the constant pumping speed of the turbo molecular pumps.

So far, the amount of impurities which will be produced in the source tube and in the enclosed infrastructure is unknown. Significant impurity contributions are expected due to gas-wall interactions and tritium interactions with materials within the twelve turbo molecular pumps [Pri13]. Therefore, activity monitoring of the gas stream is vital for KATRIN, to achieve the aimed sensitivity. The composition analysis is done by a laser Raman system, located between the pure tritium buffer vessel and the pressure controlled buffer vessel (figure 2.4). Activity monitoring of the gas column within the WGTS cryostat is done by a BIXS system. Thereby the KATRIN requirement of a monitoring precision on the 0.1 % level is unprecedented in tritium technology.

2.2. General technical requirements of activity monitoring systems in closed tritium cycles

The need for activity monitoring systems is not an exclusive requirement of KATRIN but an indispensable measure in all tritium cycles. This is first and foremost due to licensing, safety and economical reasons which requires a seamless end-to-end tritium accountancy. Moreover, there are also technical reasons for activity monitoring as it is used for process control. There are diverse requirements to monitoring systems for such purposes which can vary depending on the actual application.

General technical requirements of monitoring systems for experiments such as KATRIN are very different from those for process control. Compared to the wide parameter range that a tritium analytical tool for process control and accountancy must cover, activity monitoring for the KATRIN tritium source happens in a well-defined and rather narrow parameter range. Instead, KATRIN is aiming for an unprecedented stability of the tritium source which creates new requirements to tritium analytical systems.

In the following sections the general requirements for three monitoring tasks in the TLK closed tritium cycle are discussed and compared to existing tritium analytical tools. Open issues will be addressed which will finally lead to the goals of this work.

2.2.1. Activity monitoring for process control and accountancy

Tritium analytics in the ambit of process control and accountancy must cover a large parameter range for quantities such as pressure and tritium concentration. Depending on the actual operating site the requirements can be diverse. General technical requirements for tritium analytics at TLK evolve from the demand for high tritium throughput (up to 40 g/day [Bor06]) while having accurate accountancy and lowest possible waste production. General technical requirements are:

- **Inline/online monitoring:** As sample taking for activity measurements is time-consuming and produces radioactive waste, inline or online monitoring tools are preferable.

- **Fast:** For process control the monitoring should be reasonable fast. Activity variations should be detectable within several 100 s.

- **Measurement uncertainty:** In process control measurements, uncertainties in the range of ≈ 5 % would be desirable. For tritium accountancy pVT-c-measurements[5] are usually used. The weakest link in this measurement chain, except the activity measurement, is the volume which can be determined with an accuracy of approx. 1 % [Koe11]. So, activity monitoring with an accuracy of about $\leqslant 1$ % would be desirable for tritium accountancy.

- **Availability:** Tritium analytical tools are still part of an R&D process. Nevertheless, as they are an indispensable presupposition for the TLK infrastructure, it should be rather easy available. Therefore, standard parts are preferred wherever possible.

- **Small dead volume:** As the tritium inventory is needed for the tritium cycle, monitoring systems should have a reasonable low dead volume.

- **Easy to integrate:** A small mechanical footprint is necessary to integrate monitoring systems into existing infrastructure.

- **Reasonable cheap:** As tritium analytics is needed at several spots in the infrastructure it should be reasonably cheap.

- **Robustness:** As such monitoring systems are part of the infrastructure they should be robust against typical external influences as vibrations, magnetic fields and temperature fluctuations.

- **Pressure range:** Typical tasks require activity monitoring systems which cover pressure ranges of approx. $(10^{-3} \ldots 1000)$ mbar. For lower pressures gas-wall interactions and outgassing effects become dominant in non-baked-out systems.

- **Temperature range:** During normal operation most systems at TLK are operated at room temperature $\approx 30°$C.

- **Tritium concentration:** Tritium concentrations which must be monitored can, depending on the actual application, largely vary between ≈ 10 ppm and 100 %.

2.2.2. High stability activity monitoring of the KATRIN gaseous tritium sources

For an experiment as KATRIN, a high stability of activity monitoring of the tritium source is essential to reach the sensitivity goals on the neutrino mass measurement. Therefore, variations on the 0.1 % level in the source strength of the gaseous tritium source must be detectable. General technical requirements of the activity monitoring system evolve from the experimental environment in KATRIN:

---

[5] In a pVT-c procedure the pressure and temperature of a tritiated gas mixture are measured in a well known volume. The tritium purity is determined (e.g. by gas chromatography) and the amount of tritium is calculated according to the ideal gas law.

- **In-situ:** As the source strength of the gas column within the source tube is a crucial parameter for KATRIN, the activity should be monitored in-situ. By that, uncertainties due to gas-wall interactions on the way between the measurement system and the KATRIN source are excluded.

- **Fast:** Activity fluctuations must be detected within one KATRIN measurement interval which is about $\leqslant 1000$ s.

- **Robustness to magnetic stray fields:** As the KATRIN source uses superconducting magnets, stray fields in the order of ≈ 1 T are possible.

- **Measurement uncertainty:** Stability variations of the source activity on the 0.1 % level must be detectable.

- **Pressure range:** Depending on the location of the monitoring system it must work at low total pressures in the range of 10^{-5} mbar to 10^{-3} mbar.

- **Temperature range:** As the tritium source is baked-out, the system must resist temperatures of $\leqslant 473$ K. During normal operation the source tube is cooled down to ≈ 30 K.

- **Tritium concentration:** During normal operation KATRIN will work with tritium concentrations $\geqslant 95$ %.

2.2.3. Activity monitoring of tritium surface contamination

Tritium adsorption on and absorption in first wall materials of tritium-leading systems are usually unwanted processes but nevertheless are almost always present. This reduces the amount of tritium in the gas phase, accumulate inventories which must be taken into account in case of disposal and promotes diffusion of tritium into the wall material. In activity monitoring systems, as ICs or BIXS systems for example, it can produce an increasing background signal which distorts activity measurements of the process gas. This is often referred to as memory effect [Nis89]. In case of KATRIN it is of particular interest as it interferes with the requirement of a measurement precision of 0.1 %.

Alternative materials or coatings could help to reduce these effects. Therefore, a specialized experimental setup is needed, to investigate tritium surface contaminations on arbitrary solid sample materials. Such an experiment needs an ultra-clean environment, it must cover a large pressure and temperature parameter region and it needs an activity monitoring system which detects fractions of monolayers of tritium. General technical requirements of the activity monitoring system are:

- **In-situ:** As each exposure to other gas species or especially humidity can significantly change the amount of tritium on the sample, the monitoring system must work in-situ.

- **Fast:** Depending on the pressure range, tritium adsorption can be a rather fast process. Measurement times of $\leqslant 100$ s would be desirable to see fluctuations in the surface contamination.
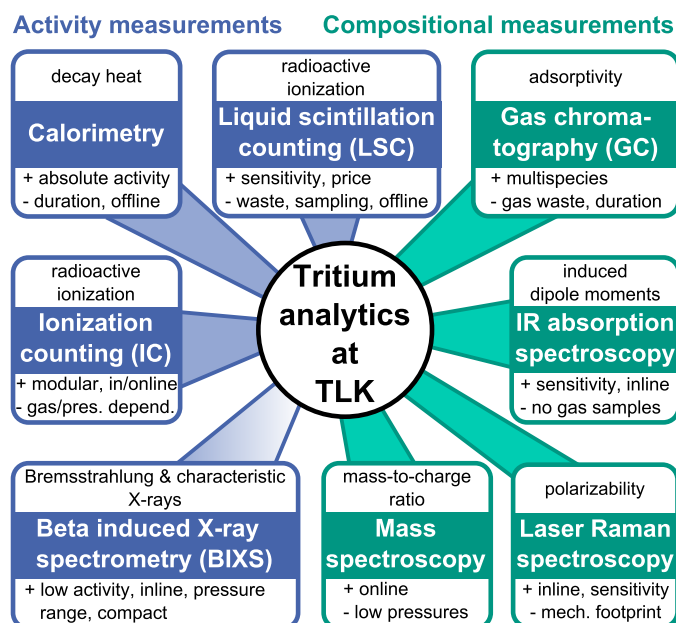
Figure 2.5.: Tritium analytical techniques at TLK.

- **Minimum detectable activity (MDA):** The MDA should be as low as possible and in the range of fractions of monolayers. For the investigation of KATRIN-relevant materials (see chapter 5) the MDA should be at least $\leqslant 1$ monolayer of tritium.

- **Pressure range:** The activity monitoring system must work at typical pressure ranges, used in tritium leading systems as previously described. These start with reasonably low pressures of about 10^{-5} mbar and so to maximum pressures of about 1000 mbar.

- **Temperature range:** Most tritium-leading systems at TLK are operated at room temperature. Nevertheless, to study tritium adsorption at low temperatures and bake-out effects, the monitoring system should work at temperatures ranges of about $-150°$C to up to $200°$C.

- **Tritium concentration:** As other hydrogen species can distort tritium adsorption measurements by blocking adsorption sites, the system should only be operated with rather high tritium concentrations ≈ 95 %.

2.2.4. Open issues for activity monitoring and accountancy in closed tritium cycles

There is a multitude of tritium analytical methods, which could be used for the three mentioned applications. However, each method comes with specific advantages and disadvantages which must be taken into account. An overview of available methods for tritium activity monitoring or composition monitoring is shown in figure 2.5. Some of them are standard tools while others are still in the R&D stage. Not all of the methods

can be used for measurement of gaseous tritium or tritium surface contamination. In table 2.1 an overview of the maturity level and the performance of potential methods is given. It also listed to what extent they fulfill the most common technical requirements.

Calorimetry is reliable standard method for tritium activity measurement of solids, liquids and gases. When it comes to process monitoring and control with high tritium throughput it has crucial disadvantages. Due to the long measurement times and the necessity to take samples, which always comes with unwanted waste production, it's not a suitable tool for process monitoring. Furthermore, the minimum detectable activity of about 10^9 Bq is rather large compared to other methods. The main focus is in tritium accountancy in case of waste disposal of tritiated components. As it is not an inline measurement method it can't be used for any of the three application scenarios.

Gas chromatography is an important standard tool for tritium accountancy as it is able to do a composition monitoring of tritiated gas mixtures. Nevertheless, due to the long measurement times in the range of hours and the need of sample taking it is neither suitable as process monitor nor as high stability monitor for KATRIN or for the measurement of surface contamination.

Mass spectroscopy is a reliable standard tool which can be used for in-line composition monitoring. If it is carefully calibrated and with no isobaric interferences disturbing the measurement, an accuracy of about ≈ 5 % is achievable. For unknown gas mixtures isobaric inferences can significantly increase the measurement uncertainty. This is further promoted by the trend of tritium to form tritiated molecules with other gas species as discussed in section 2.1. An additional disadvantage is the need for rather low total pressures of below $\lesssim 1 \cdot 10^{-4}$ mbar (depending on the mass spectrometer model) and therefore additional pumping which causes isotopic changes by demixing effects. Due to that it can't be used for any of the three application scenarios.

A method for composition monitoring without the aforementioned disadvantages is laser Raman spectroscopy. It is a fast in-line measurement method which is able to achieve an accuracy of $\leqslant 5$ % and a precision of $\leqslant 0.1$ % [Sch12], [Bab12]. Therefore, a LaRa system is used in KATRIN for gas composition monitoring. However, the activity monitoring inside the WGTS cannot be done by LaRa due to it is large mechanical footprint. Also due to the large mechanical footprint LaRa is hdifficult to integrate in existing facilities, which prevents the use as standard process monitor. Nevertheless, LaRa is in principle able to cover the necessary measurement range. At TLK it is usually used at rather high total pressure of above $\gtrsim (10-100)$ mbar [Stu10a] but the theoretical minimum detection limit is calculated as $4.9 \cdot 10^{-3}$ mbar [Fis14]. Due to the necessity of optical windows, it can't be used for the in-situ measurement of tritium surface contamination without significantly influencing the adsorption/desorption behavior within a sample chamber.

The standard tool for process monitoring at TLK are ICs. For the CAPER process alone about 20 ICs are necessary. ICs can be used inline, they are comparable fast, cheap and compact [Wag11]. This makes them easy to integrate in experimental facilities. ICs are usually operated at constant total pressures to exclude pressure dependent effects on the measurement results. They are able to measure traces of tritium in the range of 10^4 Bq/m^3. The achievable accuracy of ICs is in the range of $\leqslant 5$ % [Wag11]. Existing disadvantages are the need for rather high total pressures of above $\gtrsim 100$ mbar and the

Table 2.1.: Main analytical methods at TLK and details on performances achieved at TLK (except *) (CALO: calorimetry, IC: ionization chamber, BIXS: Beta induced X-ray spectroscopy, GC: gas chromatography, MS: mass spectrometry, LARA: laser Raman spectroscopy, LSC: liquid scintillation counting; IR: infrared spectroscopy). According to [Dem12].

Method	Measurement range	Measurement time in (s)	Pressure range in (mbar)	In-line	Achievable accuracy/precision	Reference	Maturity level
CALO	$(10^9 - 10^{16})$ Bq total activity	$3 \cdot 10^4 - 7 \cdot 10^5$		no	$< 1~\%$	[Bue13]	std. method
GC	$(10^{10} - 10^{17})$ Bq/m^3	$(2700 - 5400)$ s		no	$\leqslant 5~\%$	[Koe09]	std. method
MS	$(10^{12} - 10^{17})$ Bq/m^3	10 s	$(10^{-12} - 10^{-4})$	yes	no data		std. method
LaRa	$(3 \cdot 10^{11} - 10^{17})$ Bq/m^3	$(2 - 1000)$ s	$(10^1 - 10^3)$	yes	$5~\%/ \leqslant 0.1~\%$	[Sch13a]	R&D
IC	$(10^{4*} - 10^{17})$ Bq/m^3	15 s	$(10^2 - 10^3)$	yes	$5~\%$	[Wag11]	std. method
BIXS	$(10^8 - 10^{17*})$ Bq/m^3	$(1 - 1000)$ s	$(10^{-5} - 10^3)$	yes	$5~\%/\leqslant 0.1~\%$	[Bab12]	R&D

strong pressure and gas species dependency. Due to the need of such high total pressures and the limited precision it cannot be used as high stability monitor for KATRIN. In-situ measurement of surface contaminations is not possible as only gaseous tritium can be measured.

Each of the discussed analytical tools has specific disadvantages which limit the field of application in the closed tritium cycle of the TLK. Furthermore, there are also analytical gaps when it comes to tritium monitoring, especially in the pressure range between 10^{-4} mbar and 10^2 mbar.

Currently, open issues regarding tritium analytics at TLK which have to be tackled are

1. the development of a tritium process monitor and accountancy tool according to the requirements in section 2.2.1,

2. a benchmark of the designed high stability activity monitor of the KATRIN tritium source and

3. an instrument for the in-situ investigation of surface contaminations of arbitrary solid sample materials according to the requirements in section 2.2.3.

These open issues are in the main focus of this work and a promising method for it is Beta Induced X-ray Spectrometry (BIXS). This is illustrated in detail in the following sections which define the goals of this work.

2.3. Goals of this work

The main goal of this work is the development of tritium analytical tools based on the BIXS method. Specific goals follow from the needs of the extensive tritium infrastructure operated at TLK and the next-generation neutrino mass experiment KATRIN.

Accordingly to the three discussed activity monitoring and accountancy application scenarios in closed tritium cycles, the three goals of this work are defined in the following sections. Each goal comprises the development and/or characterization of an analytical system based on the BIXS method but with very different design foci.

2.3.1. Tritium process monitoring in closed tritium loops

Tritium process monitoring in the closed tritium cycle of the TLK is essential for technical and licensing reasons. There are several standard tools available for that, but each with significant limitations regarding its application scenarios. The aim of this work is the design and characterization of a new activity monitor for gaseous tritium based on the BIXS method. It shall fulfill the technical requirements as listed in section 2.2.1 as good as possible. Of peculiar interest is thereby the inline- or online-monitoring ability. This becomes more and more important for tritium throughputs. Furthermore, it should fill the analytical gap in the pressure range between 10^{-4} mbar to 10^2 mbar. The specific question which must be answered are:

Is tritium inline activity monitoring possible by a dedicated BIXS chamber? Can it fill the analytical gap for total pressures between 10^{-4} mbar and 10^2 mbar? What is the level of gas species dependency at higher pressures? Is it possible to monitor trace of tritium on the 10 ppm level in a helium process gas stream of about one bar?

2.3.2. High stability activity monitoring of the KATRIN tritium source

One of the major tasks in neutrino physics is the model-independent measurement of the neutrino mass. Great efforts are being made by the KATRIN collaboration to achieve this with a next-generation neutrino mass experiment. The control and monitoring of the WGTS source stability is one of the crucial tasks to achieve the aimed sensitivity on the neutrino mass. A BIXS monitoring system will be used in KATRIN to detect potential source strength fluctuations on the 0.1 % level in less then 1000 s measurement time. In this work the performance of the KATRIN BIXS system is studied by Monte Carlo simulations. The specific questions which must be answered are:

What is the expected count rate of the BIXS-detectors under normal KATRIN operation? What measurements are required to detect activity fluctuations of the WGTS on the 0.1 % level? To what amount will adsorbed tritium on the rear wall or on the X-ray windows contribute to the detector count rate?

2.3.3. Tritium surface contamination measurement

Surface contamination by tritium adsorption on and absorption in first wall materials of tritium leading systems is an ever-present problem in tritium technology. For a BIXS monitoring system as in KATRIN, which aims for a sensitivity on activity fluctuation on the 0.1 % level, this is of peculiar interest. Tritium surface contaminations can produce an increasing background signal which potentially makes the detector blind for small activity fluctuations. The aim of this work is the design and construction of a specialized experimental facility for the measurement of tritium surface contamination on arbitrary solid samples. First tritium measurements shall be performed with a gold-coated beryllium sample as it is of special relevance for the KATRIN BIXS system. Monte Carlo simulations must be performed to study systematic uncertainties and for data analysis of the tritium measurements. The specific questions which must be answered are:

Is it possible to measure tritium adsorption inline on gold-coated beryllium with sub-monolayer sensitivity? What amount of surface contamination is expected at exposure pressures in the range of 10^{-5} mbar to 10^{-3} mbar? Is there a saturation effect in surface contamination at a given exposure pressure? What are effective decontamination strategies?

3. Introduction to beta induced X-ray spectrometry

Beta **I**nduced **X**-ray **S**pectrometry (BIXS) is based on the use of bremsstrahlung X-rays for quantitative measurement of tritium activity in media as gases, liquids or solids. This technique was already known in the 1960s [Wes60] and is especially important for tritium process monitoring and tritium accountancy in closed tritium loops with high tritium throughput as in [Tor05], [Mat06], [Mat08] and [Bab12].

The basic processes happening in a BIXS system are described by the theory of tritium β-decay and the theory of interaction processes of β-electrons and X-ray photons with matter (see chapter 3.1). With that, it is possible to understand the basic design of a BIXS systems for the monitoring of tritiated media (see chapter 3.2). Among other things, the design strongly depends on the used detector technology. An explanation of the basic functional principle of the used detector in the context of this work, a silicon drift detector, is given (see chapter 3.3). A useful tool for geometrical optimization of such monitoring systems is GEANT4, a Monte Carlo simulation tool which can calculate low-energy electron transport through matter and production and transport of secondary particles as X-ray photons. Eventually, a basic introduction to GEANT4 is given and first Monte Carlo simulations with a simplified BIXS setup are performed (see chapter 3.4).

3.1. Basic theory

BIXS is a non-invasive measurement method for activity monitoring of β-radionuclides. It can be used for tritium monitoring in liquids [Wes60], solids [Tor05] and gases [Roe13], [Bab12]. The basic principle of the BIXS method is shown in figure 3.1. There are three consecutive processes happening in a BIXS system, which are characteristic for the basic function:

1. emission of electrons from the tritium β-decay,

2. electron-matter interactions and

3. X-ray photon-matter interactions.

Particles from the β-decay are emitted isotropically and absorbed in the walls or stopped in the medium. During the absorption process X-rays will be produced and a part of these can be detected by an X-ray detector outside the sample chamber. The measured X-ray intensity is related to the activity in the recipient. The measured X-ray spectrum depends on the β-radionuclide and materials which are used in the setup.
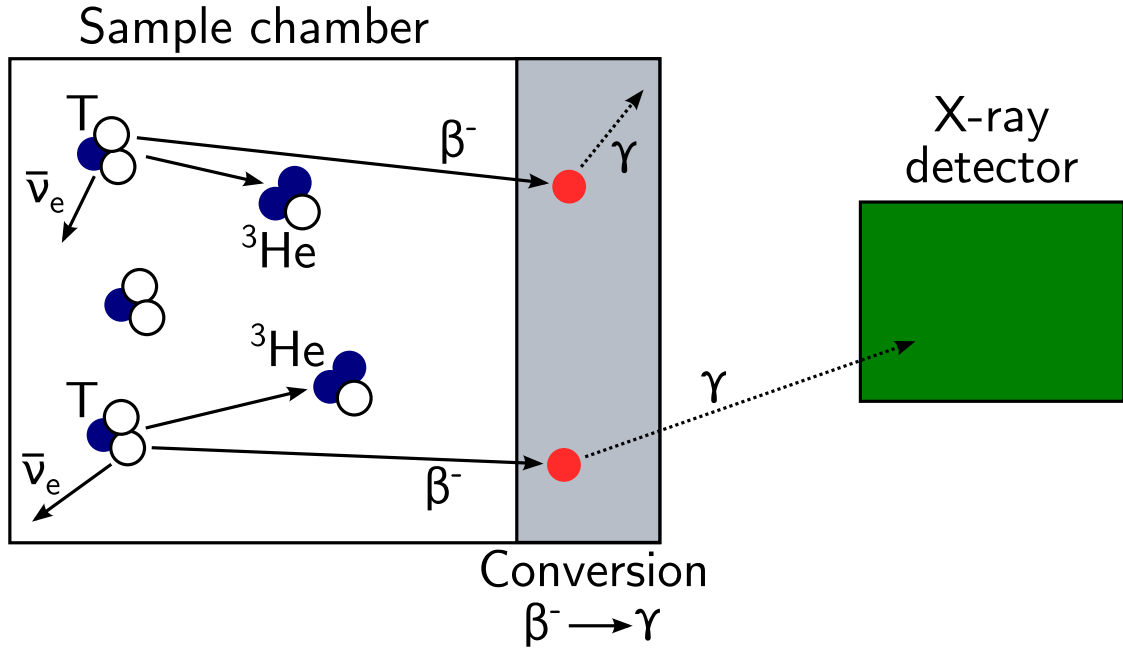
Figure 3.1.: Schematic of the BIXS principle. Tritium decays inside a recipient and the emitted β-electrons are absorbed. During absorption Bremsstrahlung and characteristic X-rays can be produced. A detector outside the system measures the X-rays.

A short theoretical description of the involved interaction processes is given in the following sections. Thereby the focus is put on the use of BIXS with tritium. This will be used then for the design of the experimental setups and the interpretation of BIXS spectra in chapter 4, 5 and 6.

3.1.1. The tritium β-decay

The tritium β-decay is a weak interaction process, in which a neutron is converted into a proton (see figure 3.2a). During that process an electron and an electron-antineutrino is emitted:

$$^3\mathrm{H} \rightarrow \mathrm{He}^+ + \mathrm{e}^- + \bar{\nu} + Q. \tag{3.1}$$

The energy surplus Q is shared between the kinetic energy of the electron E_{e^-}, the total energy of the electron-antineutrino $E_{\mathrm{tot},\bar{\nu}}$, the recoil energy of the daughter nucleus E_{rec} and excitations of the daughter molecule E_{exc}:

$$Q = E_{\mathrm{e}^-} + E_{\mathrm{tot},\bar{\nu}} + E_{\mathrm{rec}} + E_{\mathrm{exc}}. \tag{3.2}$$

In an approximation, the mass of the daughter nucleus can be treated as infinity and excitations of the daughter molecule can be neglected. In that case, the energy surplus Q is shared between the electron and the electron-antineutrino, which causes a continuous
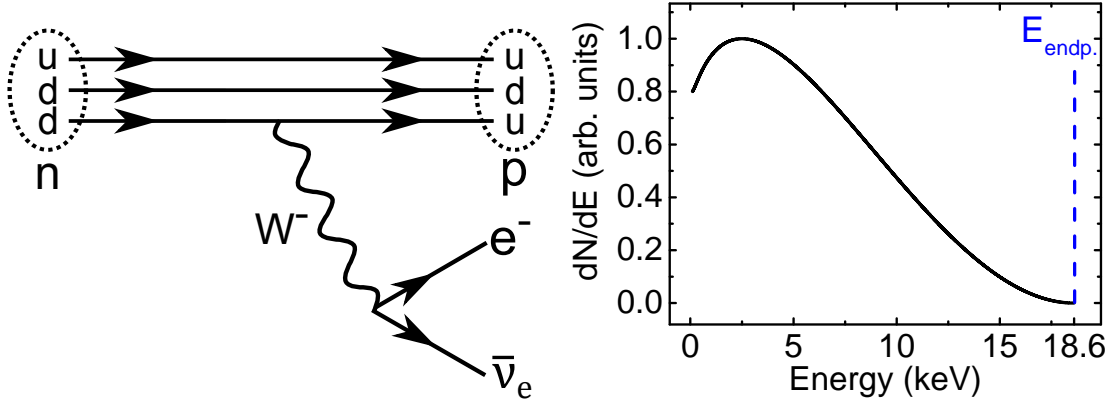
Figure 3.2.: Left: Feynman graph of the single β^--decay. A neutron decays into a proton, an electron and an electron anti-neutrino. Right: Energy spectrum of the β^--decay electrons of tritium.

β-spectrum. In figure 3.2 the resulting electron energy spectrum is shown. The energy spectrum of the β-electron is given by [KAT04]:

$$
\frac{dN}{dE} = C \cdot F(E, Z+1) \cdot p_{\mathrm{e}} \cdot (E + m_{\mathrm{e}}c^2) \cdot (E_0 - E) \tag{3.3}
$$
$$
\cdot \sqrt{(E_0 - E)^2 - m_{\bar{\nu}}^2 c^4} \cdot \Theta(E_0 - E - m_{\bar{\nu}} c^2).
$$

The Fermi function F takes into account the interaction between the emitted electron and the daughter nucleus, E is the kinetic energy of the electron, E_0 is the maximum kinetic energy of the electron in case of $m_{\bar{\nu}} = 0$ and p_{e} is the electron momentum. The Heavyside step function Θ assures that the resulting spectrum is zero for $(E - m_{\bar{\nu}} c^2) > E_0$ which can be regarded as the mathematical description of energy conservation for the tritium β-decay. The constant C is given by:

$$
C = \frac{G_{\mathrm{F}}^2}{2\pi}^3 \hbar^7 c^5 \cos^2\theta_{\mathrm{c}} |M_{\mathrm{nuc}}|^2. \tag{3.4}
$$

Whereby G_{F} is the Fermi constant, θ_{c} is the Cabibbo angle and M_{nuc} is the nuclear matrix element. For a more detailed description of the tritium β-decay with a view to direct neutrino mass measurement see section 5.2. The endpoint energy of $18.5898(12)\,(keV)$ [Nag06] of the electron is also the maximum energy which is available for interaction processes of electrons with matter.

3.1.2. Interactions processes of electrons with matter

The following depiction of charged particle interactions with matter is based on [Kri12]. For charged particles as electrons, there are the following interaction processes with an absorber material:

- elastic scattering by the atomic shell or the atomic nucleus,

- inelastic nuclear reactions,

- inelastic Coulomb scattering by the atomic shell or the atomic nucleus.

Which kind of electron interaction can happen depends on the energy of the electron and the type of absorber material. In elastic processes the electron trajectory changes but the electron energy remains essentially constant. Inelastic nuclear reactions are not relevant for electron energies in the keV-range. For the function of a tritium BIXS-system the energy loss of electrons with a kinetic energy of $\leqslant 18.6$ keV is essential. Therefore, the focus is put on inelastic Coulomb scattering.

Energy loss of electrons in matter is described by the stopping power S_{tot} which is the energy loss per path length in an absorber. It is the sum of the linear collision stopping power S_{col} and the linear radiative stopping power S_{rad}:

$$S_{\text{tot}} = \left(\frac{dE}{dx}\right)_{\text{tot}} = S_{\text{col}} + S_{\text{rad}}. \tag{3.5}$$

Calculations regarding the stopping power of electrons in matter are based on theories of H. A. Bethe [Bet32]. Electrons and heavy charged particles must be treated differently here. The linear collision stopping power S_{col} of an electron or positron in units of rest energy $m_0 c^2$ is given by

$$S_{\text{col}} = \left(\frac{dE}{dx}\right)_{\text{col}} = 0.15354 \cdot \rho \cdot \frac{Z}{A} \cdot z^2 \cdot \frac{1}{\beta^2} \cdot R_{\text{col}}^*(\beta) \quad [\text{Kri12}]. \tag{3.6}$$

Whereby ρ is the density of the absorber, Z/A is the nuclear charge number of the absorber divided by the mass number of the absorber, z is the charge number of the electron, $\beta = v/c$ is the beta velocity of the electron and $R_{\text{col}}^*(\beta)$ is a residual function (to be found in [ICRU37]) which is differently for electrons and positrons. For small impact parameters a fraction of the kinetic energy of the electron can be lost by scattering in the Coulomb field of the atomic nucleus or atomic shell electrons. Thereby Bremsstrahlung or characteristic X-rays are produced. The radiative energy loss S_{rad} of an electron in an absorber is given by

$$S_{\text{rad}} = \left(\frac{dE}{dx}\right)_{\text{rad}} = 0.349 \cdot 10^{-3} \cdot \rho \cdot \frac{Z^2}{A} \cdot E_{\text{tot}} \cdot \left(R_{\text{rad, n}} + \frac{1}{Z} R_{\text{rad, e}}\right) \quad [\text{Kri12}]. \tag{3.7}$$

Here E_{tot} is the sum of the rest mass energy and the kinetic energy $(E_0 + E_{\text{kin}})$ of the incident electron and $R_{\text{rad,n}}$ and $R_{\text{rad,e}}$ are residual functions (to be found in [ICRU37]). In figure 3.3 the calculated stopping powers for electrons in gold and beryllium are shown. For electrons in the energy range between 1 keV and 20 keV the total stopping power is strongly dominated by the collision stopping power and only a small fraction of energy per path length goes into radiation. For a 10 keV electron in gold the total stopping power is (16.8 ± 1.7) keV/μm, which means it is easily stopped in less than one micrometer. The actual range of an electron can be calculated by the continuous slowing down approximation (CSDA) [ESTAR]. In figure 3.4 examples for CSDA-ranges of electrons in gold and beryllium are shown.
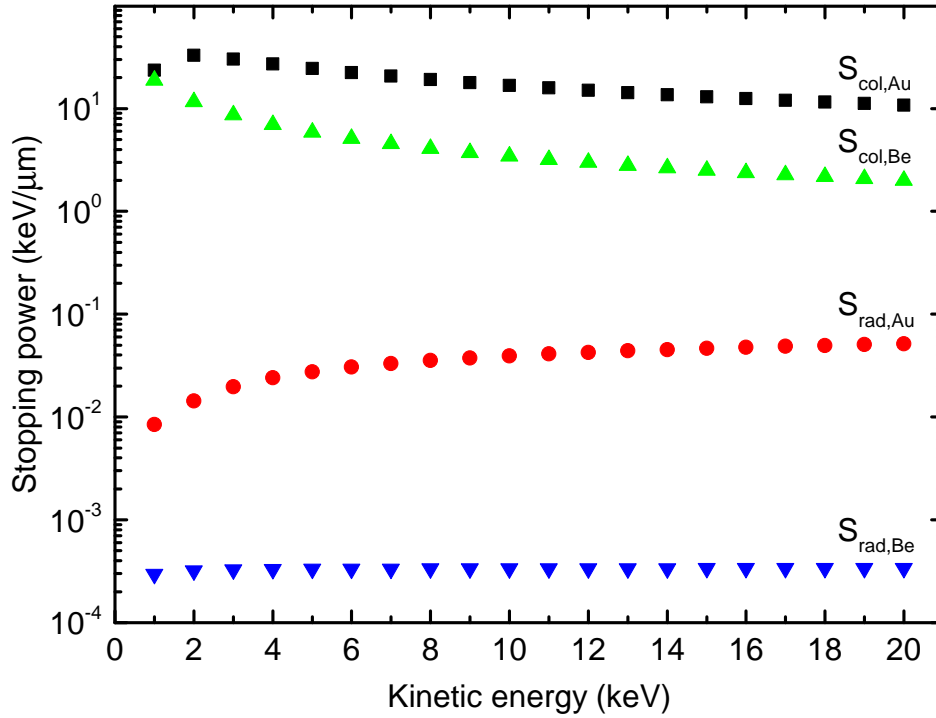
Figure 3.3.: Electron stopping power in gold and beryllium. The uncertainties of the calculated collision stopping powers are estimated to be 10% and for radiation stopping powers about 5% [ESTAR].

A crucial number for a BIXS-system is the radiation yield, which is the fraction of kinetic energy of a primary electron converted into bremsstrahlung. As seen in figure 3.4 it strongly depends on the primary kinetic energy of the electron and the atomic number of the absorber. For every BIXS-system the radiation yield should be as high as possible to produce intense X-ray radiation. This can only be influenced by the type of absorber material. As soon as the X-ray photons are produced in the absorber, interactions of X-ray photons with matter become important.

3.1.3. Interactions of ionizing electromagnetic radiation with matter

Once ionizing electromagnetic radiation is produced there are five possible interaction mechanisms with matter [Kri12]:

- **Coherent scattering:** Depending on the energy range of the photon this is elastic Thomson- or Rayleigh-scattering. The atomic shell of the target atom is unchanged.

- **Incoherent scattering:** A photon with sufficient energy can scatter off a quasi-free electron from the outer atomic shell of a target atom. The photon changes direction and energy and the electron is released from the shell and can do secondary processes e.g. Bremsstrahlung. This photon interaction process is known as Compton scattering.
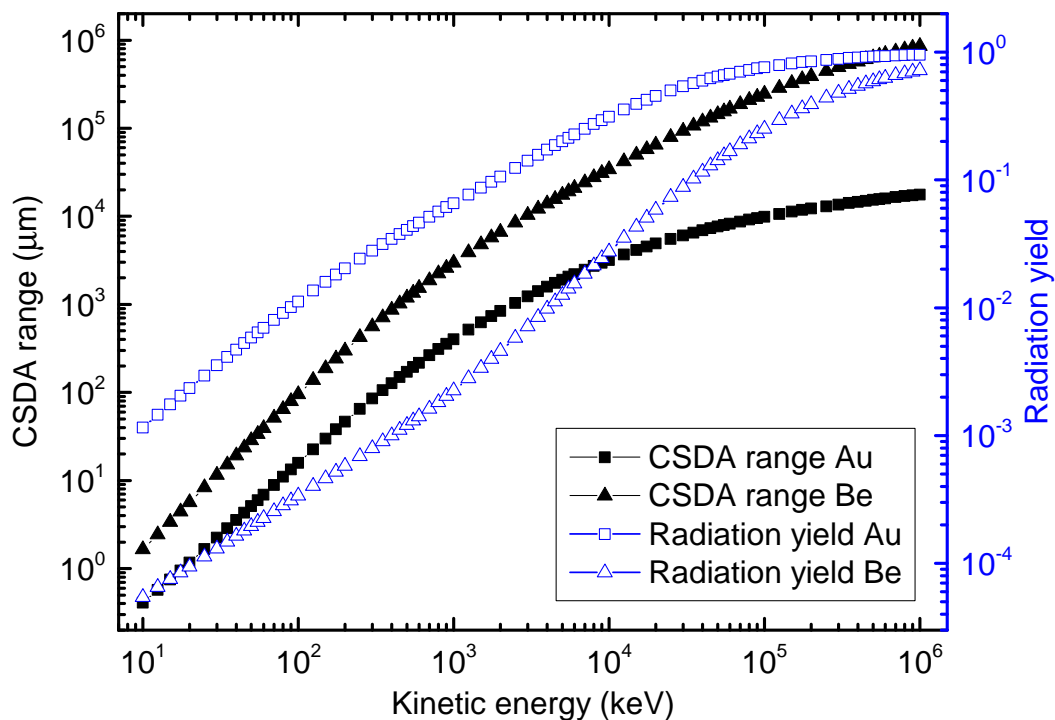
Figure 3.4.: Radiation yield and CSDA range of electrons in gold and beryllium [ESTAR].

- **Photoionization:** An electron is released from the atomic shell by photon absorption. The electron gets the energy from the photon minus the binding energy of the electron. The electron hole leads to emission of characteristic radiation or Auger electron emission.

- **Pair production:** A photon with an energy higher than twice the rest mass of an electron ($> 1022\,\text{keV}$) can interact in the Coulomb field of a nucleus and produce an electron-positron pair. The electron can do secondary processes and the positron is usually annihilated by an electron after a short time under emission of secondary radiation.

- **Nuclear photoelectric effect:** Photons in the MeV range[1] can be absorbed by a nucleus or nucleon under emission of a neutron or proton. The nucleus can then become radioactive. The nuclear photoelectric effect is often accompanied by emission of gamma radiation from the nucleus.

In a BIXS system for tritium monitoring only X-ray photons within an energy range of $(0.5 - 18.6)\,\text{keV}$ are relevant. Due to that only the Compton scattering and the photoelectric effect will be further discussed.

Compton scattering
Compton scattering is a process in which a photon scatters off a quasi-free electron and changes momentum direction and wavelength. This process was described by A. H.

---

[1]   The lower energy threshold for the nuclear photo effect is $2.18\,\text{MeV}$ which is needed for the (γ,n)-reaction of deuterium [Cha35].
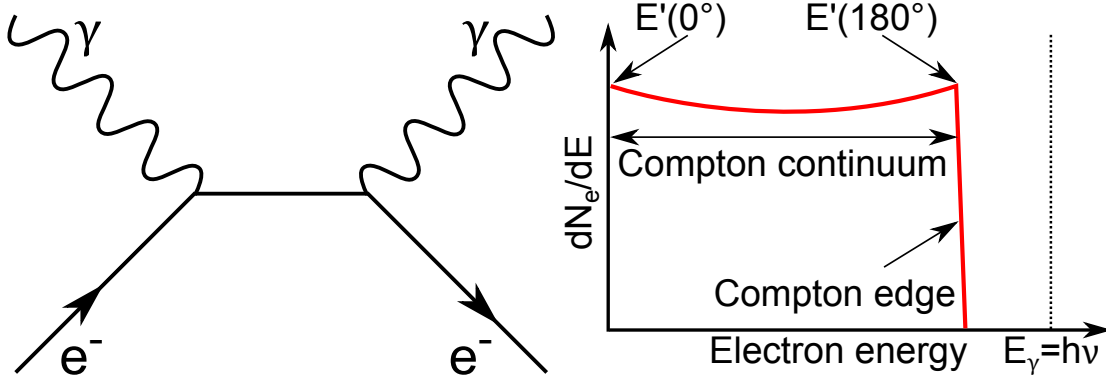
Figure 3.5.: Left: Feynman graph of Compton scattering (s-channel). Right: Energy spectrum of Compton electrons for monoenergetic photons.

Compton [Com23]. A possible Feynman graph of the scattering process is shown in figure 3.5. The rest energy of the scattered photon E_γ' is calculated by

$$E_\gamma' = \frac{E_\gamma}{1 + \frac{E_\gamma}{m_e c^2} \cdot (1 - \cos\theta)} \quad \text{[Kri12].} \tag{3.8}$$

Thereby the initial energy of the photon is E_γ, m_e is the electron rest mass, c is the speed of light and θ the scattering angle. The kinetic energy of the scattered electron is given by

$$E_{e^-} = E_\gamma - E_\gamma' - E_b \quad \text{[Kri12].} \tag{3.9}$$

In most cases the binding energy of the electron E_b is negligible compared to the photon energy E_γ. For a gold target Compton scattering is the dominating electron-photon interaction in the energy range of about 0.5 MeV to 5 MeV [XCOM]. The interaction probability can be calculated by the Klein-Nishina-Formula [Kle29] which gives the energy and angular dependent differential cross sections.

In spectroscopy the Compton effect causes distinctive shaped energy spectra (see figure 3.5). When electrons in the detector are scattered by photons, the energy of the electrons is a continuous function of the scattering angle of the photon. There is a sharp upper limit for the electron energy which is called Compton edge. The maximum energy transfer to the electron happens in case of backscattering of the photon ($\theta = 180°$). For smaller angles the energy transfer to the electron is decreased which causes the so-called Compton continuum in the spectrum. The energy of the Compton edge $E'(180°)$ is calculated according to

$$E'(180°) = \frac{E_\gamma}{1 + \frac{m_e c^2}{2 E_\gamma}}. \tag{3.10}$$

Photoionization

Photoionization is a process in which an atom or molecule interacts with a photon and

gets ionized. The photon is absorbed by an atomic shell electron which gets the energy from the photon E_γ minus the binding energy E_b of the electron:

$$E_{\mathrm{kin,\,e^-}} = E_\gamma - E_b. \qquad (3.11)$$

The electron hole is filled by an outer electron from the atomic shell. The difference in binding energy goes to the emission of a characteristic X-ray or to an Auger electron. There are different notation types for the naming of characteristic X-rays lines in spectroscopy. In this work the Siegbahn notation is used. Table A.1 gives an overview of the most important lines in different notation types.

The theory of photoionization is described in [Hei54]. The probability for photoionization depends on the energy of the photon and the electron density. About 80 % of all photoionization interactions happen on K-shell electrons [Kri12]. As seen in figure 3.6 the probability for photoabsorption is highest when the photon energy corresponds to the binding energy of the electron. For photon energies $E_\gamma << 511$ keV the photoabsorption probability goes with $\rho \cdot Z^n / E_\gamma^3$ and n between 3 to 3.5 [Kri12]. Thereby Z is the atomic number and ρ the density of the target material. For a gold target photoionization is the dominating process for photon energies of less than ≈ 500 keV (see figure 3.6).

Photon attenuation
When a narrow photon beam traverses matter there is a progressive loss of photons and consequently energy from the beam which is called photon attenuation. Any of the processes described in section 3.1.3 can cause photon losses from the beam and some of them also energy losses. Attenuation losses from a narrow monoenergetic photon beam are calculated by an exponential law [Kri12] of the form

$$I(x) = I_0 \cdot e^{-\frac{\mu}{\rho}\rho x}. \qquad (3.12)$$

Where $I(x)$ is the photon intensity of the beam at a material thickness x, I_0 is the initial photon intensity, μ is the linear attenuation coefficient and ρ is the density of the target material.

There is a direct relation between the linear attenuation coefficient and the cross section for photon interaction probabilities. The total cross section σ_{tot} of a photon which traverses a material is given by

$$\sigma_{\mathrm{tot}} = \sigma_{\mathrm{coh}} + \sigma_{\mathrm{incoh}} + \sigma_{\mathrm{photo}} + \sigma_{\mathrm{pair}} + \sigma_{\mathrm{nuc}}. \qquad (3.13)$$

In which every term represents the cross section for one of the interactions listed in section 3.1.3. The relation to the linear attenuation coefficient μ is given by

$$\frac{\mu}{\rho} = \frac{\sigma_{\mathrm{tot}}}{uA}. \qquad (3.14)$$

Where ρ is the material density, σ_{tot} is the total cross section, u is the atomic mass unit (1/12 of the mass of ^{12}C in the ground state) and A is the relative atomic mass of the target element. Usually the so-called mass attenuation coefficient μ/ρ is the listed quantity. This avoids the necessity to list these numbers for different target densities. Numbers for different target materials and photon energies can be found in [FFAST].
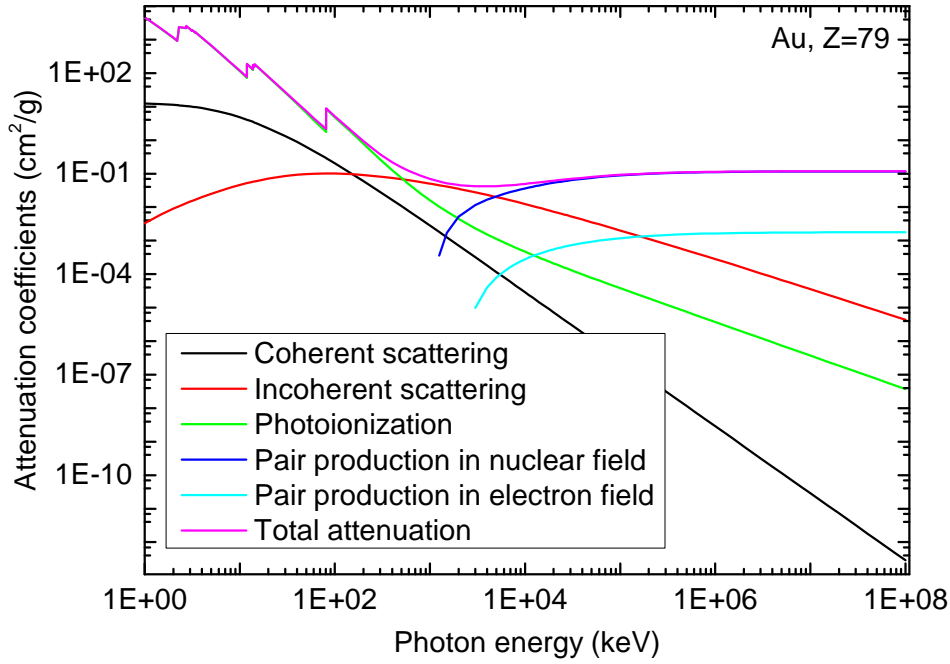
Figure 3.6.: Attenuation coefficients for photons hitting a gold target for different interaction mechanisms [XCOM].

The mass energy absorption coefficient μ_{en}/ρ is another important quantity which can be used to calculate the energy transfer from a photon beam to the electrons of a target material. Secondary electron processes which again generate photons are thereby taken into account. For a detailed explanation see [FFAST]. As seen in figure 3.7 the difference between the mass energy absorption coefficient and the mass attenuation coefficient becomes significant for higher photon energies.

Beam hardening
As the mass attenuation coefficient strongly depends on the energy (see figure 3.7) the spectral shape of a photon beam traversing a target material changes. Especially low-energy photons have much higher absorption probability. Low-energy X-ray radiation (often called soft radiation) is filtered by thin targets while high-energy X-rays (often called hard radiation) can traverse much easier. Spectral deformations due to that are called beam hardening. An example for beam hardening in a BIXS system is given in section 3.4.

3.2. Basic design of a BIXS system for the monitoring of tritiated gases

In figure 3.1 the basic principle of a BIXS tritium activity monitoring system is shown. Depending on the actual application there are a multitude of requirements (see sections 4.1, 5.2 and 6.2) regarding such tritium activity monitoring systems. Some of the requirements which all the aforementioned systems have in common are
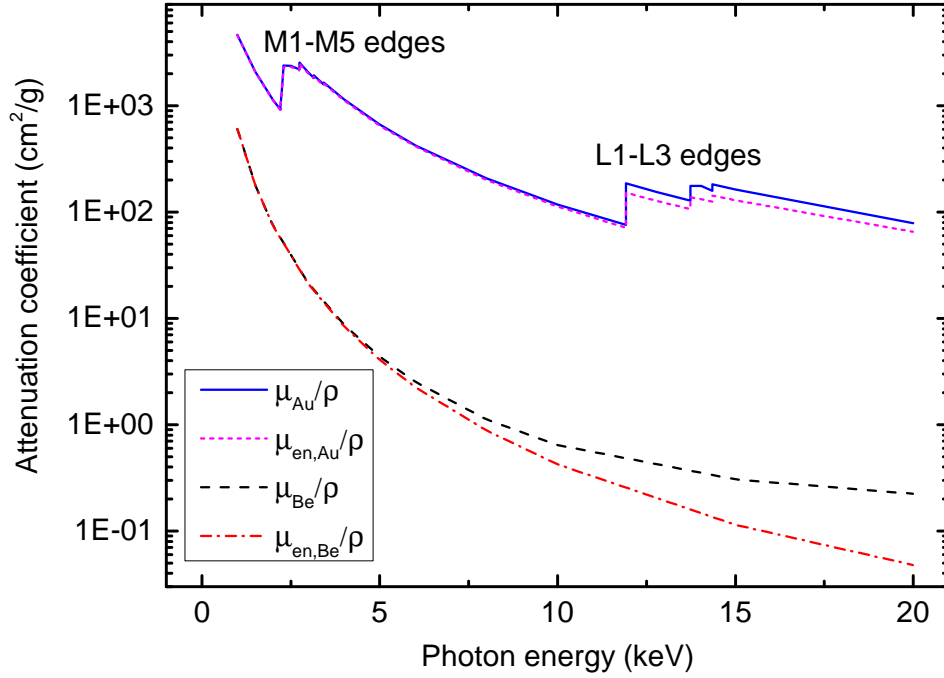
Figure 3.7.: Attenuation coefficients for photons hitting a gold/beryllium target [FFAST].

1. a high sensitivity,

2. a short measurement time and

3. a low minimal detectable activity.

All three of the requirements strongly depend on the measured X-ray intensity. To optimize this, there were three key concepts realized in the context of this work:

1. An inner gold coating of the first containment is used to maximize the X-ray production.

2. A gold-coated beryllium window is used to maximize X-ray production and X-ray transmission to the detector.

3. A low-noise silicon drift detector (SDD) is used for the detection of the low-energy X-rays.

In the following these three key concepts will be shortly motivated.

Maximizing the produced X-ray intensity
A BIXS activity monitoring system for tritium is based on the measurement of X-rays which are produced by tritium β-electrons. Comparing with equation 3.6, 3.7 the radiation losses of an electron in matter go with $S_{\mathrm{rad}} \propto Z^2/A$ while collision losses go with $S_{\mathrm{col}} \propto Z/A$. To maximize the X-ray intensity the walls of the containment should therefore be made of or coated with a high Z material. A strong candidate for this would be gold with an atomic number of $Z = 79$. Simulation results regarding the bremsstrahlung production of β-electrons hitting a gold target are given in section 3.4.2.
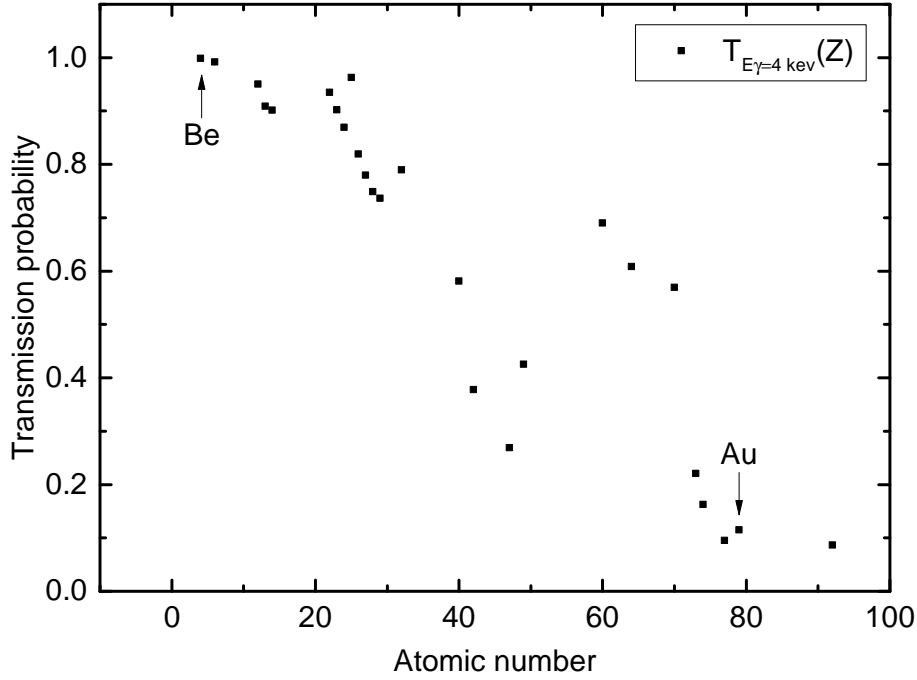
Figure 3.8.: Transmission probability for X-ray photons with an energy of 4 keV hitting a target with a thickness of one micrometer [FFAST].

Maximizing the transmitted X-ray intensity

Once the X-ray photons are produced they must reach the detector. That means the transmission probability and radiation characteristics (X-ray intensity depending on the solid angle) are important. Figure 3.8 shows the transmission probability of 4 keV X-ray photons traversing different target materials with a thickness of one micrometer. There is a trend, showing that low Z materials have higher X-ray transmission probabilities and are therefore preferred as X-ray window materials. Deviations from this trend are mainly caused by photoionization processes and the actual energy position of absorption edges as seen for gold in figure 3.7. Also the thickness of the window should be as small as possible (compare equation 3.12) while being mechanically stable enough to hold differential pressures of about one bar.

Beryllium with an atomic number of $Z = 4$ is mechanically very stable and shows a very high transmission probability even for low-energy X-rays. For the optimal X-ray production the Be-window should be gold-coated which is in contradiction to the requirement of optimal X-ray transmission. There is an optimal gold coating thickness which satisfies both requirements and maximizes the X-ray intensity going to the detector. In section 3.4.2 the optimal gold coating thickness is investigated by Monte Carlo simulations. For the optimal X-ray transmission the Be-window should be as thin as possible. Commercially available beryllium windows[2] with a diameter of 37 mm have a thickness of $\geqslant$ 125 µm. In figure 3.9 the X-ray transmission curves of a beryllium window with a thickness of 125 µm, a gold coating with a thickness of 100 nm and the combined materials are shown.

---

2   Materion Electrofusion
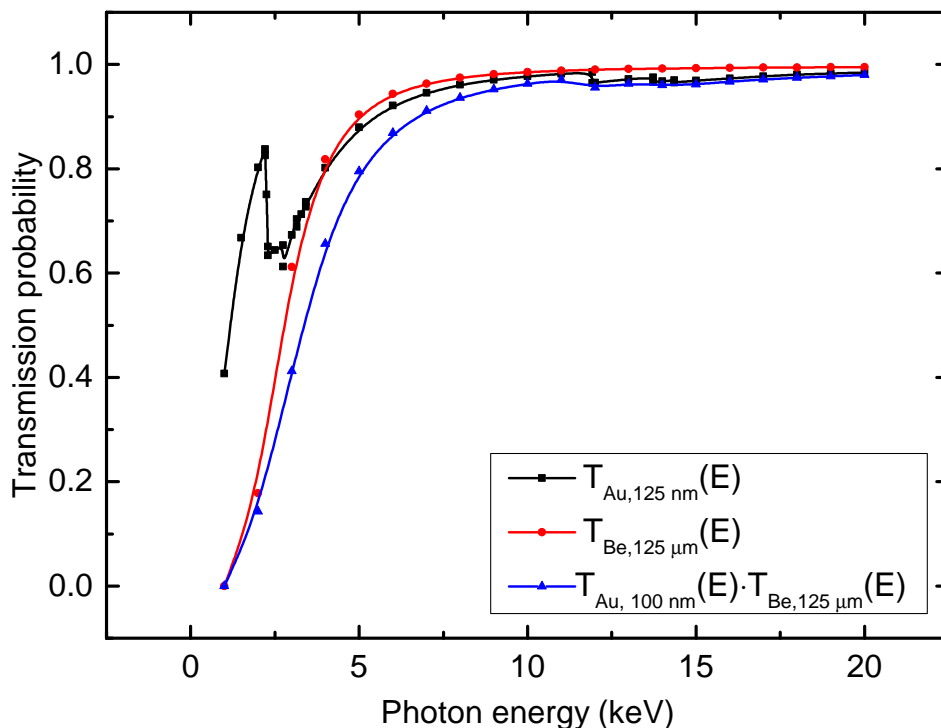
Figure 3.9.: Transmission probability for X-ray photons hitting a gold/beryllium target [XCOM] depending on X-ray energy.

There is also another way to maximize the transmitted X-ray intensity by changing the β-electron momentum direction or energy. This was not part of this work but shall be mentioned after all. An external magnetic field can be used to guide the isotropically emitted β-electrons to the gold-coated beryllium window. Thereby more X-rays are produced next to the detector and therefor the fraction of detected X-ray photons is higher. This was done in a former BIXS experiment at TLK [Roe13] and the detection efficiency of the system was nearly doubled by that. Another option would be guiding and acceleration of the β-electrons by an electrostatic field or a combination of an electrostatic and a magnetic field in the direction of the gold-coated window. This would increase the X-ray intensity and the average X-ray energy. Due to the energy-dependent mass attenuation coefficient it would also increase the transmitted X-ray intensity through the beryllium window. However, to have a significant effect one would need an acceleration voltage of several kilovolts which would cause a number of technical problems.

Maximizing the detected X-ray intensity
There are in principle three ways to maximize the detected X-ray intensity. It can be done by

1. optimizing the geometry of the outer system by placing the detector as near to the X-ray window as possible,

2. using a detector and an X-ray window as large as possible to detect a maximum fraction of the produced X-ray photons and/or
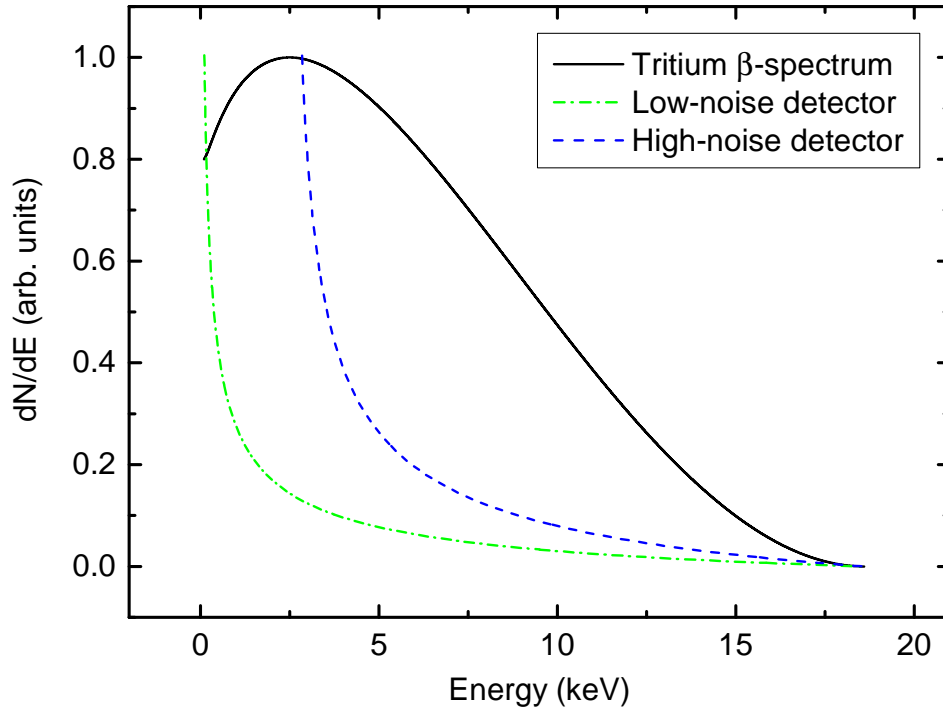
Figure 3.10.: Schematic of the influence of the detector noise on the sensitivity of a BIXS-system. The higher the detector noise the lower the part of the β-spectrum, which can be used for activity monitoring.

3. using a detector technology which is able to detect the X-ray photons in the whole energy range of tritium β-electrons.

The first point should be realized in any case because it is independent of the actual detector system and it makes the system also more compact. The second and third points are usually contrary as they require different detector technologies. Large size X-ray detectors are usually scintillators. With scintillators one is able to enclose very big sample volumes but they have a rather high intrinsic noise level which makes it impossible to detect very low-energy X-ray photons. Semiconductor detectors have a very low intrinsic noise level and are able to detect low-energy X-ray photons but they have small active areas in the range of $25\,mm^2$ and must be usually cooled down to liquid nitrogen temperatures. A compromise for this is using a silicon drift detector (SDD) which is cooled by Peltier elements and is commercially available with active areas of up to $150\,mm^2$. Figure 3.10 illustrates the advantage of using a low-noise detector for tritium activity monitoring by BIXS. In the context of this work all the BIXS-experiments are operated with SDDs. Therefore, the function principle shall be briefly explained in the following.
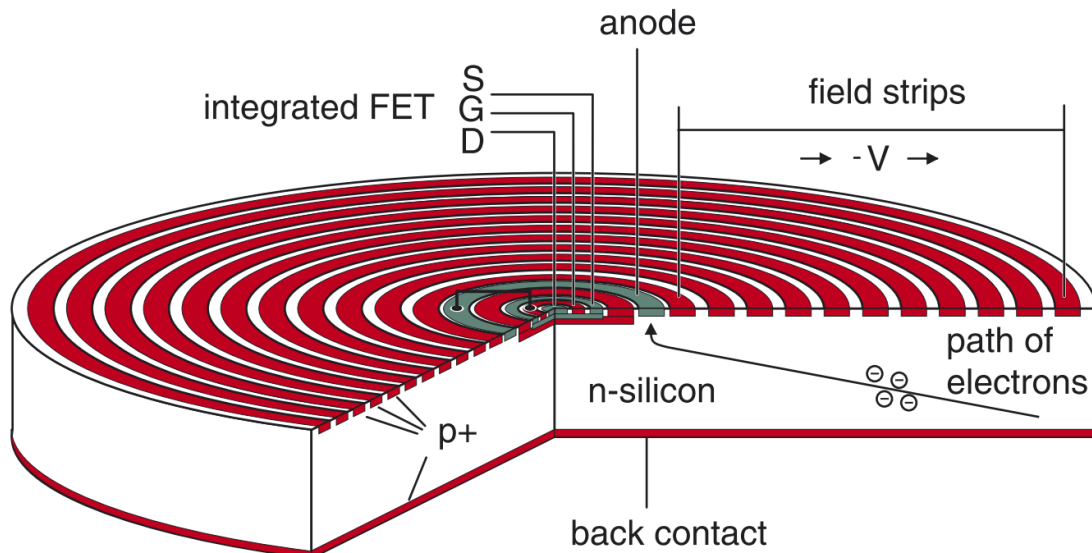
Figure 3.11.: Schematic of a silicon drift detector. The p+ back side contact is the entrance window for the radiation and the depletion voltage is applied to this. On the upper side is a p+ electrode ring structure which defines an electrostatic drift field. Ionizing radiation which enters the depleted detector volume produces electron-hole pairs. Due to the external field the electrons are drifting to the readout anode. A first amplification stage realized with a JFET is integrated on the SDD. Figure from [Egg04].

3.3. Function principle of silicon drift detectors

An X-ray detector for a BIXS-system for activity monitoring of tritium should be a low-noise system, should have a high energy resolution, a large active volume and a high absorption probability for X-rays in the energy range of 0 keV up to 18.6 keV. A suitable system for that task is a Silicon Drift Detector (SDD) which was introduced by E. Gatti and P. Rehak in 1983 [Gat84]. Due to its special geometry (see figure 3.11) it combines a large active area of up to $150\,\text{mm}^2$ with a low electronic noise level respectively a high energy resolution (FWHM $\leqslant 160\,\text{eV}$ at $5.9\,\text{keV}$ X-ray energy).

The correlation between noise level (ENC[3]) and energy resolution (FWHM[4]) is given by

$$\text{FWHM} = 2.335 \cdot w \cdot \sqrt{\text{ENC}^2 + \frac{F \cdot E_\gamma}{w}} \quad \text{[Lec04]}. \tag{3.15}$$

Thereby w is the energy necessary to generate an electron-hole pair ($w_{\text{Si}} = 3.62\,\text{eV}$ [Kno10]), E_γ is the absorbed energy of an X-ray photon and F is the Fano factor (with F_{Si} between 0.085 and 0.137 [Kno10]). The expression $F \cdot E_\gamma/w$ quantifies the noise due to statistical fluctuations of charge carries [Kno10].

---

[3]   In a detector readout systems the ENC (Equivalent Noise Charge) is the absorbed signal charge which gives a signal-to-noise ratio of one. It can be expressed in terms of absorbed energy in eV.

[4]   The FWHM (Full Width Half Maximum) gives the width of an X-ray peak in the energy spectrum at half of the highest point on a peak distribution. It's used as a measure for energy resolution in absolute terms and must be referenced to a specific X-ray energy.
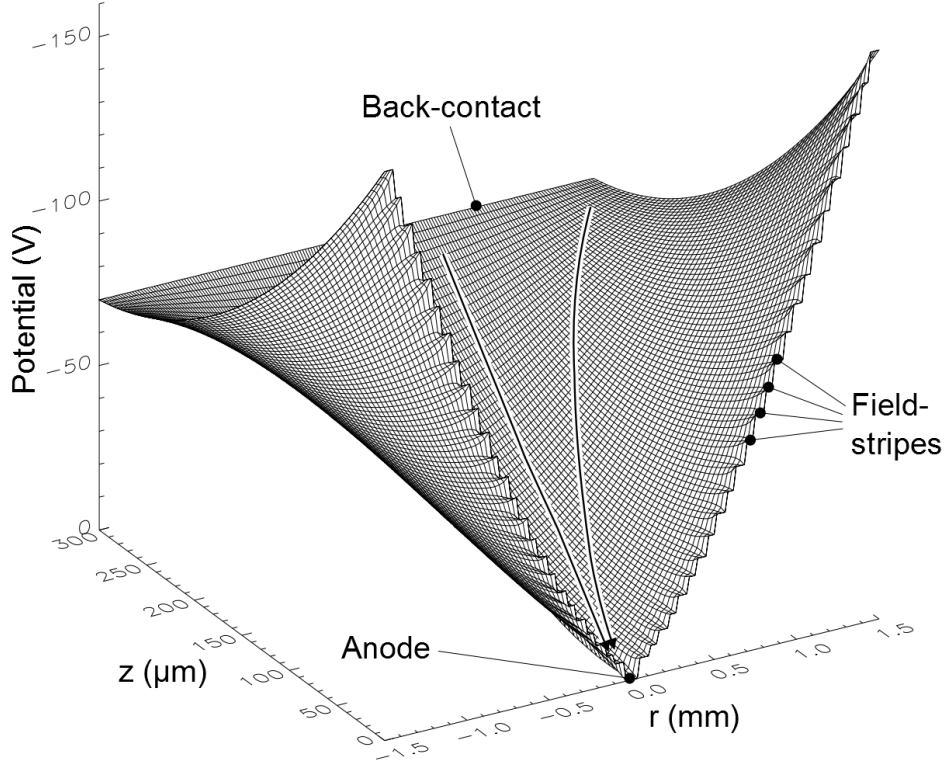
Figure 3.12.: Simulated electron potential of an silicon drift detector [Lec04]. Arrows indicate the electron drifting path to the readout anode.

There are three contributions to the equivalent noise level ENC^2 according to

$$\mathrm{ENC}^2 = \mathrm{ENC}^2_{\mathrm{white, serial}} + \mathrm{ENC}^2_{\mathrm{1/f, serial}} + \mathrm{ENC}^2_{\mathrm{parallel}}. \tag{3.16}$$

These are the series noise contribution, the 1/f series noise contribution and the parallel noise contribution:

$$\mathrm{ENC}^2_{\mathrm{white, serial}} \propto \frac{TC^2}{\tau}, \tag{3.17}$$

$$\mathrm{ENC}^2_{\mathrm{1/f, serial}} \propto C^2 \text{ and} \tag{3.18}$$

$$\mathrm{ENC}^2_{\mathrm{parallel}} \propto T^{3/2} \mathrm{e}^{-\frac{E_{\mathrm{q}}}{2k_{\mathrm{B}}T}} \tau \quad [\mathrm{Lec04}], [\mathrm{Sze81}]. \tag{3.19}$$

C is the detector capacity, T the temperature and τ the peaking time of the detector. To reduce the electronic noise, it is beneficial to reduce the capacity C of the detector as much as possible. Usually the detector capacity is correlated to the area size of the read-out anode, which implies for conventional semiconductors like pin-diodes, to limit the maximum volume. The special geometry of the SDD makes it possible to have a small read-out area anode while having at the same time a large active volume.

Figure 3.11 shows a schematic of a SDD. The SDD has a characteristic electrode structure which enables the concept of sidewards depletion [Gat84]. The idea is based on a large semiconductor wafer which can be fully depleted by a small n^+ doped electrode and

p$^+$ doped electrodes covering both surfaces of the wafer. The voltage necessary to fully deplete the volume is about four times smaller than for a conventional diode of the same thickness.

The planar p$^+$ back contact is the radiation entrance window. On the opposite side are circular shaped p$^+$ electrodes which are connected to different voltages. These electrodes are generating a parabolic potential (see figure 3.12) inside the n$^-$ doped sensitive detector volume. The potential minimum is at the anode electrode.

Ionizing radiation which enters the depleted sensitive detector volume creates electron-hole pairs. Due to the parabolic potential, holes drift to the p$^+$ contacts while electrons drift to the anode. This inhomogeneous drift field makes the area size of the anode almost independent of the active detector volume and therefore allows small detector capacities.

A further improvement is the integration of an n-channel JFET directly on the SDD which is a first transimpedance preamplifier stage. This avoids additional stray capacitances due to the connection line to an external first preamplifier. Stray capacitances would add to the detector capacity and lower the performance according to equation 3.16.

3.4. Basics of the GEANT4 Monte Carlo simulation software

Monte Carlo methods are a useful tool for physical problems which are too complex to be solved analytically. Monte Carlo methods use random-number generators to simulate many random events, taking into account the probability for different physical interactions which can occur. The result is a summation of many random events and can give an approximate solution for a given problem. Geant4 is a powerful Monte Carlo simulation software toolkit able to simulate the passage of particles through matter.

3.4.1. Introduction to GEANT4

Geant4 (for **Ge**ometry **an**d **T**racking) is a free software toolkit for simulation of particle transport through matter. The two major reference publications for GEANT4 are [Ago03] and [All06]. Originally developed for high-energy physics experiments at SLAC (**S**tanford **L**inear **A**ccelerator **C**enter), LHC (**L**arge **H**adron **C**ollider) and MINOS (**M**ain **I**njector **N**eutrino **O**scillation **S**earch) it is now widely used in medical physics, space-radiation physics and accelerator physics. Geant4 is based on the programming language C++ and developed by an international collaboration. The consistent object oriented implementation makes it easy to integrate in own applications and to replace or modify parts of the Geant4 package in order to adjust to own needs. Geant4 includes functionalities for [Ago03]:

- geometry and materials,
- particle interaction in matter,

- tracking management,

- digitization and hit management,

- event and track management,

- visualization and visualization framework and

- user interface.

There is a large number of example applications included in Geant4 to demonstrate all of these functionalities. The example files can also be used as a starting point for own applications. In the context of this work a modified "TestEM5" example of Geant4.9.6.p02 was used for all simulations. Necessary adjustments were made in the detector geometry, material definition, particle generation, selection of the electromagnetic physics package and production cuts.

Before discussing some basic Geant4 simulations some of the keywords often used in Geant4 shall be discussed to clarify the simulation structure.

- **Run:** A run in Geant4 is the analogy to a real experiment and starts with the "/run/beamOn #Events" command. During a run the geometry of the setup and the implemented physics processes cannot be changed. A run has one event loop and is a collection of simulated events.

- **Event:** An event is the basic unit of Geant4 and after successful simulation it contains information about input parameters as primary particles and vertexes and output parameters as track and detector hit collection. An event simulation usually consists of several tracks starting with the primary track calculation and ending with the secondary track calculation.

- **Track:** A track is a snapshot of a particle at a certain time and contains information as energy, momentum, position, time, mass, charge and so on.

- **Electromagnetic physics package:** Electromagnetic physics packages as for example "Livermore" describe all the interaction processes of electrons and photons with matter. Depending on the actual application scenario there are different packages available. Some of them are database-driven whereas other use analytical models or a combination of both.

- **Production cuts:** Production cuts are associated to particles. They are thresholds for the production of secondary particles. They have to be defined as lengths and are translated into energy thresholds by Geant4 for the different regions and materials in a simulation geometry. Production cuts are necessary as some processes have an infrared divergence (as Bremsstrahlung) and would let to an immense amount of secondary particles if not being cut off at a certain energy. Some processes (as decay) can ignore user-defined production cuts.
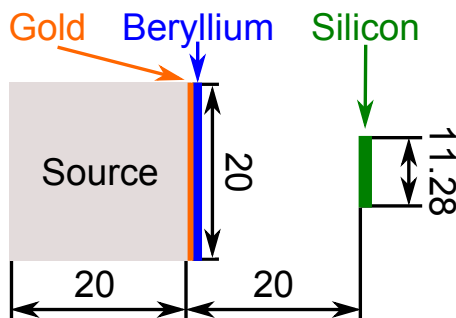
Figure 3.13.: Simulation geometry of a basic BIXS system. Dimensions are given in mm.

3.4.2. Basic BIXS simulations

In this section some basic simulations are discussed which shall demonstrate the perform-ance of the low-energy packages of Geant4. Four subjects are addressed in this section which are useful for the design of a BIXS system:

1. the energy distribution of a typical BIXS spectrum,

2. the optimal gold coating thickness for Bremsstrahlung production and transmission,

3. the influence of the beryllium window thickness on the detection efficiency and

4. the influence of the process gas pressure on the detection efficiency.

This will be studied on a very basic BIXS system with a simulation geometry as shown in figure 3.13. On the basis of these simulation results three important questions, regarding Monte Carlo simulation parameters will also be studied.

1. Which electromagnetic physics package should be used?

2. What are reasonable production cuts?

3. In which cases can a variance reduction technique called Bremsstrahlung splitting be used?

Before proceeding with the Monte Carlo simulations, Bremsstrahlung splitting shall be explained briefly. Bremsstrahlung splitting is a variance reduction technique which can be used to significantly reduce the necessary computing time. When simulating rare events as Bremsstrahlung production a large number of primary particles (electrons) must be simulated to generate one Bremsstrahlung event. In the case of the simple BIXS system as seen in figure 3.13 about 10^4 β-electrons must be simulated to gener-ate a Bremsstrahlung photon and about 10^6 β-electrons must be simulated to produce a Bremsstrahlung photon which hits the detector. To reduce the necessary computing time Bremsstrahlung splitting can be activated. Instead of generating one Bremsstrahlung photon only, a user defined number of Bremsstrahlung photons with different emission angles are generated. The number of produced photons is called splitting factor. In figure 3.14 Bremsstrahlung splitting is shown. Although it can considerably reduce com-puting time, it must be handled with care because it can significantly change simulation results.
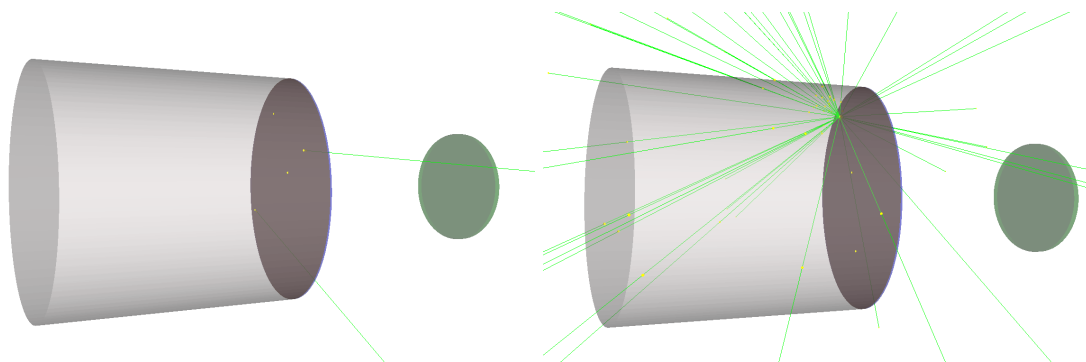
Figure 3.14.: Visualization of Bremsstrahlung splitting for a basic BIXS system. Left: Two Bremsstrahlung events (green line) after 10,000 simulated β-electrons. Right: One Bremsstrahlung event (green line) after 10,000 simulated β-electrons with activated Bremsstrahlung splitting (splitting factor 100).

All the simulations in the following sections were performed with Geant4.9.6p02 with the modified "TestEm5"-example. The used geometry is shown in figure 3.13. Primary electrons were isotropically emitted from the area which is marked as source. The energy distribution of the electrons was the tritium β-spectrum as shown in figure 3.2. If not otherwise denoted the used electromagnetic physics package is "Penelope", the production cuts are set to 10 nm for electrons and gammas and each run consists of 10^9 simulated electrons. The gold coating thickness is set to 100 nm, the beryllium window thickness to 125 µm. The process gas in the source area and in the world volume is hydrogen at $3 \cdot 10^{-20}$ mbar which is the standard setting for a vacuum in Geant4.

3.4.2.1. A typical BIXS spectrum

A typical BIXS spectrum is a superposition of a continuous Bremsstrahlung part and characteristic X-rays. In figure 3.15 the simulation results from five different electromagnetic physics packages are shown. All of them show the typical shape and the characteristic MαX-ray line from gold. The low-energy cut-off is due to the X-ray absorption of the beryllium window. A small line is visible at about 500 eV which is the escape-line of the MαX-ray line.

There are deviations in the X-ray intensity which cannot be explained by the statistical uncertainty. The Bremsstrahlung intensity corresponds well for all physics packages except the "emstandard opt1". Rather large variations are in the intensity of the Au M_α X-ray line. The "Livermore" results correspond well with the "emstandard opt0" results and the "Penelope" results correspond well with the "emstandard opt4" results. The "emstandard opt1" results are between them. As we will see in section 5.5.1, compared to tritium measurements with real BIXS-systems the intensity of the characteristic X-rays fit best for the simulations results of the "Penelope/emstandard opt4" packages.

In figure 3.16 the detection efficiencies of all the physics packages are compared. In the context of this work the detection efficiency is defined as the number of hits in the detector divided by the number of simulated electrons. In case of tritium measurements this is
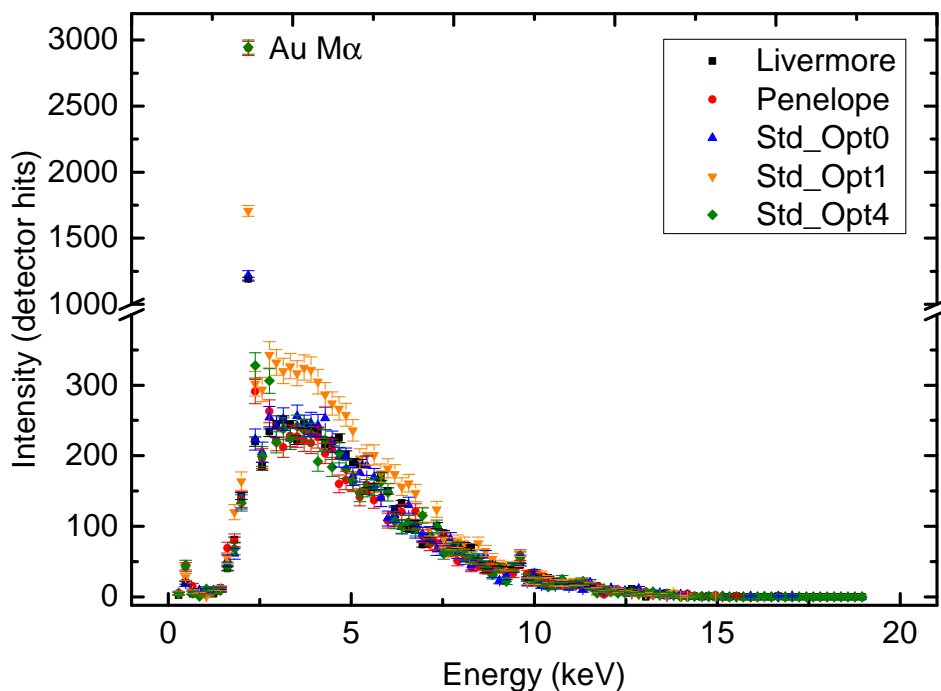
Figure 3.15.: A typical BIXS spectrum simulated with five different electromagnetic physics packages.

the number of hits in the detector divided by the number of tritium decays during the measurement time. Again the "Livermore" results correspond well with the "emstandard opt0" results and the "Penelope" results correspond well with the "emstandard opt4" results. All detection efficiencies correspond within an uncertainty interval of ± 14 %.

Regarding the calculation time there are significant variations for the "Livermore" package which is about 16 % slower and the "emstandard opt1" package which is about 24 % faster than the other packages.

Three of the five physics packages are especially optimized on low-energy electromagnetic physics. These are "Livermore, Penelope and emstandard opt4". For all the following simulations in the context of this work the "Penelope" package will be used, which is reasonable fast and shows good agreement of the simulated spectral shape with experimental results. Nevertheless, systematic errors of up to ± 15.8 % in the simulated detection efficiency as shown in figure 3.16 must be considered due to the choice of the physics package.

3.4.2.2. Optimal gold coating thickness of the beryllium window

The optimal gold coating thickness of the beryllium window is essential for all BIXS systems in the context of this work. In figure 3.17 the resulting detection efficiency for a system as in figure 3.13 is shown. The gold coating thickness was varied in the range of 0 nm to 500 nm. It shows a strong increase in the detection efficiency between 0 nm and 100 nm due to increased X-ray production, a plateau region between 100 nm and
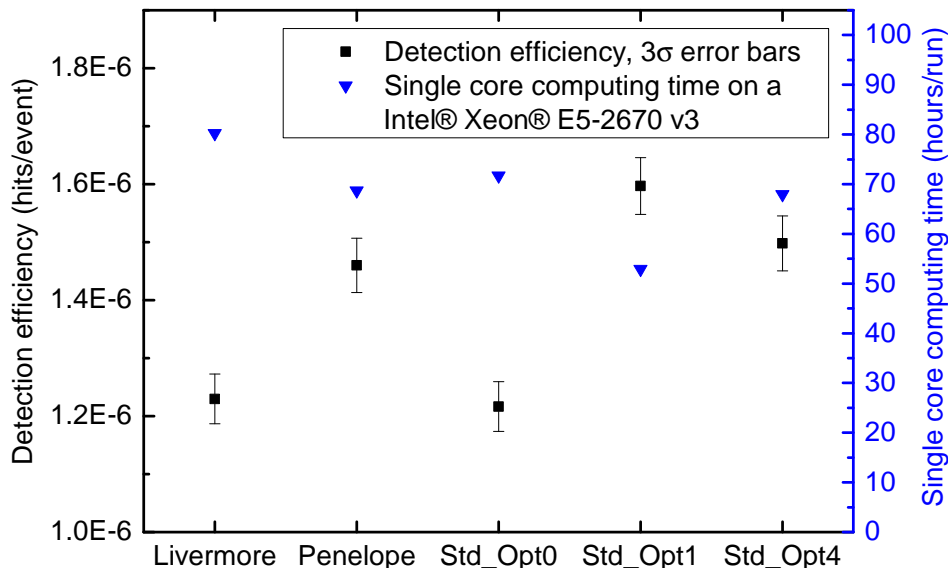
Figure 3.16.: Detection efficiency of a basic BIXS system depending on the used electromagnetic physics package.

200 nm and a slow decrease from 200 nm onwards. The decrease in detection efficiency for gold coatings thicker than 200 nm is caused by increased X-ray absorption.

For real BIXS systems as discussed in chapter 4 and chapter 6 the gold coating thickness should be at the minimum of the plateau region (figure 3.17). For an isotropic source and a more realistic BIXS setup, X-rays are also produced and emitted from the back wall of the sample chamber. These X-rays must traverse the whole gold coating thickness to be detected. Therefore, a high X-ray transparency is preferred. A gold coating thickness of about 100 nm is a good trade-off for most BIXS system for tritium monitoring. The optimal thickness depends on the geometry of the system and must be simulated for each geometry.

For a gold coating thickness of 100 nm the influence of production cuts on the detection efficiency was simulated. The general recommendation is to reduce the cut values until getting the correct physics results. However, very small production cuts can also negatively affect simulation time. Production cuts must therefore be balanced out. The conversion from a user defined cut in range to an energy threshold for a specific region is done for each particle and for each region in the simulation by Geant4. However, the lowest limit is defined by a low-energy threshold which is $E_{low} = 250$ eV in this work. User defined production cuts which would result in a lower energy in a specific region are ignored and E_{low} is used instead. In this work cuts are applied to electrons and X-ray photons.

In figure 3.18 the detection efficiency depending on production cuts is shown. Within the statistical uncertainty the results correspond below 100 nm. For higher production cuts the detection efficiency starts to significantly decrease. This is expected as the BIXS spectrum is dominated by low-energy X-rays $\lesssim 5$ keV. Increasing the cuts also means increasing the energy threshold for secondary production and reducing by this the
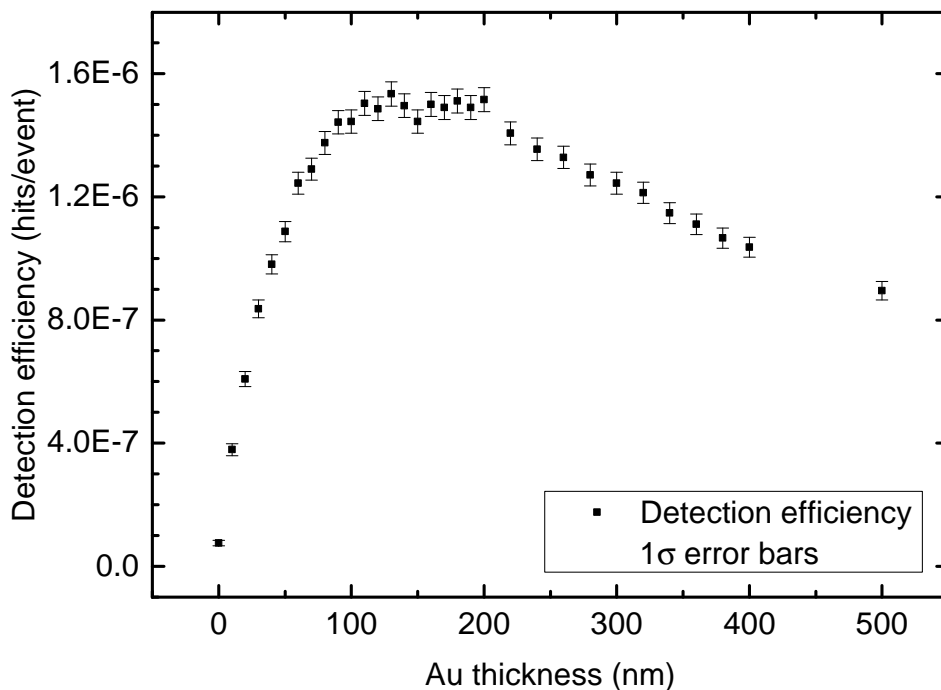
Figure 3.17.: Detection efficiency of a basic BIXS system depending on the gold coating thickness.

total detection efficiency. The difference in computing time for production cuts in the simulated range is negligible as most of the computing time is spent for electron tracking. Therefore, production cuts of 10 nm are applied for the following simulations.

3.4.2.3. Influence of the beryllium window thickness on the detection efficiency and the spectral shape

It is obvious that a beryllium window thickness as thin as possible is best for maximum X-ray transmission. However, there is a technical limit at which such a beryllium window is able to withstand differential pressures of one bar. Commercially available beryllium windows with an diameter of 37 mm have a minimum thickness of about 125 µm. Due to safety considerations it can be necessary to choose thicker beryllium windows.

The influence of the beryllium window thickness on the detection efficiency is studied without and with Bremsstrahlung splitting as a variance reduction technique. The results in figure 3.19 show that one has to be careful when using this technique. There is a difference in the detection efficiency for a 100 µm beryllium window. Without Bremsstrahlung splitting the detection efficiency is about a factor of two higher than with activated. This is expected due to the less distinctive Au M_α-line in the the spectrum with activated splitting (see figure 3.20). In principle one could compensate that by simply applying a constant factor to the detection efficiency.

But although both simulation run series show the expected decrease in detection efficiency for higher beryllium window thicknesses, the trend is rather different and the effect of
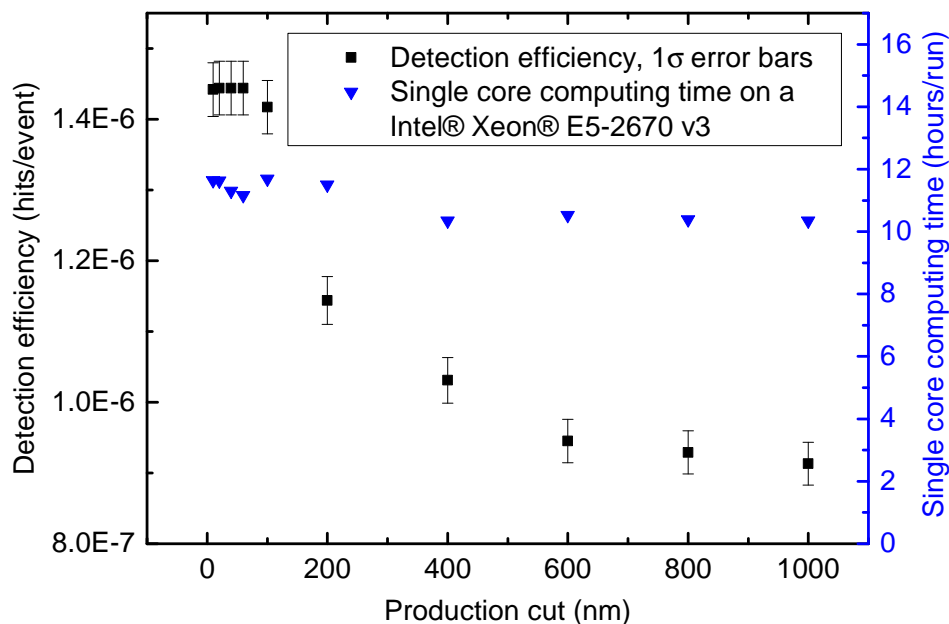
Figure 3.18.: Detection efficiency of a basic BIXS system depending on production cuts. The calculation time for every run (10^9 simulated β-electrons) is given. The same production cut length was applied to electrons and X-ray photons.

Bremsstrahlung splitting cannot be corrected by a constant factor. The reason for this is the different spectral shape of the BIXS spectrum especially in the low-energy part. The distinctive low-energy part of a typical Bremsstrahlung spectrum as shown in figure 3.15, with the rather intense characteristic Au M_α-line, is more influenced by beam hardening than a Bremsstrahlung spectrum produced with Bremsstrahlung splitting. In figure 3.20 the effect of beam hardening, especially on the low-energy part, is shown. This effect leads to a slower decrease in detection efficiency with activated Bremsstrahlung splitting compared to a typical BIXS spectrum. The influence of the beryllium window thickness on the detection efficiency is a typical example when the use of Bremsstrahlung splitting is not advisable.

3.4.2.4. Influence of the process gas pressure on the detection efficiency

As an example where Bremsstrahlung splitting is a useful technique to reduce computing time, the influence of the process gas pressure on the detection efficiency is studied. In this simulation a process gas was applied to the source volume (compare figure 4.1). As a process gas T_2 with varying pressures between 10 mbar and 1000 mbar was simulated. For higher pressures self-absorption of β-electrons in the gas is expected.

As seen in figure 3.21 there is a significant decrease in detection efficiency for process gas pressures above 10 mbar. This leads to pressure-dependent and also gas species-dependent effects which is in detail discussed in section 4.2 for a real BIXS system. The trend of the simulation runs without and with Bremsstrahlung splitting correspond very well within statistical uncertainties. This is due to the fact that no X-ray
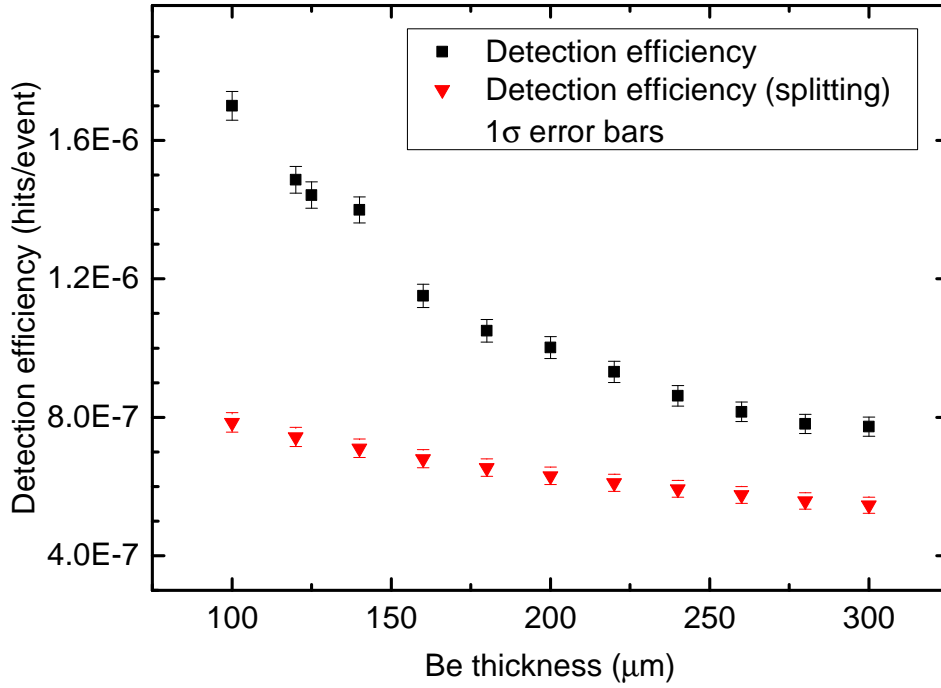
Figure 3.19.: Detection efficiency of a basic BIXS system depending on the beryllium window thickness. Two simulation series were performed without and with Bremsstrahlung splitting (factor 100).
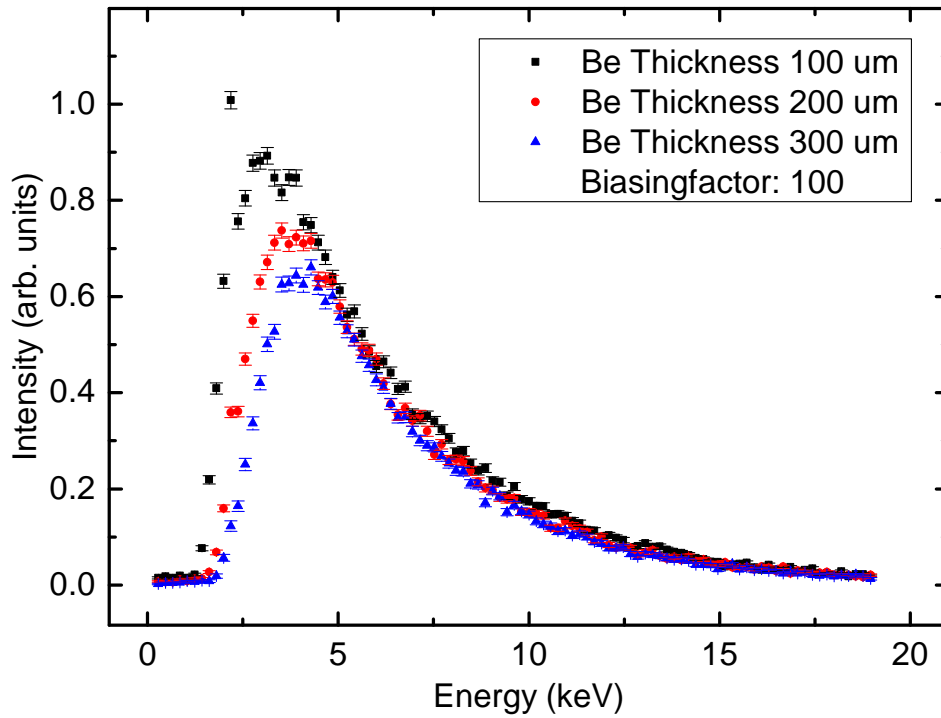
Figure 3.20.: Beam hardening on the example of Bremsstrahlung spectra for three different beryllium window thicknesses. Bremsstrahlung splitting with a splitting factor of 100 was activated.
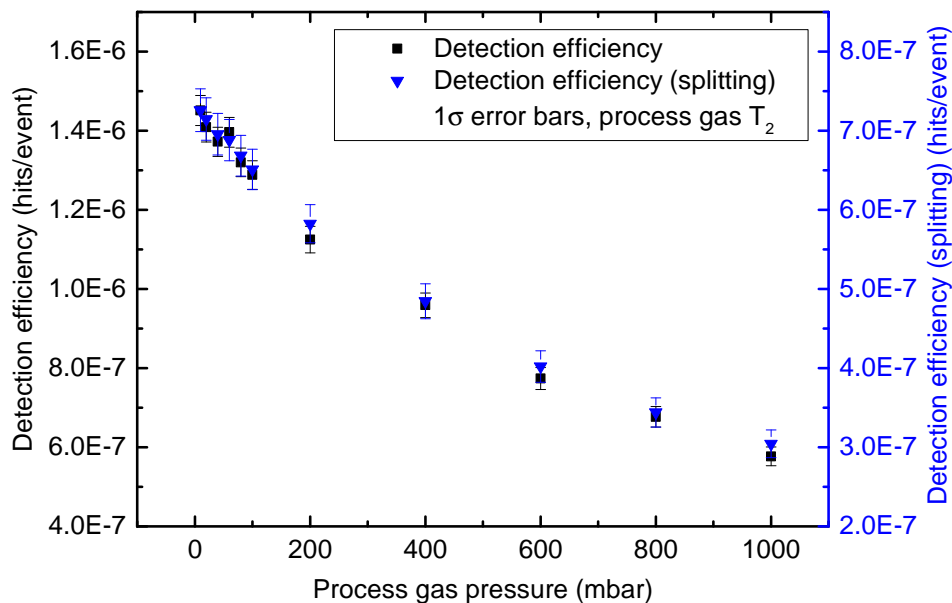
Figure 3.21.: Detection efficiency of a basic BIXS system depending on the process gas pressure without and with Bremsstrahlung splitting (factor 100).

energy-dependent effects influence the detection efficiency compared to the section before. Bremsstrahlung splitting becomes relevant in the gold layer where nearly all the X-rays are produced. Pressure-dependent effects affect foremost the energy distribution of the β-electrons. Therefore, Bremsstrahlung splitting can be applied here and the effect of the different spectral shapes on the detection efficiency can be easily corrected by applying a factor of about two to the detection efficiency. Consequently Bremsstrahlung splitting is a useful tool when studying process gas-dependent effects. Also geometrical effects can be studied as long as no X-ray energy dependent effects are expected.

The discussed Monte Carlo simulations show what amount of systematic uncertainty must be expected, what are good starting points regarding production cuts and when Bremsstrahlung splitting can be used and when not. The optimal gold coating thickness must be simulated for each system as it depends on the geometry but a good compromise is 100 nm. What an increase in the beryllium window thickness means for the detection efficiency is shown but must be decided for the respective system regarding to the experimental parameters and safety considerations. As shown, pressure and gas species dependent effects can also become relevant for real BIXS systems. Starting from these results a real BIXS tritium monitoring system is studied in the next chapter.

4. Tritium process monitoring by TRACE

Activity monitoring of tritiated gas streams is one of the basic tasks in closed tritium loops as discussed in chapter 2. An applicable activity monitoring method for that could be BIXS (**B**eta **I**nduced **X**-ray **S**pectrometry). In the following chapter the design and first tritium measurements of a new tritium activity monitoring device called TRACE (**TR**itium **A**ctivity **C**hamber **E**xperiment) is described. Starting from the physical and technical requirements of such a system (section 4.1) the potential performance is studied on the basis of Monte Carlo simulations (section 4.2). A first prototype was built at TLK (section 4.3) and first tritium measurements were taken (section 4.4). Finally, possible applications of such a system are discussed (section 4.5).

4.1. Physical and technical requirements

In the focus of this work the usability of TRACE as a process monitor in closed tritium loops shall be investigated. There are three application scenarios in the main focus of this work (see section 2.3.1).

1. Is it possible to monitor traces of tritium down to purities of ≈ 10 ppm in a 1 bar helium purge gas stream within several 100 s measurement time with an uncertainty of $\leqslant 5$ %?

2. Is inline tritium activity monitoring of low-pressure process gas streams in a range from 10^{-5} mbar to 10^{0} mbar with a tritium purity of greater than 90 % possible?

3. Is inline tritium activity monitoring of tritiated high-pressure process gas streams in a range from 10^{0} mbar to 10^{3} mbar possible?

In order to enable the BIXS measurement method with the aimed sensitivity and because TRACE is planned as a part of a closed tritium loop a number of physical and technical requirements arises. Furthermore, some technical requirements are due to safety regulations of the TLK [TLA15].

4.1.1. Physical requirements

- BIXS requirements for tritium activity monitoring are:
    - a detector which is able to measure X-rays in the energy range of $(0-20)\,\text{keV}$,

– an X-ray transparent window which is able to protect the detector from tritium contamination and has a transmission of at least 80 % to X-rays in the energy range of $(5-20)\,$keV.

- In order to minimize sources of background for the tritium activity measurements the requirements are:

  – an X-ray detector with a low background signal of the order of $10^{-2}\,$cps,

  – the minimization of tritium adsorption on all inner surfaces visible to the detector,

  – limitation of the field of view of the X-ray detector to surfaces with low tritium adsorption.

- The detection efficiency of the system shall be as gas species independent as possible.

4.1.2. Technical requirements

- Technical requirements for the implementation of the BIXS method are:

  – the X-ray window must be thin in order to maximize X-ray transmission whilst being as leak tight $(< 10^{-9}\,$mbar l/s$)$, and being an effective tritium permeation barrier to prevent the detector from contamination,

  – the X-ray window must withstand differential pressures of up to 1 bar in case of vacuum breaks or during normal operation modes,

  – the X-ray window must be coated with gold with a thickness of about 100 nm,

  – evacuation of the volume with the SDD inside to a pressure of less than 10 mbar must be possible to reduce mechanical loads on the X-ray window and for possible decontamination reasons in case of a window break.

- Technical requirements regarding the vacuum system are:

  – the tritium pressure inside the recipient must be controllable with an accuracy of $10^{-3}\,$mbar,

  – the ability of the system to transfer tritiated waste gas to the TLK infrastructure (CAPER[1] or ZTS[2]),

  – the residual gas pressure inside the recipient must be lowerable to a level of about $10^{-5}\,$mbar.

- The volume of the recipient must be minimized in order to reduce tritium inventory.

---

[1]   The CAPER facility at TLK is a reference process for the Tokamak Exhaust Processing (TEP) system of ITER [Doe08].

[2]   Central tritium retention system of the TLK [Doe08].
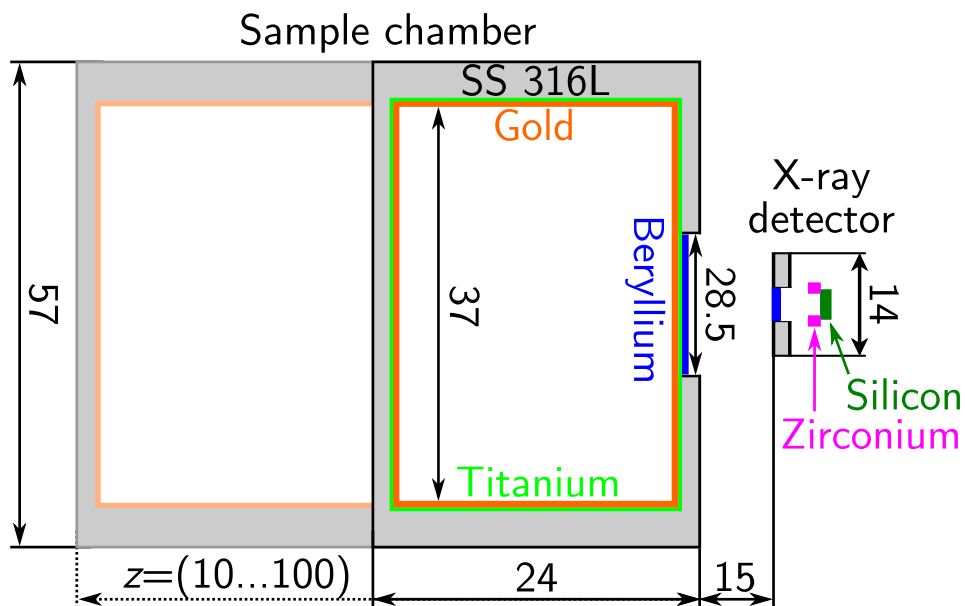
Figure 4.1.: Schematic of the simulated TRACE geometry. The length z of the system was varied between 10 mm and 100 mm in the MC simulations. In appendix A.6 the geometry of the X-ray detector can be found, which is reproduced according to the manufacturer's data for the Amptek® AXR/PA-230 X-ray detector. The original multilayer collimator of the Amptek® detector has an unknown material composition and is therefore replaced by a zirconium collimator in the simulations. Drawing is not in scale. Dimensions are given in mm.

- Furthermore, a vast number of safety requirements according to the technical terms of delivery and acceptance [TLA15] have to be met to operate an experiment at TLK. This comprises materials allowed to use in a tritium containing/processing system, regulations for first and second containment, maximum pressures and temperatures, tritium monitoring systems, tritium accountancy and commissioning procedures.

4.2. Monte Carlo studies of the potential performance of a tritium activity chamber experiment

The design of a BIXS system is always a compromise between contradictory requirements. To study the potential performance and to optimize the geometry according to the mentioned application scenarios (section 4.1) Monte Carlo simulations were done. The basic geometry of the measurement cell used for the simulations is shown in figure 4.1 and it was chosen due to the following reasons:

1. **Compactness:** The system shall be as compact as possible while being able to fulfil the requirements listed in section 4.1.

2. **Standard vacuum parts:** As a process monitoring tool it should be reasonable inexpensive and made of parts which are easily available. The use of standard

Table 4.1.: Overview of the TRACE MC simulations. The denoted CPU time is the needed single core CPU time for all the simulation runs on an Intel® Xeon® E5-2670 v3.

Description	No. of runs	Splittingfactor	Events/run	CPU time (h)
Spectral shape	30	1	$3 \cdot 10^8$	773.2
Spectral shape (splitting)	6	100	$1.5 \cdot 10^6$	8.5
System length	22	100	$1 \cdot 10^8$	64.4
Pressure dependence	46	100	$1 \cdot 10^9$	3577
Gas species dependence	7	100	$3 \cdot 10^8$	57

vacuum components is therefore preferred.

3. **X-ray detector:** As discussed in section 2.2.2 the use of a silicon drift detector is preferable in compact BIXS systems. Due to TLK regulations the detector must be housed inside the primary system which limits the minimum size of the housing.

4. **Flow-through system:** The system shall be able to be used as an inline monitoring tool which requires a flow-through system. Therefore, the sample chamber needs at least two standard vacuum ports which limits the minimum size of the system. The vacuum ports for the flow-through mode are not included in the simulated geometry as there are not in the detectors line of sight.

These design criteria leads to the use of DN40CF standard vacuum parts which have usually an inner diameter of 37 mm. This is enough to house an Amptek® X123 OEM SDD which is shown in figure 4.11. The sample chamber can be varied in length. Nevertheless the minimum length is about 10 mm which would be needed to weld two vacuum ports to the sample chamber in order to use it as a flow-through system. In terms of compactness a reasonable maximum length would be about 100 mm. Standard DN40CF beryllium windows which can withstand differential pressures of $p_{\text{tot}} = 1\,\text{bar}$ have a thickness of 125 µm. The geometry of the X-ray detector is the given geometry of the Amptek® X123 SDD capsule (see appendix A.6). According to the simulation results in section 3.4.2 a gold coating with a thickness of 100 nm is assumed for the inner surfaces of the sample chamber to maximize the detection efficiency. A titanium adherent layer with a thickness of 10 nm is between the gold coating and the stainless steel surface.

An overview of all Monte Carlo simulations is given in table 6.2. For some of the following simulations the above mentioned variance reduction technique of Bremsstrahlung splitting is used. This has been tested by simulation of a typical BIXS spectrum with and without Bremsstrahlung splitting. A comparison of the resulting spectral shapes and detection efficiencies is given in section 4.2.1. The influence of the length of the system on the overall detection efficiency is studied in section 4.2.2. With that, the length of the experimental setup can be fixed and subsequently the influence of the total pressure is studied in section 4.2.3. Gas species-dependent effects on the detection efficiency are investigated in section 4.2.4. In section 4.2.5 conclusions for the TRACE experimental setup are drawn from the Monte Carlo simulations.
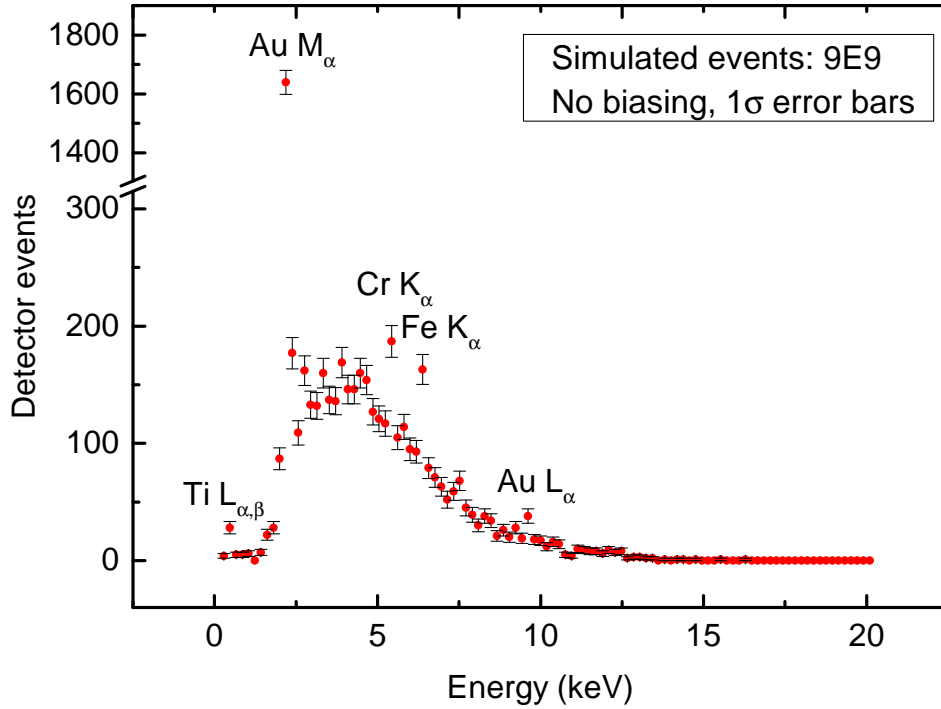
Figure 4.2.: Simulated TRACE BIXS spectrum featuring prominent characteristic X-ray lines of Au, Cr and Fe. The Ti X-ray line coincides with the escape line from Au M_α.

For all the Monte Carlo simulations in this chapter the primary simulated particles were electrons. The starting vectors were homogeneously distributed over the sample chamber volume, the electrons were emitted isotropically and the kinetic energy corresponds to the energy distribution of tritium β-electrons (section 3.4.2). Process gases were simulated according to denoted chemical formulas. In case of no process gas the standard medium for vacuum in Geant4 was used, which is hydrogen at a pressure of $3 \cdot 10^{-20}$ mbar.

4.2.1. Simulated TRACE BIXS spectrum

A first benchmark for the proper function of the Monte Carlo simulations is the successful reproduction of a BIXS-spectrum and the calculation of the detection efficiency. The results can be compared with a former BIXS-experiment [Roe13] with a similar setup. Furthermore the effects of the use of the variance reduction technique of Bremsstrahlung splitting can be studied and validated for the TRACE setup.

For the spectrum simulation a system length of z=24 mm was chosen. Six simulation runs were performed with activated Bremsstrahlung splitting. A splitting factor of 100 was used and $3 \cdot 10^8$ events/run were simulated. A total number of 30 simulation runs were performed without activated Bremsstrahlung splitting and $3 \cdot 10^8$ events/run. No process gas was in the sample chamber.

In figure 4.2 a simulated BIXS-spectrum is shown. It shows the typical spectrum features discussed in section 3.4.2.1. A continuous Bremsstrahlung part is superimposed

by characteristic X-rays. Clearly visible are characteristic X-rays produced by radiation interaction with the inner Au-coating, the Ti-adhesion layer and the dominating constituents of the stainless steel vessel Fe and Cr. The simulated spectrum is not corrected for the limited energy resolution of the detector, which can slightly change the shape of the spectrum. Nevertheless, the bin size of the spectrum of 190.5 eV/channel can be regarded as a good approximation [Roe13],[Sch13b] for the energy resolution of a real SDD detector. To get even more realistic results the simulated spectrum would need to be convoluted with the energy dependent energy resolution function of the used detector system. However, this would only be reasonable for significantly smaller bin sizes than the expected energy resolution of the detector.

The resulting detection efficiency is $(6.41 \pm 0.25) \cdot 10^{-7}$ counts/Bq. For this simulation a single core computing time of 773 hours on an Intel® Xeon® E5-2670 v3 was necessary. To study geometrical, pressure or gas species-dependent effects it is of interest to significantly decrease the necessary computing time. Therefore, the variance reduction technique of Bremsstrahlung splitting was used (see section 3.4.2). As all variance reduction techniques it must be used carefully because it can significantly change the simulation results. A first test was performed by comparing the simulated BIXS-spectra and detection efficiencies with and without Bremsstrahlung splitting. The results are shown in figure 4.3.

With activated Bremsstrahlung splitting (splitting factor 100) the spectral shape changes. Characteristic X-ray lines are now too small to be distinguished from the Bremsstrahlung part. This is expected because the Bremsstrahlung part is increased in size by the splitting factor. If one corrects the results for the splitting factor this means the characteristics are reduced in size. Within the statistical uncertainty the shape of the Bremsstrahlung part with and without splitting is the same. The overall detection efficiency changes by about 33 % from $(6.41 \pm 0.25) \cdot 10^{-7}$ counts/Bq to $(4.31 \pm 0.21) \cdot 10^{-7}$ counts/Bq. The decrease in detection efficiency is dominated by the missing Au M_α-line. Nevertheless the necessary computing time for the spectrum with activated splitting is reduced by a factor of about 100 which is a significant advantage. According to section 3.4.2 calculated detection efficiencies can be corrected for simulations with activated splitting for the missing characteristic X-ray lines afterwards.

4.2.2. Detection efficiency depending on the sample chamber length

As mentioned before the length of the sample chamber can easily be changed between 10 mm and 100 mm. It can be done without making the system significantly more expensive or making it too big to be easily handled. For a longer system one would expect higher count rates at a given tritium partial pressure but also more tritium inventory and probably a higher gas species dependency. Therefore, it is of interest to make the system as compact as possible while being still able to fulfill the application scenarios in section 4.1.

In total 22 simulation runs were performed with activated Bremsstrahlung splitting at a splitting factor of 100 and $2 \cdot 10^8$ events/run. The starting vectors of the electrons were homogeneously distributed over the sample chamber volume while the length of the
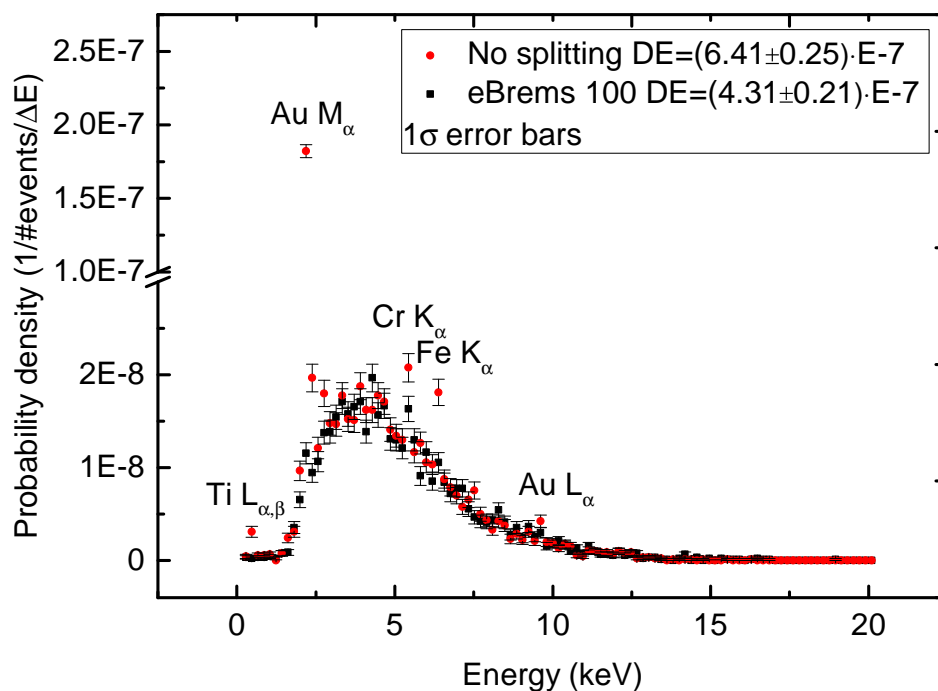
Figure 4.3.: Simulated TRACE BIXS spectrum with and without Bremsstrahlung splitting. With activated Bremsstrahlung splitting the splitting factor was 100.

system was varied between 10 mm and 100 mm. The simulation runs were performed without a process gas and with helium at 1000 mbar as a process gas in the sample chamber.

In figure 4.4 the results of the Monte Carlo simulations for the detection efficiency dependency on the sample chamber length are shown. Without any process gas and therefore no self-absorption effects, there is a strong increase in detection efficiency between 10 mm and 20 mm with a maximum at 24 mm. For longer systems the detection efficiency stays nearly constant (saturation). The same holds for helium as process gas at a pressure of 1000 mbar but the overall detection efficiency is reduced by a factor of five (at z=24 mm). This is due to absorption of β-electrons in the helium process gas.

If one fixes the tritium partial pressure instead of the total activity in the recipient one can calculate an expected number of detector counts for a given tritium partial pressure in the sample chamber depending on the length of the system. This was done and the results are shown in figure 4.5. Again there is a strong increase in the number of detector counts between 10 mm and 24 mm system length and a slower increase between 24 mm and 100 mm.

From these results an overall system length of 24 mm is a good compromise between detection efficiency and tritium inventory or gas species dependency. Also monitoring of 10 ppm of tritium in one bar of helium would be possible. The calculated detector count rate for that is (2.02 ± 0.02) cps which is well above the intrinsic detector background of a silicon drift detector which is of the order of 10^{-2} cps (see section 4.2).
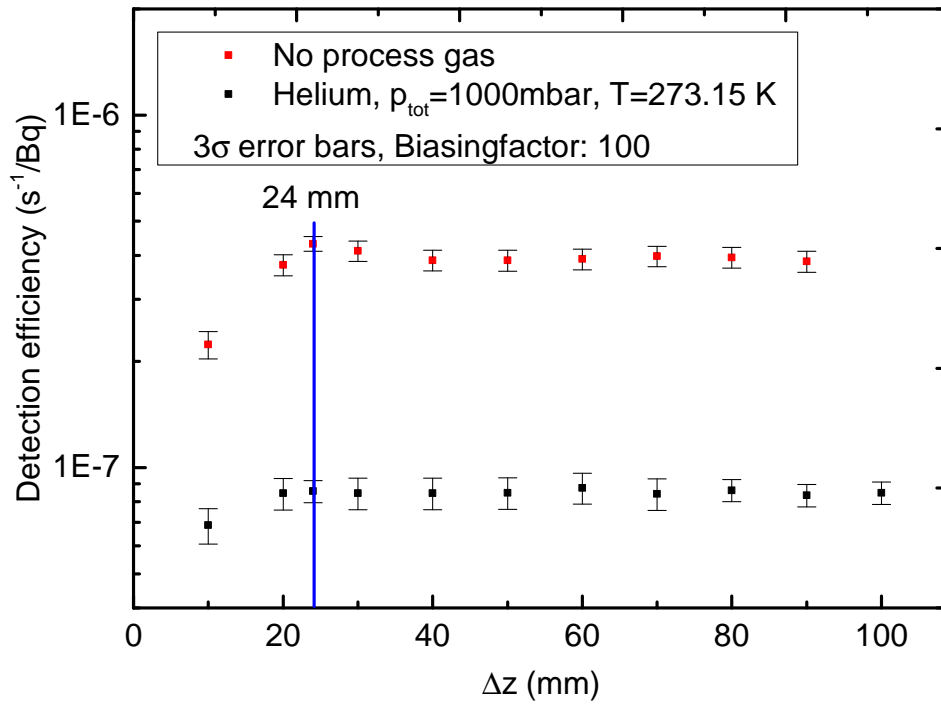
Figure 4.4.: Simulated detection efficiency depending on system length.
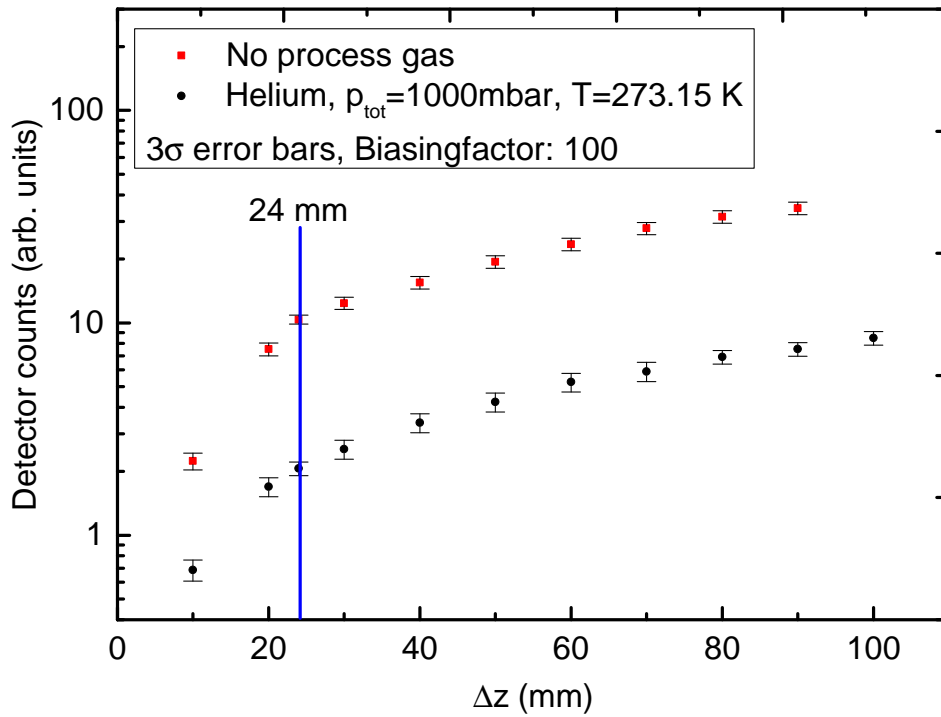
Figure 4.5.: Expected detector count rate depending on system length based on MC simulations.

4.2.3. Detection efficiency depending on the process gas pressure

The detection efficiency of a BIXS system and therefore the measured detector count rate is influenced by the process gas pressure. For low pressures it is expected that the count rate only depends on the activity in the sample chamber. As soon as absorption effects of β-electrons in the process gas become significant one must introduce a pressure correction factor to the measured count rate. In the following simulations it was investigated at which pressure level a correction should be applied to the count rate and what order of correction is necessary.

To study pressure-dependent effects a total of 46 simulation runs were performed with two process gas species (T_2, He). For each run a total of 10^9 electrons were simulated. The sample chamber length was z=24 mm. Bremsstrahlung splitting was activated with a splitting factor of 100.

In figure 4.6 the results of the Monte Carlo simulations are shown. A strong pressure-dependent effect and a rather weak gas species-dependent effect on the detection efficiency is visible. If one accepts uncertainties on the ± 2 % level, count rate measurements with total pressures of up to 10 mbar can be treated as being pressure-independent. For higher pressures one sees a decrease in detection efficiency between 1 mbar and 1000 mbar by a factor of 4.7 (T_2) or 4.1 (He).

Related to the two application scenarios in section 4.1 one can calculate the expected pressure-dependent count rate for a fixed tritium activity in helium or the pressure-dependent count rate in pure tritium.

For pure tritium one sees in figure 4.7 a steady, exponential like increase in the detector count rate for an increasing tritium pressure. Up to a pressure of about 10 mbar a linear-like behavior can be assumed and no pressure correction is necessary. For higher pressures an exponential like behavior due to absorption effects becomes visible and a pressure correction is necessary.

For monitoring traces of tritium in helium partial pressures of up to 1000 mbar a pressure correction factor must be introduced. The total count rate decreases by a factor of 4.1 between 1 mbar and 1000 mbar. Nevertheless, the projected count rate of (2.02 ± 0.02) cps of 10 ppm of tritium in 1000 mbar of helium is high enough to monitor the tritium activity with a 5 % uncertainty level in $\leqslant$ 200 s of measurement time.

4.2.4. Gas species dependency

In figure 4.6 a gas species dependency is already identifiable. As there is a large number of used process gases in tritium handling facilities like the TLK the gas species dependency of a potential BIXS activity monitoring system is of interest.

To study gas species-dependent effects at high pressures 8 Monte Carlo simulation runs were performed each with $3 \cdot 10^8$ simulated electrons. In every run the sample chamber (z=24 mm) was filled with a different process gas species with a pressure of 1000 mbar. Again Bremsstrahlung splitting was activated with a splitting factor of 100.
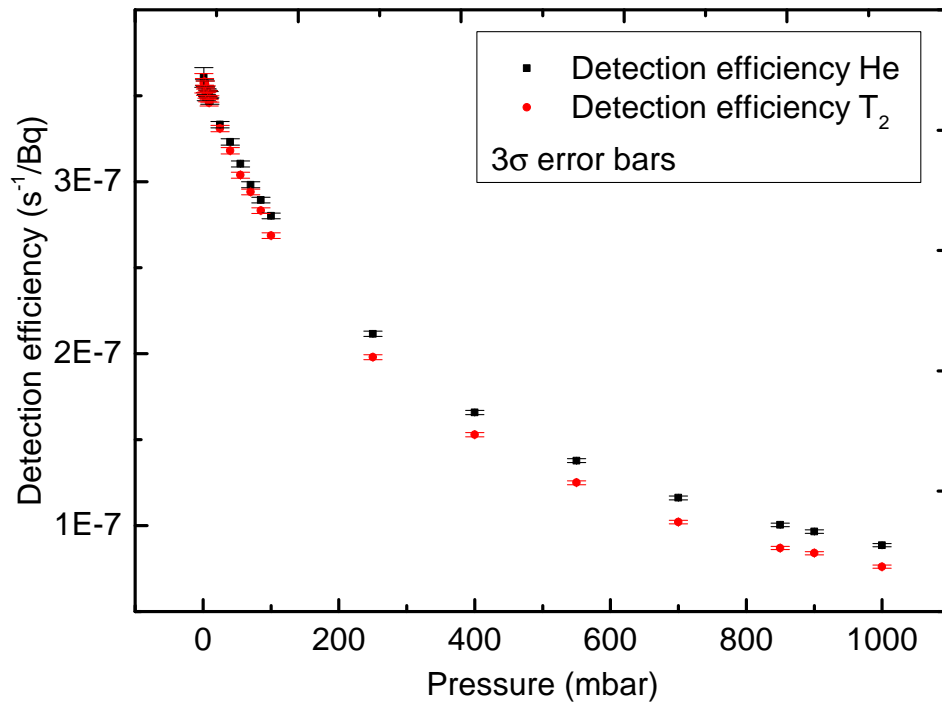
Figure 4.6.: Detection efficiency depending on total process gas pressure based on MC simulations.
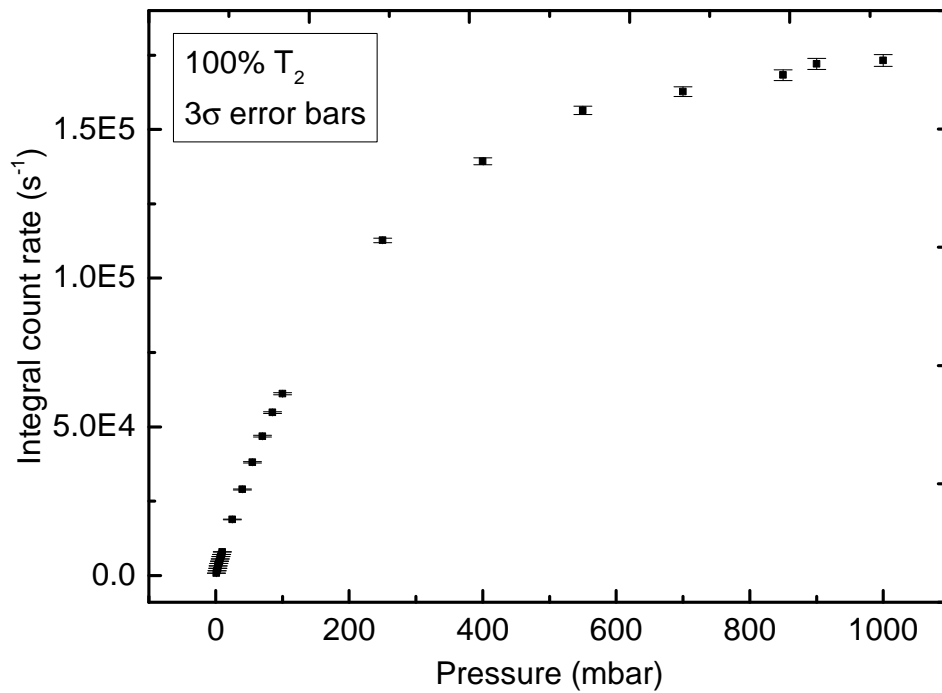
Figure 4.7.: Expected detector count rate depending on tritium partial pressure based on MC simulations.
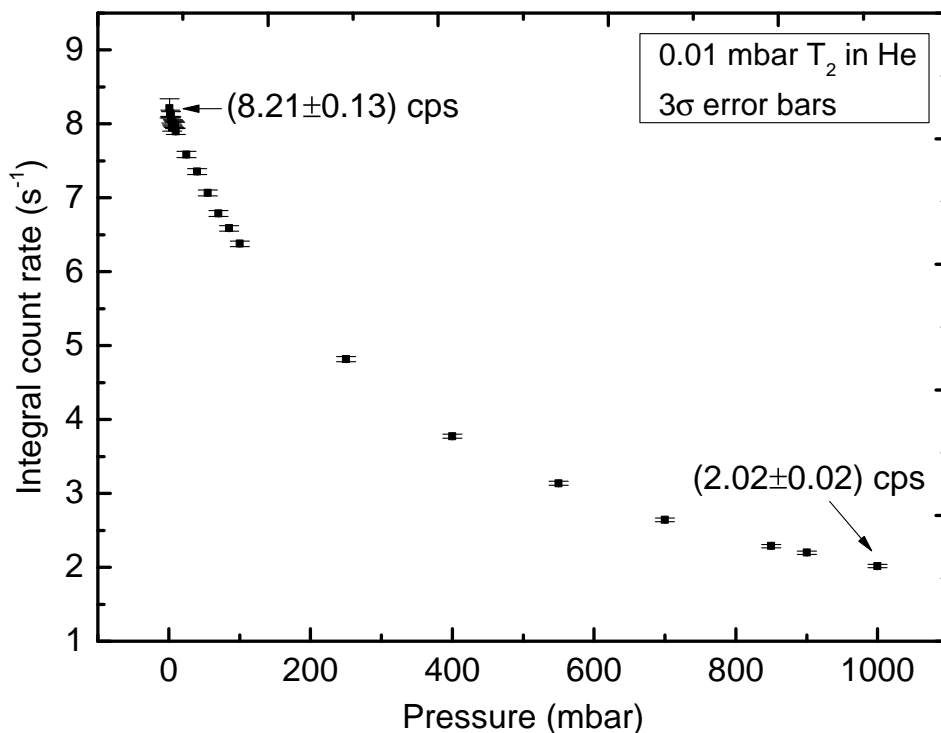
Figure 4.8.: Expected detector count rate depending on helium partial pressure for a given tritium activity in the sample chamber based on MC simulations.

In figure 4.9 the results of the gas species dependency simulations are shown. There is a significant gas species-dependent effect at 1000 mbar total pressure. For a tritium calibrated BIXS system, strong variations in the gas mixture, with the simulated gas species, can lead in the worst case to uncertainties of up to 36.4 % in the measured activity. The difference in detection efficiency for hydrogen and tritium as process gas at 1000 mbar is 5.1 %.

4.2.5. Conclusions of the MC simulations

From the Monte Carlo simulations it can be concluded, that a system with a similar setup to figure 4.1 can be a promising extension to existing tritium analytical tools.

In case of pure tritium at pressures of $p_{\text{tot}} \leqslant 10$ mbar the system can be used as a pressure and gas species independent tritium activity monitoring tool. An easy two-point calibration is enough due to the linear relationship between the tritium activity and the detector count rate at low pressures. The calculated detection efficiency is $(6.41 \pm 0.25) \cdot 10^{-7}\,\text{s}^{-1}/\text{Bq}$ for a system length of 24 mm. With that, a minimal tritium partial pressure in the order of 10^{-5} mbar in the sample chamber would cause a detector signal in the order of the typical intrinsic detector background of a silicon drift x-ray detector which is in the order of $10^{-2}\,\text{s}^{-1}$.

In case of 10 ppm of tritium in one bar of helium the projected detector count rate is
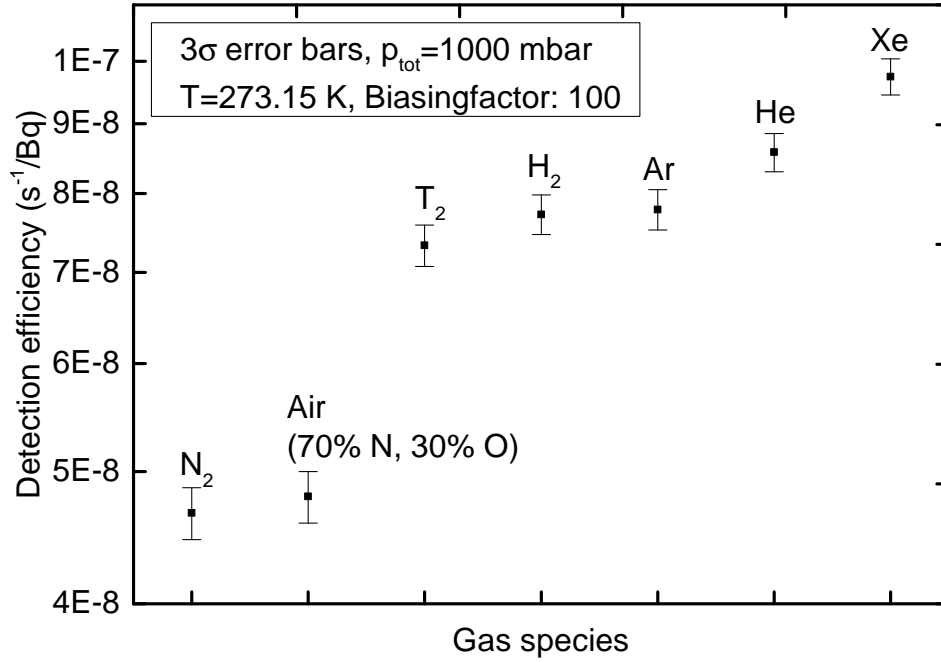
Figure 4.9.: Gas species dependency of the detection efficiency at a total pressure of 1000 mbar based on MC simulations. The calculated detection efficiencies for each process gas depend on the energy dependent cross sections and the average energy transfer per interaction. The sample chamber length is 24 mm.

$(2.02 \pm 0.02)\,\mathrm{s}^{-1}$. A measurement uncertainty of 5 % on the tritium activity can be reached in $\leqslant 200\,\mathrm{s}^{-1}$ measurement time. For varying total pressure conditions a pressure correction factor should be applied.

In case of varying pressure conditions or varying gas mixtures at total pressures of above 10 mbar one has different options to realize activity monitoring by BIXS with a measurement uncertainty of $\leqslant 5$ %.

- Instead of using the BIXS system as inline monitoring tool (see section 2.2.1), it can also be used as an online monitoring tool. Reducing the process gas pressure in the BIXS chamber by continuous pumping to $p_{\mathrm{tot}} \leqslant 10\,\mathrm{mbar}$ also reduces systematic uncertainties caused by the pressure and gas species dependency at higher pressures. The measured tritium activity of the BIXS system can than be corrected by the actual system total pressure afterwards.

- In case of a constant tritiated gas mixture and a varying total pressure the BIXS system can be calibrated to the process gas mixture. A pressure-dependent correction factor must then applied to the measured tritium activity.

- In case of variable tritiated gas mixtures, the BIXS system can be combined with a tritium analytical tool, which is able to analyze gas mixtures such as laser Raman spectroscopy or gas chromatography. The detector count rate of the BIXS system must then corrected according to the gas mixture.
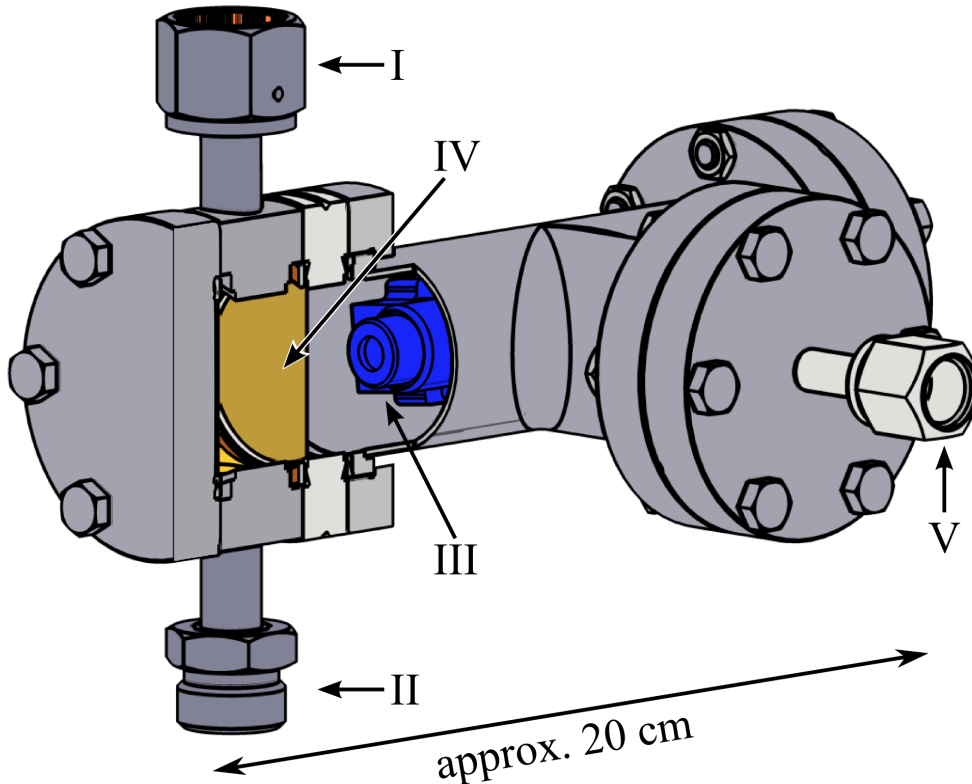
Figure 4.10.: CAD drawing of the TRACE measuring cell. The measurement cell is based on DN40CF parts. The flow-through sample volume is (25.81 ± 0.54) cm^3 and is gold coated to increase the detection efficiency and reduce the memory effect (I: Gas inlet, II: Gas outlet, III: SDD capsule, IV: gold coated Be window, V: Vacuum interface for evacuation of the detector electronics vessel).

Based on the presented Monte Carlo simulation results a BIXS system was designed and built at TLK. First tritium measurements were performed. The experimental setup and the results of the tritium measurements are described in the following sections. For the first prototype the sample cell chamber length was fixed to $z = 24$ mm.

4.3. Experimental setup

A CAD drawing of the experimental setup of TRACE is shown in figure 4.10. The sample volume is a DN40 Conflat® (CF) distance flange with two 1/2" Swagelok® VCR® ports. One side is covered with a blind flange and the other is connected with a gold-coated DN40CF beryllium window with a thickness of 125 µm and a diameter of 28.5 mm. In order to reduce tritium adsorption in the recipient and to maximize X-ray production, all inner surfaces of the recipient are sputter coated with 200 nm of gold. Only the beryllium window is coated with 100 nm of gold which is according to Monte Carlo simulations (see section 3.4.2) the optimal thickness for maximum Bremsstrahlung production and minimum X-ray absorption. The flow-through sample chamber has a volume

Figure 4.11.: Amptek® silicon drift detector and preamplifier in a PA-230 housing which provides shielding, heat-sinking, and mounting holes. Picture provided by Amptek®.

of $V_{\text{sample}} = (25.81 \pm 0.54)$ cm^3 and is separated from the detector volume by the beryllium window. According to manufacturer data the beryllium window (see appendix A.21) has a maximum leakage rate of $q_{\text{L}} \leqslant 10^{-9}$ mbar l/s.

A DN40CF standard T-piece is used as detector volume. On one side it is attached to the beryllium window and on the opposite side to a blind flange with electrical feedthroughs for the X-ray detector. Since the beryllium window is specified for differential pressures of one bar but only unidirectional loadable, the detector electronics volume must be evacuated. Therefore, a DN40CF to 1/2" VCR® adapter is connected to the T-piece and can be used for the connection to a vacuum pump. An Amptek® X-123SDD OEM X-Ray spectrometer with a Silicon Drift Detector (SDD) is used as a detector. The SDD and the preamplifier are in a PA-230 housing (see figure 4.11) and placed inside the T-piece. Internally the PA-230 is attached to the blind flange via a copper holder which fixes the position of the detector and serves as a heat spreader. The SDD is cooled to 240 K by Peltier elements and heat losses are transferred by the copper holder. In case of a break of the beryllium window, the DN40CF T-piece serves as a first wall for tritiated gases and therefore fully complies with all rules and regulations applicable at TLK. Detector signals are acquired and processed by an Amptek® DP5 OEM digital pulse processor and MCA, which is placed outside of the detector volume. Evacuation of the detector electronics volume is only done once and the volume is closed by a manual valve.

A picture of the TRACE setup is shown in figure 4.13. During the tritium measurements TRACE was installed in a fume hood at the TLK to provide it with connections to the necessary infrastructure. Figure 4.12 shows a process flow diagram of the experimental
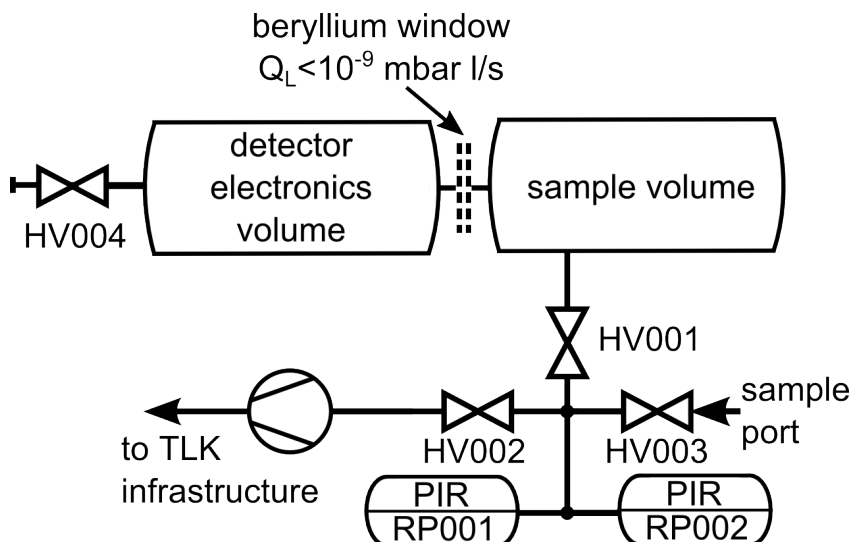
Figure 4.12.: Process diagram of the experimental setup for the characterization of TRACE. HV indicates manual valves and PIR indicating pressure sensors.

setup. Tritium gas mixtures are provided by the CAPER facility [Doe08] in a sample cylinder with a volume of $10\,cm^3$. The gas composition is analyzed by gas chromatography [Dem12]. Sample cylinders can be connected to the sample port (see figure 4.13) and the tritiated test gas mixtures are expanded into the sample cell volume. With the manual valves HV003 and HV002 the final pressure can be varied on the $10^{-3}\,mbar$ level by a controlled expansion or a step-wise pump-down of the system. The total pressure in the system is monitored by a piezo resistive pressure sensor MKS series 902 (PIR001, 1333 mbar fullscale) and a capacitive pressure sensor MKS series 626B (PIR002, 2.67 mbar fullscale). Datasheets can be found in appendix A.7, A.8.

4.4. Basic characterization of TRACE by tritium measurements

For the first characterization measurements with tritiated gas mixtures, TRACE was installed in a fume hood at TLK. Due to TLK regulations this limits the maximum handled tritium activity inside TRACE to $10^{10}\,Bq$. Thereby, static tritium measurements could only be performed at low tritium partial pressures of $p_T \leqslant 10\,mbar$. The main goals of the measurements were the investigation of:

1. the suitability for static activity monitoring of tritiated gases,

2. the detection efficiency at total pressures below 10 mbar,

3. the count rate stability of the system and

4. the ability to detect traces of tritium ($\epsilon_T \approx 10\,ppm$) in one bar of helium.
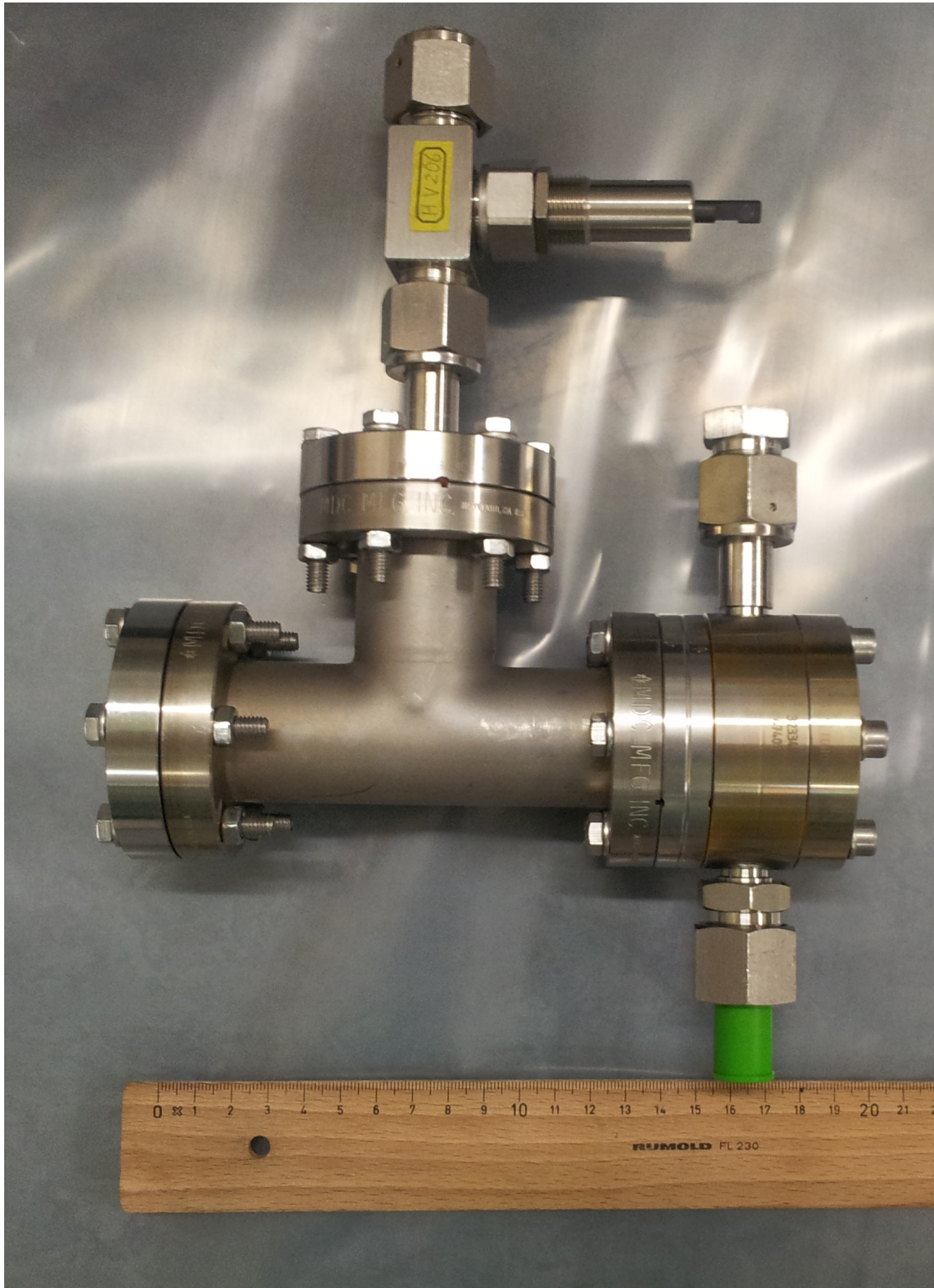
Figure 4.13.: TRACE system with detector electronics volume (left) and sample volume (right). The electrical feedthroughs for the detector are in the DN40CF blind flange on the left side. Not shown are the DAQ and power supply.

An overview of the measurement runs and the measurement procedure which were performed for it, is given in the following section.

Table 4.2.: Overview of the tritium gas mixtures provided by the CAPER facility. $p_{tot,\ sc}$ indicated the pressure in the sample cylinder.

Sample cylinder	Total pressure $p_{tot,\ sc}$ in mbar	Tritium purity ϵ_T in %
1	5	(67 ± 10)
2	5	(96 ± 4)
3	5	(94 ± 4)
4	10	(95 ± 4)

4.4.1. Overview of the tritium measurements

In total four tritium gas mixtures were used for the characterization measurements. They were provided by the CAPER facility (see section 2.1) and analyzed by gas chromatography. For the gas transfer a sample cylinder with a volume of $V_{sc} = (10 \pm 1)\,\text{cm}^3$ was used. Table 4.2 gives an overview of the test gas mixtures. Tritium measurements were performed in a five step process:

1. connecting of the sample cylinder to the sample port,

2. evacuation of residual gas in the TRACE sample cell and all volumes of the experimental setup to the TLK infrastructure,

3. pressure rise test to confirm the leak tightness of the sample cylinder connection,

4. expansion of the tritium gas mixture in one step or step-wise to the TRACE sample cell,

5. static activity measurements with the X-ray detector,

6. evacuation of the gas mixture from the TRACE sample cell, in one step or step-wise, to the TLK infrastructure.

Before and after each activity measurement, background measurements with the X-ray detector were performed.

For all the measurements the same detector parameters were used which can be found in the appendix A.3. The intrinsic detector background count rate of the Amptek® silicon drift detector was measured after installation of TRACE into the fume hood, before the first tritium measurement. It was determined to $(69.9 \pm 3.4)10^{-3}\,\text{s}^{-1}$. Compared to other background measurements with similar detectors [Sch12], [Roe11] the electronic noise level is higher by a factor of about 10 to 30. In appendix A.4 the noise characteristics of the TRACE X-ray detector is shown. A possible explanation for that are high frequency distortions on the power net due to electronic equipment in the fume hood as a turbo molecular and a multi-stage root pump. Nevertheless, the intrinsic detector background level was at all times at least one order of magnitude lower than any measured tritium signal and therefore none of the measurements in table 4.2 were corrected for it. An energy calibration was done in-situ with the characteristic X-rays in the recorded spectrum shown in figure 4.14. In appendix A.4 the results are shown.
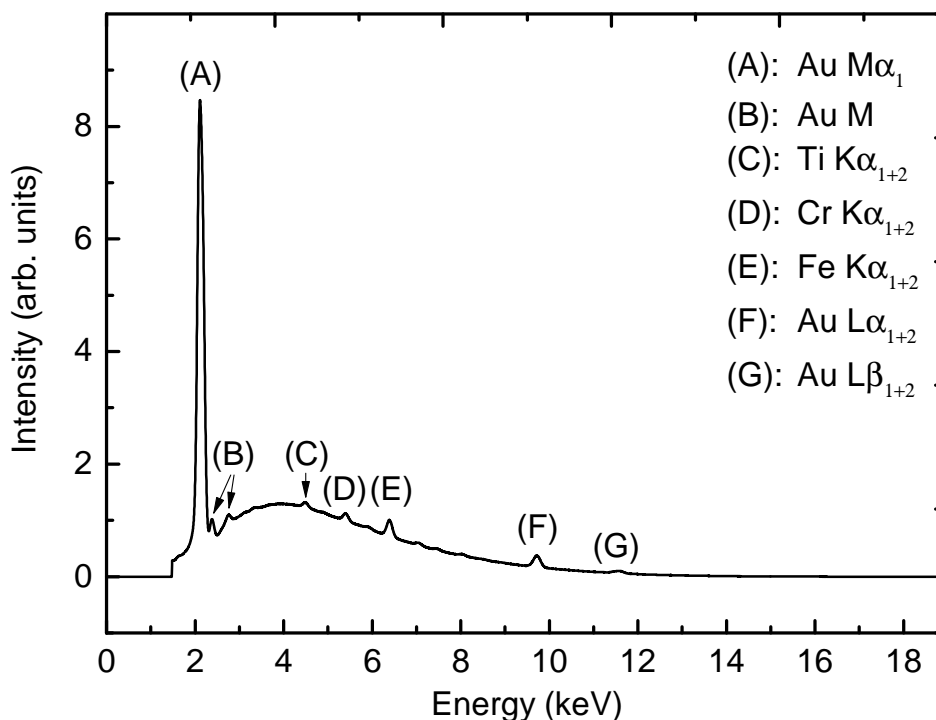
Figure 4.14.: Example of a typical BIXS spectrum measured with TRACE. Characteristic X-rays superimpose the continuous bremsstrahlung part.

4.4.2. Typical BIXS spectrum

In figure 4.14 a typical X-ray spectrum measured with the TRACE detector is shown. It shows the continuous Bremsstrahlung part superimposed by characteristic X-ray lines which was already discussed in section 3.4.2. Characteristic gold (Au) X-rays are produced due to the interaction of β-electrons with the gold coating of the recipient. Chrome (Cr) and iron (Fe) are the main alloy constituents of the stainless steel 316L vessel. The characteristic X-rays of titanium (Ti) are given by the adherent layer between the beryllium/stainless steel surface and the gold coating. The main characteristic X-rays of beryllium are not detectable due to the low energy threshold of the detector. To minimize the influence of electronic noise on the tritium measurements, a rather high detector threshold energy of approximately 1.7 keV was chosen.

4.4.3. Static activity monitoring of tritiated gas mixtures

TRACE is designed as a flow-through system for inline activity monitoring of tritiated process gas streams. Nevertheless, it can also be used for static activity monitoring of tritiated gas samples. To test the basic functionality of the system an expansion and pump-down test were performed to demonstrate the suitability to work as an activity monitor for static gas mixtures.
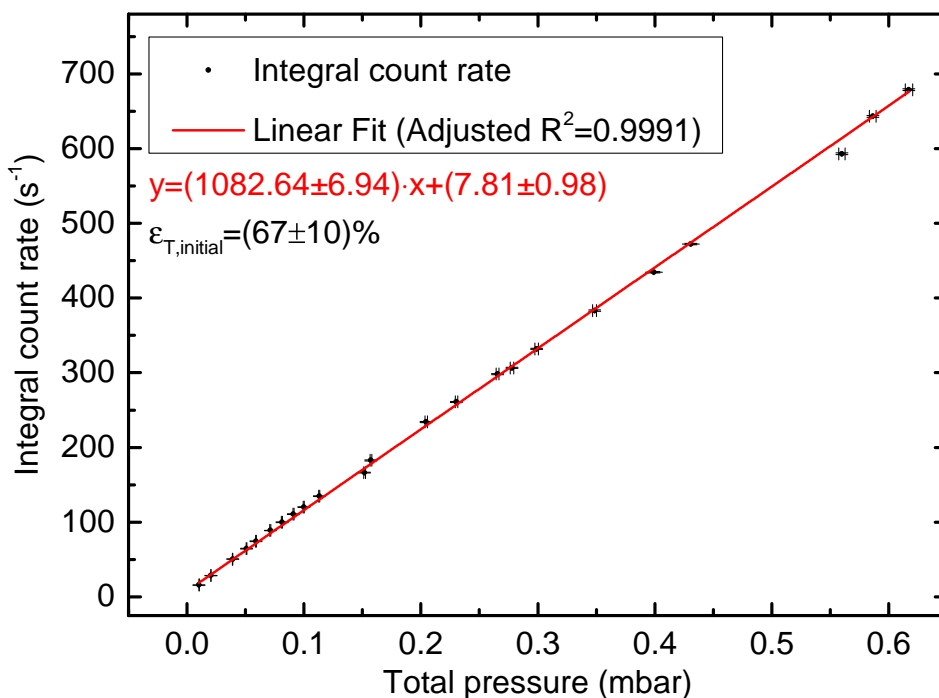
Figure 4.15.: Integral count rate over total pressure. An expansion and a pump-down test was performed from 0.6 mbar to $1 \cdot 10^{-2}$ mbar in order to determine the linearity of the system. The measurement time for each data point was 500 s.

The gas mixture from sample cylinder one (see table 4.2) was expanded into the sample cell and step-wise evacuated after that. During every step activity measurements were done with a measurement time of 500 s. During the measurements the total pressure in the sample cell stayed unchanged.

In figure 4.15 the results are shown. As expected, the system shows a linear relationship between the measured activity and the total pressure in the pressure range of 0.01 mbar to 0.6 mbar. In the high pressure regime nonlinearities could arise from self-absorption of β-electrons in the gas mixture. According to section 4.2.3, such non-linear behavior is expected for total pressures higher than $\approx$ 10 mbar. In the low pressure regime outgassing effects or demixing effects[3] during pump-down can cause nonlinearity. None of these effects were observed in the measured pressure regime.

To use TRACE as an activity monitor in this pressure regime an easy two-point calibration would be enough. In this work pressure data and a gas analysis by gas chromatography are used for the calculation of the detection efficiency of TRACE. With that, the activity in the sample cell can be calculated from the measured count rate. According to section 4.2.3 gas species-dependent effects on the detection efficiency are not expected in this pressure regime.

---

[3]   Demixing effects are unintended changes in the relative gas concentration which can be induced by gas species-dependent pumping speeds as for turbo molecular pumps.

Table 4.3.: Calculated detection efficiencies of TRACE. The measurements were performed with test gas mixture two (table 4.2).

Run	Detection efficiency in 10^{-7} cps/Bq	Accumulation time in hours	Total pressure in mbar	Integral count rate in cps
1	9.22 ± 0.43	2.14	0.6395 ± 0.0032	1288.37 ± 0.41
2	9.22 ± 0.43	0.11	0.6392 ± 0.0032	1288.71 ± 1.79
3	8.54 ± 0.41	166.30	0.6510 ± 0.0032	1214.99 ± 0.05
4	7.98 ± 0.39	0.56	0.6645 ± 0.0033	1159.39 ± 0.76

4.4.4. Detection efficiency and minimum detectable activity

The overall detection efficiency of TRACE is calculated according to equation A.8 in appendix A.5. Four tritium measurements from test gas mixture two (see table 4.2) were used for that. The calculated detection efficiencies for the four measurement runs are shown in table 4.3. These numbers depend on the used detector parameters, as gain and especially the energy threshold settings and are only valid for total pressures below 10 mbar in the sample cell. The rather large uncertainty in detection efficiency is dominated by the uncertainty in the tritium purity, according to table 4.2.

Compared to the Monte Carlo simulation results in section 4.2.2 the measured detection efficiency of the first run is higher by about 44 %. This is most likely due to the actual SDD position compared to the simulated one. Even small variations in the detector position of several millimeters can cause significant variations in the detection efficiency [Mao12].

From the first to the fourth run the calculated detection efficiency decreases by about 15 % which is reflected by the decrease in integral count rate. While at the same time the total pressure in the sample cell increases by about 4 %. Translated into a leakage rate this pressure rise corresponds to $1.06 \cdot 10^{-9}$ mbar l/s which is within the specifications for such vacuum parts and it can be assumed that it is air from outside the system. The decrease in the calculated detection efficiency and the measured count rate can be caused by a decreasing tritium purity inside the sample cell. Tritium wall interactions which cause significant changes in the tritium purity are well known in the literature [Pri13], [Fis11].

The minimum detectable activity (MDA) indicates the smallest verifiable activity which can be distinguished from background with a certain confidence level (usually 95 %). It depends on the background signal N_B, the measurement time t and the detection efficiency DE. The MDA can be calculated according to

$$MDA = \frac{4.65\sqrt{N_\mathrm{B}} + 2.71}{DE \cdot t} \qquad \text{[Kno10].} \qquad (4.1)$$

where DE is defined as integral count rate dN/dt divided by the tritium activity A in the sample chamber. Using the intrinsic background level of the TRACE X-ray detector

Table 4.4.: Count rate stability of TRACE during both measurement runs.

Run	Count rate decrease in s^{-1}/hour	SS316L surface area in cm^2	Gold surface area in cm^2
1	-0.78 ± 0.01	118 ± 11	49.4 ± 2.5
2	-0.14 ± 0.01	24.9 ± 2.5	49.4 ± 2.5

$dN/dt = (69.9 \pm 3.4)10^{-3}$ s^{-1}, the MDA in 100 s of measurement time is $A = 0.16$ MBq. The MDA corresponds to a tritium partial pressure of $7.1 \cdot 10^{-5}$ mbar. These numbers are only valid for an uncontaminated system.

BIXS systems as well as ionization chambers suffer from a so-called memory effect, a history-dependent background. Due to surface contaminations of the sample cell during tritium measurements, the detector background signal is increasing over time [Roe11]. First and foremost this limits the dynamic range of such monitoring systems. The increase in background count rate depends on the applied tritium partial pressures and the exposure time. After measurement run four, the measured background count rate was 5.70 ± 0.01 s^{-1}. This is about 0.5 % of the count rate during tritium exposure and about two orders of magnitude higher than the intrinsic detector background. Using this with equation 4.1 the MDA is $A = 1.23$ MBq which corresponds to a tritium partial pressure of $5.4 \cdot 10^{-4}$ mbar.

4.4.5. Count rate stability

In the previous section a decreasing count rate over the four measurement runs was found which is presumably due to tritium wall interactions. To investigate this in more detail two count rate stability measurement runs were performed. In run one, HV001 (see figure 4.12) was open and in run two closed. This results in different surface areas which the process gas is able to interact with and which in turn has an influence on the BIXS signal stability.

At the beginning a tritium gas mixture from sample cylinder three was expanded into the sample cell. The final pressure after expansion was $p_{\text{tot}} \approx (1 \pm 0.01)$ mbar. Repeated activity measurements were performed with 500 s accumulation time. In the first measurement run the overall measurement time was 70 hours. Thereafter HV001 was closed and measurement run two was performed for 50 hours.

In figure 4.16 the results of the first run are shown. The integral count rate decreases with (-0.78 ± 0.01) s^{-1}/hour and shows a linear relationship. Figure 4.16 displays the results of the second run. Again a linear cont rate decrease is detected but now with a ratio of (-0.14 ± 0.01) s^{-1}/hour. Even at a rather high pressure of $p_{\text{tot}} \approx (1 \pm 0.01)$ mbar no saturation effect is detectable after 130 hours of exposure time. A dominating influence of tritium gas losses due to leaks can be excluded due to the compulsory leakage test during commissioning. The measured integral leakage rate was $q_{\text{l}} \leqslant 1 \cdot 10^{-8}$ mbar l/s.

The numbers for the decrease in count rate between both runs fit to the decrease in stainless steel surface area within uncertainties. As denoted in table 4.4 the count rate decreases by a factor of 0.179 ± 0.015 while the SS316L surface area is decreased by a factor of 0.211 ± 0.045. The rather large gold surface area, which is the same in both runs, does not seem to have a measurable influence on the count rate decrease. A specialized experimental setup is necessary to measure tritium adsorption and absorption on or in gold (see chapter 6).

4.4.6. Traces of tritium in helium

With the tritium gas mixture from the fourth sample cylinder a high pressure helium test was performed. At the beginning tritium was expanded into the recipient to a total pressure of $(10.00 \pm 0.06) \cdot 10^{-3}$ mbar. Then, sample cylinder four was replaced by a sample cylinder with a volume of 0.5 l, filled with helium gas ($\epsilon_{He} \geqslant 99.999$ %) to a total pressure of about 900 mbar. The helium gas was step-wise expanded into the sample volume to a final pressure of (881.4 ± 8.8) mbar. Activity measurements with 500 s measurement time were taken after each expansion step.

In figure 4.18 the results are shown. An exponential decrease in the integral count rate is visible. The pressure dependence is caused by self-absorption of β-electrons in the gas and show the same behavior as in the simulated one in section 4.2.3. Deviations from the exponential like decay can be caused by two systematic effects. During the expansion steps of helium into the sample cell, tritium adsorbed on the SS316L surface can be purged into the volume and increase the absolute activity. Also back diffusion of tritium from the sample cell during the helium expansion can not be excluded and can decrease the absolute activity. Which effect dominates could depend on several parameters like the flow speed during expansion, the amount of adsorbed tritium on the SS316L surface and the tritium partial pressure inside the sample chamber.

After the last tritium measurement followed by ten minutes of evacuation, the measured background count rate was $(7.267 \pm 0.085)\,\mathrm{s}^{-1}$. The count rate in the final tritium measurement was $(9.62 \pm 0.14)\,\mathrm{s}^{-1}$ and is therefore clearly above the background signal. That means tritium concentrations of 10 ppm in about 900 mbar of helium are detectable with the TRACE setup.

4.5. Possible applications for TRACE and Outlook

Activity monitoring of traces of tritium on the ppm level in helium purge gas streams. TRACE has demonstrated that tritium concentrations on the ppm level in about one bar of helium can be detected. An net integral count rate of $(2.35 \pm 0.16)\,\mathrm{s}^{-1}$ was measured which is enough to monitor the tritium activity with 5 % statistical uncertainty in ≈ 180 s. Regarding the use of TRACE as a process monitor for the purge gas stream of HCPB blankets of future fusion reactors (see section 2.3.1) further efforts must be put in a proper calibration of the system. The use as a flow-through system is currently investigated by integration of TRACE in a closed loop experiment [Pri13].
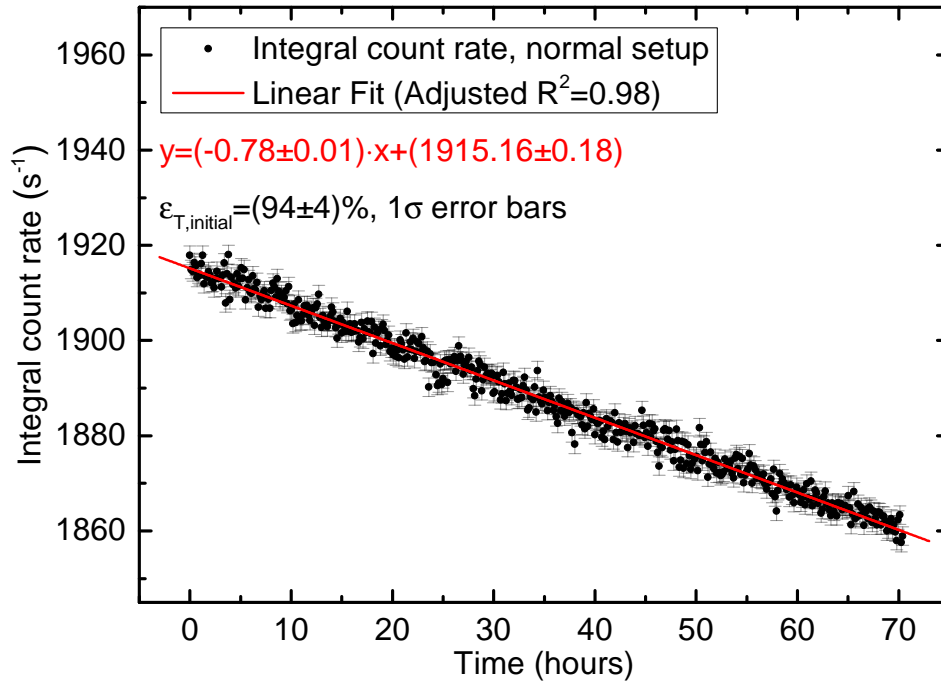
Figure 4.16.: Count rate stability of TRACE with the normal setup. The measurement time for each data point was 500 s.
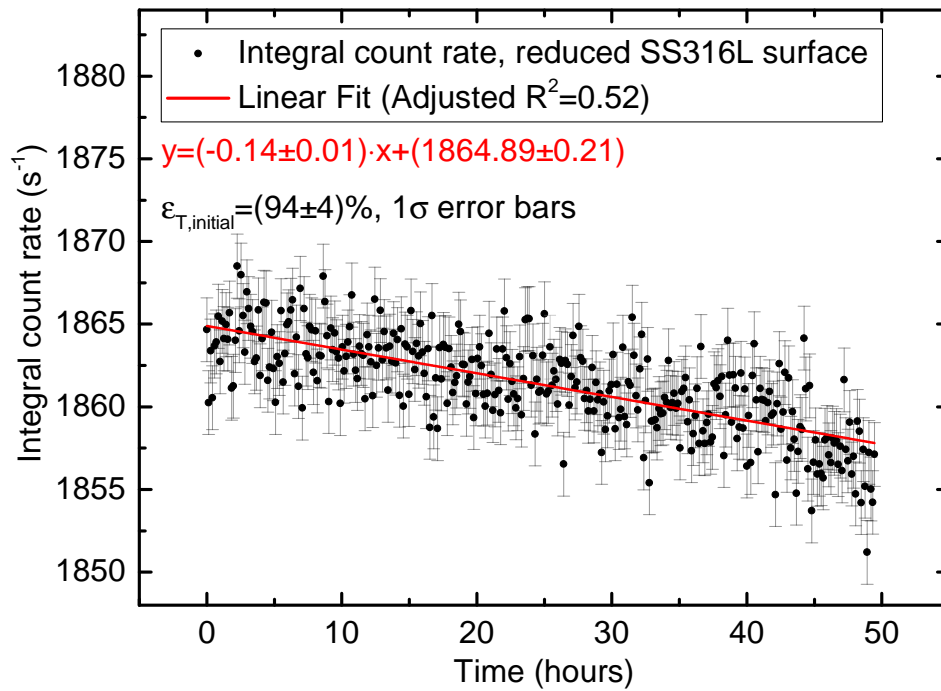
Figure 4.17.: Count rate stability of TRACE with reduced SS316L surface area. The measurement time for each data point was 500 s.
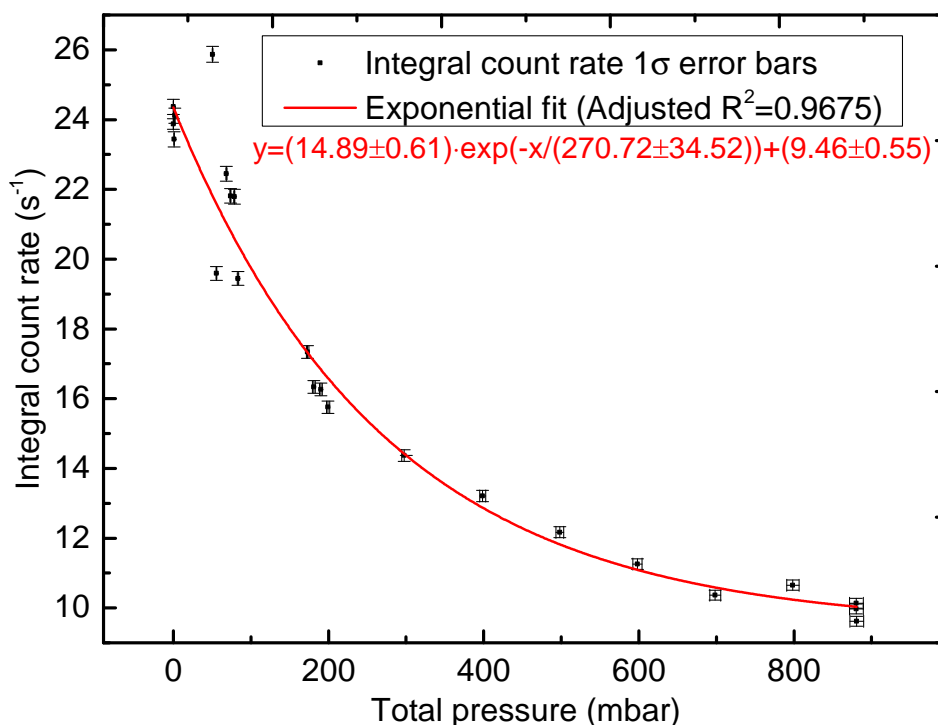
Figure 4.18.: Integral count rate decrease due to selfabsorption of β-electrons in helium of up to one bar. The y-error bars indicate the statistical errors of the count rate measurements.

The minimum detectable activity of TRACE is in principle low enough to also be used as an activity monitoring tool for the KATRIN CPS [KAT04] purge gas stream during regeneration cycles (see section 2.3.1). An estimated tritium concentration of about 1 ppm in 500 mbar of helium would cause a detector signal in the order of 0.1 s^{-1} which is still above the intrinsic detector background. However, tritium wall interactions could dominate the detector signal at such low partial pressures. Further investigations regarding tritium wall interactions are necessary. Furthermore, a system is necessary which is able to prepare gas mixtures on that concentration level.

Activity monitoring of tritium at low pressures. As stated in section 2.2.4 activity monitoring of tritiated gases at total pressures below 10 mbar is currently a challenging task. TRACE can fill this gap and it is the optimal parameter range for it. Pressure or gas species-dependent effects are negligible here if one aims for uncertainties on the 5 % level. A calibration is easily done by a tritium concentration measurement with gas chromatography or Laser Raman spectroscopy, combined with a volume and pressure measurement. The system shows a linear behavior. Further development should be put on the minimization of background caused by tritium contamination of the inner walls. This changes the background signal over time during tritium exposure and limits the minimum detectable activity and the dynamic range of the system.

Activity monitoring of tritium at high pressures. TRACE can also be used at high total pressures of about one bar as a compact and robust alternative to an ioniz-

ation chamber. As an ionization chamber it shows a significant gas species and pressure dependency here. Nevertheless, if properly calibrated, TRACE can reach very low measurement uncertainties of less $\leqslant 5\,\%$ which is a significant advantage over ionization chambers. Especially tritium accountancy in closed loop systems as the KATRIN WGTS (see section 2.2.4) could profit from that. To this day, it is unclear how much tritium the KATRIN WGTS will accumulate over the three years of measurement time. Two TRACE systems in a differential mode, at the inlet and the outlet of the WGTS combined with mass flow meters could provide tritium accumulation data. This would give useful information for the handling of the system in case of maintenance or for disposal after the final tritium measurements.

5. High stability activity monitoring of the KATRIN tritium source

One of the major task of the Tritium Laboratory Karlsruhe (TLK) is providing the necessary tritium infrastructure for the Karlsruhe Tritium Neutrino (KATRIN) experiment and developing new tritium analytical tools which meet the challenging analytical requirements of KATRIN. The focus of this chapter are Monte Carlo simulations regarding an activity monitoring system for one of the major KATRIN components, the Windowless Gaseous Tritium Source (WGTS). The monitoring system is based on the BIXS method and the Monte Carlo simulations shall show that the system is able to meet the KATRIN requirements.

The goal of KATRIN is the model-independent measurement of the neutrino mass with an unprecedented sensitivity. Therefore, a brief introduction into neutrino physics is given in section 5.1. KATRIN and its measurement principle are described in section 5.2 with a special focus on the WGTS.

Activity monitoring of the tritium inside the WGTS is a crucial task to reach the aimed sensitivity on the neutrino mass. In section 5.3 a previous test experiment is outlined which demonstrated the feasibility of activity monitoring of gaseous tritium by BIXS. The actual BIXS setup of KATRIN is then described in section 5.4. In section 5.5 Monte Carlo simulation results are given which allow to project the performance of the KATRIN BIXS system. Finally, in section 5.6 the consequences for KATRIN are discussed.

5.1. A brief introduction into neutrino physics

The quest for the understanding of neutrino properties started in the early 20th century with the first β-decay experiments. Since the beginning, neutrino physics research opened up a whole new research field which stimulated significant progress in fundamental particle physics and cosmology. Even the discovery of the neutrino started as one of the most interesting physics puzzles at that time.

In 1911 O. v. Baeyer, L. Meitner and O. Hahn reported about "magnetic spectra of β-radiation of radium" [Bae11]. Thereby, first hints for a non-discrete energy spectrum were reported. This could be validated by James Chadwick in 1914. He combined a magnetic spectrometer with one of Hans Geiger's counters. With that, he measured a continuous instead of a discrete β-spectrum [Cha14] which was unexpected at that time. Discrete energy spectra had been observed before in two-body α- and γ-decays. This was also expected for the β-decay. In order to avoid a violation of the energy conservation law, W. Pauli postulated in 1930 an undetectable spin-1/2 particle participating in the

interaction and carrying away energy and angular momentum. This was the starting shot for the discovery of the neutrino and the measurement of its fundamental properties.

5.1.1. Neutrinos and their properties

Today neutrinos are part of the lepton group of the standard model and feature three different flavors (ν_e, ν_μ, ν_τ). Neutrinos are uncharged, spin-1/2 fermions and only interact via the weak interaction. This makes them extremely difficult to detect and it took about 25 years to successfully proof their existence.

Neutrinos interact in two ways, by charged (CC) and neutral currents (NC):

- charged currents via (W^+, W^-) in which a neutrino converts into an equivalent charged lepton and

- neutral currents via (Z^0) in which a neutrino transfers energy and momentum to an interacting particle.

In 1956, the experimental validation of the neutrino was done by the use of the charged current interaction

$$\bar{\nu}_e + p \rightarrow n + e^+. \tag{5.1}$$

F. Reines and C. L. Cowan used the Savannah River fission reactor as an intense source of electron anti-neutrinos $\bar{\nu}_e$ and utilized the inverse β-decay (Eq. 5.1) for the detection of the neutrinos. A tank, filled with a water target with dissolved $CdCl_2$ and enclosed by liquid scintillator detectors and PMTs, was placed about 12 m under the reactor core. Positrons e^+ were detected by the annihilation radiation in which two 511 keV gammas are produced and neutrons n by the gamma radiation from the capture reaction

$$e^+ + e^- \quad \rightarrow \quad \gamma + \gamma, \tag{5.2}$$
$$n + {}^{113}\text{Cd} \quad \rightarrow \quad {}^{114}\text{Cd} + \gamma. \tag{5.3}$$

The measured cross section of $6.3 \cdot 10^{-44}$ cm^2 was within 5% agreement with theoretical expectations [Cow56]. Subsequently the two other neutrino flavors (ν_μ, ν_τ) were observed in particle accelerator experiments [Dan62], [Kod01].

5.1.2. Sources of neutrinos

Neutrinos are ubiquitous particles and except for photons more abundant than any other known particle in the universe. The sources of neutrinos are very different and are briefly discussed here.

Relic neutrinos
Relic neutrinos are remnants of the big bang and they are forming a cosmic neutrino background (CνB) comparable to the cosmic microwave background (CMB). During expansion and cooling-down of the universe the neutrinos decoupled from the reaction

$$\nu + \bar{\nu} \rightarrow e^+ + e^- \rightarrow \gamma + \gamma \tag{5.4}$$

at a neutrino temperature of about 1.95 K [Zub98]. Today, these relic neutrinos are assumed to be distributed rather isotropically and homogeneously in the universe with a density of 337 cm^{-3} [Zub98]. They are important in cosmology for structure formation in the early universe and contribute to the energy density in the universe as hot dark matter. To the present day, they are undiscovered due their very low energies and their very small interaction cross sections.

Particle accelerator neutrinos
Artificial neutrino sources as particle accelerators are useful tools to produce neutrino fluxes with defined properties. By hitting a static target with a high-energy proton beam, high neutrino fluxes can be produced. The neutrino beam is derived from the decay of charged pions π and kaons K, which are produced as secondaries when the p beam hits the target. A collimation of the beam is achieved by the relativistic boost of secondary particles in forward direction. Secondary mesons can also be focused by *magnetic horns* [Mee61] to further increase the neutrino flux. As the exact position of the source and the parameters of the neutrino flux are known they are often used to test fundamental neutrino physics.

Reactor neutrinos
Another artificial neutrino source are fission reactors. The decay chain of fission products of uranium and plutonium produce intense electron-neutrino fluxes via β^--decays according to the reaction

$$n \rightarrow p + e^- + \bar{\nu}_e. \tag{5.5}$$

This can be used for precision measurements of fundamental neutrino parameters such as the mixing angle θ_{13} (see section 5.1.3). Examples are Daya Bay [Pen15], Double Chooz [Cab12] and Reno [Joo12].

Atmospheric neutrinos
High-energy cosmic particles continuously impinge on the upper atmosphere. Most of them are protons which can collide with the nuclei of molecules from the atmosphere (e.g. ^{14}N) and produce intense shower cascade. Typical produced secondaries are pions and muons, decaying among other particles into neutrinos. Typical decay reactions for positive charged pions and muons are

$$\pi^+ \quad \rightarrow \quad \mu^+ + \nu_\mu, \tag{5.6}$$

$$\pi^+ \quad \rightarrow \quad e^+ + \nu_e, \tag{5.7}$$

$$\mu^+ \quad \rightarrow \quad e^+ + \nu_e + \bar{\nu}_\mu. \tag{5.8}$$

The produced neutrinos are typically in the GeV range. Since the production point is not exactly known the distance between the production point and the detector can vary from ≈ 10 km of up to $\approx 12,700$ km.

β-decay neutrinos
A neutrino source often used in experiments are β-emitter radionuclides. In a β-decay the nuclear charge Z is changed by ± 1 (except for the double β-decay, which is discussed later). Depending on whether there is an excess of neutrons or protons in the mother

nuclei X, β^--decay or β^+-decay can occur.

$$\ {}^A_Z X = {}^A_{Z\pm1} Y + e^\mp + \bar{\nu}_e / \nu_e \tag{5.9}$$

The atomic number A of the daughter nuclei Y stays hereby constant. A prerequisite for the decay is that the Q value of the reaction is higher than the necessary energy for the rest mass of the two created leptons. Most of the kinetic energy surplus $E = Q - (m_e + m_\nu) \cdot c^2$ is continuously distributed between the leptons.

Of peculiar scientific interest is the so-called neutrinoless double β-decay ($0\nu\beta\beta$). In that reaction two neutrons decay into two protons under emission of two electrons and the annihilation of the two neutrinos within the nuclei. This has not yet been observed and can only happen if neutrinos are Majorana particles [Maj06].

Solar neutrinos
Solar neutrinos are produced in the exothermic fusion processes of the sun. In the most prominent proton-proton chain reaction hydrogen is fused to helium by

$$4p \rightarrow {}^4\text{He} + 2e^+ + 2\nu_e + 28 \text{ MeV}. \tag{5.10}$$

Electron neutrinos, produced in this reaction, can have energies in the range of (0-0.42) MeV. Most of them can leave the sun without being scattered as the mean free path is in the range of $\approx 1/3$ pc. The solar neutrino flux on earth Φ_ν can be estimated using equation 5.10 and the observed solar luminosity L according to

$$\Phi_\nu \quad = \quad \frac{2L}{28 \text{ MeV}} \cdot \frac{1}{4\pi r^2}, \tag{5.11}$$

$$\Phi_\nu \quad = \quad \frac{2 \cdot 3.9 \cdot 10^{33} \text{ erg s}^{-1}}{28 \cdot 1.6 \cdot 10^{-6} \text{ erg}} \cdot \frac{1}{4\pi (1.5 \cdot 10^{13} \text{ cm})^2}. \tag{5.12}$$

The factor 2 comes from the number of neutrinos in equation 5.10 and r is the average distance between the sun and the earth. This results in a neutrino flux of

$$\Phi_\nu = 6 \cdot 10^{10} \ \nu_e / (\text{cm}^2 \text{s}). \tag{5.13}$$

For a more sophisticated calculation other solar reactions (pep, hep, ^{7}Be, ^{8}B) must be included as part of the standard solar model. Theoretical expectations for the neutrino flux on earth compared to neutrino measurements can give valuable insights into solar processes. Furthermore, investigations like this also led to the discovery of one of the most interesting neutrino features, the so-called neutrino oscillations.

5.1.3. Neutrino oscillations and mass properties

In the late 1960th R. Davis and J. N. Bahcall were the first who measured the solar neutrino flux with the Homestake experiment [Dav64]. They discovered a deficit of solar neutrinos when comparing their measurement results to theoretically models of the sun. This became known as the solar neutrino problem. The reason for the deficit in the measured neutrino flux are neutrino oscillations. These are periodic changes of the probability that a neutrino is measured as a certain flavor. Quantum-mechanically it

is described by the Maki-Nakagawa-Sakata (MNS) matrix [Mak62]. It is a unitary 3x3 matrix defined as

$$U = \begin{bmatrix} U_{e1} & U_{e2} & U_{e3} \\ U_{\mu 1} & U_{\mu 2} & U_{\mu 3} \\ U_{\tau 1} & U_{\tau 2} & U_{\tau 3} \end{bmatrix} \quad \text{[Giu07].} \tag{5.14}$$

The relation between the three flavour-eigenstates ($\alpha = e, \mu, \tau$) and the three mass-eigenstates ($i = 1, 2, 3$) is given by

$$|\nu_\alpha> \quad = \quad \sum_i U^*_{\alpha i} |\nu_i>, \tag{5.15}$$

$$|\nu_i> \quad = \quad \sum_\alpha U_{\alpha i} |\nu_\alpha> \quad \text{[Giu07].} \tag{5.16}$$

Matrix U can also be expressed in a factorized way with only six free parameters [Aga14]. These are three mixing angles Θ_{ij} which define the neutrino mixing and three complex phases which characterize CP-violation (δ) and whether neutrinos are Majorana particles or not (ϕ_2, ϕ_3).

Using the simplifying assumption of only two neutrino flavors and mass states (ν_e, ν_μ and ν_1, ν_2) and one mixing angle (Θ), one can calculate the probability P for a neutrino with flavor α to be detected as flavor $\beta \neq \alpha$ after traveling a distance d by

$$P(\alpha \to \beta) = \sin^2(2\theta)\sin^2\left(\frac{\Delta m^2 d}{4E}\right) \quad \text{[Giu07].} \tag{5.17}$$

E is the neutrino energy and $\Delta m^2 = m^2_{\nu 1} - m^2_{\nu 2}$ the mass square difference. The oscillation length $L = 4\pi E / \Delta m^2$ is a characteristic value to find maxima and minima in the transition probabilities. $P(\alpha \to \beta)$ is maximal for half-integral d/L and minimal for integral d/L.

Experimental investigations of neutrino oscillations can be done by appearance experiments or dis-appearance experiments using neutrino sources with well-known properties. Dis-appearance experiments measure the survival probability of certain flavor α in a neutrino beam $P(\alpha \to \alpha)$. Appearance experiments use neutrino beams with initial flavor α and search for flavor β to determine $P(\alpha \to \beta)$.

Neutrino oscillation experiments can be used to determine the neutrino mixing angles Θ_{ij} or measure mass differences Δm^2. A comprehensive overview of experimental results can be found in [Aga14]. As neutrino oscillations are experimentally well validated neutrinos must have non-vanishing masses. The determination of the absolute mass scale of neutrinos is an ongoing task of crucial importance in neutrino physics.

5.1.4. Impact of the neutrino mass

The absolute neutrino mass or constraints on the neutrino mass are of major importance in cosmology and particle physics. Although neutrinos are assumed to be massless in the standard model, neutrino oscillations clearly show that this is not true. Current
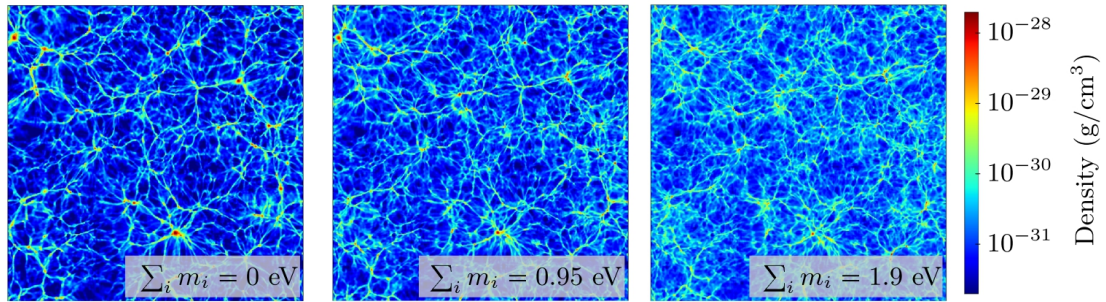
Figure 5.1.: Simulation of the baryon density in the universe as function of the neutrino mass sum. Each slice is 200 h^{-1} Mpc wide and shows the averaged baryon mass of a grid cell of $\approx$ 391 h^{-1} kpc. An increasing neutrino mass smears out small scales structures. Figure from [Fis14], adopted from [Aga11].

measurement results show that neutrinos must be very light (see next section) but the significance of the neutrino mass is justified due to their huge number density in the universe and the not yet fully understand mechanism which creates the neutrino mass.

In cosmology neutrinos play in important part in structure formation. On large scales (> 100 Mpc) the universe can be considered as homogeneous and isotropic. Density fluctuations in the early universe grew via gravitational clustering which led to density distributions as shown in figure 5.1. The free-streaming neutrinos in the early universe had the opposite effect and led to a damping of gravitational clustering. As shown in figure 5.1 this has significant effect on the structure formation of the universe and depends on the total neutrino mass $m_{\text{tot}} = \sum_i m_{\nu i}$ [Per09].

The neutrino mass also contributes to the total energy density in the universe as hot dark matter. In this context hot means that cosmic neutrinos are relativistic and dark due to the fact that they only undergo weak interactions. Considerations of the energy density in the universe are connected to the question of its spatial geometry. The geometry of the universe is described by the Friedmann equations in which the neutrino mass enters in the density parameter.

In particle physics the absolute neutrino mass is important as it helps to understand how mass generation works. The seesaw mechanism [Xin11] is one of the extensions to the standard model which includes non-vanishing neutrino masses. There are several types of seesaw mechanisms (I, II, III, linear, inverse) [Xin11]. An important step forward in the formulation of a generalized model would be the determination of the neutrino mass scale (see figure 5.2). If $m_{\nu 1}$ is large the mass eigenvalues are quasi-degenerate and if it is small the eigenvalues are hierarchical. In case of hierarchical eigenvalues the order is also of scientific interest [Qia15].

5.1.5. Mass measurement methods for neutrinos

In this section neutrino mass measurement methods are briefly introduced. A comprehensive overview can be found in [Alt03]. The focus here is on the observables of the
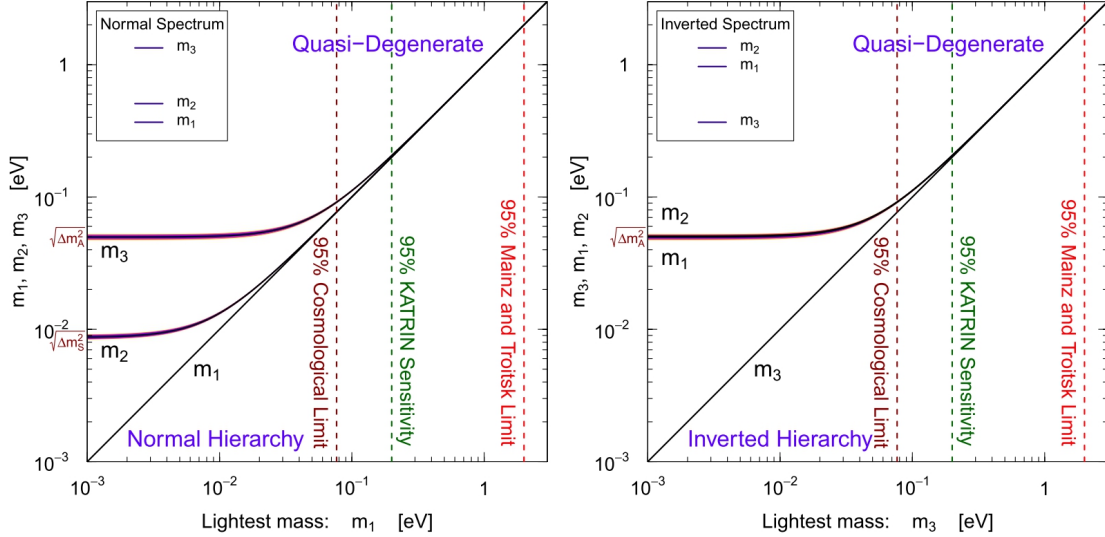
Figure 5.2.: Left, neutrino masses are shown in normal hierarchy as function of the lightest mass m_1. Right, neutrino masses are in inverted hierarchy as function of the lightest mass m_3. Mass differences can be obtained by neutrino oscillation experiments. Figure from [Bil15].

respective methods. Neutrino mass measurement by kinematic β-decay is discussed in more detail.

Measurement methods are often split up into two groups. Indirect methods rely on neutrino model assumptions to extract the neutrino mass from the measured observable. They can be used to test specific models but are therefore susceptible to model-dependent uncertainties. Typical examples are 0νββ-experiments or cosmological observations. Direct methods are based on kinematics and only rely on the energy-momentum relation

$$E^2 = p^2 c^2 + m^2 c^4 \tag{5.18}$$

where E is the energy of the particle, p the momentum, m the mass and c the speed of light. Neutrino model dependent assumptions are not necessary. Typical examples are time-of-flight measurements and the investigation of β-decays.

Neutrinoless Double Beta Decay

In 0νββ-experiments the reaction

$$(Z, A) \rightarrow (Z + 2, A) + 2\mathrm{e}^- \quad (0\nu\beta\beta) \tag{5.19}$$

is searched. In this reaction two neutrons of the same nucleus decay into two protons under exchange of a virtual neutrino. As the neutrino is emitted and absorbed in one reaction it needs to be its own anti-particle. Therefore, (0νββ)-decays are only possible in case of Majorana neutrinos. The half life time is the observable of such experiments and depends on the Majorana mass according to

$$T_{1/2} = \left(G^{0\nu}(Q, Z) |M_{nuc}|^2 \left(\frac{m_{\beta\beta}}{m_e} \right)^2 \right)^{-1} \quad \text{[Zub12]}. \tag{5.20}$$

Thereby $G^{0\nu}$ is a phase space factor as function of the Q-value and the atomic number Z of the nucleus. M_{nuc} is the nuclear matrix element, m_{e} the electron mass and $m_{\beta\beta}$ the Majorana mass which is given by

$$m_{\beta\beta} = \left| \sum_i U_{\text{e}i} m_i \right|. \tag{5.21}$$

Even for non-zero m_i the Majorana mass $m_{\beta\beta}$ can vanish due to the complex factor. The search for ($0\nu\beta\beta$)-decays is a very active field in neutrino physics and there are many experiments. Examples are EXO [Aug12] and KamLAND-Zen [Kam13] both using ^{136}Xe, GERDA [Ago13] and MAJORANA [Gre15] using ^{76}Ge, CUORE [CUO14] is using ^{130}Te.

Cosmological observations
As neutrinos have a distinct role in structure formation of the universe and contribute to the energy density, the neutrino mass $m_{\text{tot}} = \sum_i m_{\nu_i}$ can be deduced from astrophysical observations. There are many cosmological probes for the matter distribution in the universe (e.g. cosmic microwave background (CMB), galaxy distribution, gravitational lensing of the CMB or galaxies, Lymann α-forest), which can also be used to search for the signature suppression of non-vanishing neutrino masses. An overview with an explanation of the basic principle can be found in [Aba11].

Cosmological constraints on m_{tot} can be rather sensitive as for example a recent result from the Planck collaboration

$$m_{\text{tot}} < 0.23 \text{ eV/c}^2 \quad \text{[Pla15]}. \tag{5.22}$$

Nevertheless, they are also very susceptible to systematic uncertainties due to the complexity of cosmological models.

Time-of-flight measurements
On the 24th February 1987, a supernova was observed in the Large Magellanic Cloud in a distance of about $1.6 \cdot 10^5$ ly. A neutrino burst from this supernova, with 11 events within 13 s, was detected by the Kamiokande detector [Kam87]. The energy of the neutrinos was between 7.5 MeV to 36 MeV. About three hours later the first optical record of SN1987a occurred. From the different arrival times of the neutrinos and their energy one can derive an upper limit for the neutrino mass of $m_{\nu_{\text{e}}} \leqslant 12$ eV/c^2 [Arn87]. More stringent limits can be derived by including model-dependent assumptions on neutrino emission profiles.

Kinematic β-decay
Investigations of the kinematics of β-decays are the most sensitive ways for a model-independent neutrino mass measurement. The observable in such experiments is

$$m^2(\nu_{\text{e}}) = \sum_i |U_{\text{e}i}|^2 m_i^2. \tag{5.23}$$

An electron energy spectrum of the β^--decay is shown in figure 5.3. The effect of a non-vanishing neutrino mass becomes apparent close to the endpoint E_0. A careful measurement of the shape of the electron spectrum close to the endpoint region can
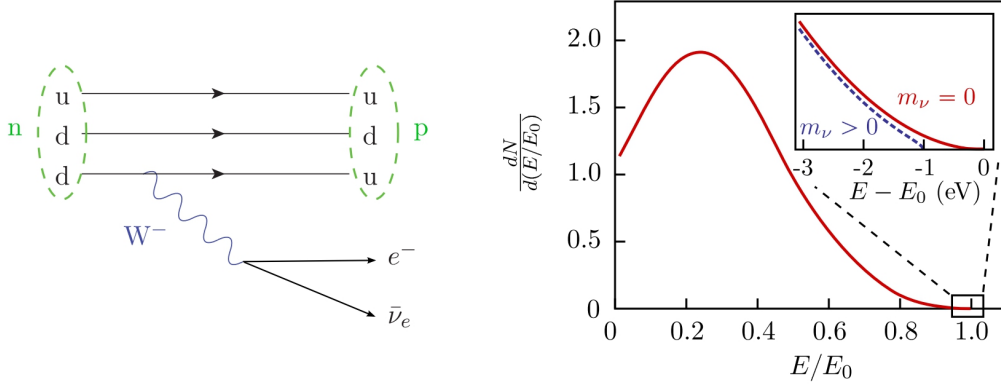
Figure 5.3.: β^--decay and electron energy spectrum. Left, Feynman diagram of a β^--decay. Right, electron energy spectrum. A non-vanishing neutrino mass changes the spectral shape in the endpoint region according to equation 5.24. Figure from [Fis14].

therefore be used for deriving $m^2(\nu_e)$. It is done by fitting the measured energy spectrum according to the equation [Kra05]

$$
\begin{aligned}
\frac{\mathrm{d}R}{\mathrm{d}E} = {} & N\frac{G_\mathrm{f}^2}{2\pi^3\hbar^7c^5}\cos^2(\theta_c)|M|^2F(E,Z+1)p(E+m_\mathrm{e}c^2) \\
& \cdot\sum_{ij}P_i(E_o-V_i-E)|U_{ej}|^2\sqrt{(E_0-V_i-E)^2-m^2(\nu_j)c^4}
\end{aligned}
\tag{5.24}
$$

in which the neutrino mass is a free fit parameter. N is the number of mother nuclei, G_f is the universal Fermi coupling constant, θ_c is the Cabibbo angle, M is the nuclear matrix element, $F(E, Z+1)$ is the Fermi function, p is the electron momentum, m_e is the electron mass and E_0 is the endpoint energy.

Different β^--emitters can be used for that. One prominent candidate is ^{3}H (also denoted as T) due to several reasons:

1. T has a short half live time of about 12.3 y due to the super-allowed decay. Hence, to achieve sufficiently high statistics in the endpoint region of the β^--spectrum only a rather small amount of T is needed.

2. T has a rather low endpoint value of about 18.6 keV. This is beneficial due to technical reasons when using an electro-static filter for the energy determination. High voltages of 18.6 kV are still manageable.

3. T has an atomic number of $Z = 1$ and a simple electronic shell structure. This minimizes Coulomb interactions of the emitted β-electron and allows precise theoretical calculations.

4. T forms molecules with other hydrogen isotopes (T$_2$, DT, HT). This is disadvantageous as molecular excitations change the electron spectrum but due to rather simple structure of the daughter molecules (e.g. (^{3}HeT)$^+$) it still allows precise calculations.
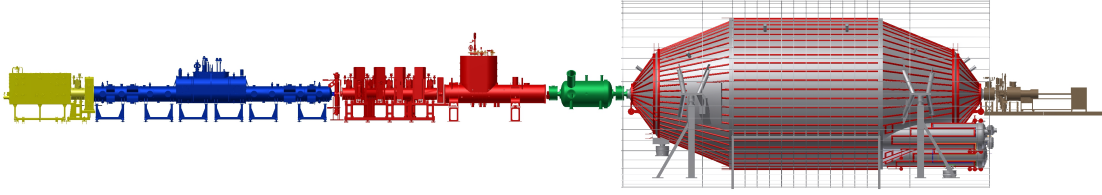
Figure 5.4.: Overview of the KATRIN experiment. The STS-section consists of the **C**alibration and **M**onitoring **S**ystem (CMS, yellow), the **W**indowless **G**aseous **T**ritium **S**ource (WGTS, blue) cryostat, the **D**ifferential and the **C**ryogenic **P**umping **S**ection (DPS and CPS, red). The SDS-section consists of the prespectrometer (green), the main spectrometer (grey) and the **F**ocal **P**lane **D**etector (FPD, rightmost in brown). Drawing is not to scale.

Currently the most stringent upper limits for a model-independent neutrino mass measurement come from tritium β-decay experiments.

$$m(\nu_\mathrm{e}) \quad \leqslant \quad 2.3 \ \mathrm{eV}/\mathrm{c}^2 (95\% \ C.L.) \quad [\mathrm{Kra05}] \tag{5.25}$$

$$m(\nu_\mathrm{e}) \quad < \quad 2.05 \ \mathrm{eV}/\mathrm{c}^2 (95\% \ C.L.) \quad [\mathrm{Ase11}] \tag{5.26}$$

Significant steps forward in the sensitivity were mainly due to the introduction of a new type of spectrometer, the so-called MAC-E filter. This spectrometer type is also used in the next-generation neutrino mass experiment KATRIN which is discussed in the following section.

5.2. The KATRIN experiment and the windowless gaseous tritium source

The aim of KATRIN is the model independent measurement of the effective electron neutrino mass with an sensitivity of $0.2 \ \mathrm{eV}/\mathrm{c}^2$ (90% C.L.). Therefore, the tritium beta electron spectrum is investigated near the kinematical endpoint of 18.6 keV. To reach this unprecendented sensitvity in the sub-eV region KATRIN uses a windowless gaseous tritium source with an activity of $1.1 \ 10^{11}$ Bq and a high resolution tandem spectrometer with an energy resolution of $\Delta E = 0.93$ eV at $E = 18.6$ keV [KAT04].

5.2.1. Overview of the KATRIN experiment

The KATRIN experiment, as shown in figure 5.4, can be subdivided into two functional parts. The tritium leading **S**ource and **T**ransport **S**ection (STS) which is located inside the TLK and the non-tritium leading **S**pectrometer and **D**etector **S**ection (SDS) outside the TLK.

The STS part of KATRIN consists of

1. the **C**alibration and **M**onitoring **S**ystem (CMS),

2. the **W**indowless **G**aseous **T**ritium **S**ource (WGTS) cryostat,
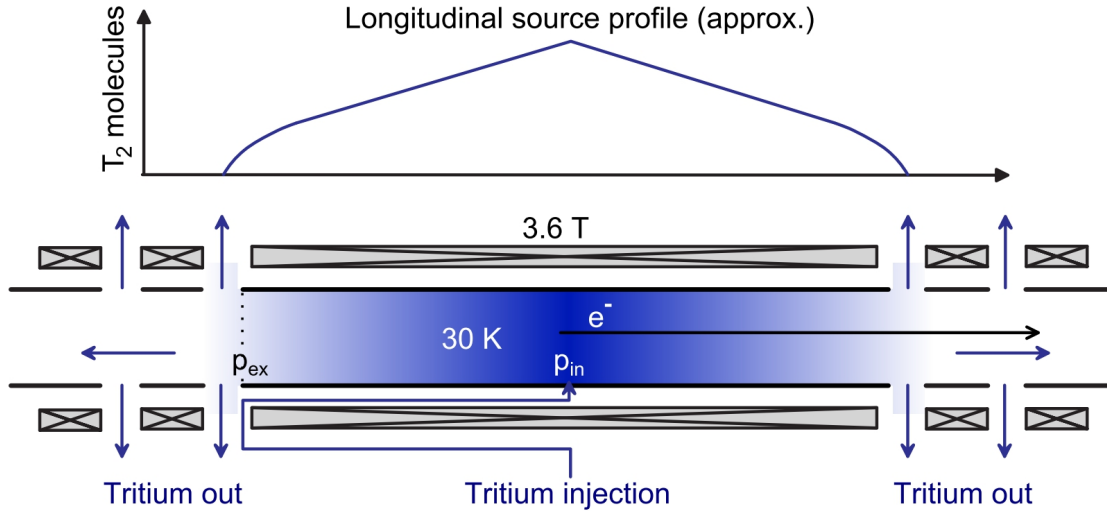
Figure 5.5.: Schematic drawing of the Windowless Gaseous Tritium Source (WGTS). Molecular tritium gas is injected in the middle of the source tube and freely streams towards both ends. There, it is pumped out and recirculated. A system of superconducting solenoids (3.6 T) is used to magnetically guide the β-electrons towards the spectrometer. Image from [Bab12].

3. the inner and outer tritium loop,

4. the **D**ifferential **P**umping **S**ection (DPS) and

5. the **C**ryogenic **P**umping **S**ection (CPS).

From a physics point of view the WGTS is a tritium gas column in an open cylinder with a diameter of 90 mm and 10 m length. The gas column is inside a homogeneous magnetic field of 3.6 T generated by superconducting solenoids. In the middle of the source tube tritium gas is continuously injected through a system of 300 capillaries, with a rate of 40 g/day and a tritium purity of $\geqslant 95$ %. In figure 5.5 the resulting gas density profile is shown. The gas freely streams to both ends of the source tube and is evacuated there by 12 turbo molecular pumps. This first pumping stage is the DPS1-R/F and reduces the tritium flow by a factor of 10^2. Pumped out gas is reinjected to the inner tritium loop for purification. β-electrons which are produced inside the WGTS are magnetically guided in z-direction by forcing them on cyclotron trajectories.

The transport section (DPS and CPS) has the task to reduce the tritium flow from the WGTS to the pre-spectrometer by a factor of 10^{14} while adiabatically guiding the tritium β-electrons through the transport section. Four differential TMPs at the DPS2-F reduce the tritium flow by a factor of 10^5. The CPS reduces the tritium flow by a factor of 10^7 by cryogenic pumping. This is done by cooling the beam tube down to a temperature of 3 K and freezing out argon snow on the inner surface. During operation tritium is adsorbed on the argon snow. As soon as the tritium coverage reaches about 1 % ($\approx 3.7 \cdot 10^{10}$ Bq) the CPS is regenerated. This is done by heating up to beam tube to about 100 K and the argon tritium mixture is extracted by a helium purge gas stream to the outer loop. The basic principle was successfully demonstrated in [Kaz08]. In both

pumping sections chicanes are implemented to block the direct line-of-sight for tritium molecules. β-electrons from the WGTS are adiabatically guided through the transport section to the pre-spectrometer by magnetic fields with field strengths between 0.5 T and 5.6 T which are produced by superconducting coils in the CPS and DPS.

The CMS fulfills several calibration and monitoring tasks. The implemented electron gun is used for the determination of several crucial parameters of the WGTS. The so-called *rear wall* defines the starting potential of β-electrons inside the WGTS relative to the analyzing plane of the main spectrometer. In normal measuring mode about 99.99 % of all β-electrons produced in the WGTS impinge on the *rear wall* and produce there X-rays. The intensity of the produced X-rays is a measure for the amount of tritium inside the WGTS. This principle is used by the implemented BIXS-system for tritium activity monitoring of the WGTS.

The inner and outer tritium loop provides the stabilized tritium gas flow to the WGTS with a tritium purity of $\geqslant 95$ %. Furthermore, it is responsible for tritium removal from exhaust gases from the DPS and CPS. This part of KATRIN was already explained in section 2.1.4.

The SDS part of KATRIN consists of

1. the pre-spectrometer,

2. the main-spectrometer and

3. the Focal Plane Detector (FPD).

The pre-spectrometer and the main-spectrometer are based on the MAC-E (magnetic adiabatic collimation with an electrostatic filter, [KAT04]) principle. With a diameter of 1.7 m the pre-spectrometer is used to reduce the electron flow to the main spectrometer. β-electrons with an energy of about $\leqslant 18.4$ keV are reflected. By that, ionization process caused by low-energy electrons in the residual gas of the main spectrometer are also reduced.

The main-spectrometer has an maximum inner diameter of 9.8 m, which is necessary to reach the aimed energy resolution of 0.93 eV at an energy of 18.6 keV [KAT04]. According to the MAC-E filter principle, an inhomogeneous magnetic field is used to transform the cyclotron energy of the β-electrons which enter the spectrometer into longitudinal motion. In the middle of the main spectrometer, where the magnetic field is weakest (0.3 mT) this effect is strongest and the energy analysis took place. A precise electrostatic retarding potential is applied to the analyzing plane and β-electrons with an energy lower than that are reflected. β-electrons which overcome the potential barrier are re-accelerated and guided to the FPD which is used as an electron counter. By varying the retarding potential the spectrometer can scan through the β-spectrum. The MAC-E filter principle is illustrated in figure 5.6.

β-electrons which pass the pre- and main-spectrometer are counted by the FPD. It is a segmented PIN-diode (148 segments) with a total diameter of about 10 cm. It covers the whole technical flux tube of 210 (T cm^2) from the WGTS.
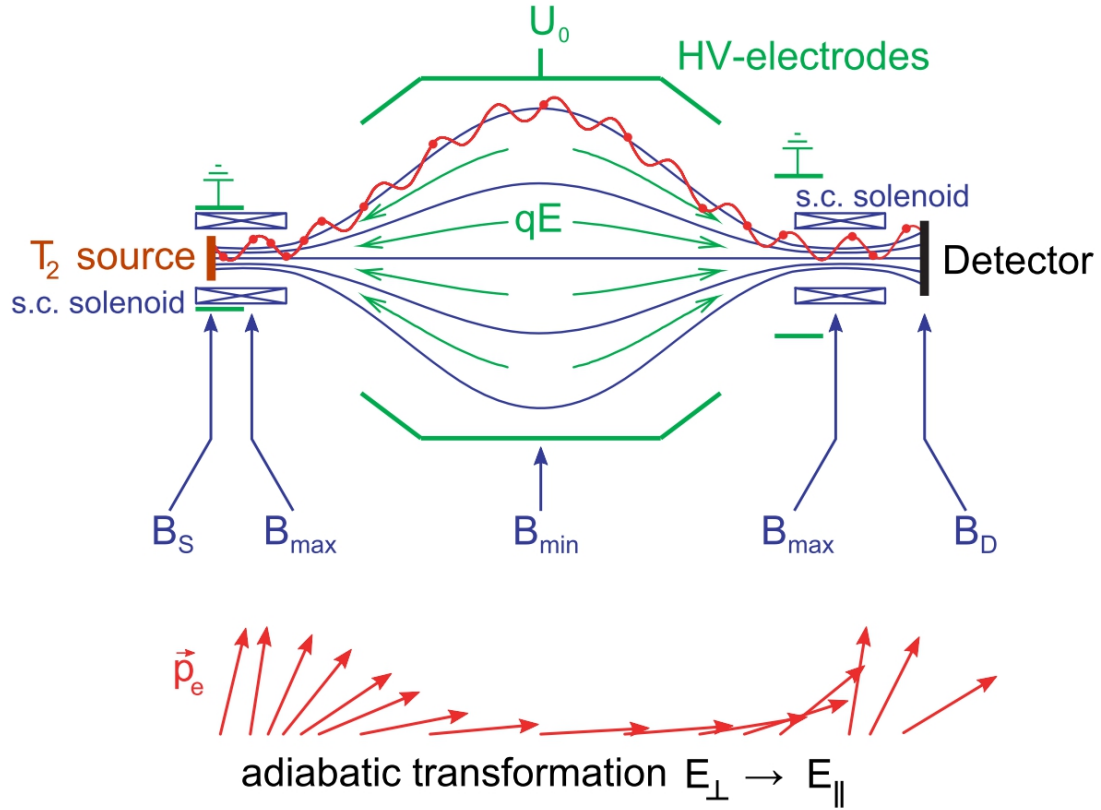
Figure 5.6.: Basic principle of the MAC-E filter. Two superconducting solenoids form a inhomogeneous magnetic field with field strengths of $B_{max} = 20\,000 \cdot B_{min}$. β-electrons from the source follow the magnetic field lines on spiral trajectories. Due to the conservation of the magnetic moment $\mu = E_\perp/B$ the kinetic energy of the cyclotron motion $E_\perp$ is converted into longitudinal motion in the weak field area. An electrostatic retarding potential is created by ring electrodes and is strongest in the middle of the vessel where the magnetic field strength is lowest. Electrons which are able to pass the retarding potential, are re-accelerated and guided on the FPD for counting. By variation of the retarding potential the shape of the β-spectrum can be step-wise measured. Image from [Fis14].

5.2.2. Key parameters of the WGTS

To achieve a high statistical sensitivity in the neutrino mass measurement of KATRIN one of the key parameters is the column density $\mathcal{N}$. As the count rate S of the FPD scales with

$$S \propto \epsilon_{\mathrm{T}} \mathcal{N}, \tag{5.27}$$

the tritium purity ϵ_{T} and column density $\mathcal{N}$ must be carefully stabilized and monitored.[1] ϵ_{T} is thereby defined as the number of tritium atoms in the gas column divided by the total number of atoms in the gas column. $\mathcal{N}$ is defined as the number of molecules within a flux tube volume of unit cross section ($\mathcal{N} = \rho \cdot d$).

Both parameters can significantly contribute to systematic uncertainties in deriving the neutrino mass. Due to different recoil energies and molecular final state distributions, non-T_2 impurities in the gas column require corrections of the β-electron spectrum. Variations in the column density change energy losses of β-electrons by inelastic collisions with the gas inside the source. The envisaged KATRIN operating values are $\epsilon_{\mathrm{T}} \leqslant 0.95$ and $\mathcal{N} = 5 \cdot 10^{17}$ molecules/cm^2.

Key parameters which must be stabilized to stabilize $\mathcal{N}$ are

- the inlet pressure $p_{\mathrm{in}} \approx 3 \cdot 10^{-3}$ mbar,

- the outlet pressure $p_{\mathrm{out}} \approx 0.05 \cdot p_{\mathrm{in}}$ and

- the beam tube temperature T_{BT}.

KATRIN requires the stabilization of these three parameters at the 0.1 % level. The inlet and the outlet pressure are stabilized by the pressure controlled buffer vessel of the inner loop and the constant pumping speed of the turbo molecular pumps as discussed in section 2.1.4. Also the monitoring of ϵ_{T} on the 0.1 % level is done in the inner loop by a laser Raman system. T_{BT} is stabilized and monitored on the 0.1 % level by a complex cooling system which is discussed in [KAT04] and was succesfully tested [Gro13].

A complementary way to monitor the column density is composition monitoring by laser Raman spectroscopy and activity monitoring by **B**eta **I**nduced **X**-ray **S**pectrometry (BIXS). As the stability of the column density is a crucial parameter for KATRIN in-situ monitoring would be strongly desirable and BIXS has the potential to reach the necessary 0.1 % level.

Previous test experiment performed at TLK already demonstrated that BIXS activity monitoring of a gaseous tritium source is possible. The main results are briefly discussed in the next section. Experiences gained from these experiments helped to design a BIXS system for KATRIN which was done in [Bab14]. The design of this BIXS system is outlined in section 5.4.

The main questions in the focus of this work are: *What is the expected count rate of the BIXS-detectors under normal KATRIN operation? In what measurement is it possible to*

---

[1] This approximation is only valid in a reasonable small region around the envisaged operating parameters of the WGTS [Bab12]. Strong variations of these parameters can give rise to strong non-linear effects.
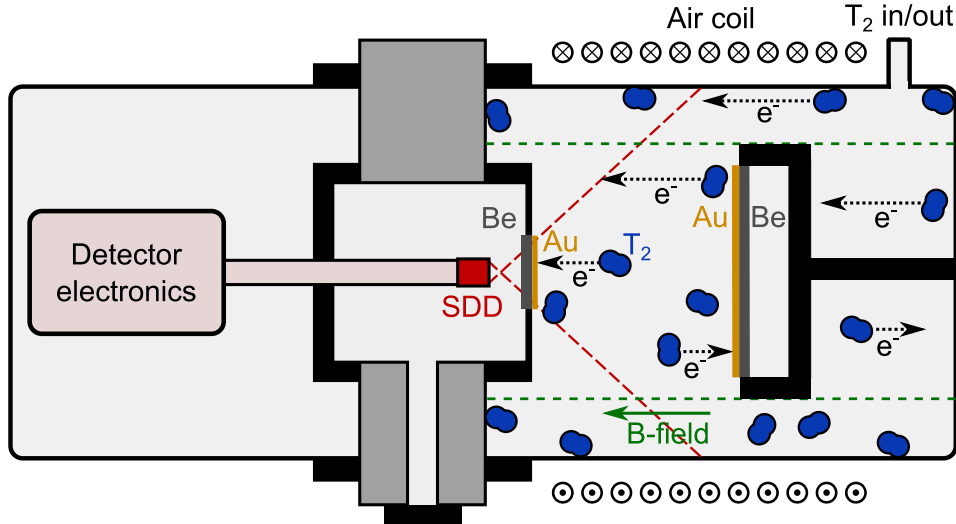
Figure 5.7.: Schematic of the TriReX BIXS setup (not in scale). The main section consists of three separate vacuum chambers. The detector electronics of the SDD is housed inside the left chamber at a pressure of about one bar. The SDD chip is at the top of a cooling finger in the middle volume is at a pressure of $\approx 10^{-2}$ mbar and is looking on the backside of a gold coated beryllium window which limits the solid angle for the detector. The right chamber contains the Q_2 gas sample and the two gold coated beryllium windows. An air coil outside the recipient produces the B-field for the magnetic guiding of the beta decay electrons. The recipient volume visible for the X-ray detector is $V = 0.76$ l.

detect activity fluctuations of the WGTS on the 0.1 % level? To what amount contributes adsorbed tritium on the rear wall or on the X-ray windows to the detector count rate?

These questions are investigated by Monte Carlo simulations. This is discussed in section 5.5 and consequences for KATRIN are drawn in section 5.6.

5.3. Measurement results of previous test experiments for activity monitoring of gaseous tritium sources

The feasibility of activity monitoring of a gaseous tritium source under KATRIN near conditions was investigated at TLK with the **Tri**tium **Re**ar Wall **Ex**periment (TriReX) [Roe13]. In figure 5.7 a schematic of the core components is shown. The main section consists of three separate volumes. These are

- the left volume which houses the X-ray detector electronics,

- the middle volume which houses the X-ray detector and

- the right volume which works as a recipient and contains the tritium gas mixture.

A small X-ray transparent beryllium window ($\varnothing$39 mm) is used to protect the X-ray detector from tritium contamination. A second X-ray transparent beryllium window ($\varnothing$50 mm) which is blind flanged on the back side is used as a reference surface. Both
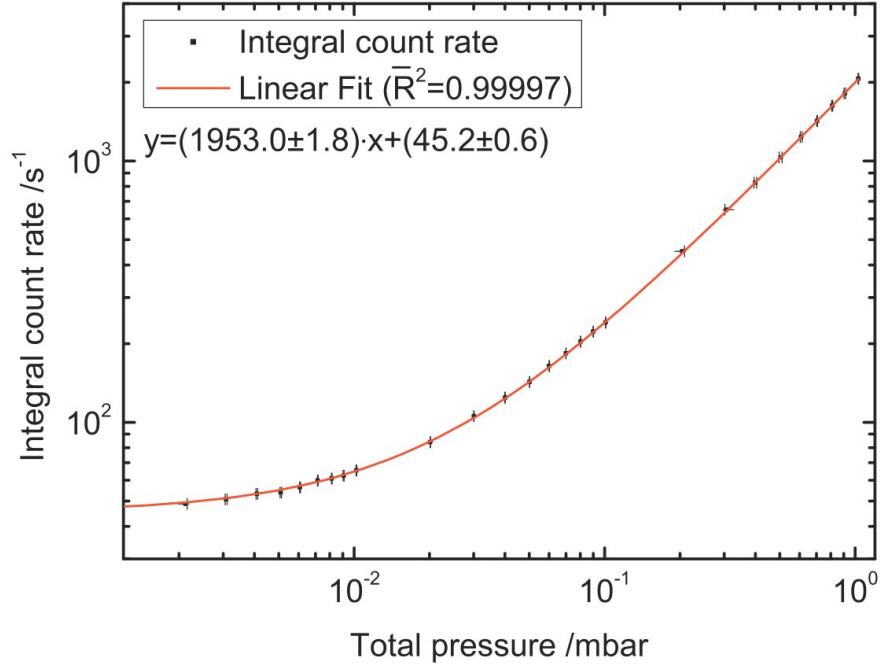
Figure 5.8.: Integral count rate over total pressure. A pump-down test over three decades of total pressure was performed to investigate the linearity of the system. The tritium purity was $\epsilon_T = (95 \pm 4)$ % and the measurement time for each data point varies from 100 s to 250 s. Error bars indicate 1σ statistical errors.

windows are sputter coated with 100 nm gold for efficient X-ray production. The feasibility of activity monitoring of gaseous tritium was tested in a pressure range between 10^{-3} mbar to 1 mbar and was reported in [Roe13]. In figure 5.8 the result is shown. The maximum activity inside the recipient was $(6.87 \pm 0.47) \cdot 10^9$ Bq. In the applied pressure range the system showed a linear behavior.

Further measurements were performed to demonstrate the ability of the system to detect activity fluctuations of the order of 0.1 %. This test was successfully performed and is reported in [Bor15]. It was also found out that a major contribution to systematic uncertainties on the detector count rate is caused by the used digital pulse processor. An alternative pulse processor was idintified and characterized[2]. It was shown that it is a suitable system for high stability activity monitoring on 0.1 % level.

These promising results led to the design of the KATRIN BIXS system as part of the CMS, which is discussed in the following section.

---

[2]   Bachelor thesis: Characterization of a detector system consisting of a KETEK AXAS-M1 X-ray detector and an Amptek DP5 data acquisition unit, Woo-Jeong Baek

Table 5.1.: Parameters of the β-electron flux from the WGTS impinging on the *rear wall*.

Description	Flux tube (T cm^2)	∅ on the rear wall (cm)	No. of e$^-$ (s^{-1})
outer	229	13.9	$1.13 \cdot 10^{11}$
technical	210	13.4	$1.04 \cdot 10^{11}$
inner	192	12.8	$0.95 \cdot 10^{11}$

5.4. Final setup of the KATRIN BIXS system

The BIXS monitoring system for activity monitoring of the KATRIN WGTS is part of the CMS which fulfills crucial calibration and monitoring tasks within the KATRIN experiment. A detailed description of the CMS is given in [Bab14]. The BIXS relevant parts of the CMS comprise the re-condensing superconducting magnet (RSCM) and the rear wall vessel with the X-ray detectors and the *rear wall*. These components are located at the interface between the CMS and DPS1-R/WGTS. A CAD drawing of this is shown in figure 5.9.

The functionality of the *real wall* as the electrical termination of the WGTS plasma, the definition of the plasma potential and the activity monitoring by BIXS requires the collimation of the magnetic flux tube to the *real wall* surface. As defined before there is the outer flux (229 T cm^2), the technical flux (210 T cm^2) and the inner flux (192 T cm^2) tube. The flux tubes are contained inside the rear wall vessel by the RSCM with a maximum magnetic field of 4.7 T and magnetic stray fields from DPS1-R/WGTS superconducting magnets. To ensure that the full flux tube hits the *rear wall*, it's placed inside the exit cone of the DPS1-R which is part of the rear wall vessel. The diameter of the *rear wall* is 14.6 cm and it is located in a magnetic field between 1.4 T and 1.6 T in z-direction. Therefore, the technical flux intersects only with the gold-coated part of the *rear wall* with a remaining clearance of 1.3 mm to the PEEK mounting ring. It can be increased or decreased by the adjustable z-position of ±5 mm of the *rear wall* [Bab14].

Nearly all of the β-electrons which are produced inside the WGTS are eventually absorbed in the *rear wall*. β-electrons emitted in the direction of the spectrometer or backscattered from the *rear wall* can be reflected back to the *rear wall* by the magnetic mirror effect. As the electrons start in a magnetic field of 3.6 T about 44 % would be reflected back due the 6 T pinch magnet between the main spectrometer and the FPD. Even without that more than 99.99 % of the β-electrons are reflected back due to the retarding potential of the tandem-spectrometer. About 10^{11} β-electrons per second impinge on the gold coating of the *rear wall* and therefore produce intense X-ray radiation which can be used for activity monitoring by BIXS. The electron flux from the outer-, inner- and technical flux tube and the corresponding diameter on the *rear wall* is noted in table 5.1.

Two KETEK AXAS-M SDDs, each with an active area of 92 mm^2, are used for the detection of the X-ray radiation. Amptek DP5 digital pulse processors are used for the data acquisition. Contamination of the X-ray detectors by the tritium gas mixture in the rear wall vessel is prevented by X-ray transparent beryllium windows with a thickness of 250 µm. The leakage rate of the beryllium windows is specified with $q \leqslant$
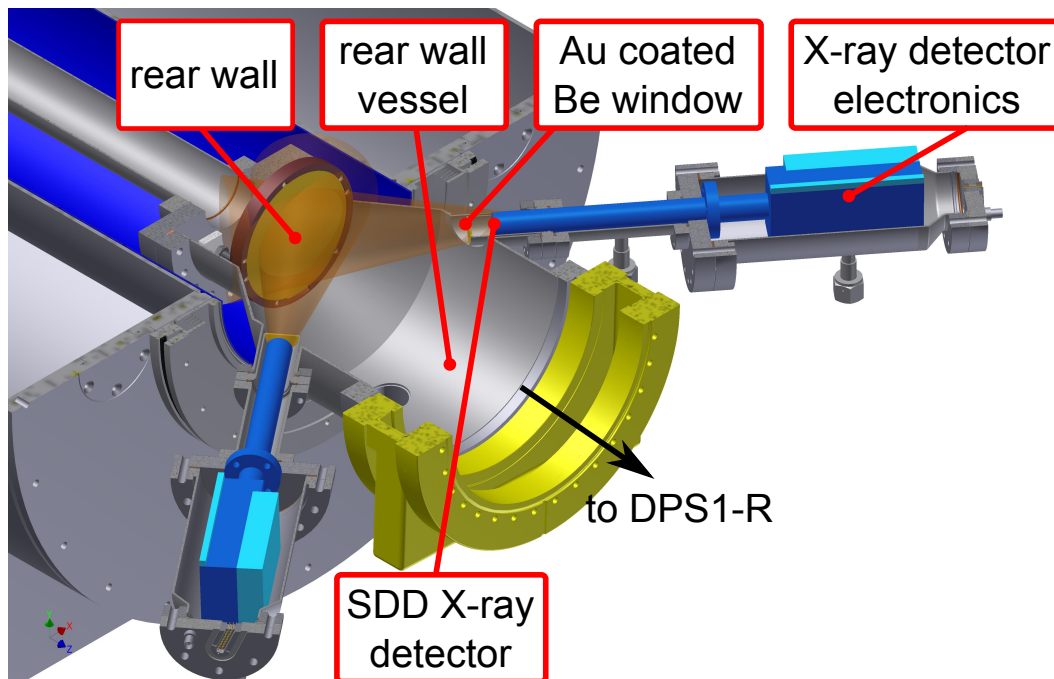
Figure 5.9.: CAD drawing of the CMS-DPS1-R interface region. β-electrons from the WGTS impinge on the *rear wall* and produce X-rays which are detected by two Ketek AXAS-M X-ray detectors. Each detector is protected from tritium contamination by an X-ray transparent gold-coated beryllium window.

10^{-9} mbar l/s. Both windows can be gold coated to reduced tritium adsorption or used with bare beryllium substrates to minimize X-ray production by adsorbed tritium. Further measurements with the TLK TRIADE setup (see chapter 6) must be performed for that to evaluate.

The SDD capsules of the X-ray detectors must be operated at vacuum conditions ($<$ 0.1 mbar) to reduce heat input on the peltier cooled SDD (operated at about -55 °C), whereas the detector electronics must be operated at normal pressure. The cooling finger which connects the SDD capsule with the detector electronics is internally sealed by an elastomer sealing which has a significant leakage rate in the order of 10^{-7} mbar l/s. Gas which permeates from the detector electronics volume to the SDD volume is therefore pumped back by a scroll pump.

As the geometry of the KATRIN BIXS system is very different from all previous test experiments, the count rate of the BIXS detectors under normal KATRIN operation can only be predicted by Monte Carlo simulations.
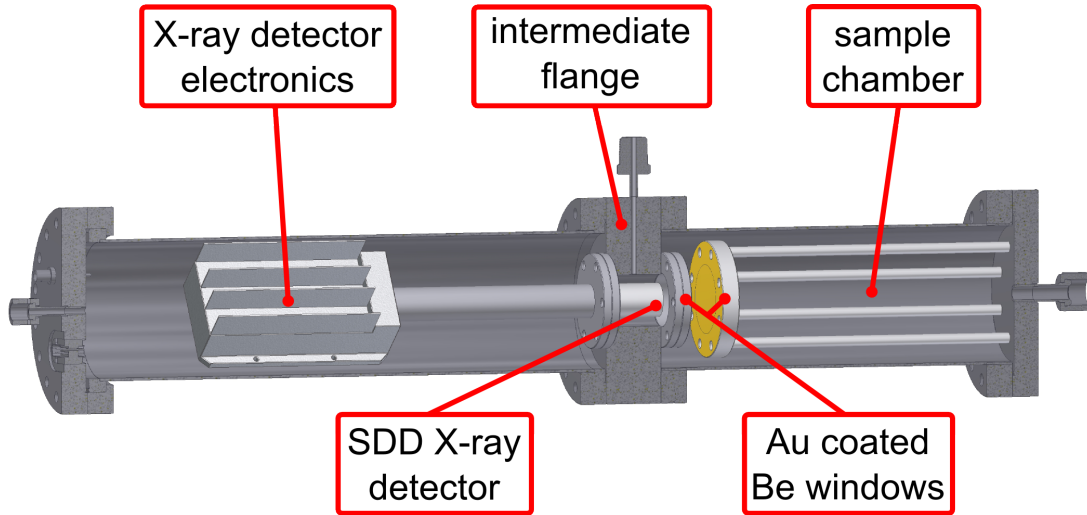
Figure 5.10.: CAD drawing of the TriReX experiment.

5.5. Performance study of the KATRIN BIXS system by Monte Carlo simulations

The potential performance of the KATRIN BIXS system crucially depends on three issues:

1. To reach a 0.1 % sensitivity on activity fluctuations of the WGTS, the statistical uncertainty on the measured count rate must be better than 0.1 % within one measurement interval t_{meas}. That means, during normal KATRIN operation the count rate must be higher than 10^3 s^{-1} ($t_{\mathrm{meas}} = 1000$ s) or 10^4 s^{-1} ($t_{\mathrm{meas}} = 100$ s).

2. Tritium surface contamination on the inner surfaces of the system can cause a background signal. If this background contribution is too high, it can make the BIXS system blind for small variations of the source activity. Therefore, it must be quantified.

3. As there are mechanical tolerances in the detector position, it must be studied what those mean in terms of count rate decrease/increase if the detector position is shifted.

This is done by Geant4 simulations. Before coming to these simulations, the software is benchmarked on tritium measurement results of a previous BIXS experiment.

5.5.1. Benchmark of the GEANT4 software with TriReX results

As mentioned in section 5.3, activity monitoring of a gaseous tritium source by BIXS was demonstrated at TLK by TriReX measurements. Due to its simple geometry (see figure 5.10) and its careful calibration by pVT-c measurements, this is also a suitable test case for the simulation accuracy of Geant4.
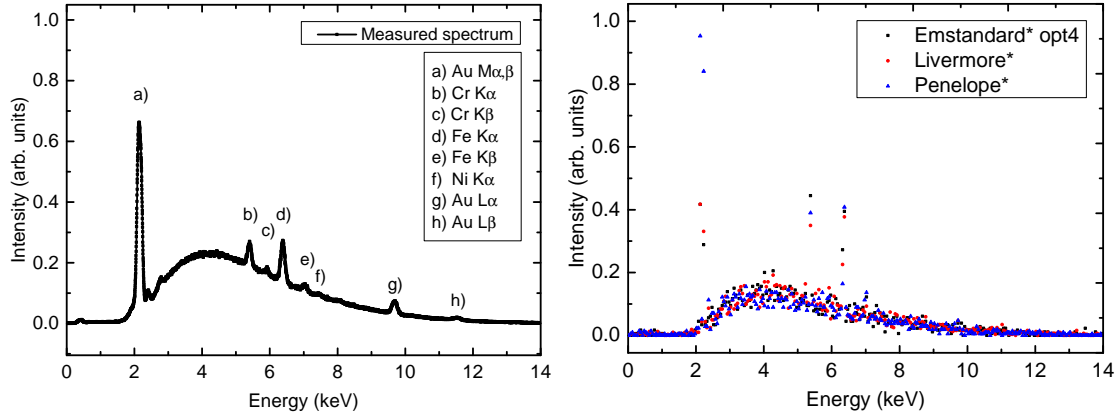
Figure 5.11.: Comparison of a measured TriReX BIXS spectrum (left) and simulation results (right).

The simulated TriReX geometry is given in appendix A.17. Compared to the mechanical dimensions of the actual setup, the uncertainties are estimated to be smaller than 1 mm. A modified version of the "TestEM5" example of Geant4.9.6p02 was used. The starting vectors for the primary particles were homogeneously distributed over the cylindrical volume between the two gold coated beryllium windows. Electrons were emitted isotropically with an energy distribution according to the energy spectrum of the β-decay of tritium. No process gas was simulated.

Three different Geant4 physics packages were used ("Penelope", "Livermore", "emstandard opt4") to simulate a typical BIXS spectrum. Each of them is specialized on low-energy physics (see also section 3.4). In figure 5.11 a measured tritium spectrum and the Monte Carlo simulation results are shown. The continuous Bremsstrahlung background and the most prominent fluorescence lines are visible in all of the simulated spectra. Noticeable differences are only in height of the Au M_α line. In the "Penelope" spectrum the intensity is more than (2-3) times higher than in the "Livermore"/"emstandard opt4" spectra. For a real comparison with the measured spectrum the simulated spectra would have to be convoluted with a response function (e.g. Gaussian distribution with a FWHM of about 160 eV) to regard for the energy resolution of the detector. This was here not possible due to the rather low energy resolution in the simulated spectra (50 eV/channel) and insufficient statistics. Nevertheless, comparing the intensity ratios of the fluorescence lines, the "Penelope" package seems to give the best results.

Comparing the integrated intensities of the plots in figure 5.11 (right) and normalize it to the "Penelope" result, the "emstandard opt4" package gives a (3.1 ± 2.2) % lower intensity and the "Livermore" package a (6.1 ± 2.5) % lower intensity. Whithin a 2σ interval all three physics package results coincede.

In table 5.2 the tritium measurement results[3] and the simulation result for the detection efficiency of TriReX are given. Four measurement runs with four different gas mixtures were performed. In each run the gas-mixture in the sample chamber was step-wise

---

[3] Bachelor thesis: Systematic Investigations of an X-Ray Detector System for Monitoring the KATRIN Tritium Source, Sylvia Ebenhöch, 2012

Table 5.2.: Measured and simulated detection efficiencies (*DE*) for TriReX. Tritium purities are determined by gas chromatography measurements.

Description	*DE* $(10^{-7}\text{s}^{-1}/\text{Bq})$	Tritium purity (%)
Run#1	$3.18 \pm 0.06_{\text{fit}}$	95 ± 4
Run#2	$3.37 \pm 0.07_{\text{fit}}$	91 ± 6
Run#3	$3.10 \pm 0.05_{\text{fit}}$	95 ± 4
Run#4	$3.27 \pm 0.05_{\text{fit}}$	94 ± 4
Penelope	$3.44 \pm 0.34_{\text{stat}}$	-

evacuated. After each step, count rate measurements were performed and the results were fitted to the calculated activity within the sample chamber. The detection efficiency is then given as the slope of the best fit line. Gas chromatography measurements were used for the determination of the tritium purity.

Within the statistical uncertainty the simulated detection efficiency fits well to the measured ones. Deviations from the measured detection efficiencies are expected to be mainly caused by geometrical uncertainties (see section 4.2) and the choice of the physics package (see section 3.4.2). Nevertheless, the results fit well within a ≈ 10 % limit.

5.5.2. Monte Carlo simulations of the KATRIN BIXS system

In this section Monte Carlo results of the KATRIN BIXS system are discussed. In total 6 simulations have been performed with about 150 runs. An overview of all performed simulations is given in table 5.3. As the needed simulation time (in total $3.5 \cdot 10^4$ single core CPU hours on an Intel® Xeon® E5-2670 v3) would have been drastically increased when simulating the whole source, with its gas profile and its electromagnetic conditions, some simplifications must be made. This concerns foremost the simulated geometry and electromagnetic configuration.

5.5.2.1. Simulated geometry and simulation parameters

For the sake of calculation time the simulated geometry in simulations No. 1, 4-6 in table 5.12 was reduced to the rear wall vessel, the *rear wall* and the BIXS detectors. It was designed according to the technical drawings in appendix A.20 and is shown in figure 5.12. Only one of the two detectors was active in the simulation (highlightned detector). As the detector configuration is rotationally symmetric all simulation results are valid for both detectors. The C++ listing of the geometry description is given in the appendix A.18.

As in simulations No. 2 and No. 3 (table 5.12) only backscattering effects and β-electron transmission through a gas column were studied, the geometry was further simplified to save computing time. Only a *rear wall*-like disk and a gas column have been simulated without a rear wall vessel, X-ray transparent windows or X-ray detectors. The disk have
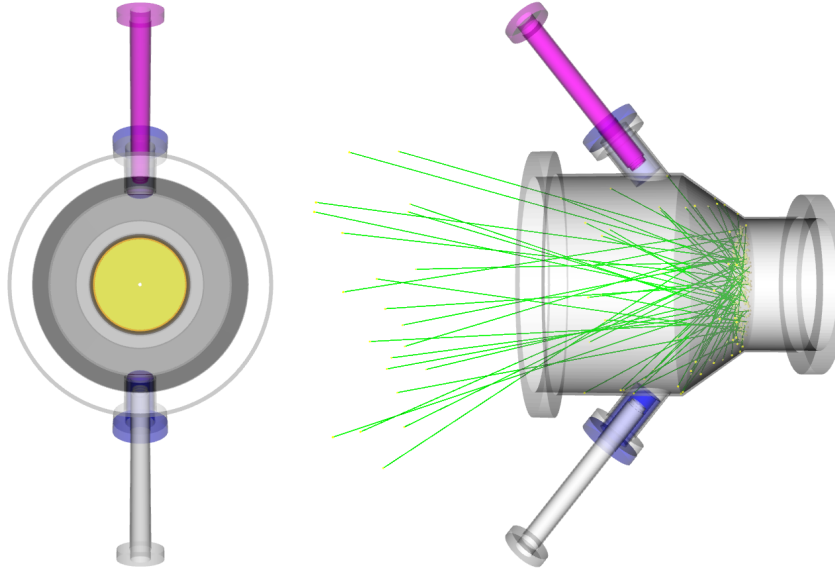
Figure 5.12.: Simulated geometry of the KATRIN BIXS system. Left: View in the axial direction. The *rear wall* is marked in yellow. Right: Side view with 10^5 simulated β-electron events. Electrons are filtered in the figure and only the produced X-rays are drawn. The cooling finger of the active detector in the simulation is highlighted in magenta.

the same layer configuration as the simulated *rear wall* (100nm of gold on a stainless steel disk), except there is no hole in the middle of the disk. The cylindrical gas column was simulated with a length of 1 cm and a density of 0.01 kg/m^3 which corresponds to a column density of $1 \cdot 10^{18}$ molecules/cm^2. This is twice the density of the WGTS gas column [KAT04].

In each simulation the primary particles were electrons with an energy distribution corresponding to the β-spectrum of tritium. The source descriptions vary in geometry and angular distribution according to the listed parameters in table 5.3 and in the positions. The choice of the respective parameters is justified for each simulation in the following subsections.

5.5.2.2. Projected count rate of the KATRIN BIXS detectors

In simulation No. 1 the detection efficiency for X-rays produced by β-electrons from the WGTS was calculated. β-electrons in the WGTS are emitted isotropically in a field of 3.6 T. Half of the β-electrons start on a helical trajectory in direction of the *rear wall*. Depending on the starting vector they must traverse a column density of $\leqslant 5 \cdot 10^{17}$ molecules/cm^2 before hitting the *rear wall*. The maximum polar angle $\theta_{\max}$ is transforming from 90° in the WGTS to 40° in front of the *rear wall* according to

Table 5.3.: Overview of the KATRIN Monte Carlo simulations. The denoted CPU-time is the needed single core CPU-time for all the simulation runs on an Intel® Xeon® E5-2670 v3.

No.	Description	No. of runs	Simulated β-events	CPU-time (hours)	Source type	Source shape	B-field (T)	Max. θ (deg)
1	source activity	120	$1.575 \cdot 10^{10}$	$2.5 \cdot 10^4$	plane	circular	1.5	40
2	backscattering	5	$5 \cdot 10^6$	19	point	point	1.5	40/90
3	electron transmission	1	$1 \cdot 10^6$	4	point	point	3.6	90
4	adsorbed T RW	13	$1.3 \cdot 10^{10}$	$6.5 \cdot 10^3$	plane	circular	1.5	90
5	adsorbed T Be-window	1	$2 \cdot 10^8$	$4.0 \cdot 10^2$	plane	circular	1	90
6	SDD shifts (± 2 mm)	9	$1 \cdot 10^{10}$	$3.2 \cdot 10^3$	plane	circular	1.5	40
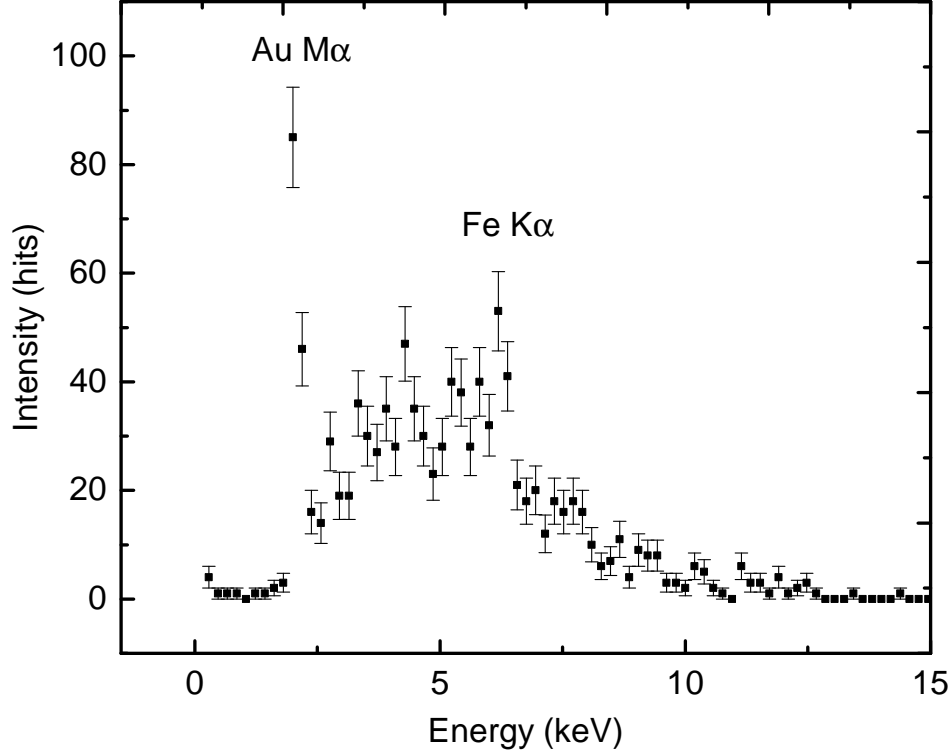
Figure 5.13.: Simulated KATRIN X-ray spectrum. β-electrons from the WGTS impinge on the *rear wall* and produce Bremsstrahlung and characteristic X-rays. These X-rays are detected by two BIXS detectors.

equation

$$\mu \approx \frac{E_\perp}{B} \quad = \quad \frac{E_{\text{kin}} \cdot \sin^2(\theta_1)}{B_1} = \frac{E_{\text{kin}} \cdot \sin^2(\theta_2)}{B_2} = \text{const.,} \tag{5.28}$$

$$\rightarrow \theta_{\text{max}} \quad = \quad \arcsin\left(\sqrt{\frac{B_{\text{RW}}}{3.6 \text{ T}}}\right). \tag{5.29}$$

β-electrons, starting on a helical trajectory in the direction of the tandem-spectrometer, are most probably reflected back in direction of the *rear wall*. Depending on their kinetic energy and emission angle either by the magnetic mirror effect when going from the WGTS to the DPS or by electrostatic reflection in the pre- or main-spectrometer (see section 5.2). Before they hit the *rear wall* they must traverse a column density of $\leqslant$ $1 \cdot 10^{18}$ molecules/cm^2. The fraction of β-electrons which is transmitted to the FPD is negligible for the X-ray production on the *rear wall*. Only a fraction of about 10^{-10} of all decays is in the last 10 eV of the β-spectrum.

To save computing time, β-electron interactions with the gas in the WGTS have been neglected in this simulation. All β-electrons start in front of the real wall in a distance of 1 mm, in a field of 1.5 T with a maximum θ of 40°. The technical flux tube of 210 T cm^2 is simulated, corresponding to an area of 140 cm^2 on the *rear wall* and a β-electron flux of $1.04 \cdot 10^{11}$ β-electrons/s.

Table 5.4.: Simulated backscattering probability of β-electrons from the KATRIN *rear wall*. The denoted 1σuncertainties indicate statistical errors.

Physics package	Backscattering (%)	B-field (T)	Max. polar angle θ (°)	Order
Emstandard opt4	44.34 ± 0.03	1.5	40	1st
Livermore	48.82 ± 0.03	1.5	40	1st
Penelope	44.29 ± 0.03	1.5	40	1st
Penelope	55.78 ± 0.04	1.5	90	2nd
Penelope	54.73 ± 0.04	1.5	90	3rd

In figure 5.13 the resulting X-ray spectrum is shown. It shows the typical shape as shown before. The simulated $1.575 \cdot 10^{10}$ events correspond to about 0.15 s of KATRIN operation. Clearly visible is the characteristic X-ray line Au $M_{\alpha,\ \beta}$. A total number of 1083 hits in the detector was calculated. This results in a total detection efficiency of $(6.88 \pm 0.21) \cdot 10^{-8}$ s^{-1}/Bq and a count rate of (7155 ± 218) s^{-1} per detector.

Two effects have the potential to add significant systematic uncertainties to this calculated count rate. These are backscattering of β-electrons on the *rear wall* and β-electron absorption in the gas column of the WGTS.

5.5.2.3. Backscattering of β-electrons from the rear wall

In the previous simulation, all β-electrons which are backscattered from the *rear wall* are killed as soon as they leave the world volume (see figure 5.12). Compared to the real setup this leads to an underestimation of the produced X-ray intensity. Backscattered β-electrons are either absorbed in the WGTS or reflected back to the *rear wall*. Reflection mechanisms are

- the magnetic mirror effect, when going from the low-field region of the rear-wall vessel (≈ 1.5 T) to the high field region of the WGTS/DPS (3.6 T/5.5 T) or

- the electrostatic reflection by the retarding potential of the tandem-spectrometer.

Which reflection mechanism occurs depends on the polar-angle after backscattering. If reflected back, the β-electrons interact again with the *rear wall* and can produce X-ray radiation.

In this section the backscattering probability from the *rear wall*, the energy distribution after backscattering and the energy spectrum after transmission through the source have been calculated (see table 5.3, No. 2, 3). Due to the huge calculation time the detection efficiency of backscattered and subsequently reflected β-electrons have not been simulated. Instead, the potential count rate contribution is approximated.

According to equation 3.7 the Bremsstrahlung energy losses of an electron in an absorber per unique length scales with E_{tot}. The total detection efficiency for backscattered electrons which are reflected back to the source can therefore be approximated from the sim-
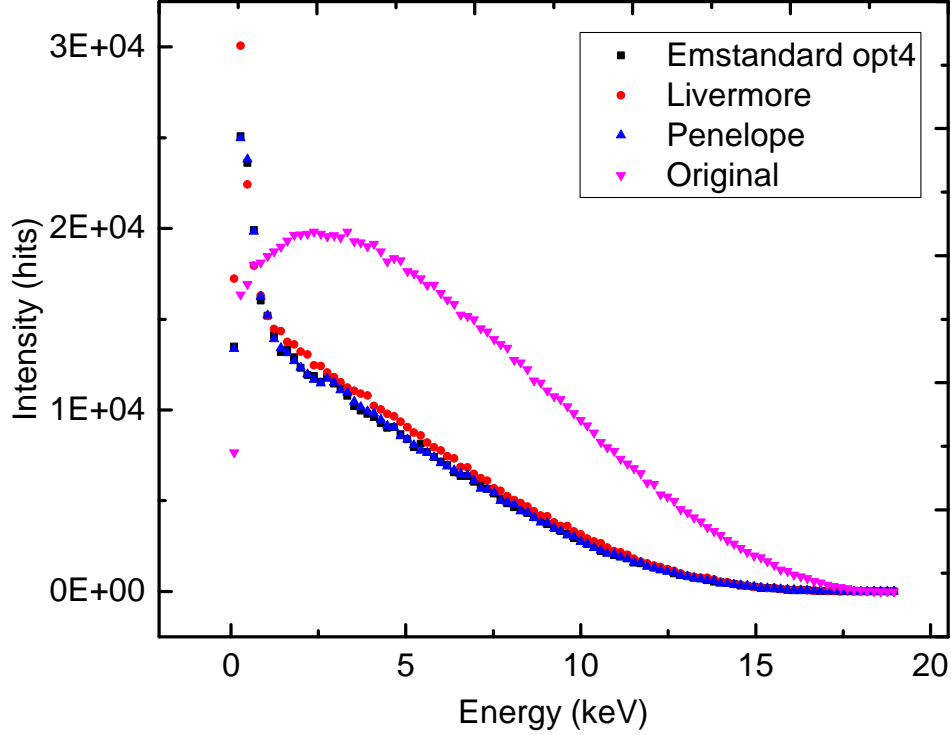
Figure 5.14.: Simulated energy spectrum of backscattered electrons from the KATRIN *rear wall*.

ulated detection efficiency for β-electrons (DE_{0th}, see section 5.5.2.2) and from the energy spectra of non-backscattered β-electrons and backscattered electrons (see figure 5.14). It is calculated according to

$$DE_{1st} = DE_{0th} \cdot \frac{\sum_i PD_{0th}(ch) \cdot \Delta E_{0th} \cdot E_{0th}(ch)}{\sum_j PD_{1st}(ch) \cdot \Delta E_{1st} \cdot E_{1st}(ch)}. \tag{5.30}$$

With the probability density *PD* for each channel of the simulated energy spectrum, the bin size per channel ΔE, the average energy of the respective channel $E(ch)$ and the number of channels in the simulated spectra i, j. Both energy spectra are thereby normalized according to

$$\sum_i PD_{0th}(ch) \overset{!}{=} 1 \quad \text{and} \quad \sum_j PD_{1st}(ch) \overset{!}{=} 1 \cdot P_{back,1st} \tag{5.31}$$

with the total probability $P_{back,1st}$ for once backscattered electrons. Using the backscattering probability from table 5.4 of $P_{back,1st} = (44.29 \pm 0.03)$ % this results in a detection efficiency of $DE_{1st} = (2.34 \pm 0.07) \cdot 10^{-8}$ s^{-1}/Bq for once backscattered and back-reflected electrons. This is about 34 % of DE_{0th} and increases the projected count rate of the X-ray detectors under normal KATRIN operation by (2429 ± 74) s^{-1}.

This approximation neglects changes in the angular distribution after backscattering, count rate contributions by characteristic X-rays which do not follow equation 5.30 and the fact that the backscattering probability $P_{back,1st}$ depends on the kinetic energy of the
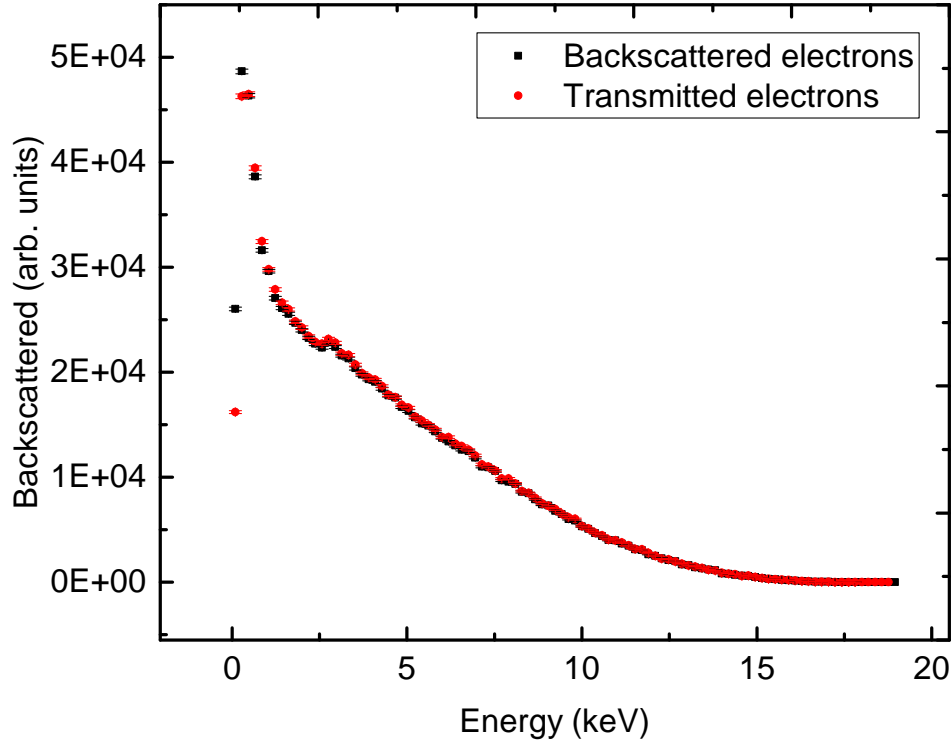
Figure 5.15.: Electron energy absorption in a tritium gas column of $1 \cdot 10^{18}$ molecules/cm^2. Electrons with an energy distribution according to the "backscattered" spectrum were emitted through a tritium gas column with twice the column density of the KATRIN WGTS. The simulated angular distribution of the electrons is isotropic and the magnetic field strength is 3.6 T.

electron. Contributions of higher order backscattered electrons (2nd, 3rd, …) to the X-ray detector count rate are expected to be smaller than the first order contribution. This is due to the electron energy loss after each backscattering and back-reflection cycle.

5.5.2.4. Influence of tritium surface contamination on the BIXS-detector count rate

Tritium surface contamination on the inner walls of the KATRIN BIXS system can cause a history dependent background signal which is known as memory effect in tritium analytical systems [Roe13], [Wag11]. In this section the detection efficiency for tritium surface contamination on the *rear wall* and on the X-ray transparent window is studied. These results, combined with tritium measurement results of a gold coated sample done with the TRIADE experimental facility (see chapter 6), can be used to quantify the count rate contribution due to tritium surface contamination during normal KATRIN operation.

For tritium surface contamination an isotropic angular distribution was assumed in the simulation runs No. 4 and No. 5. All primary particles are started on the respective surface. The magnetic field of 1.0 T in simulation run No. 5 can be regarded as an upper

Table 5.5.: Influence of tritium adsorption on the *rear wall* and on the X-ray transparent window on the detector count rate. The projected count rate is calculated for one monolayer of tritium, assuming an ideal (111) gold surface (see appendix A.1). Errors indicating 1σ statistical uncertainties.

Adsorbent	Detection efficiency (s^{-1}/Bq)	Area (cm^2)	Proj. count rate (s^{-1})
Rear wall	$(2.4 \pm 0.1) \cdot 10^{-8}$	167.4	(11.0 ± 0.6)
X-ray window	$(2.1 \pm 0.1) \cdot 10^{-6}$	9.6	(55.7 ± 2.7)

limit. In the final KATRIN setup the magnetic field is expected to be lower but there are no simulation data available yet.

In table 5.5 the results of the Monte Carlo simulation are listed. As expected, for the same coverage tritium surface contamination on the X-ray window is the dominating background contribution. Due to the small distance between the X-ray window surface and the SDD the detection efficiency is very high. Assuming one monolayer of tritium on the X-ray window this would result in a count rate of (55.7 ± 2.7) s^{-1}. Thereby contributions due to multiple backscattering are fully included. Due to the simulated magnetic field of 1.0 T electrons can not escape the simulated geometry. Instead, they propagate between the window and the rear wall vessel surface (see figure 5.12) until absorption.

Tritium surface contamination on the *rear wall* can cause a background count rate of (11.0 ± 0.6) s^{-1} assuming one monolayer of tritium. In this simulation run backscattered electrons can leave the simulated geometry and are therefore not included in the background count rate contribution. It is expected, that the count rate increase due to backscattered and back-reflected electrons is comparable to the calculations done in the previous section.

Assuming one monolayer of tritium on the X-ray transparent window and the *rear wall* would result in background count rate which is in the range of 0.6 % to 0.8 % of the total count rate under normal KATRIN operation.

5.5.2.5. Influence of small shifts in the SDD position on the detector count rate

As shown in [Mao12] small variations in the simulated geometry of a BIXS system can cause strong variations in the detection efficiency of the system. In case of the KATRIN BIXS system there are two major sources of uncertainty in the mechanical dimensions. The first is the absolute position of the *rear wall*, which has an adjustable mounting system (see [Bab14]). As the *rear wall* position can be shifted within a reasonable safety margin[4] it is neglected in the context of this work. The second major source of mechanical uncertainty is due to the sealing system of the used Conflat® ultra high vacuum components. Conflat® flanges are screwed together with a copper sealing between them.

4
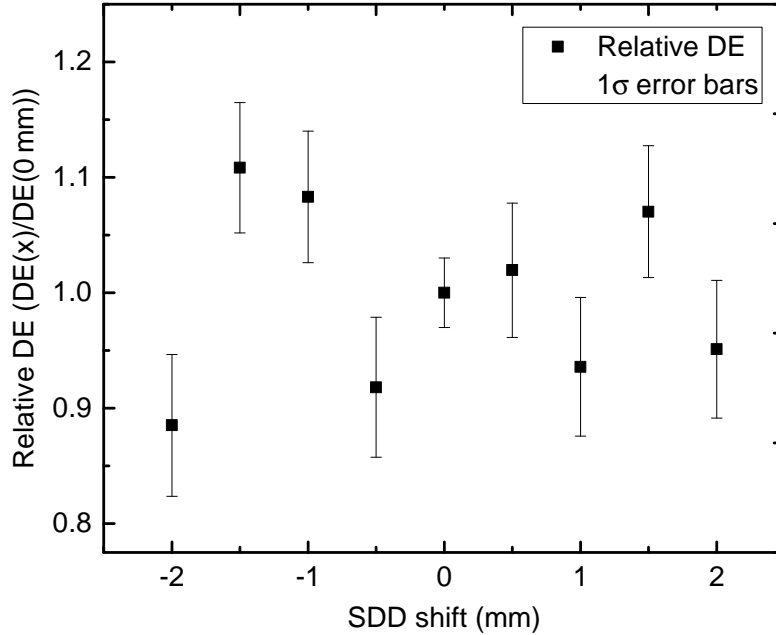
Figure 5.16.: Relative detection efficiency of the KATRIN BIXS system depending on the SDD position. Error bars indicating 1σ statistical errors. Bremsstrahlung splitting was used (splitting factor 100).

Depending on the type of copper sealing and the used angular moment the distance between to flanges can vary on a millimeter scale.

To quantify the impact of such small shifts in the SDD position nine additional simulation runs were performed (see table 5.3). In each run the SDD position was changed by 0.5 mm according to figure 5.12. To reduce the computing time the previous mentioned variance reduction technique Bremsstrahlung splitting (see section 3.4.2) was used.

The simulation results are shown in figure 5.16. Within the statistical uncertainty of $\leqslant 8$ % (1σ), the simulation results for the detection efficiency coincede. Large variations could only occur due to an increased collimation effect by the X-ray transparent window.

5.6. Consequences for KATRIN

The activity in the KATRIN WGTS must be stabilized and monitored on the 0.1 % level to reach the aimed KATRIN sensitivity on the neutrino mass. A BIXS system will be used for the activity monitoring. The performed Monte Carlo simulations in this chapter show, that the projected count rate under normal KATRIN operation will be $\geqslant (7155 \pm 218)$ s^{-1} per detector. Therefore, the statistical uncertainty of the combined count rate of both BIXS detector systems will be below 0.1 % in a measurement time of (69.9 ± 2.1) s. Electrons which are backscattered from the *rear wall* and back-reflected from the retarding potential of the tandem-spectrometer or by the magnetic mirror effect

are neglected in this calculated count rate. Therefore, this must be regarded as an upper limit in the necessary measurement time.

Without simulating the whole WGTS and the electromagnetic configuration of KATRIN, which would result in a huge increase of necessary computing time, the influence of backscattering effects can only be approximated. The additional count rate contribution of once-only backscattered electrons from the *rear wall* and back-reflected to the *rear wall* is calculated to be $\approx (2429 \pm 74)$ s^{-1}. Further count rate contributions due to multiple backscattering and back-reflection of electrons are assumed to be smaller than this. Nevertheless, further simulations will be performed to quantify this.

As shown, small shifts in the absolute SDD position are of minor concern. Count rate variations are expected to be smaller than $\leqslant 8$ %. It is expected that variations in the projected count rate due to the absolute *rear wall* position will have a stronger impact. This is also subject of further Monte Carlo simulations.

Tritium surface contamination on the *rear wall* and on the X-ray transparent window can be responsible for a significant background signal. Assuming one monolayer of tritium surface contamination on both surfaces can cause a background signal of about 0.5 % to 0.9 % of the total count rate under normal KATRIN operation. Aiming for a sensitivity of 0.1 % for the KATRIN BIXS system, the expected amount of tritium surface contamination must be further investigated. This is done with TRIADE experimental facility which was built in the context of this work. The experimental setup and tritium measurement results with a gold coated sample are described in the next chapter.

6. Tritium adsorption, absorption and desorption measurement by TRIADE

Tritium adsorption, absorption and desorption are important processes in tritium technology and lead to unwanted effects, in particular the so-called memory effect, on systems such those as discussed in chapter 4 and 5. Furthermore, it leads to unwanted stored inventories (safety risk) and problems during disposal. An important task in the focus of this work was the investigation of tritium surface contamination under tritium exposure. Therefore, a specialized instrument was built at TLK: the TRIADE (**Tri**tium **A**dsorption **D**esorption) experiment.

Starting with a basic introduction into the theory of sorption processes in section 6.1, the physical and technical requirements of an experiment for the investigation of tritium surface contamination are described in section 6.2. The experimental setup is described in detail in section 6.3. For the interpretation of the measurement data Monte Carlo simulations are necessary. These are discussed in section 6.4. Tritium measurement data are given in section 6.5. A final discussion of the results and an outlook is given in section 6.6.

6.1. Theory of sorption processes at gas-solid interfaces

Sorption at gas-solid interfaces is a collective term for all processes which cause enrichment or decrease of a substance on a solid. Adsorption processes induce a coverage of the solid with atoms or molecules from the gas phase and are usually exothermic [Rut84]. Desorption processes induce the leaving of atoms or molecules of the solid surface into the gas phase. This process requires at least the binding energy of the adsorbed particle and is therefore endothermic.

For the general understanding of sorption processes an introduction is given in section 6.1.1. Details and characteristics of individual sorption models are discussed in section 6.1.2. In section 6.1.3 literature data for hydrogen adsorption on gold are discussed. Finally, in section 6.1.4 the objectives of this work are summarized.

6.1.1. Sorption fundamentals

At gas-solid interfaces, interactions as shown in figure 6.1 occur between atoms/molecules from the gas phase and the solid surface. Particles from the gas phase which impinge on the solid interface have a certain sticking probability due to different surface interaction mechanisms [Chr88]. This can lead to accumulation of particles from the gas phase on
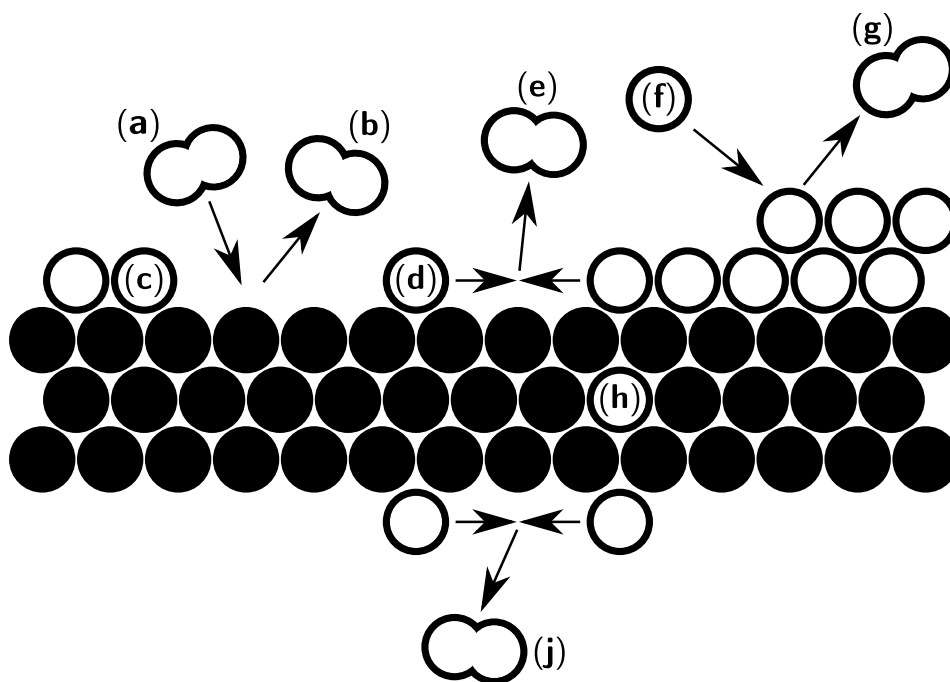
Figure 6.1.: Sorption processes at solid-gas interfaces. Atoms or molecules which impinge on the solid surface (a) can either bounce back (b) or adsorb (c). They may stick molecular or as dissociated atoms. The reverse process of desorption can occur via the Langmuir-Hinshelwood mechanism or the Eley-Rideal mechanism [Mas96]. The first-mentioned occurs when adatoms diffusing over the surface (d), reassociate and desorb (e). The second-mentioned happens when an adatom associate with an impinging gas atom (f) and desorbs (g). Adatoms can also dissolve into the bulk (h), permeate through the material and desorb on the opposite side (j). Depending on the mechanism, adsorption can happen in (sub-) monolayers or multilayers.

the solid surface which is called adsorption. The initial substrate is called adsorbent and the film of adsorbed particles is called adsorbate.

Adsorbed particles can diffuse on the surface, can build structured patterns or cluster [Chr88]. Adatom diffusion on the surface is influenced by surface defects as steps, kinks and vacancies. Adsorbed particles change material properties as the work function [Lüt97]. They can also leave the surface by dissolving into the bulk of the substrate. Such absorbed particles can permeate through the substrate and desorb from its back side. Desorption is the reverse process in which particles leave the surface.

Adsorption can occur in multiple layers and strongly depends on the temperature, the constituents of the gas and the solid and the surface properties. Technically, adsorption is used for instance in vacuum technology for sorption pumps [Jou10] or in the chemical industry for heterogeneous catalysis [Gru12].

For adsorption and desorption different mechanisms are possible which will be discussed in the subsequent section.

6.1.2. Sorption mechanisms

A mathematical description of the time dependent surface coverage of a solid sample exposed to a gas needs the combination of adsorption and desorption mechanisms. Both will be described in the following based on the underlying interaction forces.

6.1.2.1. Adsorption mechanisms based on fundamental interactions

Molecules interact with surfaces either by van-der-Waals interaction which is called physisorption [Iba06] or by hybridization of atomic orbitals which is called chemisorption [Chr91][1]. Physisorption corresponds to low binding energies between 10 meV/particle up to 500 meV/particle [Hen91]. Van-der-Waals forces and therefore physisorption is always present. Mathematically it can be described by a Lennard-Jones potential as shown in figure 6.2. Dipole fluctuations in the charge distribution of the gas particles and the corresponding screening effect of the surface causing an attractive potential [Lüt97]. The repulsive potential at close distances stems from Pauli repulsion. Due to the weak binding the minimum potential is at relatively large distances from the surface between 3 Å and 10 Å [Lüt97]. Physisorption can cause multilayer adsorption and needs no appreciable activation energy. Due to the weak binding physisorbed particles have very low desorption temperatures and the reversibility is usually very high. Numbers for hydrogen adsorption on gold are given in section 6.1.3. Physisorption is a non-dissociative sorption mechanism. Compared to chemisorption it is a long range interaction with all surface atoms [Iba06].

Chemisorption is caused by strong short range bonding forces [Zan88] as covalent or ionic bonding and is characterized by high binding energies of several eV. Typical distances

---

[1] The differentiation between physisorption and chemisorption in literature is not always done by the underlying fundamental interactions. Instead, it is sometimes defined by energy ranges for the measured binding energy in meV/particle.
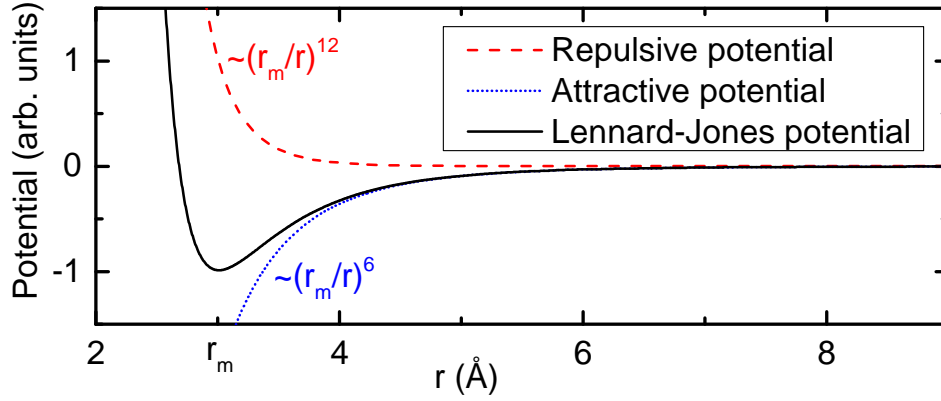
Figure 6.2.: Lennard-Jones potential for physisorption. Dipole fluctuations in the charge distribution of a gas atom induce an attractive potential with the surface by the screening effect (dotted blue). Pauli repulsion between the ad-atom and the surface causes a repulsive potential at close distances (dashed red). The resulting potential has its minimum at the distance r_{m} which is typically between 3 Å and 10 Å [Lüt97].

of adsorbed particles from the surface are between 1 Å and 3 Å [Lüt97]. Chemisorption has significant activation energies and is limited to one monolayer. It can be dissociative and due to the potential strong binding, it can have high desorption temperatures and therefore a low reversibility. In contrast to physisorption it also depends on crystal orientation. An energy scheme for adsorption of hydrogen molecules on a metal surface is shown in figure 6.3.

The following depiction of adsorption and desorption mechanisms is based on [Lüt10]. An increase of adsorbed particles on a surface scales with the incoming stream of particles j and the sticking probability $S(\Theta)$ which depends on the coverage Θ:

$$\frac{dN_{\mathrm{ad}}}{dt} = j \cdot S(\Theta). \tag{6.1}$$

Whereby Θ is defined as the number of adsorbed particles N_{ad} divided by the total number of surface sites N_{sites}. The incoming stream of particles j is given by:

$$j = \frac{p}{\sqrt{c \cdot m \cdot T}}. \tag{6.2}$$

Here p is the pressure of the gas, T is the temperature, m is the mass of the particle and c is a constant. The probability to stick to the surface is given by the sticking coefficient $S(\Theta)$:

$$S(\Theta) = \sigma \cdot f(\Theta) \cdot \exp\left(\frac{E_{\mathrm{act}}}{k_{\mathrm{B}} \cdot T}\right). \tag{6.3}$$

Here σ is a coefficient which accounts for energy transfer during adsorption, E_{act} is the necessary activation energy and $f(\Theta)$ is an occupation factor which is given for non-dissociative adsorption by:

$$f(\Theta) = 1 - \theta. \tag{6.4}$$

In case of dissociative adsorption two adjacent adsorption sites are needed. For low coverages and high ad-atom mobility it can be approximated by:

$$f(\Theta) \approx (1 - \theta)^2. \tag{6.5}$$
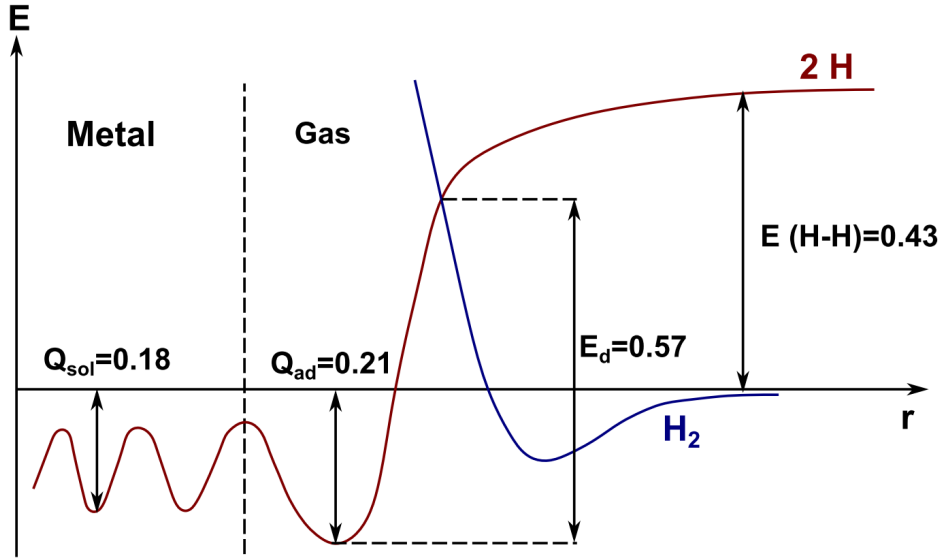
Figure 6.3.: Model for the interaction potential of H-Au. The model illustrates the interaction potential for hydrogen molecules (H$_2$) and dissociated hydrogen (2H) near a gold film surface and in the bulk material. Atomic hydrogen can chemisorb with a binding energy of 0.21 eV. Due to the small solubility heat there is a high probability for tritium absorption into the bulk after adsorption. For associative desorption an energy of 0.57 eV is given. Molecular hydrogen physisorption needs no appreciable activation energy and is a long range interaction. All values were determined by thermal desorption spectroscopy measurements at 78 K with hydrogen and an ultra-clean gold sample. Model and data according to [Sto94], figure from [Bab14].

The sticking coefficient S can be determined from a measurement of the coverage Θ as a function of dosage $p \cdot t$. As the coverage is given by:

$$\Theta = \int \frac{dN_{ad}}{dt} dt. \tag{6.6}$$

one can derive an expression for the sticking coefficient S:

$$S = \sqrt{c \cdot m \cdot T} \frac{1}{p} \frac{d\Theta}{dt}. \tag{6.7}$$

The relationship between coverage, dosage and sticking coefficient is illustrated in figure 6.4.

6.1.2.2. Desorption mechanisms

As adsorbed particles are at the bottom of a potential well, a desorption energy E_{des} is needed to break the bond between the adsorbate and the substrate particles. Desorption can be caused by several processes as thermal excitation, impinging particles (ions, electrons, photons), high electric fields, chemical reactions with other particles of
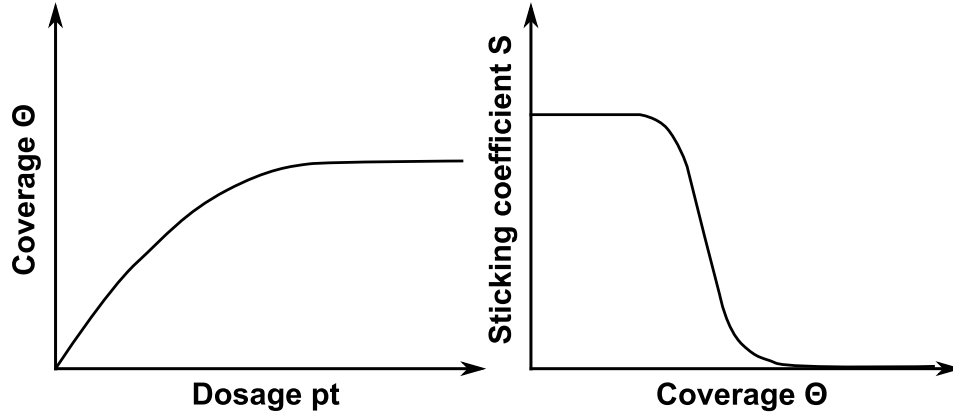
Figure 6.4.: The dependence of coverage Θ and dosage $p \cdot t$ (left) and the dependence of sticking coefficient S and coverage Θ (right). Figure according to [Lüt10].

the adsorbate or the gas phase [Hen91]. Two desorption mechanisms which are especially significant for the interpretation of the measurements made with TRIADE are the Langmuir-Hinshelwood mechanism and the Eley-Rideal mechanism.

The Langmuir-Hinshelwood mechanism is via the chemical reaction of two adsorbed particles which recombine and subsequently desorb from the surface. As it is a two particle process it scales with the quadratic surface coverage Θ^2. As it depends on the surface mobility of the adsorbed particles it also scales with the temperature T:

$$\frac{dN_{\text{L.}-\text{H.}}}{dt} = -\nu \cdot \Theta^2 \cdot \exp\left(-\frac{E_{\text{ad}}}{k_{\text{B}}T}\right) \tag{6.8}$$

The scaling factor ν characterizes the recombination speed. The adsorption energy E_{ad} and the temperature T strongly influence the reaction speed.

The Eley-Rideal mechanism is based on adsorbed particles which react with particles from the gas phase and desorb. It scales with the surface coverage Θ and the incoming stream of particles from the gas phase j:

$$\frac{dN_{\text{E.}-\text{R.}}}{dt} = -\gamma \cdot j \cdot \Theta \tag{6.9}$$

The recombination factor γ must be taken from literature for different material combinations. Both desorption mechanisms are shown in figure 6.1.

In thermal desorption spectroscopy (TDS) desorption rates are often described by the so-called Polanyi-Wigner equation [Chr91]:

$$\frac{dN_{\text{W.}-\text{H.}}}{dt} = -\nu_m \cdot \Theta^m \cdot \exp\left(-\frac{E_{\text{des}}}{k_{\text{B}}T}\right) \tag{6.10}$$

The pre-exponential factor ν_m and the activation energy of desorption E_{des} must be determined experimentally. Both values can depend on temperature and coverage [Hen91]. The order of the desorption process m must also be determined experimentally but in practice values of $x = 0, 1/2, 1, 2$ occur more frequently [Chr91].
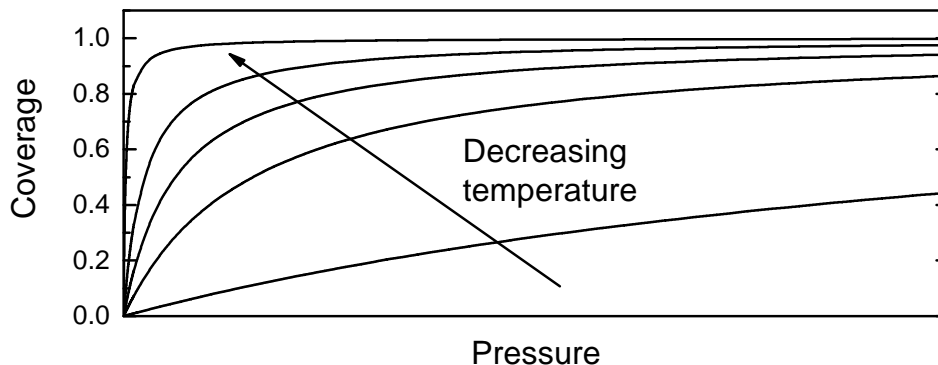
Figure 6.5.: Example plot of the surface coverage according to the Langmuir adsorption model.

6.1.2.3. Time dependence of the surface coverage

Adsorption and desorption happen at the same time and may reach an equilibrium state. The surface coverage is than described by:

$$\frac{dN}{dt} = \frac{dN_{\text{ad}}}{dt} + \frac{dN_{\text{des}}}{dt} = 0. \tag{6.11}$$

Depending on the actual choice of desorption model and occupation factor $f(\Theta)$ one can derive from that mathematical expressions for the equilibrium coverage Θ_{eq} and the time dependent surface coverage $\Theta(t)$ as done in [Bab14]. Functions which describe the surface coverage depending on pressure p at a given temperature are called adsorption isotherms. Various models are used for that, as for instance Langmuir isotherms [Chr91]:

$$\Theta = \frac{K(T) \cdot p}{1 + K(T) \cdot p} \tag{6.12}$$

Experimental data can be fitted to isotherms like this by adjusting the equilibrium constant $K(T)$. Langmuir isotherms are derived under the presumption of non-interacting particles in the adsorbate and a coverage independent adsorption enthalpy. It is the easiest mathematical description for adsorption processes which are limited to one monolayer. Other adsorption isotherms as BET-isotherms [Bru38] or Temkin isotherms [Atk10] regard for multilayer adsorption or coverage dependent adsorption enthalpies. Typical Langmuir-isotherms are shown in figure 6.5. A mathematical description which accounts for interacting particles according to equation 6.8, 6.9 is given in [Bab14].

6.1.3. Sorption of hydrogen on gold

Since there is a significant lack of literature data on tritium adsorption on gold, the literature data on hydrogen adsorption on gold is reported here. Although there are isotope effects expected, this can be used to understand the underlying physics. A detailed report about the chemisorptive and physisorptive behavior of hydrogen, interacting with different solid surfaces, is given in [Chr88].

Molecular hydrogen adsorption is not expected at temperatures above 20 K. This is due the highest possible temperature for hydrogen physisorption of about 20 K [Chr88] and as reported in [Iba06], molecular hydrogen does not chemisorb. Therefore, at higher temperatures only atomic hydrogen adsorption is possible. Desorption of atomic hydrogen occurs by recombination and desorption via the Eley-Rideal and Langmuir-Hinshelwood mechanism [Chr88].

Studies of hydrogen adsorption on gold at higher temperatures were reported in [Sto92], [Sto94] and [Sto96]. The adsorption behavior was investigated at temperatures of around 78 K by TDS measurements. The gold was prepared under vacuum conditions. It was found that hydrogen adsorb on thin (70 nm) sintered and unsintered gold films. The activation energy for thermal desorption of mono-atomic hydrogen at very low coverages of about $\Theta \cong 0.01$ was found to be (57 ± 5) kJ/mol corresponding to (0.59 ± 0.05) eV/-particle. At higher coverages another weakly bound adspecies were found [Sto92]. A model for dissociative hydrogen adsorption on gold was developed which is shown in figure 6.3. For hydrogen and deuterium sorption isotope effects have been observed [Sto96]. A peak in the desorption rate was reported at a temperature of 125 K. It was also found that the adsorption behavior depends on the nanostructure of the gold surface [Sto99].

All measurements were performed with hydrogen or deuterium far below room temperature with ultra-clean samples prepared under vacuum-conditions. As shown in figure 6.3 diffusion into the bulk is also a relevant effect due to the small solubility heat of 0.18 eV/particle [Sto94] compared to the associative desorption energy of (0.59 ± 0.05) eV/particle.

6.1.4. Objectives of this work

As described in section 2.2.4 tritium adsorption on metallic surfaces and absorption in metallic solids is a known and unwanted effect in tritium technology. It reduces the amount of tritium available for processing and limits the detection limit of tritium analytical tools as ionization chambers or BIXS monitors. It is also relevant in case of disposal.

For a high sensitivity tritium β-experiment as KATRIN it is essential to investigate the adsorption behavior because it can have a serious impact on the uncertainty of the neutrino mass measurement. Variations in the tritium coverage on the *rear wall* (see section 5.2) would change the work function of the *rear wall* and consequently the source potential of the WGTS in the order of several hundred meV [Lüt97]. Such shifts would be unacceptable for the aimed sensitivity of KATRIN. Long term shifts also changing the stability of the source due to the fact that one monolayer of tritium on the *rear wall* corresponds to 1/247 of the whole source strength. Despite of the monitoring of this effect by the BIXS-system of KATRIN [Bab12], tritium adsorption on the gold coated beryllium windows of the BIXS-system (see section 6.3) can cause long-term drifts of the measured activity independently of the actual source strength [Roe11].

There is a lack in literature data for tritium adsorption due to the experimental challenges when handling tritium. It is know that the adsorption behavior is influenced by isotopic effects. Radiochemical effects can further promote distinctions between tritium

and hydrogen/deuterium. The amount of adsorbed tritium also depends on the amount of oxygen and residual water on the surface which can lead to formation of HTO by isotopic exchange [Hir84]. Reliable predictions regarding the tritium adsorption on the KATRIN *rear wall* or the gold coated beryllium windows (see section 5.2) based on hydrogen data are therefore impossible. The special precautions which have to be made in tritium experiments [TLA15] only allowing non-invasive methods.

As BIXS is a non-invasive method which can be used for high stability tritium monitoring [Bab12], it has been chosen for the investigation of tritium adsorption on KATRIN relevant materials and under KATRIN near conditions. The specific questions which shall be answered are:

- Does tritium adsorb in significant amounts on gold coated beryllium at room temperature?

- What is the expected saturation coverage for tritium adsorption on gold?

- How much time is needed to reach a saturation coverage?

- What are effective decontamination strategies?

For answering these questions the Tritium Adsorption Desorption Experiment (TRIADE) was built at TLK. In the following, the specific requirements on TRIADE are described.

6.2. Physical and technical requirements

In section 6.2.1 the physical requirements of the TRIADE experiment are given. Technical requirements which arise from physical requirements and safety regulations [TLA15] are described in section 6.2.2.

6.2.1. Physical requirements

The TRIADE experiment is designed to measure tritium adsorption on arbitrary material samples with a sensitivity of less or equal one monolayer. This sensitivity limit is chosen because of KATRIN requirements regarding the *rear wall*. From the aimed sensitivity limit further physical requirements emerge.

- BIXS requirements for adsorption and desorption measurement are:

  - a detector which is able to measure X-rays in the energy range of $(0 - 20)\,\text{keV}$,

  - an X-ray window which is able to protect the detector from tritium contamination and is as transparent as possible to X-rays in the energy range of $(0 - 20)\,\text{keV}$,

  - an environment in which the sample surface can be exposed to tritium under controlled temperature and pressure conditions.

- RGA requirements for desorption measurement are:

- the possibility to heat or cool the sample with constant heating or cooling power in a temperature range of approximately $(-100\ldots 200)\,°C$,

- the minimization of outgassing from the inner surfaces of the experimental setup.

- Adsorption, desorption and diffusion are temperature and pressure dependent effects. To meet the KATRIN conditions of the *rear wall* (section 5.2) and to study these dependencies the pressure in the sample volume must be controlled in the range of $10^{-9}\,\mathrm{mbar}$ to $1\,\mathrm{bar}$ and the temperature in the range of $(-100\ldots 200)\,°C$.

- Tritium decontamination procedures with purge gas and by system outbaking must be implemented.

- In order to minimize sources of background for the tritium adsorption measurements the requirements are:

  - an X-ray detector with a very low background signal in the order of $10^{-3}\,\mathrm{cps}$,

  - the minimization of tritium adsorption on other surfaces than the sample,

  - the minimization of the residual tritium gas pressure during measurements,

  - the minimization of the humidity inside the recipient,

  - limitation of the field of view of the X-ray detector to the sample.

6.2.2. Technical requirements

In order to enable the BIXS measurement method and mass spectrometry with the aimed sensitivity in the TRIADE experiment a number of technical requirements arises. Furthermore, some technical requirements are due to safety regulations of the TLK [TLA15].

- Technical requirements for the implementation of the BIXS method are:

  - the X-ray transparent window must be as thin as possible in order to maximize X-ray transmission whilst being as leak tight as possible $(< 10^{-9}\,\mathrm{mbar\ l/s})$, and being an effective tritium permeation barrier to prevent the detector from contamination,

  - the X-ray transparent window must withstand differential pressures of up to $1\,\mathrm{bar}$ in case of vacuum breaks or during normal operation modes,

  - the X-ray transparent window must be sputter coated with gold with a thickness of about $100\,\mathrm{nm}$,

  - evacuation of the volume with the SDD inside to a pressure of less than $1\,\mathrm{mbar}$ must be possible to reduce mechanical load on the X-ray transparent window during normal operation (sample chamber evacuated),

  - the detector electronics must be operated at a pressure of $1\,\mathrm{bar}$ and a temperature of less than $40\,°C$.

- To operate the quadrupole mass spectrometer the vacuum system must be able to evacuate the sample chamber to a total pressure of $\leqslant 10^{-6}$ mbar.

- Technical requirements regarding the vacuum system are:

  - the tritium pressure inside the recipient must be controllable on the 10^{-5} mbar level in order to reproduce the vacuum conditions in front of the KATRIN *rear wall* (see section 5.2),

  - the vacuum system must be connected to the TLK infrastructure (CAPER[2] or ZTS[3]) for the transfer of tritiated waste gases,

  - the residual gas pressure inside the recipient must be reducible to a level of about 10^{-9} mbar.

- The temperature control system must be able to achieve bake-out temperatures of up to 200 °C to reduce humidity inside the recipient. Due to safety regulations, the maximum temperature must not exceed 200 °C otherwise a more complex safety philosophy for the TRIADE setup is required.

- Furthermore, a vast number of safety requirements according to the technical terms of delivery and acceptance [TLA15] must be fulfilled to operate an experiment at TLK. This comprises materials allowed to use in a tritium leading system, regulations for first and second containment, maximum pressures and temperatures, tritium monitoring systems, tritium accountancy and commissioning procedures like leakage tests. The maximum allowed integral leak rate of the primary system is 10^{-8} mbar l/s. The maximum allowed tritium activity inside TRIADE is 10^{10} Bq.

6.3. Experimental setup

In the following chapter the design and setup of the **Tri**tium **A**dsorption **De**sorption (TRIADE) experiment is described. The TRIADE setup is located at the Tritium Laboratory Karlsruhe (TLK) and is designed and built according to the TLK regulations regarding tritium leading experiments [TLA15]. In section 6.3.1 an overview of the experimental setup is given. In Section 6.3.2 the design of the core components and in section 6.3.4 the mass spectrometry setup is outlined. Section 6.3.5 describes the pumping system and the main instrumentation and in section 6.3.6 the procedural setup is outlined.

6.3.1. Experimental overview of TRIADE

In figure 6.6 a schematic of the TRIADE core components is shown. The core system consists of three volumes, which is necessary for the operation of the BIXS-system and is explained in detail in the next section. Tritiated gas mixtures can be expanded from

---

[2] The CAPER facility at TLK is a reference process for the Tokamak Exhaust Processing (TEP) system of ITER [Glu02].
[3] Central tritium retention system of the TLK [Bes93].
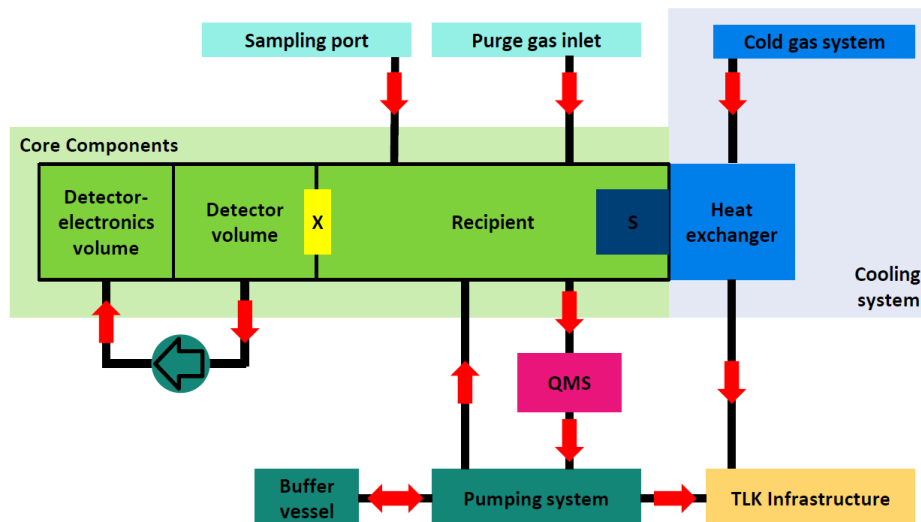
Figure 6.6.: Schematic of the TRIADE setup. The red arrows marking gas flows. QMS stands for quadropole mass spectrometer, X for the X-ray transparent window and S for the sample holder and the mounted sample.

a sample cylinder, connected to the sample port, to the recipient. Material samples which are mounted in the recipient can be exposed to tritiated gas mixtures. Surface contamination of the sample under tritium exposure is studied by a Silicon Drift Detector (SDD) which is located in the detector volume. After exposure, the test gas mixture can be evacuated by the pumping system to the buffer vessel or to the TLK infrastructure for tritium removal. A quadrupole mass spectrometer is between the recipient and the pumping system and can be used for desorption studies. The sample holder inside the recipient is thermally connected to an outer flange, which can be cooled down by a cold gas system or heated up by a heating sleeve. Because of TLK safety regulations the whole setup is mounted inside a fume hood. A CAD drawing of this is shown in figure 6.7.

6.3.2. Design of the core components

There are three different volumes needed for the TRIADE core setup because the pressure must be controlled independently for the detector electronics, the SDD and the sample (see chapter 6.2). The detector volume and the detector electronics volume are per definition part of the primary system, even if there is no significant amount of tritium inside of them during normal operation. The first containment around these three volumes is according to the TLK safety regulations regarding first containment materials and sealings. A CAD drawing of this is shown in figure 6.8.

It is important for the BIXS measurement principle that the SDD primarily detects X-rays coming from the sample surface or the X-ray transparent window. For these X-rays the SDD shall have a high detection efficiency and a low backscattering probability to improve the sensitivity of the system. Detection of X-rays which are starting from other parts of the inner surface shall be suppressed as good as possible by the geometry of the setup. This leads to the following design issues of the core geometry:
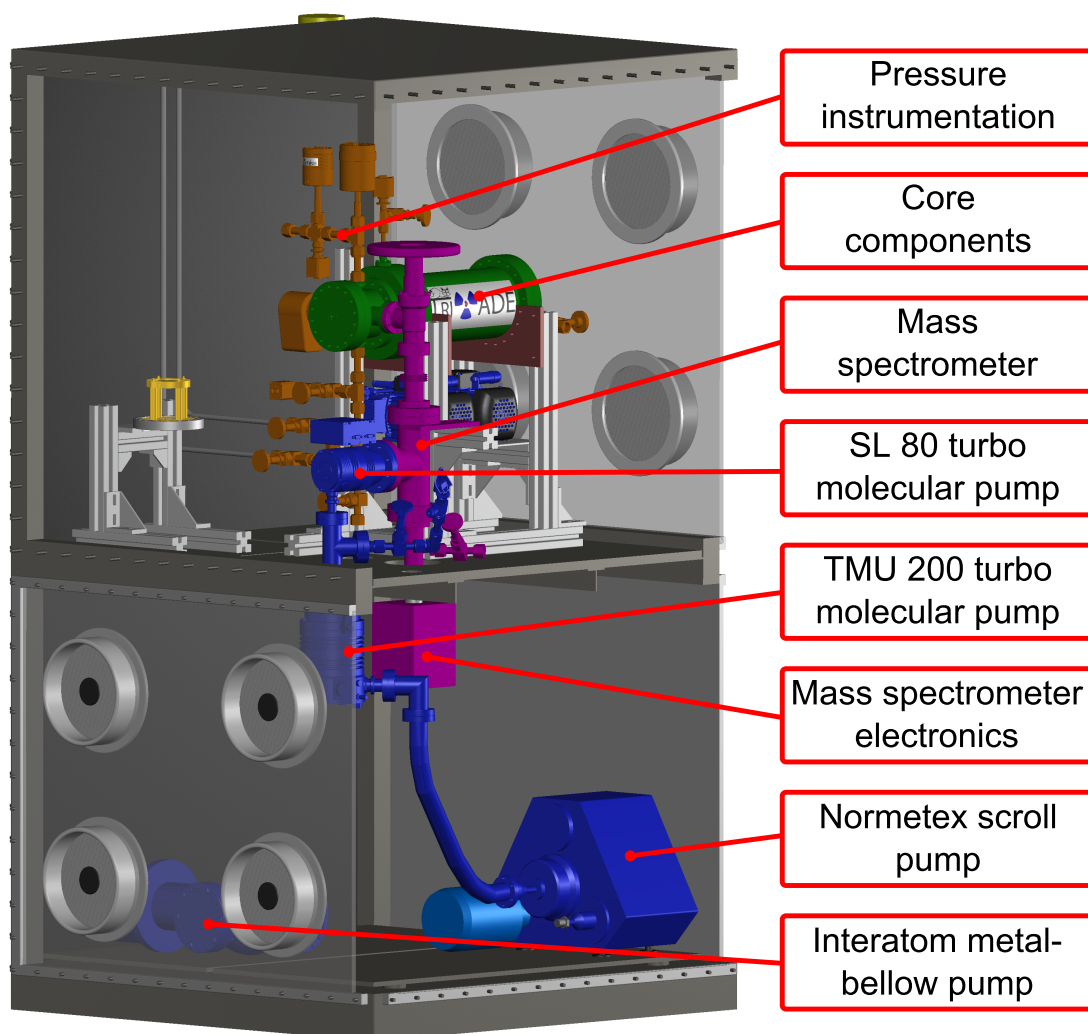
Figure 6.7.: CAD drawing of the TRIADE experiment. In the upper part of the fume the core components (green) of TRIADE are located. Pressure and instrumentation equipment (orange) is connected to the recipient. The sample holder (yellow) is mounted on a stainless steel flange which can be connected to the recipient. Between the core components and the vacuum system the mass spectrometer setup (magenta) is located. The mass spectrometer electronics can be dismounted for bake-out of the system. The four-stage pumping system is optimized to achieve the lowest possible final pressure in the recipient. The metal-bellow and the scroll pump are mounted on the base plate of the lower part of the fume hood. They are the forepumps for the two-stage turbo molecular pumping system.
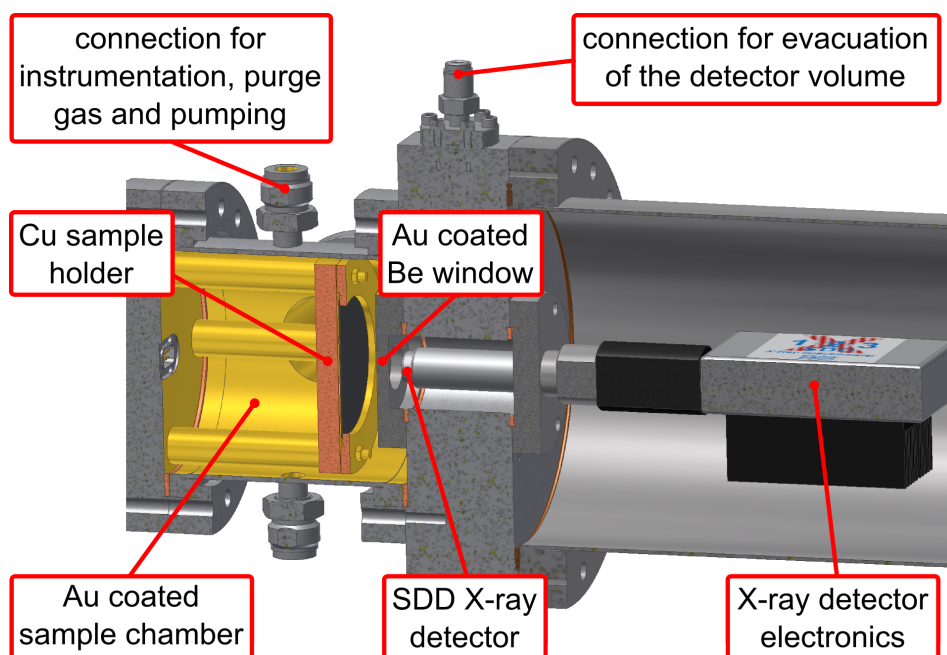
Figure 6.8.: Sectional CAD drawing of the TRIADE core setup. Explanation can be found in the text.

- the detectors field of view must be restricted to the sample surface,

- the maximum angle of X-rays entering the detector must be restricted to 45° and

- the detectable X-ray intensity because of adsorbed tritium must be maximized which means

  - a large sample surface,

  - a large X-ray transparent window surface and

  - a minimal distance between sample and detector.

Whenever reasonable, the use of standard vacuum components with standard dimensions was preferred instead of special parts. This necessarily had influence on the geometry of the system. The exact dimensions of the core setup are a crucial input for the Monte Carlo simulations. The Monte Carlo results are used for the later data analysis of the tritium measurements. Figure 6.14 shows the dimensions of the sample, X-ray transparent window and SDD setup used for the simulations.

The recipient
A DN100CF cross piece with two DN100CF flanges, two 1/2 inch VCR male connectors and two DN40CF flanges is used as recipient. The two VCR connectors and two DN40CF flanges are used for pressure instrumentation, connection to the pumping system and infrastructure (see section 6.3.5,6.3.6). One of the DN100CF flanges is used for the sample holder which is mounted on a DN100CF blind flange. The second DN100CF flange is connected to a custom-made intermediate flange which serves as the detector volume.
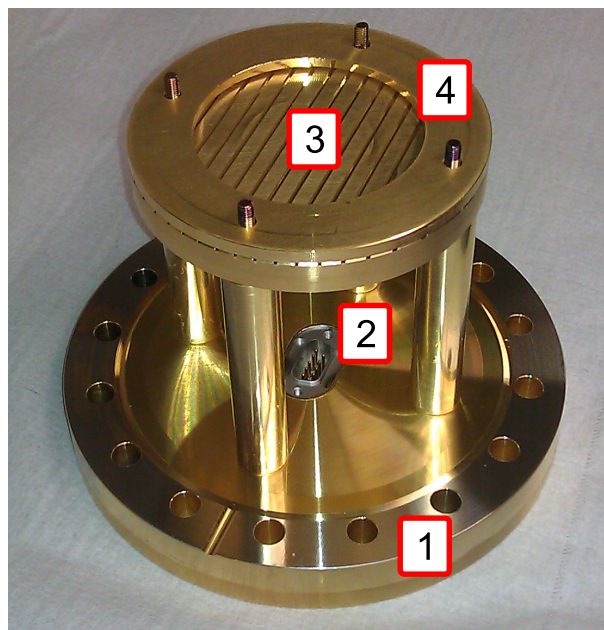
Figure 6.9.: The sample holder of TRIADE is mounted on a blind flange (1) with an electrical feedthrough (2). To avoid virtual leaks, slots are milled into the base plate (3) where the sample is mounted on. The sample is fixed by a holder ring (4).

The detector volume and detector electronics volume
A custom-made intermediate flange with a central bore serves as detector volume. The side facing the recipient, has a DN100CF flange used to connect it to the recipient and a DN40CF flange used to mount the X-ray transparent window which protects the SDD from tritium contamination. On the other side is a DN160CF flange for connecting a DN160CF standard pipe which serves as the detector electronics volume. The second DN40CF flange is used for the detector feedthrough which separates the detector volume from the detector electronics volume. A further 1/4 inch VCR male connector is at the intermediate flange. It is connected to a vacuum pump for the evacuation of the detector volume.

The sample holder
The sample holder (see figure 6.9) consists of a base plate with a holder ring. Between them, a sample can be mounted. The base plate is connected to four rods which are mounted to a DN100CF blind flange. A Pt100 sensor is mounted to the back side of the sample holder and connected to an electrical feedthrough in the blind flange. All parts of the sample holder are made out of copper for better heat conduction. The base plate has a number of venting slots to avoid virtual leaks[4].

The X-ray transparent window
The X-ray transparent window is a beryllium substrate built by Materion Electrofusion[5]

---

[4]   Virtual leak is a term for a trapped gas volume inside a vacuum system which cannot easily pumped out because of a low conductance to the sample chamber. It increases the necessary time to reach a certain pressure during a pump-down of the system and cannot be detected by helium leak testing.

[5]   Materion Electrofusion, 44036 South Grimmer Boulevard, Fremont, CA 94538-6346

with a thickness of 100 μm and a minimum purity of 99.8%. It is mounted by diffusion bonding to a DN40CF flange and has an aperture size of 20 mm to limit the field of view of the detector to the sample area. As stated in section 3.4, the X-ray transparent window side, facing the sample material, must be coated with 100 nm gold. This was done by Siegert Thinfilm Technology[6] by sputter coating. For a temperature stable gold coating there is an additional adhesive layer of 10 nm of titanium between the beryllium substrate and the gold coating. The window is bakeable to 450 °C and the leakage rate is better than $< 10^{-10}$ mbar l/s. The maximum differential pressure is $\Delta p = 1$ bar and can be applied bi-directional. The beryllium window must be handled with care because in case of a break there can be hazardous beryllium dust [Jak15]. Due to that and because of the mechanical stability of the window, it is per definition not regarded as an safe first containment material according to [TLA15].

For the mechanical dimensions of the intermediate flange, the sample holder and the X-ray transparent window see appendix A.21.

The Coatings
The following parts of the recipient had to be coated with gold to reduce tritium adsorption:

- all parts of the sample holder (rods, base plate, holder ring),

- the blind flange on which the sample holder is mounted,

- the side of the intermediate flange which faces the sample chamber,

- the stainless steel holder of the X-ray transparent window,

- all threaded bolts and screws which are used to mount the X-ray transparent window and the holder ring of the sample holder,

- the inner surfaces of the recipient.

There were two different techniques used for gold coating. Sputter coating by Siegert Thinfilm Technology and electrochemical coating by Collini AG[7] and the KIT workshop. Electrochemical coating was used whenever sputter coating was not possible because of geometry. See table 6.1 for the individual coatings.

6.3.3. Amptek X123 X-ray detector

For the detection of X-rays produced by the β-radiation of tritium an Amptek X123 silicon drift detector is used (see section 3.3). This kind of detector meets the requirements mentioned in section 6.2. The datasheet is shown in appendix A.11. The Amptek X123 is a complete X-ray spectrometer system, which consists of:

- a peltier cooled silicon drift detector,

- a preamplifier,

Table 6.1.: Overview of the coatings of the core components of TRIADE.

Part	Process	Manufacturer	Gold thickness	Adhessive layer
Sample holder	sputtered	Siegert TFT	1 µm	Cr
Blind flange	sputtered	Siegert TFT	1 µm	Cr
Intermediate flange	sputtered	Siegert TFT	1 µm	Cr
SS X-ray window	sputtered	Siegert TFT	1 µm	Cr
Beryllium substrate	sputtered	Siegert TFT	100 nm	Ti 10 nm
Bolts and nuts	electroplated	KIT workshop	5 µm	Ni 2.5 µm
Recipient[8]	electroplated	Collini AG	5 µm	Ni 2.5 µm

- a DP5 digital pulse processor and a PC5 power supply.

A similar detector except for a different geometry was already explained in chapter 4.3. In appendix A.11 and A.12 the mechanical dimensions and the detector parameters are given. The aimed detection limit of TRIADE is less than one monolayer of tritium. In order to reach it the noise level of the detector should be as low as possible. A good energy resolution is also useful to analyze characteristic X-rays and to see shifts in the energy spectra due to e.g. temperature drifts of the detector system. The most important detector parameters for TRIADE, which have influence on the noise level or the energy resolution, are

- the peaking time in the slow and in the fast channel,

- the energy threshold for the slow and the fast channel,

- the voltage gains of the amplifier stages and

- the SDD temperature.

These parameters were optimized during the commissioning measurements which are explained in detail in [Sch13b]. The used detector parameters for the tritium measurements in the context of this work are listed in section A.12.

6.3.4. Mass spectrometry setup

In order to analyze test gas mixtures and for the detection of desorbing tritium a quadrupole mass spectrometer (QMS) was included in the experimental setup. In TRIADE a MKS[9] Microvision Plus is used. The specifications and mechanical dimensions of this spectrometer can be found in section A.13. An explanation of the working principle of a RGA is given in e.g. [Hof13].

The QMS in TRIADE is located as near to the sample as possible (see figure 6.7) to minimize the influence of desorbing gas species from other surfaces than the sample

---

[9] MKS Instruments, 2 Tech Drive, Suite 201, Andover, Massachusetts 01810, U.S.

surface. In addition, it must be assured that the maximum allowed total pressure of the QMS ($p_{tot,max} = 10^{-4}$ mbar) is not exceeded. For that the QMS is located between the recipient and the pumping system in the volume of a DN63CF tee piece. Desorbing gas from the recipient or the sample is pumped through this volume and is passing the QMS.

The geometry of the core setup is optimized for the BIXS measurement method which causes some limitations to the mass spectrometry system. Desorbing gas from the sample surface must leave the recipient, pass a stainless steel angle valve and a stainless steel tee piece to enter the QMS. Therefore, on the way to the QMS, there are lot of possible interaction sites. Furthermore, there is also the possibility of gas desorption from the inner stainless steel surfaces which may mask a small signal caused by the sample surface.

6.3.4.1. Temperature management

In order to reduce moisture in the core components of TRIADE and to study the temperature behavior of adsorption and desorption a cooling/heating system is necessary. The core components have to be bakeble up to 200 °C. Thereby it is necessary to control the sample temperature independently from the other parts of the core system in a rather large range of $(-100\ldots200)$ °C.

A schematic of the TRIADE temperature monitoring system is shown in figure 6.12. The core components can be baked out to 200 °C to reduce moisture in the system. This temperature limitation is because of TLK safety regulations. Higher temperatures would only be possible with an additional containment. Another limitation is the temperature at the high vacuum flange of the first TMP. Temperatures higher than $(60\ldots70)$ °C causing an emergency shutdown of the pump. With this limitations in mind, heating tapes were affixed to:

- the volume which the sample cylinder is connected to,

- the recipient volume,

- the blind flange with the sample holder and

- the volume with the QMS inside.

Pt100 sensors were mounted for temperature monitoring. For safety reasons the heating bands are connected to adjustable transformers for power limitation. The necessary voltage settings for the transformers were determined during commissioning measurements [Sch13b].

The sample holder must be heated/cooled independently from the other components. This is done by controlling the temperature of the blind flange which the sample holder is thermally connected to (seen in figure 6.9). Heating is done by a heating sleeve mounted to the blind flange and cooling is done by a professional cold gas system and a self-made heat exchanger mounted to the blind flange. The basic principle of temperature stabilization of the sample by cooling/heating the blind flange was tested in [Sch13b].
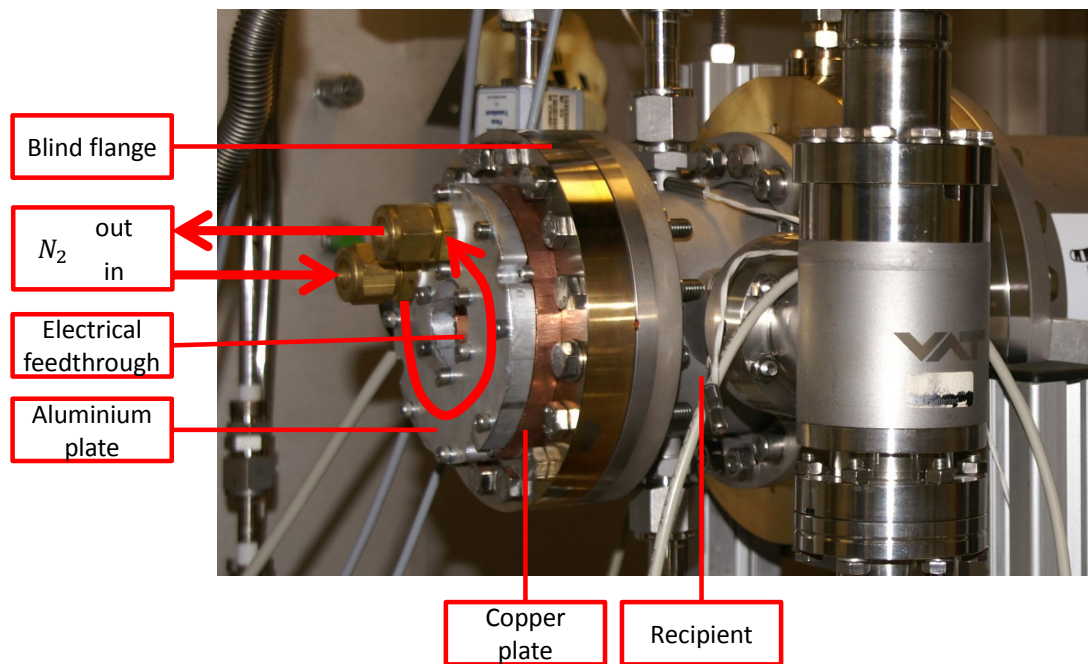
Figure 6.10.: Heat exchanger for the TRIADE sample holder. The inlet flange is connected to an external N_2 cold gas system manufactured by KGW isotherm. The outlet flange is connected to the ZTS of the TLK.

In figure 6.10 the self-made heat exchanger is shown. An aluminum plate with gas in- and outlet is screwed to a copper plate. A circular track is milled into the plates and connects gas in- and outlet. Both plates are screwed to the blind flange. For thermal insulation the blind flange is covered with polystyrene foam during cooling operation. Gaseous nitrogen is pumped through the system for cooling. After passing the heat exchanger it goes to the ZTS of the TLK infrastructure.

The gaseous nitrogen used for cooling is provided by a professional cold gas machine built by KGW Isotherm[10]. The working principle is outlined in [Sch13b]. Nitrogen from a 250 l dewar vessel is evaporated by a 500 W heater cartridge. An additional 630 W heater warms up the expanding gas to a preset temperature. The gas flow and the gas temperature can be regulated. A vacuum isolated, flexible metal tube leads the gas to the heat exchanger inside the fume hood. Because of safety reasons the isolation vacuums of the flexible metal tubes inside and outside the fume hood are separated.

6.3.5. Pumping and instrumentation

For background reduction during BIXS measurements and to have a rather clean environment, the pumping system of TRIADE is designed to reach a final pressure in the range of $(10^{-10} \ldots 10^{-9})\,\text{mbar}$ (according to section 6.2.1). Tritiated exhaust gases must

---

[10] Karlsruher Glastechnisches Werk - Schieder GmbH, Gablonzer Straße. 6, 76185 Karlsruhe, Germany
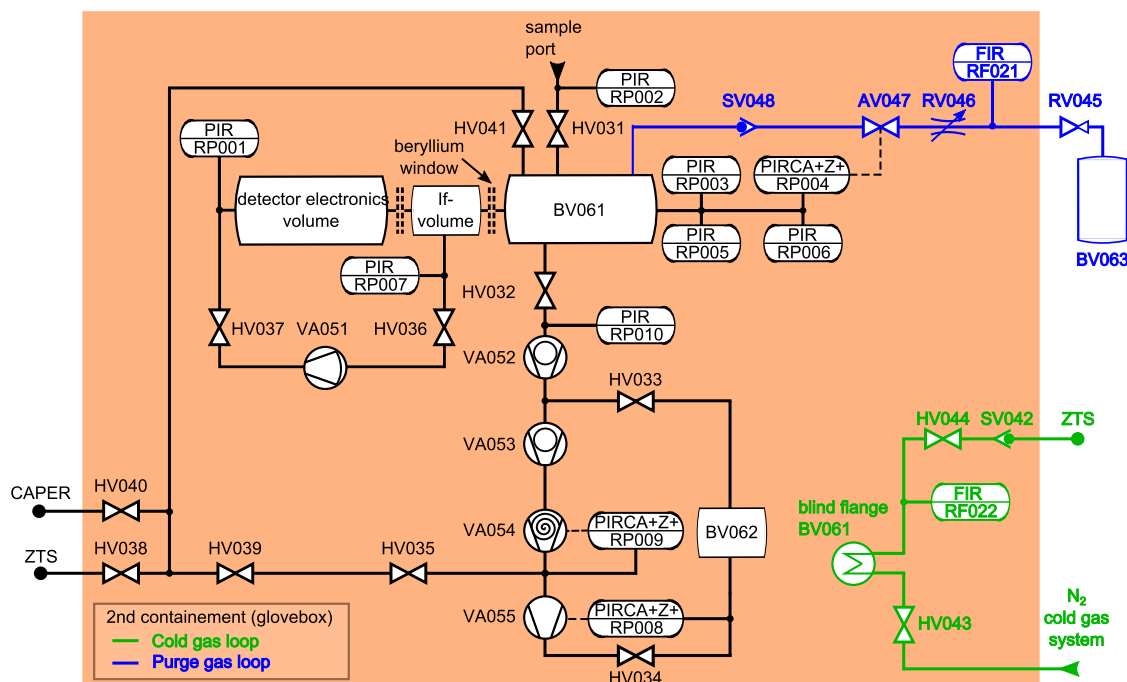
Figure 6.11.: The TRIADE vacuum system. Manual valves are indicated by (HV), pumps by (VA), pressure sensors by (PIR), flow sensors by (FIR), buffer vessels by (BV), safety valves by (SV), automatic valves by (AV) and regulation valves by (RV). Further explanation can be found in the text.

be transferable to a buffer vessel and to the TLK infrastructure. That means the pumping system must be able to pump against pressures of up to 1000 mbar. Furthermore each pump must be tritium compatible according to TLK safety regulations.

To reach such high compression factors of 10^{12} to 10^{13} a four-stage differential pumping system is necessary. A metal bellow pump (VA055), a scroll pump (VA054) and two turbo molecular pumps (VA053, VA052) are used (see figure 6.7). Particular focus was set on TMP (VA052) which is located as near as possible to the recipient and is connected with a pipe with a cross-size as high as reasonable achievable. Short connections and as few bendings as possible between the pumps were also design constraints.

The whole pressure range of 10^{-10} mbar to 1000 mbar in the recipient is monitored by four pressure sensors with overlapping pressure ranges. In table A.4 the pressure sensors and in table A.3 the used pumps are listed.

6.3.6. Procedural setup and interfaces to the infrastructure

In figure 6.11 a flow diagram of the TRIADE vacuum system is shown. The three volumes of the core system, namely the recipient-, intermediate- and detector electronics volume, are separated but in terms of safety considerations regarded as one volume. This is indicated by dashed lines between these volumes in figure 6.11.

Experiences from a similar experiment [Roe11] showed that it is necessary to pump the intermediate volume on a regulary basis (about once a week). This is because the detector feedthrough, which separates the intermediate volume from the detector electronics volume, is sealed by an elastomeric sealing[11]. The gas which goes to the intermediate volume is pumped back by VA055 to the detector electronics volume.

Decontamination procedures of the recipient and the sample can be performed by using purge gas. The purge gas system is showed in blue in figure 6.11. A high pressure gas cylinder (BV063) with helium or hydrogen can be connected outside of the fume hood. A pressure reducer (RV043) and a flow controller (RV042) are used to control the purge gas stream. For safety reasons the automatic valve (AV041) closes when the pressure in the recipient is higher than 800 mbar. To prevent reflux of tritiated gases from the recipient to the gas cylinder (BV063) a safety valve (SV044) is integrated. After passing the recipient the purge gas goes to the TLK infrastructure (ZTS). Alternatively the purge gas can be collected in a buffer vessel (BV062).

Exhaust gases like tritium gas mixtures which are used for BIXS measurements can be pumped to a buffer vessel (BV062) by (VA052, VA053, VA054, VA055). Alternatively it can be given to the TLK infrastructure (CAPER) for tritium removal (see section 2.1.2). For transfers to CAPER, the gas is not pumped by VA055 due to safety regulations (pull-principle[12]). This means the CAPER facility is responsible for providing the forepressure for VA054 which is about 1 mbar.

In figure 6.11 the cooling system is shown in green. It has no connection to the primary system. The cooling gas comes from the outside of the fume hood from a professional cooling gas machine, is passing the heat exchanger and is then pumped to the TLK infrastructure (ZTS). A flowmeter (RF002) monitors the cooling gas stream and a safety valve (SV002) prevents reflux from tritiated ZTS gases to the cooling circuit.

In figure 6.12 the temperature monitoring system is shown. There are six Pt100 sensors and one Pt1000 sensor. For monitoring of the sample temperature RT016 is used. All the other sensors are used for the monitoring of the heating bands and the cold gas stream. All measurement points and the measurement ranges are listed in table A.5.

The commissioning of the whole TRIADE experimental setup (see figure 6.13) was done within the scope of a diploma thesis and is described in detail in [Sch13b].

---

[11]   Elastomeric sealings have usually a leakage rate of about $(10^{-7} \ldots 10^{-6})$ mbar l/s.

[12]   Gas transfers between tritium leading facilities at TLK are following the pull-principle. That means the facility which shall receive the tritiated gas is actively pumping. This avoids emergency shutdowns due to overfilling of the receiving buffer vessel and unnecessary tritium inventory in the pipe connection between the facilities.
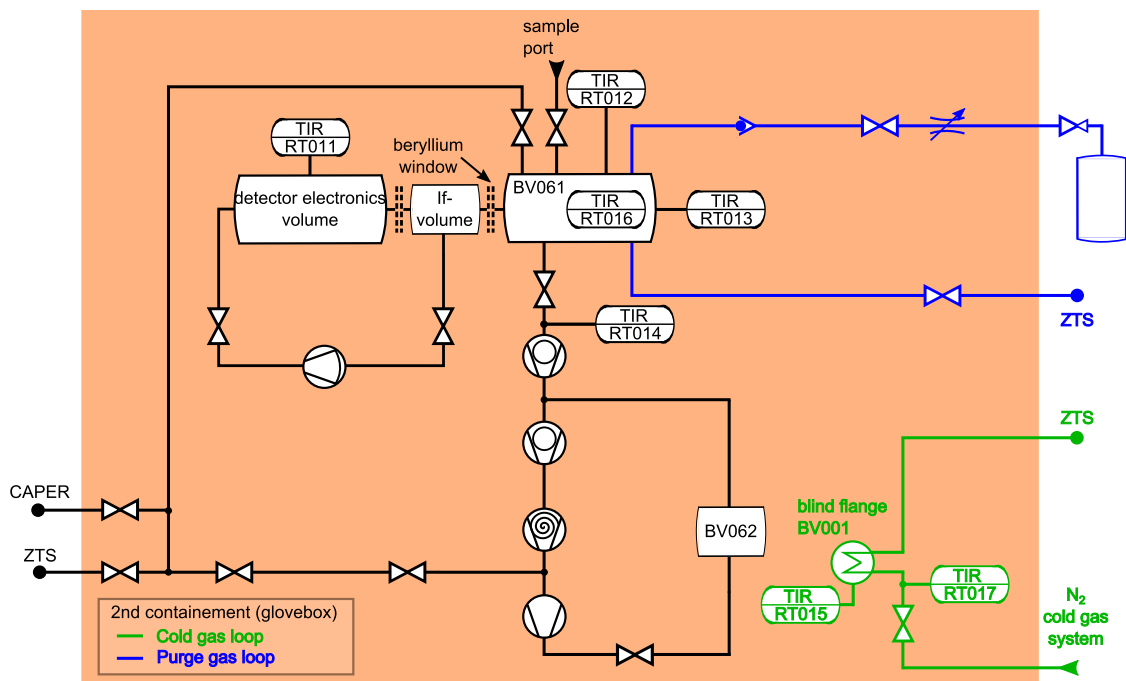
Figure 6.12.: Overview of the TRIADE temperature sensors. The location of each temperature sensor in the TRIADE setup is shown. Further explanation can be found in the text. Temperature sensor types and ranges can be found in table A.5.
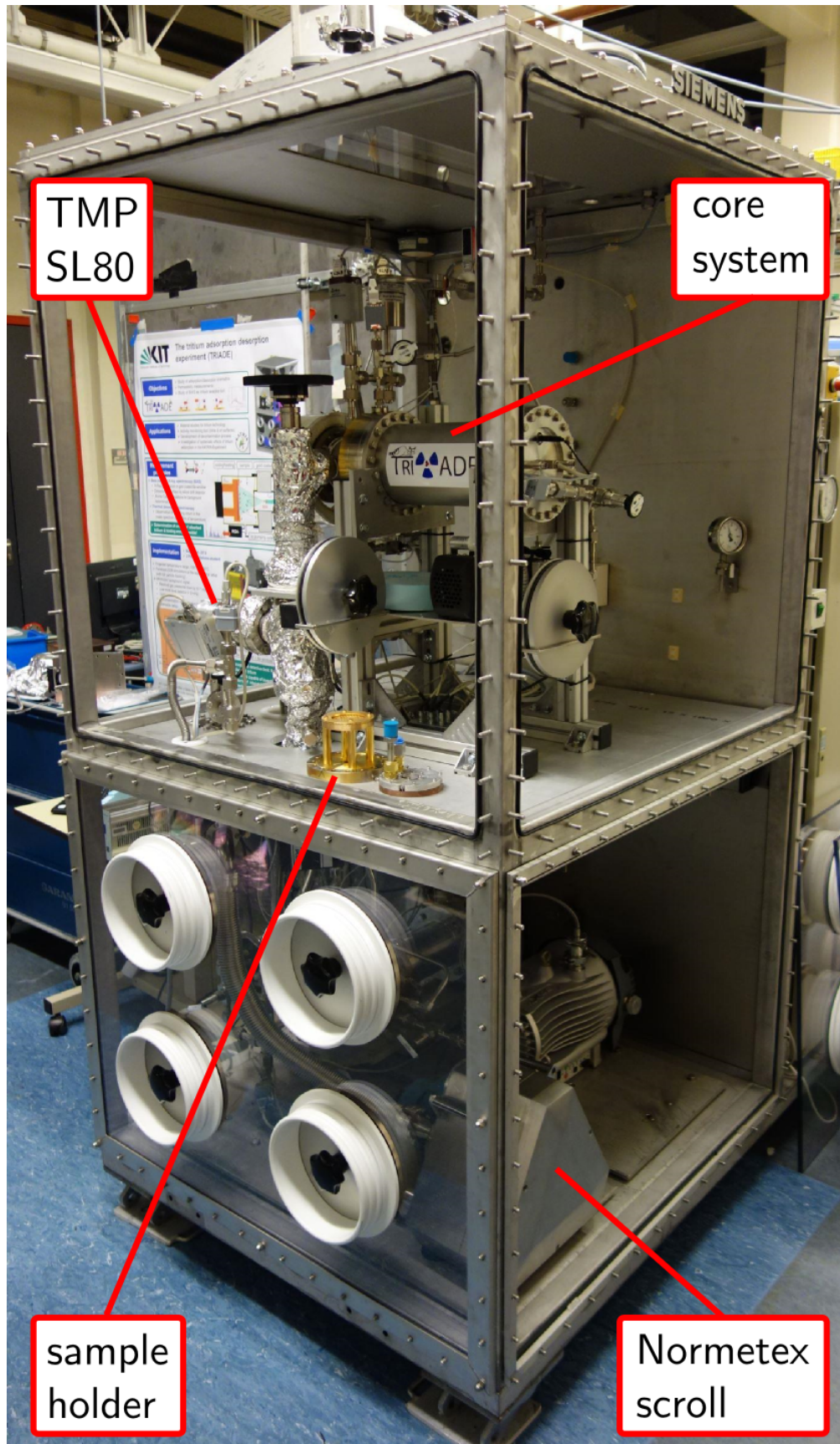
Figure 6.13.: Finalized TRIADE setup in its fume hood at TLK.

6.4. Determination of detection efficiencies by Monte Carlo simulations

In this section Monte Carlo simulations of the TRIADE BIXS setup are described. These simulations are necessary for data analysis of the X-ray detector data. In section 6.4.1 the objectives of these simulations are motivated. The simulated geometry, the used simulation parameters and an overview of all simulation runs is given in section 6.4.2. In section 6.4.3 calculated detection efficiencies for different tritium sources inside the TRIADE setup and projected detector count rates are given. Finally, the influence of tritium in the bulk of the sample on the detector count rate is discussed in section 6.4.4. Effects of small deviations of the actual SDD position are discussed in section 6.4.5.

6.4.1. Objectives of the simulations

In order to quantify the surface contamination on the sample from the measured X-ray detector count rate, the detection efficiency for tritium adsorbed on the sample surface is a necessary input. The detection efficiency DE is defined as number of detected events N_{det} divided by the number of β-decays N_{decays} during the measurement time. Due to the measurement principle of TRIADE there are other sources which also have an influence on the measured count rate. These are

1. tritium adsorbed on the sample,

2. tritium adsorbed on the beryllium window,

3. tritium adsorbed on the holder ring of the sample holder,

4. tritium adsorbed on the recipient wall and

5. tritium in the residual gas of the recipient.

All these sources can produce X-rays which can be detected by the X-ray detector. Since only the amount of tritium on the sample is of interest, all the other sources are considered as background. It is not possible to distinguish between them by data analysis of the spectral shape. Therefore, they must be suppressed as effective as possible by the geometry of the setup and quantified by simulations. The intrinsic detector background which is an additional source of background can be determined experimentally.

Tritium which is diffused into the bulk of the sample can also produce detector background. To have an idea in what way it influences the detector count rate and the spectral shape, the detection efficiencies for tritium in different layer depths of the sample bulk must be determined. Details of the layer depth configuration are given in the next section.

Finally, the influence of the detector position on the projected detector count rate is studied. Small deviations in the actual detector position can possibly cause large variations in the count rate. Therefore, an estimated uncertainty of ± 2 mm in the actual SDD position is simulated. The impact on the detector signal for tritium adsorbed on the sample and on the beryllium window will be discussed.
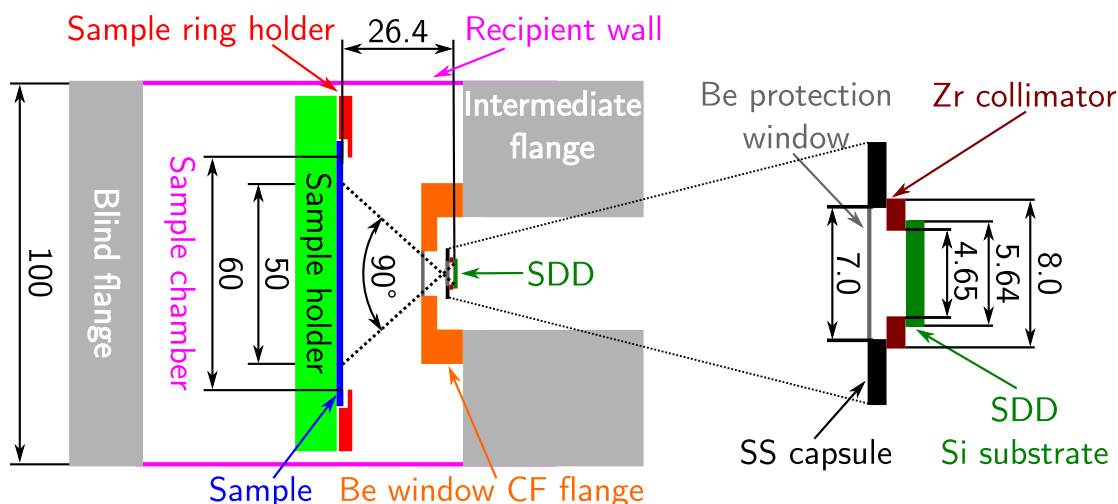
Figure 6.14.: Schematic of the simulated TRIADE geometry. The simulation source code which describes the geometry can be found in appendix A.19. Specified dimensions are given in mm, drawing is not in scale.

6.4.2. Simulated geometry and used simulation parameters

In figure 6.14 the simulated TRIADE geometry is shown. For all the Monte Carlo simulations in this chapter the simulated primary particles were electrons. The starting vectors were homogeneously distributed over the source area/volume, the electrons were emitted isotropically and the kinetic energy corresponds to the energy distribution of tritium β-electrons (section 3.4.2). Hydrogen at a pressure of $3 \cdot 10^{-20}$ mbar, which is the standard material for a vacuum in Geant4, was applied to all areas which are not marked otherwise in figure 6.14.

Although the components in the sample chamber have different substrate materials, as described in section 6.3, they were simplified for the geometry definition. As they are all gold coated, the blind flange, the intermediate flange, the sample holder, the sample holder ring, the recipient and the flange of the beryllium window are defined as completely made of gold. The SDD is simulated as a silicon substrate which has the dimensions of the active volume of the Amptek® detector used in TRIADE. The foil of the window and the sample are simulated as gold coated beryllium substrates.

Table 6.2.: Overview of the TRIADE Monte Carlo simulations. The denoted CPU-time is the needed single core CPU-time for all the simulation runs on an Intel® Xeon® E5-2670 v3.

No.	Description	No. of runs	Events/run	CPU-time (h)
1	Residual gas	2	10^9	161.77
2	Be window CF flange	10	10^9	750.78
3	Sample ring holder	10	10^9	625.30
4	Recipient wall	2	10^9	159.88
5	Be entrance window	2	10^9	144.78
6	Au sample surface	15	10^9	1113.14
7	Be sample surface	2	10^9	91.90
8	Au sample bulk (20-100) nm	$5 \cdot 8$	10^9	3971.1
9	SDD position ± 2 mm	$10 \cdot 4$	10^9	3098.53

An overview of all simulations is given in table 6.2. In simulation number 1-7 the influence of different sources on the detector count rate is studied. The residual gas is simulated as a cylindrical source volume which fills the space between the sample holder ring and the beryllium window. The outer diameter is equal to the inner diameter of the sample chamber. As there are no gas species or gas pressure dependent effects expected in the pressure regime below one mbar, the source volume was defined as a vacuum. Adsorbed tritium on the Be window CF flange (no. 2) and on the sample ring holder (no. 3) was simulated as annulus shaped surface plane on the top of the respective components. An open cylinder surface shaped source was chosen for the simulation of tritium adsorbed on the inner sample chamber surface (no. 4). Adsorbed tritium on the Be entrance window (no. 5) and the sample surface (no. 6) was simulated as circular shaped surface plane on the top of the 100 nm thick gold coating. In simulation no. 7 a sample without a gold coating was assumed which was not part of the tritium measurements.

Tritium diffused in the gold coating of the sample can also produce detectable X-rays. In simulation no. 8 circular shaped sources in different depths of the gold coating (20, 40, 60, 80 and 100) nm were simulated. The diameter of the sources was equal to the sample diameter of 60 mm.

As the detector count rate can significantly vary with the detector position, the influence of a detector shift was studied in simulation no. 9. The silicon substrate was shifted in 0.5 mm steps up to ± 2 mm. Source definitions were the same as in simulation no. 5 and no. 6.

All simulations were split into individual runs according to table 6.2. Different random seeds were used in each run to make the results statistically independent. The total single core computing time on an Intel® Xeon® E5-2670 v3 was 421.55 days.

6.4.3. Detection efficiencies and projected count rates

In table 6.3 the results of the simulations are listed. The highest detection efficiency of $(1.61 \pm 0.03) \cdot 10^{-6}$ $(\text{s}^{-1}/\text{Bq})$ is given for tritium adsorbed on the gold coated beryllium window which is the closest tritium source to the X-ray detector and has a direct line of sight. Nevertheless, due to the small surface area of $3.14\,\text{cm}^2$ it is not the dominant source. Projected detector count rates for one monolayer of tritium on each plane or surface source geometry are given. The highest count rate of $(24.7 \pm 0.5)\,\text{s}^{-1}$ is achieved for one monolayer of tritium on the gold coated sample surface. An equivalent of one monolayer of tritium on all surfaces would induce a detector count rate of $(57.6 \pm 1.9)\,\text{s}^{-1}$. The contribution of the sample surface contamination to the projected count rate is $(42.8 \pm 1.6)\%$ assuming a residual tritium gas pressure of $10^{-7}\,\text{mbar}$. With the contribution of tritium adsorbed on the gold coated beryllium window, $(67.2 \pm 1.7)\%$ of the projected count rate are induced by surface contamination of gold coated beryllium.

The largest source of background is tritium adsorbed on the gold coating of the stainless steel flange of the beryllium window which induces a projected count rate of $(11.8 \pm 0.7)\,\text{s}^{-1}$ for an equivalent of one monolayer of tritium. This is $(20.5 \pm 1.4)\%$ of the total count rate. Although tritium adsorbed on this surface is not in a direct line of sight for the detector, the large backscattering probability of tritium β-electrons for gold (about 40 %, see section 5.5.2) and the large surface area of $35.34\,\text{cm}^2$ causes this rather high contribution. Backscattered β-electrons from this surface can hit the gold coated sample and produce X-rays which are in direct line of sight of the detector. This contribution is hardly to supress by geometry. A larger window would increase other background contributions and a larger distance between the detector and the sample surface would decrease the minimum detectable activity. Only a further reduction of the distance between the sample holder and the gold coated beryllium window could effectively reduce this background contribution.

The count rate contribution of residual tritium gas is negligible. Even at the highest applied exposure pressure of $10^{-3}\,\text{mbar}$ (see section 6.5) the projected count rate is $(0.35 \pm 0.02)\,\text{s}^{-1}/\text{Bq}$. This is due to the small distance of 1.6 cm between the sample and the X-ray transparent window. Count rate contributions from other possible background sources as the sample ring holder and the recipient wall are efficiently suppressed by the chosen geometry.

6.4.4. Influence on the detector count rate by tritium diffusion into the sample bulk

Due to the measurement principle of TRIADE also tritium absorbed in the bulk of the sample or the X-ray transparent window can cause a measurable signal. This has been simulated for tritium absorbed in the gold coating of the sample material and the results are listed in table 6.3. As expected the detection efficiency for absorbed tritium in the gold coating is significant and in the same order as the detection efficiency for tritium adsorbed on the sample. Nevertheless, the detection efficiency decreases for tritium absorbed deeper ($\gtrsim 50\,\text{nm}$) in the bulk.

Table 6.3.: Detection efficiencies and projected count rates for different tritium sources inside TRIADE. Except for the residual gas source, count rates are calculated assuming one monolayer of tritium on an ideal Au (100) surface.

Source	Type	Surface material	Detection efficiency (s^{-1}/Bq)	Volume (cm^3) / Area (cm^2)	Count rate(s^{-1})
Residual gas	volume		$(8.05 \pm 0.63) \cdot 10^{-8}$	51.05	(0.35 ± 0.02) at 10^{-3} mbar
Be window CF flange	plane	Au	$(1.20 \pm 0.09) \cdot 10^{-7}$	35.34	(11.8 ± 0.7)
Sample ring holder	plane	Au	$(1.20 \pm 0.07) \cdot 10^{-8}$	41.12	(1.4 ± 0.1)
Recipient wall	surface	Au	$(6.00 \pm 1.73) \cdot 10^{-9}$	344.73	(5.8 ± 1.7)
Be entrance window	plane	Au	$(1.61 \pm 0.03) \cdot 10^{-6}$	3.14	(14.1 ± 0.3)
Au sample surface	plane	Au	$(3.12 \pm 0.04) \cdot 10^{-7}$	28.30	(24.7 ± 0.5)
Be sample surface	plane	Be	$(8.60 \pm 0.66) \cdot 10^{-8}$	28.30	-
Au sample bulk 20 nm	plane	Au	$(3.88 \pm 0.10) \cdot 10^{-7}$	28.30	(30.6 ± 0.8)
Au sample bulk 40 nm	plane	Au	$(3.92 \pm 0.10) \cdot 10^{-7}$	28.30	(30.9 ± 0.8)
Au sample bulk 60 nm	plane	Au	$(3.71 \pm 0.10) \cdot 10^{-7}$	28.30	(29.2 ± 0.8)
Au sample bulk 80 nm	plane	Au	$(2.98 \pm 0.09) \cdot 10^{-7}$	28.30	(23.4 ± 0.7)
Au sample bulk 100 nm	plane	Au	$(1.56 \pm 0.04) \cdot 10^{-7}$	28.30	(12.3 ± 0.4)
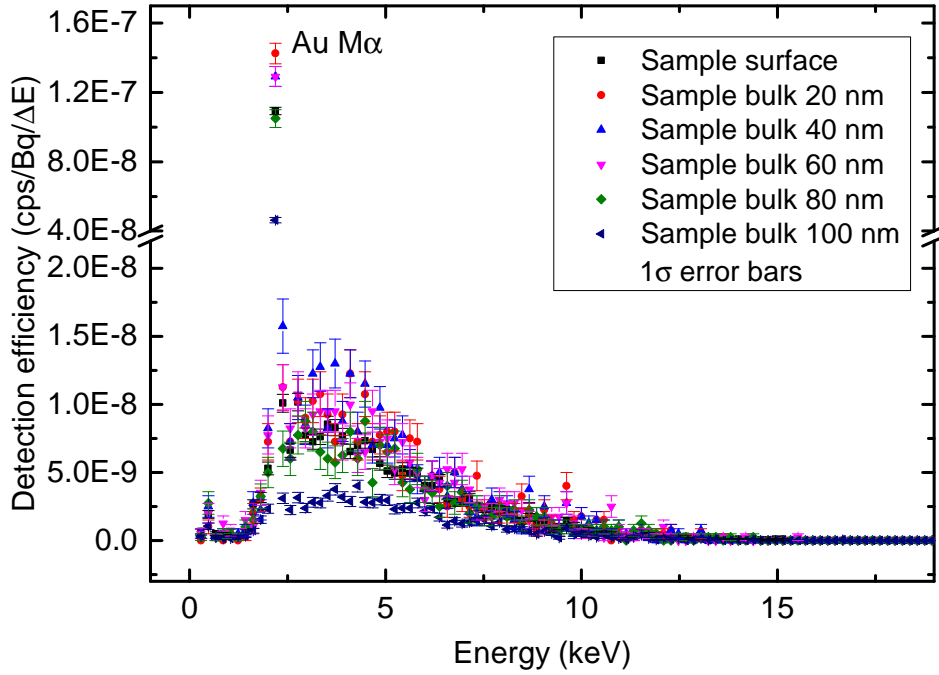
Figure 6.15.: BIXS spectra for tritium sources in different bulk depths of the Au coating of the sample. Each spectrum is scaled to $1.6 \cdot 10^{10}$ emitted β-electrons. The characteristic X-ray line at 2.1 keV is the Au M_α line [XRD09].

The decrease in detection efficiency is caused by the increased attenuation of X-rays produced deeper in the bulk. Also the probability for β-electrons to be transmitted through the gold coating and to be absorbed in the beryllium substrate is increased. As shown in section 3.1.2 the radiation yield for electrons absorbed in beryllium is about two orders of magnitude smaller than for gold. In figure 6.15 BIXS spectra for different bulk depths are shown. They show the typical shapes as described in section 3.4.2.1. A beam hardening effect (see section 3.1.3) in the spectral shape is not identifiable and they are indistinguishable among each other. Only the total intensity changes according to the detection efficiency numbers listed in table 6.3. Therefore, TRIADE measurements can only give an upper limit for tritium adsorption on a sample material. Tritium depth-profiling by a detailed spectral analysis is not possible for bulk depths in the range of 100 nm.

6.4.5. Influence of the SDD position on the detector count rate

As reported in [Mao12] geometrical uncertainties can cause rather large uncertainties on the calculated detection efficiencies of a BIXS system. How large, strongly depends on the geometry and has been investigated for the uncertainty of the SDD position in the TRIADE setup. In total 9 detector positions have been simulated. The SDD position as shown in figure 6.14 has been varied in 0.5 mm steps to a maximum displacement of ±2 mm. Effects on the calculated detection efficiencies for tritium adsorbed on the
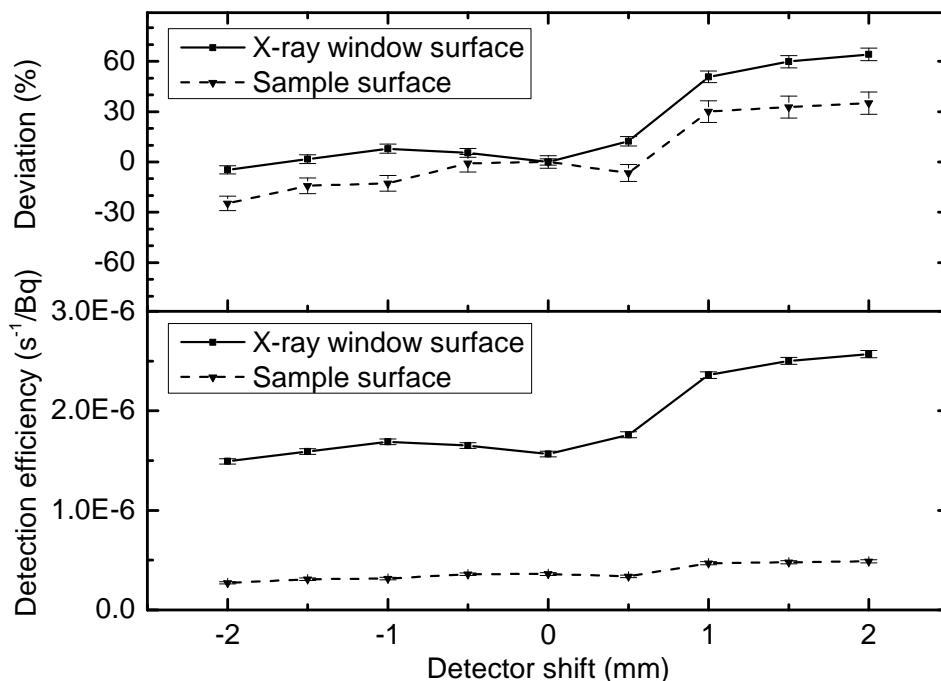
Figure 6.16.: Influence of the SDD position on the detection efficiencies for tritium adsorbed on the sample and on the X-ray transparent window surface. Deviations in the detection efficiency have been calculated compared to the zero position of the SDD. Statistically errors are given with a 1σ confidence interval.

sample surface and adsorbed on the gold coated beryllium window have been studied, as listed in no. 9 of table 6.2.

In figure 6.16 the results are shown. Both detection efficiencies, for tritium adsorbed on the sample and tritium adsorbed on the X-ray transparent window, increase with smaller distances between the SDD and the X-ray transparent window or the sample. For a detector shift of $+2$ mm the deviation is $(+64.1 \pm 3.7)\%$ (X-ray transparent window) or $(+35.1 \pm 6.6)\%$ (Sample). Detector shifts between 0 mm and -2 mm have a rather small impact. The deviation of the detection efficiency for tritium adsorbed on the X-ray transparent window is below 10% and can be regarded as constant within the statistical uncertainty. For tritium adsorbed on the sample the deviation is $(-24.6 \pm 4.3)\%$ at -2 mm.

The results show that the SDD position in the TRIADE setup should be determined as accurate as possible. Even small uncertainties in the SDD position of ± 2 mm have a strong impact on the calculated detection efficiencies and therefore on the data interpretation of the tritium measurements. This was expected and therefore special focus was put on that during construction of TRIADE. The actual mechanical tolerances regarding the SDD position are expected to be $\leqslant 1$ mm.
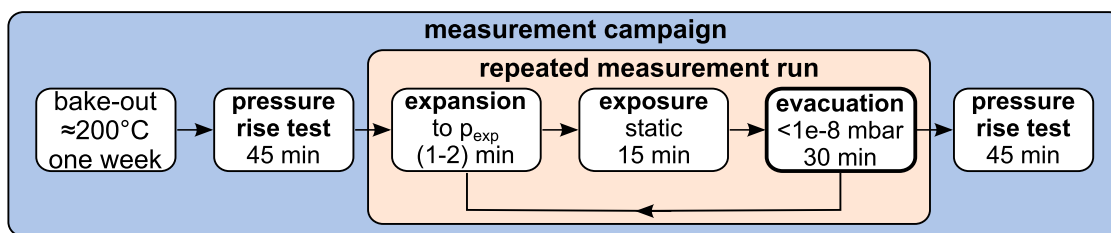
Figure 6.17.: Measurement procedure for each measurement campaign. A detailed description is in the text.

6.5. First tritium measurements with a gold coated beryllium sample

The first sample material which is investigated with the TRIADE setup is gold coated beryllium. This is of particular importance due to the use in the BIXS system of KATRIN. Furthermore, it allows projections for the adsorption behavior of the gold coated *rear wall* of KATRIN which determines the source potential (see section 5.2). Five tritium measurement campaigns have been performed to answer the questions raised in section 6.1.4:

- Does tritium adsorb/absorb in significant amounts on/in gold coated beryllium at room temperature?

- What is the expected saturation coverage for tritium adsorption on gold?

- How much time is needed to reach a saturation coverage?

- What are effective decontamination strategies?

Each campaign and each run were performed according to the measurement procedure described in section 6.5.1. First evidence for tritium adsorption is described in section 6.5.2. In section 6.5.3 the saturation coverage is determined. The time dependence of the surface contamination is investigated in section 6.5.4 and decontamination studies are described in section 6.5.5. Measurement results are discussed and summarized in section 6.6.

6.5.1. Description of the tritium measurement procedure

An overview of the five performed measurement campaigns is given in table 6.4. Each campaign was performed during one working day and included 12 to 17 measurement runs. In figure 6.17 the standard measurement procedure is outlined.

Measurement preparations before the campaign
Except MC#4.2 which was on the consecutive day of MC#4.1, the same preparations were made before each campaign. A transfer of the tritium gas mixture from the CAPER facility to TRIADE was performed using a sample cylinder with a volume of (10 ± 1) cm^3. The total pressure in the sample cylinder was either 1 mbar (MC#1, MC#2) or 5 mbar (MC#3, MC#4). After connecting the cylinder to the sample port (compare process

Table 6.4.: Overview of the five measurement campaigns. The tritium gas mixtures were provided by the CAPER facility. The maximum pressure in the sample chamber during the exposure phase is denoted as p_{exp}. MC#4.1 and MC#4.2 were performed on consecutive days.

Campaign	MC#1	MC#2	MC#3	MC#4.1	MC#4.2
Date	7-8-14	27-8-14	16-9-14	29-10-14	30-10-14
Number of runs	17	15	15	15	12
Tritium purity (%)	94 ± 5	94 ± 5	77 ± 5	98^{+2}_{-5}	98^{+2}_{-5}
Exposure pressure p_{exp} (mbar)	$5 \cdot 10^{-5}$	$5 \cdot 10^{-5}$	$1 \cdot 10^{-3}$	$1 \cdot 10^{-3}$	$1 \cdot 10^{-3}$
Dosage $p \cdot t$ (mbar·h)	$(1.6 \pm 0.1) \cdot 10^{-4}$	$(9.1 \pm 0.8) \cdot 10^{-5}$	$(5.5 \pm 0.5) \cdot 10^{-3}$	$(7.7 \pm 0.7) \cdot 10^{-3}$	$(8.3 \pm 0.8) \cdot 10^{-3}$
Temperature T (°C)	$(33.3 \cdots 34.0)$	$(32.3 \cdots 32.9)$	$(32.4 \cdots 32.9)$	$(32.0 \cdots 32.4)$	$(32.0 \cdots 32.7)$
BIXS memory effect (s⁻¹)	0.77 ± 0.03	0.89 ± 0.02	0.97 ± 0.02	2.12 ± 0.04	5.35 ± 0.06

diagram in figure 6.11) a leakage test of the connection was performed. Atmospheric air in the connection volume was evacuated to buffer vessel BV062 reaching a pressure of $\leqslant 10^{-5}$ mbar in the connection volume. A bake-out of the connection line between the sample cylinder and the sample chamber was performed at $\approx 195°\text{C}$ for at least one day to reduce residual water.

Bake-out and pressure rise tests
Before the first expansion of the tritium gas mixture the recipient and the sample were decontaminated. This included an exposure to atmospheric air for 30 minutes at a pressure of about 40 mbar. Afterwards a bake-out at $\approx 195°\text{C}$ was performed for one week. The bake-out temperature was limited to reduce the risk of damaging the gold coatings inside the recipient, to be as near to KATRIN conditions as possible and due to TLK restrictions regarding higher temperatures[13]. The final measurement conditions were monitored by the residual gas analyzer. In case of no expansion or exposure phase the recipient was continuously evacuated, even between the measurement campaigns.

Before and after each run a pressure rise test of the recipient was performed for 20 minutes to quantify the leakage and outgassing rate. After the first pressure rise test the recipient was evacuated for 30 min before starting with the measurement runs.

Expansion phase
With the begin of each run the tritium gas mixture was expanded into the recipient. This was controlled by a manual valve. Each gas expansion took about (1 to 3) minutes and ended as soon as the pressure p_{exp} according to table 6.4 was reached in the recipient. Due to manual regulation the peak pressures ranged between $(4.5 \ldots 5.6) \cdot 10^{-5}$ mbar in MC#1 and MC#2 and between $(9.4 \ldots 10.7) \cdot 10^{-5}$ mbar in MC#3, MC#4.1 and MC#4.2. A MKS903 cold cathode ionization sensor was used for this and all values are nitrogen calibrated values. BIXS measurements were performed in 10 s intervals.

Exposure phase
After expansion all manual valves were closed and the sample was exposed to the tritium gas mixture for 15 min. During that time the pressure could change due to outgassing effects, leakage rates and adsorption. BIXS measurements were performed in 10 s intervals.

Evacuation phase
After exposure the recipient was evacuated to a pressure of $\leqslant 10^{-8}$ mbar for about 30 min. During that time activity measurements of the remaining surface contamination were performed without significant influence from the residual gas. BIXS measurements were performed in 10 s intervals for the first 5 min of each evacuation phase and then switched to 100 s intervals for the remaining 25 min.

As each step was controlled manually the actual times for each phase can vary in the range of ± 1 min.

---

[13] At operating temperatures higher than 200°C of a component in a tritium processing facility several additional safety measures are necessary due to TLK regulations [TLA15]. This comprises for instance a second housing and additional temperature monitoring.
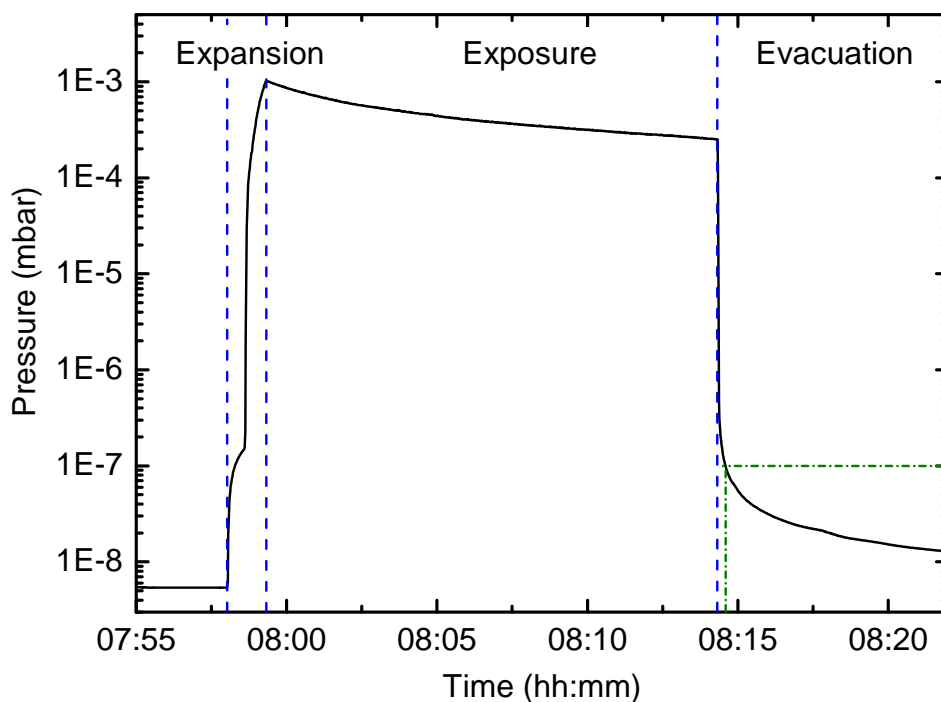
Figure 6.18.: Sample chamber pressure during one TRIADE measurement run. The plot shows the three phases of measurement run one of MC#4.2. The kink during the expansion phase indicates a re-adjustment of the manual valve. During the exposure phase the sample chamber is closed for 15 min. A pressure decrease due to tritium adsorption on the inner surfaces of the sample chamber is identifiable. Finally, the sample chamber is evacuated for 30 min. The pressure threshold of 10^{-7} mbar is a trigger for the automated data analysis. If not otherwise denoted, later presented count rate measurements are only regarded as soon as this threshold is undershot. Pressure data are recorded with a MKS903 cold cathode gauge (see appendix A.9) and are nitrogen calibrated.

6.5.2. Evidence for tritium adsorption on gold at room temperature

Figure 6.18 shows an pressure plot of run one of MC#4.2 which is exemplary for all runs. It shows the three phases of each run consisting of an expansion, an exposure and an evacuation phase. During the expansion phase there is a kink in the pressure trend due to a re-adjustment of the manual valve used for gas expansion. After reaching the maximum exposure pressure of 10^{-3} mbar the manual valve is closed and the exposure phase starts. An ideal system with no tritium adsorption would show a constant pressure trend during exposure phase or a rising pressure trend due to outgassing effects. In figure 6.18 a pressure decrease to about $3 \cdot 10^{-4}$ mbar is shown.

Three different reasons could be responsible for the pressure decrease:

1. internal leaks,

2. pumping by the cold cathode [Pat57] or

3. tritium adsorption on the inner surfaces of the sample chamber.
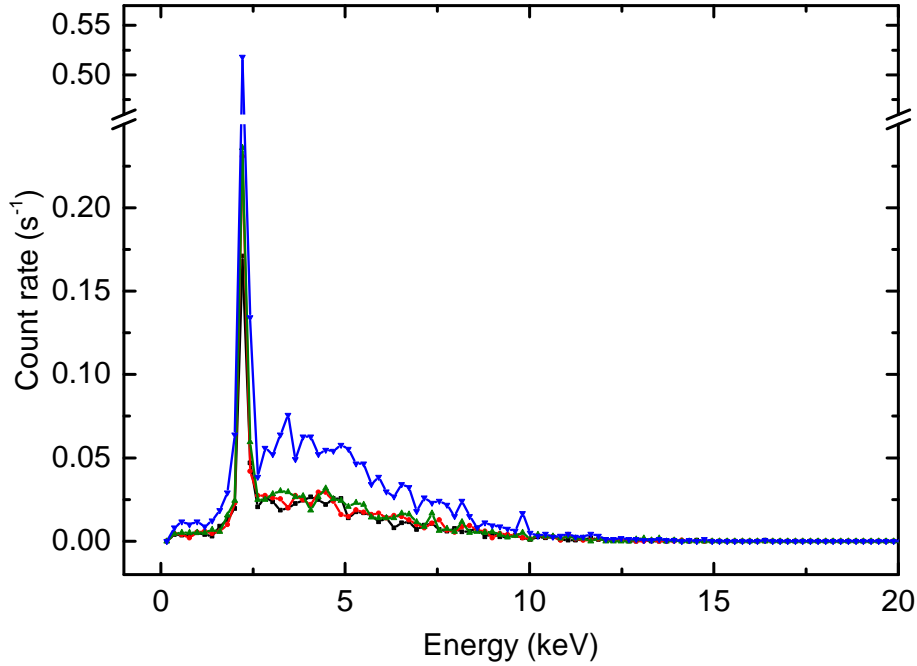
Figure 6.19.: Initial X-ray spectra of the TRIADE measurement campaigns. Each spectrum was taken 30 min before the initial pressure rise tests. The initial BIXS spectrum of MC#1 could be made due to commissioning measurements with tritium. The characteristic X-ray line at 2.1 keV is the Au M_α line [XRD09].

Internal leaks can be excluded due to the commissioning leakage tests which confirmed a leakage rate of $\leqslant 10^{-9}$ mbar l/s. An internal leak of that magnitude would cause a maximum pressure decrease of about $1 \cdot 10^{-6}$ mbar during the expansion phase. Furthermore, the final exposure pressure shows a distinctive trend as reported in section 6.5.3 and shown in figure 6.24. Pressure decrease by an internal leak should show the same behavior in each run or a statistical behavior if it's caused for instance by a not completely closed manual valve. For the same reason pumping behavior of the cold cathode as reported in [Pea91] can be excluded. Therefore, the pressure drop must be caused by tritium adsorption on the inner surfaces of the sample chamber.

Since the core system of TRIADE is not completely gold coated it's likely that stainless steel parts, as the angle valve or the pressure sensors, adsorb the tritium lost from the gas or at least contribute to the tritium adsorption process. Nevertheless, count rate contributions to the BIXS signal, due to β-electrons emission from the stainless steel surface and subsequent X-ray production, are regarded as negligible. The geometry of the core system, as shown in figure 6.14, effectively shields these X-rays. BIXS-spectra as shown in figure 6.19 are therefore due to tritium adsorption on the gold coated surfaces of the sample chamber as listed in table 6.3. All recorded spectra show the same characteristic shape and only differ in the intensity.

The pressure trend during the exposure phase and the BIXS signal of the X-ray detector clearly show that tritium adsorption on gold coated surfaces at room temperature is possible.
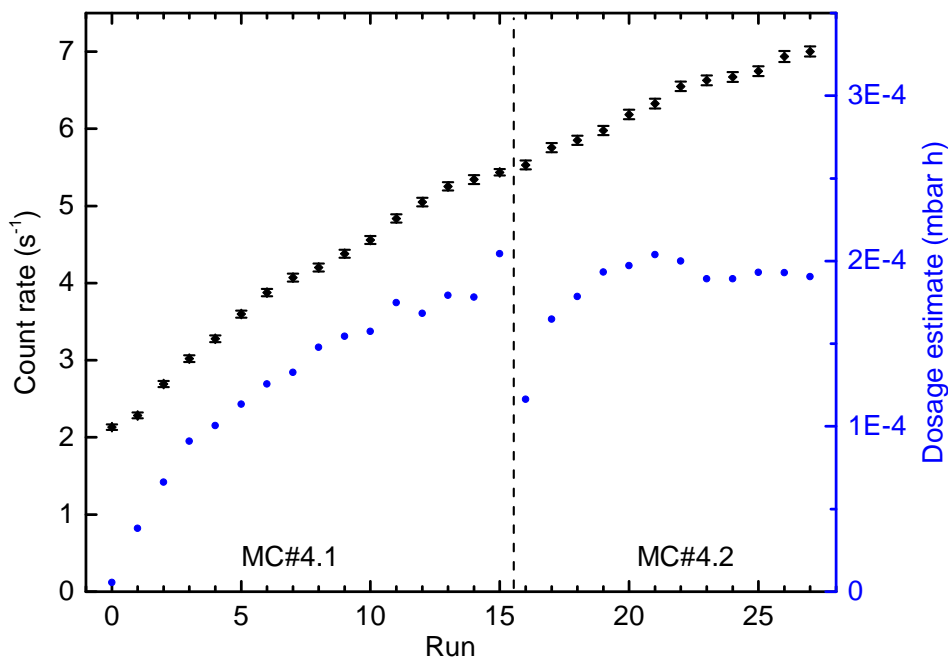
Figure 6.20.: BIXS count rate trend during measurement campaigns MC#4.1 and MC#4.2. Error bars indicating 1σ uncertainty of the mean value.

6.5.3. Determination of the saturation coverage

As tritium adsorption is possible, the BIXS count rate trend and the final exposure pressure trend during repeated measurements were investigated. Two scenarios are considered:

- constant, pressure dependent tritium accumulation on the sample surface or in the bulk or

- exponential like increase in the surface contamination while reaching an exposure pressure dependent saturation coverage.

Figure 6.22 shows the results of the count rate measurements during the evacuation phase of four measurement campaigns. In all campaigns there is a steady increase in the count rate for consecutive tritium runs. This is due to the memory effect discussed in section 2.2. MC#1 and MC#2 were performed with a maximum exposure pressure of $5 \cdot 10^{-5}$ mbar. Both campaigns showing a linear increase in count rate and demonstrating the level of reproducibility which can be achieved with the setup and the measurement procedure.

In MC#3 and MC#4.1 an exposure pressure of 10^{-3} mbar was used. Comparing these two campaigns with MC#1 and MC#2 a strong exposure pressure dependent effect on the course of the count rate and on the absolute count rate values is identifiable. The standard decontamination procedure, consisting of one week of bake-out at $\approx 200°$C, between MC#3 and MC#4.1 didn't fully recover the initial background count rate.
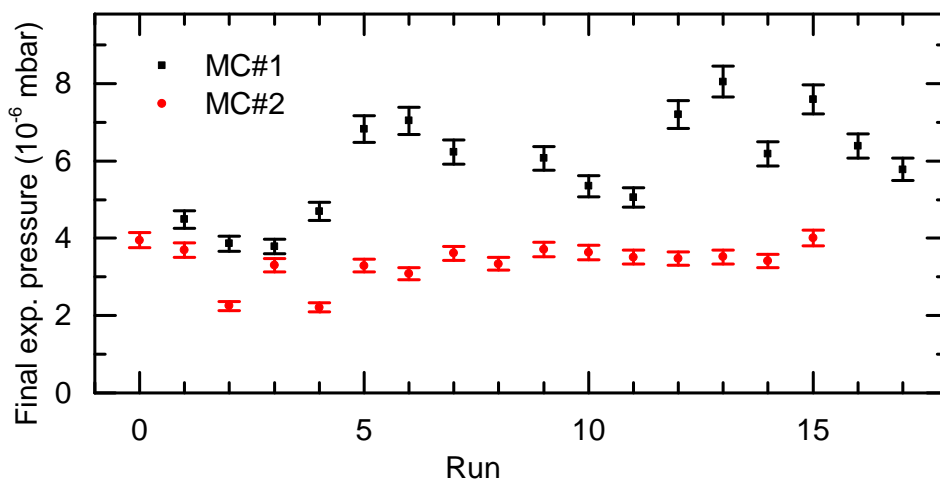
Figure 6.21.: Final exposure pressure during measurement campaigns MC#1 and MC#2. Error bars indicating 1σ uncertainty of the mean value.

Excluding the higher initial background of MC#4.1 both campaigns show a similar count rate trend which shows first signs of a saturation effect.

Figure 6.20 shows the combined count rate results of MC#4.1 and MC#4.2. They were performed on consecutive days without a bake-out between. Instead, the sample chamber was continuously evacuated between the campaigns. The final count rate during
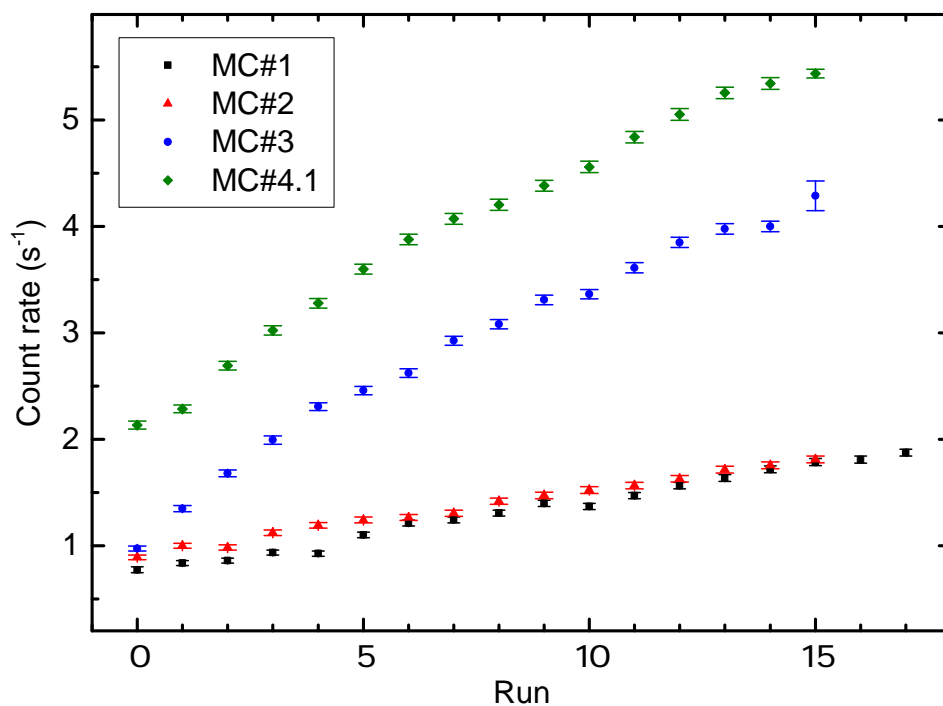
Figure 6.22.: BIXS count rate trend during the measurement campaigns. Error bars indicating 1σ statistical uncertainty.
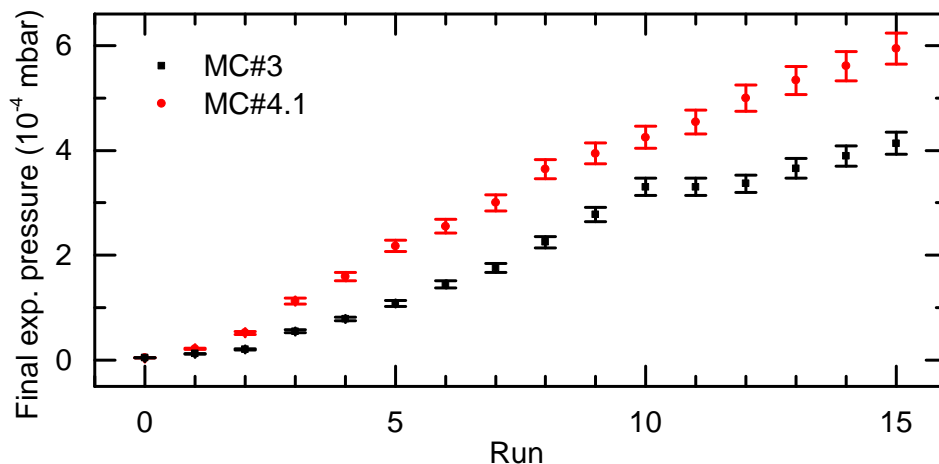
Figure 6.23.: Final exposure pressure during measurement campaigns MC#3 and MC#4.1. Error bars indicating 1σ uncertainty of the mean value.

the evacuation phase of run 27 was $(7.00 \pm 0.06)\,\mathrm{s}^{-1}$. Additionally, the dosage $p \cdot t$ [Lüt97] was calculated as an indicator for the exposure conditions during each run. There is an exponential-like increase in the dosage reaching its maximum at about $2 \cdot 10^{-4}$ mbar h. The kink at run 16 is due to the measurement break between both campaigns and the overnight evacuation. As the exposure time and the initial exposure pressure was constant during each measurement campaign the final exposure pressure must change to produce such a dosage trend.

In figure 6.21 in MC#1 and MC#2 the final exposure pressure at the end of the exposure phase is rather constant. During exposure phase the pressure drops from $5 \cdot 10^{-5}$ mbar to $\approx 5 \cdot 10^{-6}$ mbar. That means nearly all the tritium is adsorbed or absorbed during exposure phase. The residual amount of gas is not enough to be analyzed by the mass spectrometer of TRIADE or to prepare a test gas cylinder for further analysis. Therefore, the amount of tritium in the residual gas cannot be determined. It can be dominated by non-adsorbing impurities of the initial gas mixture. Also outgassing effects during exposure phase can contribute to the final exposure pressure.

In figure 6.23 the final exposure pressure of MC#3 and MC#4.1 is shown. Compared to the previous measurement campaigns there is a trend to higher final exposure pressures identifiable. This means an increasing amount of tritium is not adsorbed during exposure phase. In run 15 of MC#4.1 about 60% of the initial gas filling stays in the gas phase and is not adsorbed on the inner surfaces. The final exposure pressure trend implies that the surface contamination of the system becomes saturated during the measurement campaign. In figure 6.24 this trend continues during the consecutive campaigns MC#4.1 and MC#4.2. There is a distinctive kink in the final exposure pressure in the first run of the second day. This is most likely due to the overnight evacuation of the sample chamber. On the second day the final exposure pressure rises more quickly than on the first day and reaches again about 60% of the initial exposure pressure.

The final exposure pressure trend in figure 6.24 implies more than one adsorption or absorption process. Whereas a clear saturation effect is identifiable still about 40% of
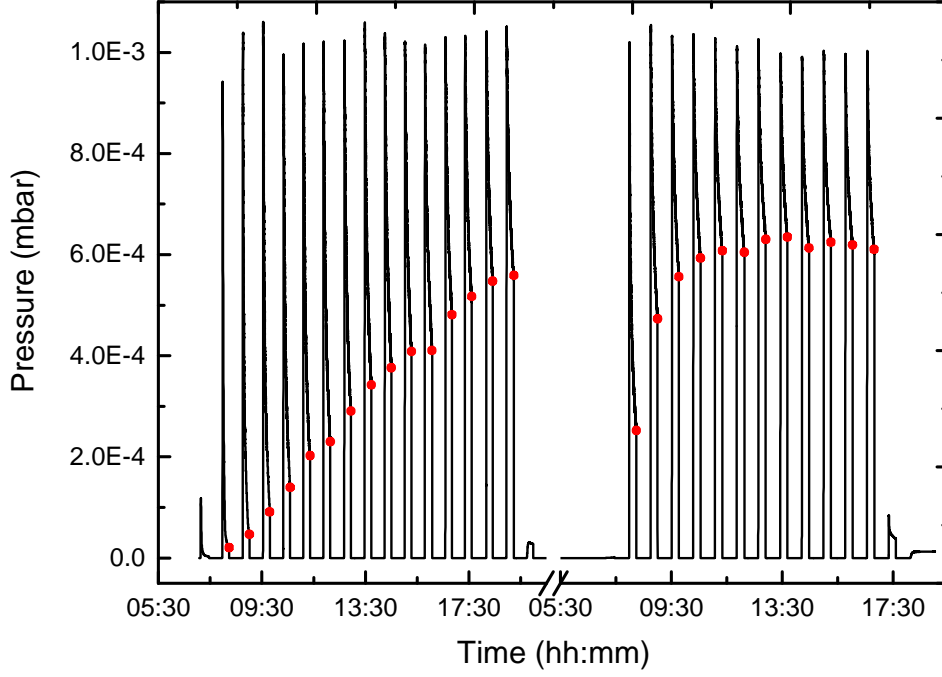
Figure 6.24.: Final exposure pressure during measurement campaigns MC#4.1 and MC#4.2.

the initial gas amount are adsorbed or absorbed. An obvious explanation for that would be a different adsorption/absorption behavior of the stainless steel parts and the gold coated parts of the sample chamber. Stainless steel is known to absorb large amounts of tritium [Pri13] and to be rather easily permeable [Ste83]. Adsorption and consecuent absorption of tritium in the stainless parts can cause the constant loss of tritium from the gas phase during exposure phase. As the same effect can not be excluded for the gold coated surfaces the BIXS count rate trend is further investigated.

For the quantitative investigation of the saturation effect two different fit models are used. Since in MC#1 and MC#2 no saturation effect is identifiable a linear model is assumed. For MC#3, MC#4.1 and MC#4.2 an exponential model is used. The surface activity $A(t)$ is related to the detector signal $y(t)$ by the detection efficiency DE_i. Whereas the index i denotes the different detection efficiencies for different areas (as listed in table 6.3) in which tritium adsorption can happen. An initial background count rate due to tritium in the bulk is considered with a constant activity A_{bg} which is also related to the detector signal by a detection efficiency DE_i.

$$y_{1,2}(t) = \sum_i \left(DE_i \cdot A \cdot t + DE_i \cdot A_{\mathrm{bg}} \right) \tag{6.13}$$

$$y_{3,4.1,4.2}(t) = \sum_i \left(DE_i \cdot A(t) \cdot (1 - \mathrm{e}^{-t/\tau}) + DE_i \cdot A_{\mathrm{bg}} \right) \tag{6.14}$$

A time constant τ is introduced to characterize the speed of adsorption during the course of the measurement campaign in the exponential model. As the detector signal can not

Table 6.5.: Results of the fits of the BIXS count rates.

Campaign	Model	y_{bg}	C	τ	$\bar{R}^2$
MC#1	linear	(0.753 ± 0.017)	(0.067 ± 0.002)		0.990
MC#2	linear	(0.917 ± 0.012)	(0.060 ± 0.001)		0.993
MC#3	exponential	(1.00 ± 0.03)	(4.6 ± 0.3)	(12.8 ± 1.3)	0.997
MC#4.1	exponential	(2.06 ± 0.04)	(5.8 ± 0.5)	(16.8 ± 2.2)	0.997
MC#4.2	exponential	(0.24 ± 1.20)	(8.2 ± 0.7)	(15.3 ± 3.8)	0.992
MC#4 comb.	exponential	(2.10 ± 0.03)	(6.7 ± 0.2)	(21.1 ± 1.2)	0.998

be distinguished for different sources of tritium activity the sum over different detection efficiencies must be substituted by an average detection efficiency. This can be justified by the fact that all relevant sources are gold coated and should show a similar behavior. Except the walls of the sample chamber which have a minor influence on the detector signal (see section 6.4), all components were gold coated with the same sputtering method. For simplicity the amplitude A and the detection efficiency DE are substituted to one parameter y_{bg} for the background signal and C for the surface activity signal in the fit calculations.

$$y_{1,2}(t) = C \cdot t + y_{bg} \qquad (6.15)$$
$$y_{3,4.1,4.2}(t) = C \cdot (1 - e^{-t/\tau}) + y_{bg} \qquad (6.16)$$

The results of the fits are listed in table 6.5. MC#1 and MC#2 show a good repeatability taking into account the possible high systematic uncertainties due to the manually controlled expansion. The linear model shows a good visual agreement for both campaigns (see appendix A.16). Using the average dosage per run of $(0.94 \pm 0.06) \cdot 10^{-5}$ mbar·h for the first campaign and $(0.61 \pm 0.05) \cdot 10^{-5}$ mbar·h for the second campaign one can project a count rate increase per dosage at an tritium exposure pressure in the order of 10^{-5} mbar. This results in a count rate increase of (0.071 ± 0.005) s^{-1}/10^{-5} mbar h for MC#1 and (0.098 ± 0.008) s^{-1}/10^{-5} mbar h for MC#2 and can be used to project the drift of the count rate of the KATRIN BIXS system during operation. This is discussed in section 6.6.3.

Also the applied exponential model shows a good visual agreement of the fit calculations with the measured BIXS count rates of the last three campaigns (see appendix A.16). In figure 6.25 the fit curve of the combined campaigns MC#4.1 and MC#4.2 is shown. The calculated background signal y_{bg} of MC#3 and MC#4.1 matches with the measured background count rate at the begin of both campaigns before the first run. For campaign MC#4.2 it also matches but only due to the large uncertainty on the fit value. This is most likely due to the fact that no initial bake-out was performed in MC#4.2. Only a small decontamination effect is expected due to the overnight evacuation between MC#4.1 and MC#4.2 ($\approx$ 12 hours). The combined fit calculation of these two runs gives a background signal which matches with the one of MC#4.1 within uncertainty.
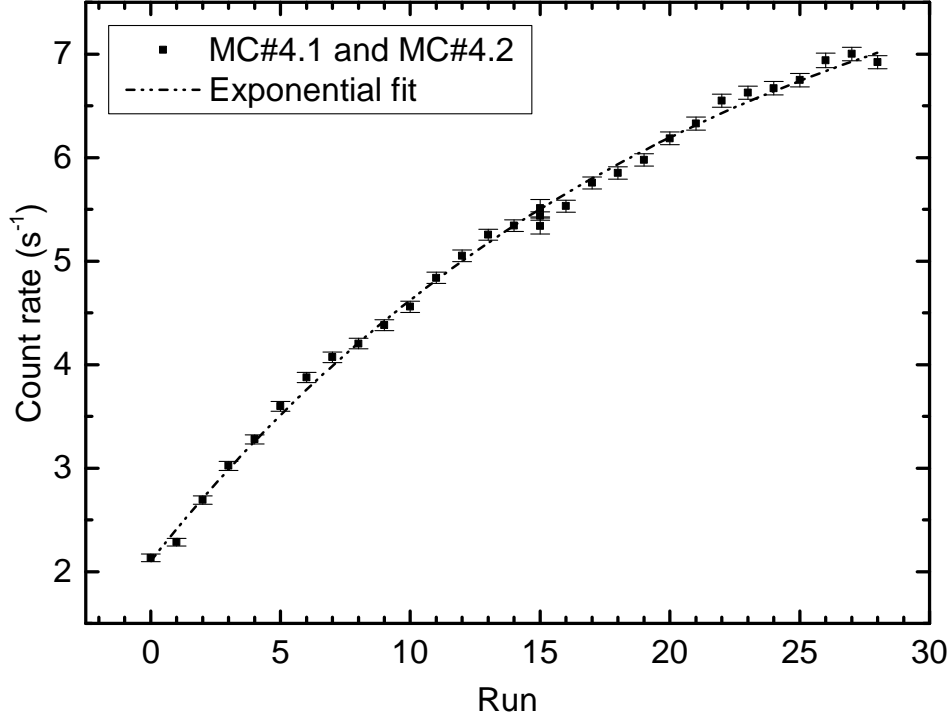
Figure 6.25.: BIXS count rates of campaigns MC#4.1 and MC#4.2, fitted with an exponential model. Error bars only representing 1σ statistical uncertainties of the measured count rates.

In the exponential model the maximum amplitude C is between 4.6 s^{-1} and 8.2 s^{-1}. The amplitude of the combined fit calculation MC#4 comb. is with 6.7 s^{-1} between the individual ones. Variations in the maximum amplitude C can be due to unconsidered systematic uncertainties as discussed in section 6.6 or due to the fit model.

As there are large variations in the tritium partial pressure during individual runs (see figure 6.21) the BIXS count rate can be plotted depending on the dosage D. Thereby the dosage for a run n is calculated according to

$$D_n \quad = \quad \sum_{i=1}^{i=n} \int_{t_{\text{start}}}^{t_{\text{end}}} p(t)dt. \tag{6.17}$$

Whereby t_{start} is the starting time of the exposure phase of run i. The end time t_{end} marks the point during evacuation phase of run i when the pressure drops below 10^{-7} mbar. In figure 6.26 the BIXS count rate depending on the dosage for MC#4.1 and MC#4.2 is shown. The course of the count rate is best described by a combined linear/exponential
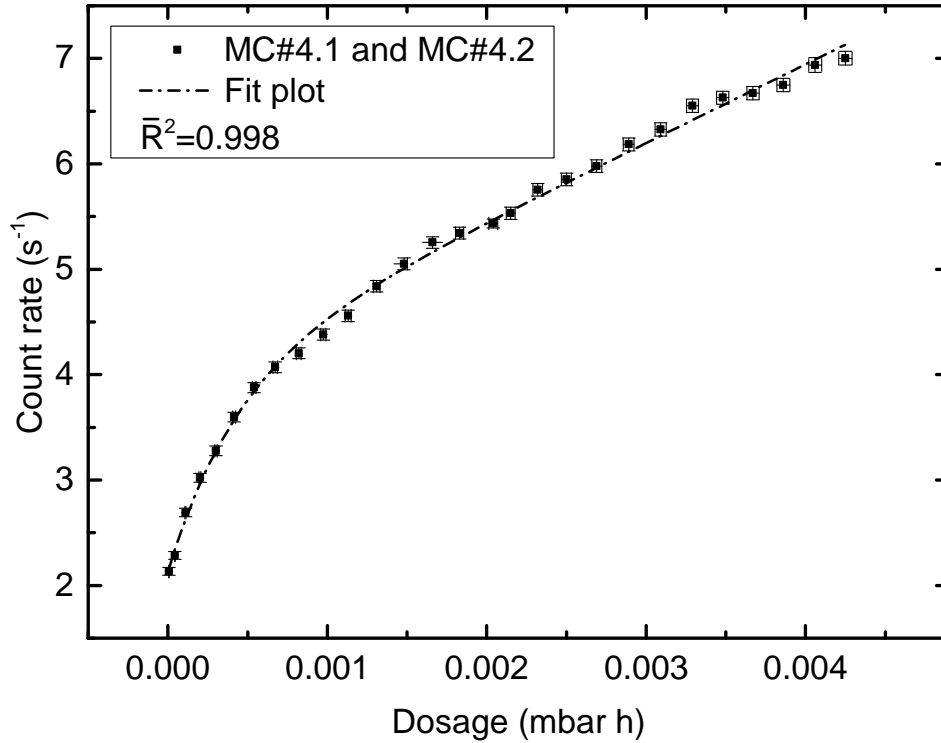
Figure 6.26.: BIXS count rates of campaigns MC#4.1 and MC#4.2 depending on the applied dosage, fitted with a combination of a linear and an exponential model. Y-error bars representing 1σ statistical uncertainties of the measured count rates and X-error indicating 1σ uncertainty of the mean value.. Pressure data are measured with a nitrogen calibrated ionization vacuum gauge MKS903. The fit calculation is according to equation 6.19.

model:

$$
\begin{aligned}
y_4(D) &= C_{D,\mathrm{exp.}} \cdot (1 - \mathrm{e}^{-D/\tau_D}) + y_{D,\mathrm{bg}} + C_{D,\mathrm{lin.}} \cdot D. \qquad (6.18)\\
C_{D,\mathrm{exp.}} &= (1.83 \pm 0.07)\,\mathrm{s}^{-1}\\
y_{D,\mathrm{bg}} &= (2.13 \pm 0.04)\,\mathrm{s}^{-1}\\
\tau_D &= (4.3 \pm 0.4)\cdot 10^{-4}\,\mathrm{mbar\ h}\\
C_{D,\mathrm{lin.}} &= (745.7 \pm 24.9)\,\mathrm{s}^{-1}/\mathrm{mbar\ h}
\end{aligned}
$$

With the calculated fit results, long-term projections can be made regarding the memory effect of the KATRIN BIXS system. This is discussed in section 6.6.3. Short-term fluctuations of the count rate are discussed in the following.

6.5.4. Short time fluctuations of the surface contamination

Up to now, all tritium measurement results in this chapter were measured during the evacuation phase. The measurements were started as soon as the total pressure was below 10^{-7} mbar and lasted for each run ≈ 2000 s. These measurements are related to the memory effect which is characterized by long-term tritium surface contaminations as discussed in section 2.2.
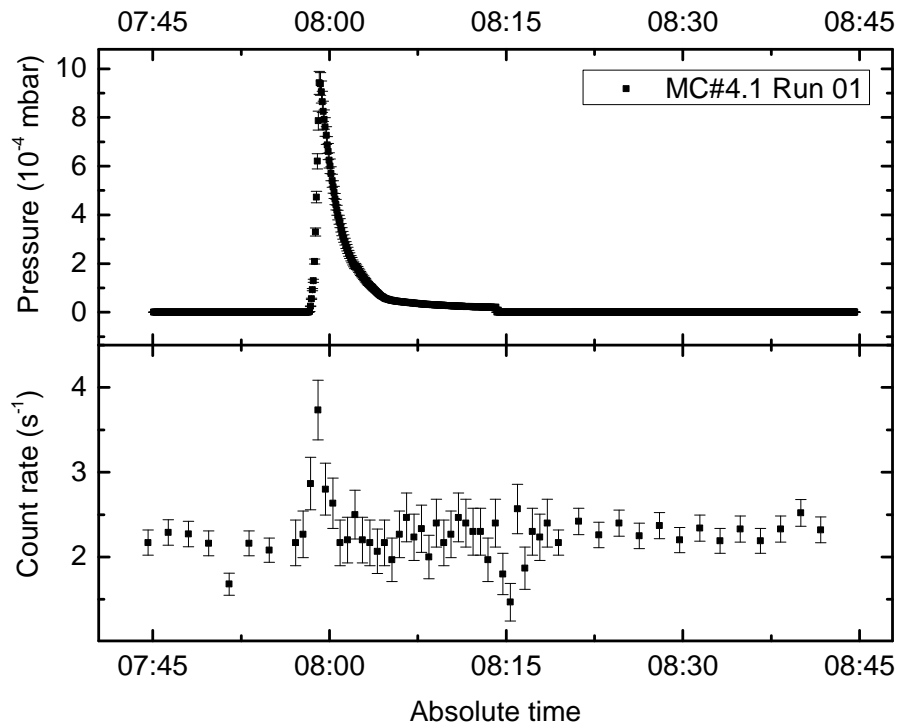
Figure 6.27.: BIXS count rate trend and pressure trend during MC#4.1 Run 01. Error bars indicating 1σ uncertainties.
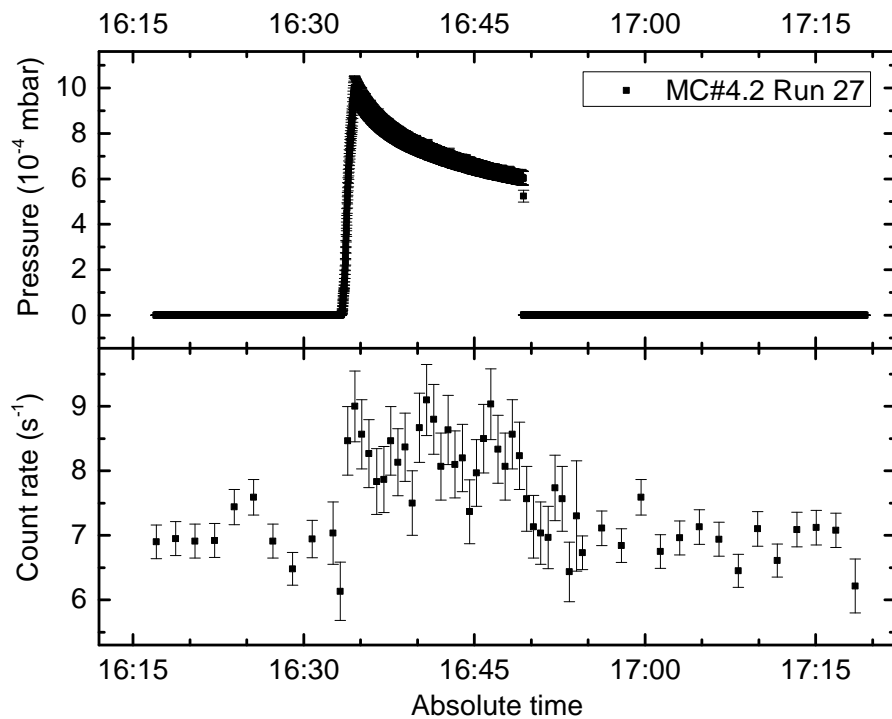
Figure 6.28.: BIXS count rate trend and pressure trend during MC#4.1 Run 27. Error bars indicating 1σ uncertainties.

The measurement of short-term fluctuations of the tritium surface contamination during expansion, exposure and evacuation phase is more challenging. It needs significantly shorter measurement intervals while still having a low detection limit on a sub-monolayer level. This is analyzed for two exemplary measurement runs. In figure 6.27 and figure 6.28 the BIXS count rates during run 01 of MC#4.1 and run 27 of MC#4.2 are shown in measurement intervals of (30 s/100 s). The actual measurement interval of 10 s during expansion phase and exposure phase were binned to 30 s intervals to reduce statistical uncertainty.

Both runs are non-equilibrium measurements as there are large variations in the tritium partial pressure during exposure. Nevertheless, due to the identified saturation effect which was discussed in the previous section, the pressure conditions in run 27 are much more stable than in run 01. In run 27 the pressure decreases from the initial exposure pressure of $(10.0 \pm 0.5) \cdot 10^{-4}$ to $(6.03 \pm 0.30) \cdot 10^{-4}$ within 15 min. The same pressure drop in run 01 takes only (65 ± 5) s.

During the first minute of the exposure phase of run 01 the maximum BIXS count rate is (3.73 ± 0.35) s^{-1}. While the background before exposure is (2.12 ± 0.05) s^{-1} and after exposure (2.31 ± 0.04) s^{-1}. The difference in count rate is between (1.42 ± 0.36) s^{-1} and (1.61 ± 0.35) s^{-1} and is a first hint on short-term pressure dependent fluctuations of the surface contamination. According to section 6.4.3 only an increase in count rate of (0.35 ± 0.02) s^{-1} at a tritium partial pressure of 10^{-3} mbar would be expected due to the activity in the gas column between the sample and the X-ray transparent window.

In run 27 the average count rate during the exposure phase is (8.32 ± 0.11) s^{-1}. The background before exposure is (7.01 ± 0.09) s^{-1} and after exposure (6.96 ± 0.07) s^{-1}. Resulting in a count rate difference between (1.31 ± 0.14) s^{-1} and (1.36 ± 0.16) s^{-1} which corresponds to the result from run 01 within uncertainty.

Taking into account the background before and after exposure and the count rate fraction due to the activity in the gas column, the count rate during exposure phase is ≈ 1 s^{-1} higher than expected in both runs. A more precise measurement of short-term fluctuations in the surface activity due to tritium partial pressure increase would need a stabilized gas source which is discussed in section 6.6.1.

6.5.5. Investigation of decontamination methods

Decontamination runs were performed after each measurement campaign. Different methods have been used to reduce surface contaminations in the sample chamber

1. continuous evacuation,

2. air exposure and subsequent evacuation and

3. air exposure and subsequent evacuation with bake-out.

The level of decontamination which could be achieved with each method is discussed in the following.
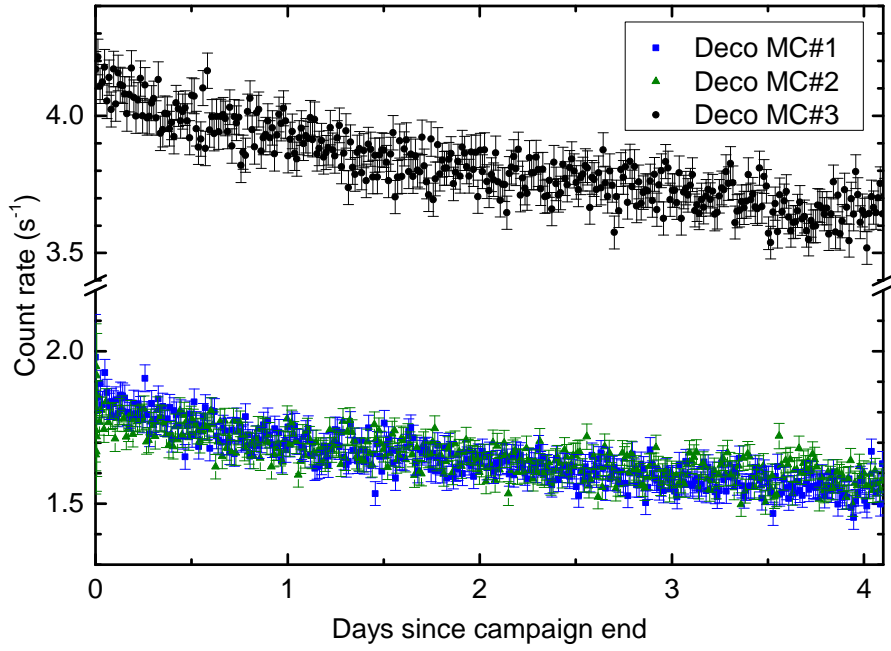
Figure 6.29.: BIXS count rate decrease due to evacuation of the sample chamber. Count rate measurements were performed for four consecutive days after the final pressure rise test of each run. The pressure in the sample chamber was below 10^{-8} mbar during the measurements. Error bars indicating 1σ statistical uncertainty.
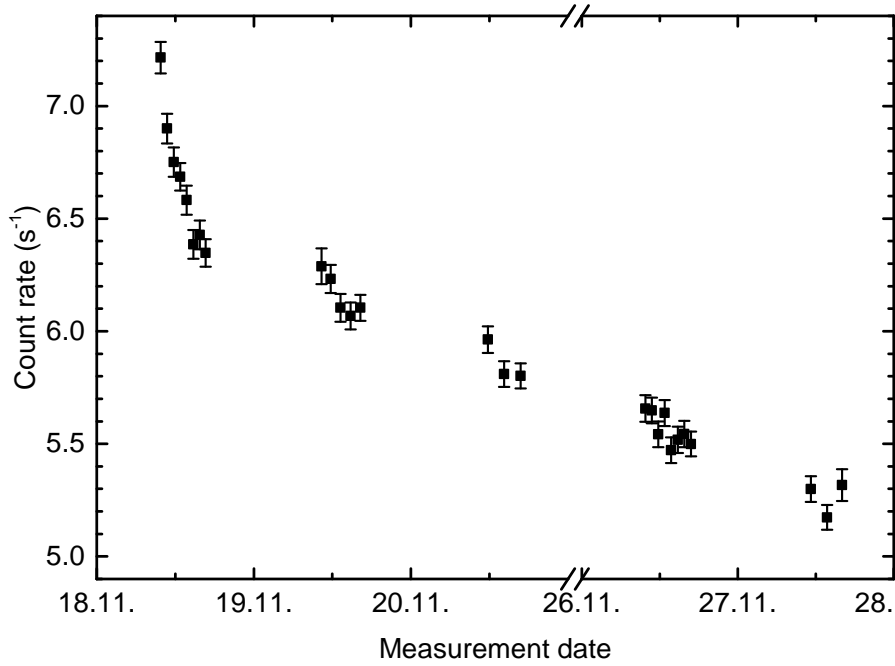
Figure 6.30.: BIXS count rate decrease due to exposure of the sample chamber to atmospheric air. Exposure pressures and exposure durations are listed in table 6.4. A total number of 27 decontamination runs were performed after MC#4.2. The count rate measurements were done for $(1000\ldots2000)\,\mathrm{s}^{-1}$ in each run and the 1σ error bars indicate statistical errors.

Table 6.6.: BIXS count rate results of the decontamination measurements by air exposure and bake-out. Bake-outs were performed overnight after exposure and subsequent evacuation of the sample chamber. The exposure duration was varied between 30 min and 120 min and the exposure pressure between 42 mbar and 1000 mbar. The bake-out temperature was $(195 \pm 5)°$C.

Run	Date	Duration	Pressure	Count rate	Bake-out
#		(min)	(mbar)	(s^{-1})	(yes/no)
$1 \ldots 8$	18.11.14	30	42	$7.21 \pm 0.07 \ldots 6.35 \pm 0.06$	no
$9 \ldots 13$	19.11.14	60	43	$6.29 \pm 0.08 \ldots 6.10 \pm 0.06$	no
$14 \ldots 16$	20.11.14	120	43	$5.96 \pm 0.06 \ldots 5.80 \pm 0.06$	no
$17 \ldots 24$	26.11.14	30	229	$5.66 \pm 0.06 \ldots 5.50 \pm 0.06$	no
$25 \ldots 27$	27.11.14	120	228	$5.30 \pm 0.06 \ldots 5.32 \pm 0.07$	no
28	01.12.14	40	225	(5.04 ± 0.05)	no
29	02.12.14	40	233	(4.30 ± 0.05)	yes
30	03.12.14	40	755	(3.69 ± 0.05)	yes
31	04.12.14	40	1000	(3.69 ± 0.04)	yes
32	05.12.14	40	1000	(3.41 ± 0.04)	yes
33	08.12.14	40	1000	(3.36 ± 0.04)	yes

The simplest method is continuous evacuation which was performed after end of MC#1, MC#2 and MC#3 for four consecutive days. In figure 6.29 a constant decrease of the BIXS count rate is identifiable for each run. The pressure in the sample chamber was below 10^{-8} mbar during all measurements. In the first two decontamination runs the BIXS count rate is reduced by about 10% after four days of pumping. Both measurement runs starting at similar count rate levels. The decontamination run after MC#3 starts at a higher level due to the increased exposure pressure (see table 6.4) of $1 \cdot 10^{-3}$ mbar compared to $5 \cdot 10^{-5}$ mbar in MC#1 and MC#2. The decrease in count rate of about 10% during the four days of evacuation is comparable to the other runs. A more effective decontamination method is air exposure and subsequent evacuation. Due to the atmospheric humidity isotope exchange reaction as H_2O to HTO can promote decontamination. In figure 6.30 the results of 27 decontamination runs are shown which were performed within nine days after MC#4.2. In each run the sample chamber was exposed to atmospheric air with different pressures and exposure durations. In the 27 decontamination runs the count rate level dropped from $(7.21 \pm 0.07)\,s^{-1}$ to $(5.32 \pm 0.07)\,s^{-1}$ which is a decrease of about 26% in count rate. Compared to decontamination by continuous evacuation, a count rate drop of about 10% was already achieved during one day of constant pumping. The parameters of the decontamination runs as exposure pressure and exposure duration are listed in table 6.6.

During decontamination runs $25 \ldots 27$ no count rate decrease could be measured. The count rate decrease between run 27 and run 28 is expected to be mainly due to continuous

evacuation for the four days between the runs. Five additional decontamination runs with subsequent bake-outs at $(195 \pm 5)^\circ$C were performed. Bake-out phases were overnight except for run 33 where the bake-out lasted for 3 days. Before bake-out the system was exposed to atmospheric air with different exposure pressures as listed in table 6.6. The count rate could be reduced from $(5.04 \pm 0.05)\,\mathrm{s}^{-1}$ to $(3.36 \pm 0.04)\,\mathrm{s}^{-1}$ corresponding to a decrease of about 33% during one week of decontamination. Taking into account that previous decontamination runs already decreased the surface activity in the sample chamber this is the most effective method.

In total three weeks of decontamination with all three methods are not enough to completely restore the background at the beginning of MC#4.1 of $(2.06 \pm 0.04)\,\mathrm{s}^{-1}$. Further decontamination is necessary with probably longer bake-out times, continuous purge gas streams or alternative methods of decontamination as discussed in the next section.

6.6. Discussion of the results and outlook

TRIADE is a versatile instrument for the investigation of tritium adsorption and absorption of different sample materials. This is of relevance in tritium closed loop systems as it is in fusion technology or in KATRIN. The discussion of the results is therefore divided in three parts with regard to the performance of the TRIADE experiment, the tritium measurement results for gold coated beryllium sample which was investigated and the implications for the KATRIN experiment.

6.6.1. Performance of TRIADE

TRIADE is designed to measure tritium adsorption, absorption and desorption with a detection limit of less than one monolayer equivalent by BIXS. Therefore, the geometry is designed in a way that tritium surface contamination become the dominant source for Bremsstrahlung production. A low-noise silicon drift detector is used to measure these X-rays.

Monte Carlo simulations with Geant4.9.6p02 (see section 6.4) demonstrating that sub-monolayer sensitivity can easily be reached. One monolayer of tritium on all inner gold coated surfaces of the sample chamber would cause a detector count rate of $(57.6 \pm 1.9)\,\mathrm{s}^{-1}$ assuming an adsorption site density of $1.56 \cdot 10^{15}\,\mathrm{1/cm}^2$ ($\mathrm{N}_{\mathrm{Ads}}^{\mathrm{ML}}(111)$, see appendix A.1) and a ideal plane surfaces. Comparing this to the intrinsic detector background of $(4.11 \pm 0.13) \cdot 10^{-3}\,\mathrm{s}^{-1}$ shows the sub-monolayer sensitivity of the system.

Nevertheless, simulations also show that measured count rates can only be used for calculation of upper limits for tritium adsorption. Tritium absorbed in the first 100 nm of the gold coating can also cause detectable X-rays with comparable detection efficiencies as for adsorbed tritium. Solely the time response of the detector count rate on tritium partial pressure changes can give hints on the actual source. This is part of future investigations.

First tritium measurements with a gold coated beryllium sample and exposure pressures of $5 \cdot 10^{-5}$ mbar (N_2 calibrated) cause surface contamination which is detectable with

TRIADE setup. Detector count rates between $0.8\,\mathrm{s}^{-1}$ and $1.9\,\mathrm{s}^{-1}$ which were measured in MC#1 are already two orders of magnitude above the intrinsic detector background. Repeated measurements show a reproducible count rate progression during the measurement campaigns but with varying background signals.

The main uncertainties of the TRIADE results are due to

1. uncertainties on the detection efficiencies due geometric tolerances of the setup,

2. uncertainties on the detection efficiencies due differences in the low-energy physics packages,

3. different sources of background within the setup besides the sample and the X-ray window surface,

4. a missing precise and accurate gas correction factor for tritium for the ionization vacuum gauge MKS903,

5. limited statistical significance because of count rates below 10 s^{-1} and rather short measurement times of 10 s/100 s and

6. tritium measurements in non-equilibrium mode.

Especially the last three uncertainties can be handled by hardware upgrades of the experimental setups or dedicated experiments. The measured count rate can be improved by using a SDD with a larger active area. Commercially available models have up to $50\ \mathrm{mm}^2$ compared to the $25\ \mathrm{mm}^2$ of the used detector. This can be done without changing the DAQ and the developed data analysis software[14]. In the context of a bachelor thesis[15] it has been shown that the Amptek®DP5 DAQ can be used with SDDs from other manufacturers without significant performance losses.

Tritium measurements in equilibrium mode can be realized by a constant tritium gas flow through the sample chamber. By that, the pressure inside the sample chamber can be stabilized and the tritium purity is also stabilized by the continuous pump-out of desorbed gas species. This needs a tritium compatible flow-controller at the inlet of the sample chamber and a control loop for the flow regulation. Monte Carlo simulations show that tritium adsorption of a monolayer equivalent would dominate the measured X-ray intensity with respect to the activity in the gas column for exposure pressures of at least 10^{-2} mbar (N_2 calibrated).

An accurate and precise determination of the gas correction factor for tritium for the ionization vacuum gauge MKS903 must be done with a dedicated experiment or with the TRIADE setup during a long-time tritium exposure run at pressure of 10^{-3} mbar.

The geometry of the TRIADE setup is already optimized to reduce the influence of other surface contamination than the sample and the X-ray window on the detector count rate. Further improvements can be achieved by shifting the detector several millimeters away from the sample. Monte Carlo simulations show that the uncertainty due to geometrical tolerances of the actual SDD position would be reduced (see section 6.4.5) and it would increase the collimation effect of the X-ray window. This would be further improved

---

[14]   Manuel Klein Masters thesis
[15]   Woo-Jeong Bachelor thesis

by applying an external magnetic field in the axial direction of the sample-SDD. The efficiency of such measures needs further simulations.

6.6.2. Tritium measurement results of the gold coated beryllium sample

In five measurement campaigns tritium surface contamination of gold coated beryllium were investigated to answer four questions.

- Does tritium adsorb/absorb in significant amounts on/in gold coated beryllium at room temperature?

- What is the expected saturation coverage for tritium adsorption on gold?

- How much time is needed to reach a saturation coverage?

- What are effective decontamination strategies?

Does tritium adsorb/absorb in significant amounts on/in gold coated beryllium at room temperature?
The answer to this question is yes. In all five measurement campaigns detector count rates between $0.5\,\mathrm{s}^{-1}$ and $7\,\mathrm{s}^{-1}$ were measured which is clearly above the background. Due to the measurement principle it cannot be distinguished whether it is caused by tritium adsorbed on the surface or dissolved in the gold coating. Nevertheless, a monolayer equivalent for tritium adsorption during the measurements can be calculated from the detections efficiencies calculated in section 6.4. The following assumptions are used:

- all tritium is on the surface no absorption processes occur,

- all gold coated surfaces in sample chamber showing the same adsorption behavior and

- the gold surfaces are ideal (100) or (111) planes without any surface defects.

From the detector count rate measured in the last measurement run an equivalent of (0.122 ± 0.004) monolayer for a (111) surface and an equivalent of (0.316 ± 0.011) monolayer for a (100) surface can be calculated. Unconsidered surface defects and tritium absorption would further reduce these numbers. Adsorption site densities for (111) and (100) gold surfaces are calculated in section A.1. Even in the last measurements the count rate was still increasing in each run. Therefore, these numbers are not regarded as upper limits.

What is the expected saturation coverage for tritium adsorption on gold?
In repeated measurement runs it was tried to find a hint for a saturation effect of the surface contamination. For higher exposure pressures of $1 \cdot 10^{-3}\,\mathrm{mbar}$ (N_2 calibrated) an exponential like behavior of the detector count rates were found. Strongly bound tritium stays on/in the gold coating even after several hours of evacuation. The amount of surface activity is increasing during the course of the measurement campaigns. This effect is normally referred as memory effect. The fit results for the detector count rate as a function of measurement runs in MC#4.2 implies an upper limit of $(8.2 \pm 0.7)\,\mathrm{s}^{-1}$

in the detector count rate. Using the same assumptions as before this corresponds to an upper limit of of (0.142 ± 0.013) monolayer for a (111) surface and an equivalent of (0.370 ± 0.034) monolayer for a (100) surface.

As to the varying pressure conditions during the exposure phases the detector count rate was also plotted as a function of dosage $p \cdot t$. The best working fit model for this was a combination of a linear and an exponential model. Tritium absorption in the gold coating can explain the linear term. For the exponential term a maximum count rate of $(1.83 \pm 0.07)\,\mathrm{s}^{-1}$ was calculated. This corresponds to to an upper limit of of (0.032 ± 0.002) monolayer for a (111) surface and an equivalent of (0.083 ± 0.004) monolayer for a (100) surface.

Also short-time fluctuations of the surface contamination have been found which strongly depend on the pressure. This is due to weakly bound tritium and is not correlated to the memory effect. The increase in detector count rate is $\approx 1\,\mathrm{s}^{-1}$ which corresponds to to an upper limit of ≈ 0.02 monolayer for a (111) surface and an equivalent of ≈ 0.05 monolayer for a (100) surface.

How much time is needed to reach a saturation coverage?
For long-term surface contaminations which are related to the memory effect the time needed to reach a saturation coverage can be calculated from the exponential part of the fit model. The calculated time constant (see equation 6.19) in units of dosage is $(4.3 \pm 0.4) \cdot 10^{-4}$ mbar hour (N_2 calibrated). At an exposure pressure of $1 \cdot 10^{-3}$ mbar (N_2 calibrated) 99.3% of the saturation coverage are reached in an exposure time of about 2.2 hours.

The previous mentioned short-term contaminations follow the pressure within the measurement interval of the X-ray detector. That means the saturation is reached within about $30\,\mathrm{s}^{-1}$ at a pressure of $1 \cdot 10^{-3}$ mbar (N_2 calibrated).

What are effective decontamination strategies? Three decontamination methods have been tested and all of them showed a significant effect on the surface contamination. Evacuation without any other measures showed the slightest effect. A combined decontamination procedure with air exposure and consecutive bake-out was the most effective one. Nevertheless, even after three weeks of decontamination the background at the beginning of MC#4.1 could not be restored.

More time is needed for decontamination to completely restore the background or more effective decontamination strategies must be found. Another method which will be tested in TRIADE in the near future is decontamination by a UV-light desorption system.

6.6.3. Implications for KATRIN

The TRIADE measurements show that tritium surface contamination on the X-ray transparent windows and on the *rear wall* will occur. Thereby two contributions must be distinguished according to the performed measurements. There are strongly bound tritium surface contaminations which are known as memory effect. These contaminations strongly depend upon the applied dosage and remain on the surface or in the bulk even in case of strong pressure drops. Elaborate and time consuming measures are necessary

for an effective decontamination. Weakly bound tritium surface contaminations, which are indicated by TRIADE measurements, strongly depend upon the pressure and show a fast time response in the order of $\leqslant 10$ s at tritium partial pressures in the range of 10^{-3} mbar.

In the memory effect measurements an exponential and a linear fit model was used to describe the correlation between the measured count rate and the dosage. The saturation count rate of the exponential term was calculated to be $(8.2 \pm 0.7)\,\text{s}^{-1}$ and was reached after a total dosage of $(2.2 \pm 0.2) \cdot 10^{-3}$ mbar hour ($5 \cdot \tau_D$, N_2 calibrated). Using the calculated detection efficiencies of TRIADE and KATRIN, the expected background count rate of the KATRIN BIXS system due to surface contaminations on the X-ray transparent window is $(7.9 \pm 0.8)\,\text{s}^{-1}$. It is in the range of ≈ 0.1 % of the projected detector count rate under normal KATRIN operation. Assuming a pressure of 10^{-5} mbar in front of the X-ray transparent window and using the calculated gas correction factor in appendix A.15, the saturation value is reached after (15.5 ± 1.6) days of KATRIN operation.

The linear term was determined with $C_{D,\text{lin.}} = (745.7 \pm 24.9)\,\text{s}^{-1}/\text{mbar h}$. Using the same assumptions as before this would result in a background count rate increase of the KATRIN BIXS system of $(0.10 \pm 0.01)\,\text{s}^{-1}/\text{day}$. After 60 days of KATRIN operation this would be about 0.1 % of the projected count rate.

The background contribution due to the linear term is easy to handle during KATRIN operation. Background measurements before and after each measurement campaign can be done and the measured count rate of the X-ray detectors can be accordingly corrected. However, the exponential term can be problematic if there is a decontamination procedure of the *rear wall* and the X-ray transparent windows after each measurement campaign. If this cannot be avoided due to other KATRIN restrictions, regular background measurements during the measurement campaigns of KATRIN are necessary to reach a 0.1 % sensitivity. Short term fluctuations of the tritium surface contamination are expected to have a minor influence on the background count rate of the KATRIN BIXS system. In the TRIADE measurements, no short term fluctuation have been observed at pressures of $5 \cdot 10^{-5}$ mbar.

All count rate calculations so far were made for tritium surface contaminations on the X-ray transparent windows of the KATRIN BIXS system. This was justified by the Monte Carlo simulations for the detection efficiencies in chapter 5. They showed that surface contaminations on the X-ray transparent windows are dominant in terms of background count rate, compared to the surface contamination on the *rear wall*. This is only true, when assuming the same amount of surface contamination in Bq/cm^2 for all surfaces. However, the surface contamination on the KATRIN *rear wall* is expected to be higher due to the magnetic guiding of T^+-ions from the WGTS to the *rear wall* surface. To study these effects, TRIADE would need a hardware upgrade to apply a magnetic guiding field.

7. Summary and outlook

The context of this thesis was the development of tritium analytical tools, based on the BIXS (**B**eta **I**nduced **X**-ray **S**pectrometry) method, for the closed KATRIN loop at TLK (**T**ritium **L**aboratory **K**arlsruhe). KATRIN (**Ka**rlsruhe **Tri**tium **N**eutrino Experiment) is a next generation neutrino mass experiment which aims for the model-independent measurement of the electron antineutrino mass with a sensitivity of 0.2 eV/c^2 (after three years measurement time, 90 % C.L.). The measurement principle is based on the determination of the shape of the tritium β-spectrum in the endpoint region. Since only a small fraction of β-electrons is in the endpoint region, a high intensity tritium source is needed for KATRIN. Variations of the source intensity during the measurements would increase the systematic uncertainty on the neutrino mass. Therefore, the activity inside the tritium source must be stabilized and monitored on the 0.1 % level. The in-situ activity monitoring shall be done by a BIXS system.

Variations of the tritium purity inside the source also lead to systematic uncertainties on the neutrino mass. Therefore, the tritium gas stream through the KATRIN tritium source is continuously monitored and impurities are removed. Due to the high tritium throughput of 40 g/day this needs a large amount of infrastructure for exhaust gas processing. It is done by the KATRIN inner and outer loop which is part of the TLK. Processing of such high tritium throughputs creates also new requirements regarding tritium process monitoring. Conventional methods as calorimetry, gas chromatography and ionization chambers have strong disadvantages regarding measurement time, in-situ capability or measurement precision/accuracy. Furthermore, there is an analytical gap in the pressure range between 10^{-4} mbar and 10^2 mbar. A process monitoring tool based on BIXS could help to overcome some of the disadvantages of standard monitoring tools.

A common problem of tritium analytical systems for the measurement of gaseous tritium (including BIXS) is the so-called memory effect, a history dependent background signal. During exposure, tritium is adsorbed on the inner surfaces of the monitoring system and absorbed in the wall material. This causes an increasing background signal which can make the monitoring system blind for activity changes in the gas stream. To improve existing tritium analytical systems an experimental facility is needed to study in-situ surface contamination under tritium exposure in a wide pressure and temperature range.

Consequently, the three task which were focused in this work are

1. the design and construction of a tritium process monitor and accountancy tool according to the requirements in section 2.2.1 and first characterization measurements with tritium,

2. a benchmark of the potential performance of the designed high stability activity monitor of the KATRIN tritium source by Monte Carlo simulations and

3. the design and construction of an instrument for the in-situ investigation of surface contaminations of arbitrary solid sample materials and first tritium measurements with a gold coated sample.

Monte Carlo simulation results were used for the design of a compact tritium process monitor for measurement of gaseous tritium in a process gas stream. The focus was put on compactness and the use of standard components (due to availability and cost considerations). Furthermore, a high sensitivity and a low gas-species dependency was required. As a result the TRACE system was designed and constructed and first characterization measurements were performed. The system was successfully calibrated and a minimum detectable activity of 0.16 MBq in a sample volume of 26 cm^3 was determined. It is able to monitor traces of tritium (10 ppm) in a helium process gas stream with 5 % statistical uncertainty in a measurement time of $\approx$ 180 s. It also shows a good stability and is able to fill the analytical gap for pressure ranges between 10^{-4} mbar and 10^2 mbar. An improved accuracy of the system could be achieved by a careful cross calibration with a calorimeter. This is one of the tasks which will be done with the TRACE system in the near future.

The ability of BIXS tools for in-situ high stability activity monitoring also qualifies this method for KATRIN. KATRIN requires stability monitoring of the activity in the WGTS on the 0.1 % level in measurement times below 1000 s. Monte Carlo simulation results show that the projected count rate of the X-ray detectors will be high enough to achieve a statistical uncertainty of $\leqslant$ 0.1 % in $\leqslant$ 70 s of measurement time during normal KATRIN operation. This fully complies the KATRIN requirements regarding the measurement time. Backscattering effects of β-electrons from and subsequent back-reflection to the *rear wall*, due to the KATRIN retarding potential and magnetic mirroring, are not included in this calculation. This will further increase the count rate and decrease the necessary measurement time. Monte Carlo results which account for multiple backscattering will need about four times the already spent computing time. An approximation for the additional count rate contribution due to once backscattered and back-reflected β-electrons, based on existing Monte Carlo results, is given and is in the order of $\approx$ 34 %.

Systematic uncertainties regarding the measured activity inside the WGTS will arise especially due to tritium surface contamination on the *rear wall* and on the X-ray transparent windows of the BIXS system. This will cause an increasing history dependent background signal. To quantify these effects an unique experimental facility was designed and constructed in the context of this work. With the TRIADE experiment in-situ measurements of tritium surface contamination of arbitrary solid samples in a temperature range of $-100°$C to $200°$C and pressure range of 10^{-9} mbar to 1000 mbar are possible. First tritium measurements with a gold coated sample were performed at total pressures of $5 \cdot 10^{-5}$ mbar and 10^{-3} mbar. A memory effect was observed in the tritium measurements and the anticipated influence on the KATRIN BIXS system was calculated by using the Monte Carlo results for the detection efficiencies of the TRIADE system and the KATRIN BIXS system. The results show that the BIXS system of KATRIN can achieve the aimed 0.1 % sensitivity level. In the first tritium measurements it will need about 15 days to reach a saturation level for the exponential-like behavior of the tritium

surface contamination. The linear like increase of the background signal is expected to reach the 0.1 % level after 60 days of measurement time but can easily be corrected by background measurements before and after each tritium run. Further TRIADE measurement runs with other samples must be performed to quantify the level of reproducibility. Tritium measurements with stainless steel samples will help to quantify the KATRIN tritium inventory. This is especially important in case of maintenance measures for tritium related parts of KATRIN. Additional hardware upgrades of TRIADE are planned to decrease systematic uncertainties and to reproduce a more KATRIN-like behavior. This is of particular interest for the determination of the expected amount of tritium on the KATRIN *rear wall*.

The results of this thesis clearly show that BIXS is a promising method for future needs in tritium technology. It can provide very compact and precise tritium analytics for in-situ activity measurements. Due to the low-noise silicon drift detector technology used for the BIXS systems in this work, the BIXS method has the potential to become even more sensitive than it already is. At present, the sensitivity of BIXS systems is limited by the memory effect and not by the intrinsic background of the used detector technology. Alternative coatings could help to overcome this problem and further increase the sensitivity. With the TRIADE experimental facility, for the first time there is a possibility to study surface contamination effects in-situ on arbitrary solid samples in a wide pressure and temperature range.

A. Appendix

A.1. Estimation of the activity of one monolayer of tritium on an ideal gold surface

It is assumed that for gold atom on the surface one tritium atom can adsorb. The number of surface sites is estimated based on the density of gold and the molar mass. It is calculated according to:

$$\rho \quad = \quad n \cdot \frac{A_{\text{Au}} \cdot u}{a^3} \tag{A.1}$$

$$a^2 \quad = \quad \left(\sqrt[3]{n \cdot \frac{A_{\text{Au}} \cdot u}{\rho}} \right)^2 = 1.661357 \cdot 10^{-15} \tag{A.2}$$

$$N_{\text{Ads}}^{\text{ML}}(100) \quad \approx \quad \frac{1}{a^2} = 0.60 \cdot 10^{15} \, \frac{\text{adsorption sites}}{\text{cm}^2} \tag{A.3}$$

$$N_{\text{Ads}}^{\text{ML}}(111) \quad \approx \quad \frac{2}{\sqrt{3}a^2} \cdot \frac{9}{4} = 1.56 \cdot 10^{15} \, \frac{\text{adsorption sites}}{\text{cm}^2} \tag{A.4}$$

With the atomic mass unit $u = 1.669539 \cdot 10^{-27}$ kg, the relative atomic mass of gold $A_{\text{Au}} = 196.966569 \, u$, the density of gold $\rho = 19.32$ kg/cm^2 and the number of atoms per unit cell $n = 4$. The calculated number a is the lattice constant. $N_{\text{Ads}}^{\text{ML}}$ is the number of adsorption cites per square centimeter and is calculated for the (100) and (111) surface plane. The activity per surface area is calculated according to:

$$A^{\text{ML}} \quad = \quad \frac{\ln 2}{T_{1/2}} \cdot N_{\text{Ads}}^{\text{ML}} = \frac{\ln 2}{12.32 \text{ years}} \cdot N_{\text{Ads}}^{\text{ML}} \tag{A.5}$$

$$A^{\text{ML}}(100) \quad = \quad 1.07 \cdot 10^6 \, \frac{\text{Bq}}{\text{cm}^2} \tag{A.6}$$

$$A^{\text{ML}}(111) \quad = \quad 2.78 \cdot 10^6 \, \frac{\text{Bq}}{\text{cm}^2} \tag{A.7}$$

$T_{1/2}$ is the tritium half-life time and A^{ML} the surface activity of one monolayer of tritium per square centimeter on an ideal gold surface plane in (100) or (111) configuration.

A.2. Siegbahn notation

Table A.1.: Selected atomic electronic transitions and characteristic X-ray lines in Siegbahn notation, IUPAC notation and corresponding quantum numbers.

Siegbahn notation	IUPAC notation	n	l	j
K_{α_1}	$K - L_3$	2	1	1/2
		1	0	3/2
K_{α_2}	$K - L_2$	2	1	1/2
		1	0	1/2
K_{β_1}	$K - M_3$	3	1	1/2
		0	0	3/2
K_{β_3}	$K - M_2$	3	1	1/2
		1	0	1/2
L_{α_1}	$L_3 - M_5$	3	2	5/2
		2	1	3/2
L_{α_2}	$L_3 - M_4$	3	2	3/2
		2	1	3/2
L_{β_1}	$L_2 - M_4$	3	2	3/2
		2	1	1/2
L_{β_2}	$L_3 - N_5$	4	3	5/2
		2	1	3/2

A.3. Detector parameters of the TRACE X-ray detector

«DP5 CONFIGURATION»
RESC=?; Reset Configuration
CLCK=80; 20MHz/80MHz
TPEA=3.200; Peaking Time
GAIF=0.9067;
GAIN=59.990; Total Gain (Analog * Fine)
RESL=3276; Detector Reset Lockout
TFLA=0.200; Flat Top
TPFA=400; Fast Channel Peaking Time
PURE=ON; PUR Interval On/Off
RTDE=OFF; RTD On/Off
MCAS=NORM; MCA Source
MCAC=8192; MCA/MCS Channels
SOFF=OFF; Set Spectrum Offset
AINP=POS; Analog Input Pos/Neg
INOF=DEF; Input Offset
GAIA=15;
CUSP=0; Non-Trapezoidal Shaping
PDMD=NORM; Peak Detect Mode (Min/Max)
THSL=7.006; Slow Threshold
TLLD=OFF; LLD Threshold
THFA=188.81; Fast Threshold
DACO=OFF; DAC Output
DACF=0; DAC Offset
RTDS=0; RTD Sensitivity
RTDT=0.00; RTD Threshold
BLRM=1; BLR Mode
BLRD=3; BLR Down Correction
BLRU=0; BLR Up Correction
GATE=OFF; Gate Control
AUO1=ICR; AUX OUT Selection
PRET=OFF; Preset Time
PRER=OFF; Preset Real Time

PREC=OFF; Preset Counts
PRCL=0; Preset Counts Low Threshold
PRCH=0; Preset Counts High Threshold
HVSE=-140; HV Set
TECS=240; TEC Set
PAPS=ON; Preamp 8.5/5 (N/A)
SCOE=RI; Scope Trigger Edge
SCOT=87; Scope Trigger Position
SCOG=1; Digital Scope Gain
MCSL=0; MCS Low Threshold
MCSH=0; MCS High Threshold
MCST=0.00; MCS Timebase
AUO2=ICR; AUX OUT2 Selection
TPMO=OFF; Test Pulser On/Off
GPED=FA; G.P. Counter Edge
GPIN=AUX1; G.P. Counter Input
GPME=OFF;
GPGA=OFF;
GPMC=OFF;
MCAE=OFF; MCA/MCS Enable
BOOT=ON; Turn Supplies On At Power Up
«DP5 CONFIGURATION END»
«DPP STATUS»
Device Type: DP5
Serial Number: 11937
Firmware: 6.06
FPGA: 6.01
HV Volt: -141V
TEC Temp: 239K
Board Temp: 42°C
«DPP STATUS END»

A.4. Energy calibration and intrinsic detector background of the TRACE X-ray detector
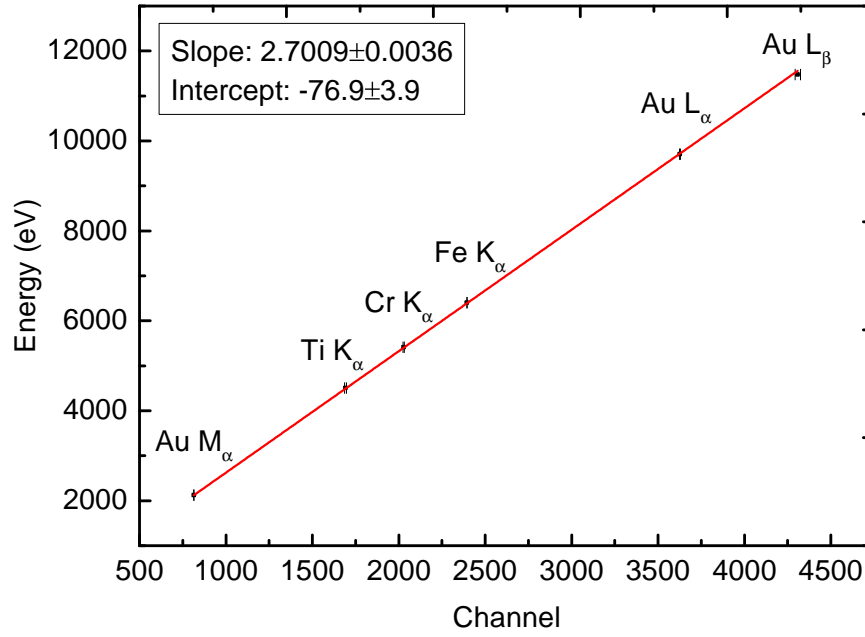
Figure A.1.: In-situ energy calibration of the TRACE X-ray detector with a BIXS-spectrum.
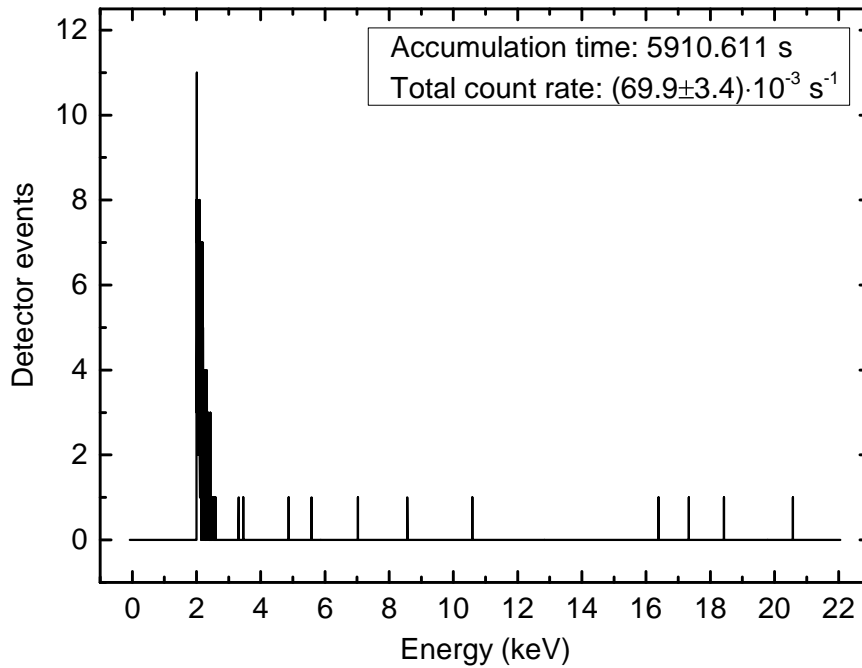
Figure A.2.: Noise characteristics of the TRACE X-ray detector.

A.5. Calculation of the TRACE detection efficiency

The detection efficiency can be calculated from the measured integral count rate dN/dt, total pressure p_{tot} and tritium purity ϵ_{T_2} according to

$$\text{DE} \quad = \quad \frac{\frac{dN}{dt}}{A} = \frac{\frac{dN}{dt}}{\frac{2\ln 2}{T_{1/2}} \cdot N_{\text{T,atoms}}} = \frac{\frac{dN}{dt}}{\frac{2\ln 2}{T_{1/2}} \cdot \epsilon_{\text{T}_2} \cdot \frac{p_{\text{tot}}V}{k_{\text{B}}T}} \tag{A.8}$$

where A is the activity in the sample cell, $T_{1/2}$ the half-life of tritium, $N_{\text{T,atoms}}$ the number of tritium atoms, ϵ_{T_2} the tritium purity, V the sample cell volume, k_{B} the Boltzmann constant, T the temperature.

A.6. Mechanical dimensions of the X-ray detector of TRACE

Figure A.3.: Mechanical dimensions of the Amptek® AXR X-ray detector. Picture provided by Amptek®.

A.7. Datasheet pressure sensor MKS902

Specifications and Ordering Information

Dimensions

Flange	A
NW 16 KF	2.26/(57)
4 (1/4") VCR®-F *	2.59/(66)
8 (1/2") VCR®-F *	2.93/(74)

Dimensions: in (mm)

Pinout

PIN 1   PIN 5
PIN 6   PIN 9

Series 902 Digital	Series 902 Analog
1 - Relay NO	1 - Relay NO
2 - Relay NC	2 - Relay NC
3 - Power (+)	3 - Power (+)
4 - Power (-)	4 - Power (-)
5 - Analog Output (+)	5 - Analog Output (+)
6 - Relay Common	6 - Relay Common
7 - RS485 (-) / RS232 TXD	7 - Relay Disable
8 - Analog Output (-)	8 - Analog Output (-)
9 - RS485 (+) / RS232 RXD	9 - Relay Setpoint Voltage

Specifications

Full Scale Range (absolute)	1,000 Torr
Set Point Range	1 to 1,000 Torr
Accuracy (including non-linearity, hysteresis, and non-repeatability)	< 1% of reading
Temperature Coefficients	
Zero	0.02% of F.S./°C
Span	0.02% of F.S./°C
Resolution	1×10^{-4} of F.S.
Calibration Gas	Gas independent
Operating Temperature Range	0° to 50°C (32° to 122°F)
Maximum Bakeout Temperature	85°C (185°F), non-operating
Communication	RS485 / RS232 / Analog
Controls	Zero adjust, span adjust, analog output, pressure units, baud rate, address, factory default, setpoint functions: value, hysteresis, direction, enable
Status	Absolute and differential pressure reading, units, setpoint, operating time, transducer temperature, user tag, model, device type, serial number, firmware and hardware versions
Analog Output (Absolute Pressure)	0 to 5 or 0 to 10 VDC, 1 K maximum output impedance linear or logarithmic
Relay	1 relay SPDT
Relay Contact Rating	1 A @ 30VAC/DC, resistive
Relay Response	50 msec maximum
Power Requirements	12 to 30 VDC, 30 mA, <.5 W max
Accuracy	<1% of reading
Repeatability	± 0.03% of full scale
Overpressure Limit	2,000 Torr
Installation Orientation	Any
Internal Volume	0.21 in.³ (3.4 cm³)
Materials Exposed to Vacuum	304, 316 Stainless Steel
Electronic Casing	304 Stainless Steel, Aluminum
Weight (with KF Flange)	3.4 oz (97 g)
CE Certification	EMC Directive 89/336/EEC

Ordering Information:

Part Number	Description	Price
902-1112	Series 902 Transducer, NW 16 KF, RS485	
902-1212	Series 902 Transducer, 4 VCR®-F*, RS485	
902-1312	Series 902 Transducer, 8 VCR®-F*, RS485	
902-1113	Series 902 Transducer, NW 16 KF, RS232	
902-1213	Series 902 Transducer, 4 VCR®-F*, RS232	
902-1313	Series 902 Transducer, 8 VCR®-F*, RS232	
902-1105	Series 902 Transducer, NW 16 KF, 0-10V	
902-1205	Series 902 Transducer, 4 VCR®-F*, 0-10V	
902-1305	Series 902 Transducer, 8 VCR®-F*, 0-10V	
902001	Series 902 LED Display (Torr)	
902002	Series 902 LCD Display (Torr)	
100011739	Series 902 product manual	

mks Technology for Productivity
HPS® Products

MKS Global Headquarters
2 Tech Drive, Suite 201
Andover, MA 01810
Tel: (978) 645.5500
Tel: (800) 227.8766 (in USA)
Web: www.mksinst.com
Email: mks@mksinst.com

MKS Vacuum Technology
HPS® Products
5330 Sterling Drive
Boulder, CO 80301
Tel: (303) 449.9861
Tel: (800) 345.1967 (in USA)

MKS Denmark ApS
Ndr. Strandvej 119G
DK-3150 Hellebaek
Denmark
Tel: +45 4492 9299
Email: mksdenmark@mksinst.com

MKS products provided subject to the US Export Regulations. Diversion or transfer contrary to US law is prohibited.
* VCR®-compatible parts may be used. Specifications and prices are subject to change without notice.
mksinst™ is a trademark and HPS® is a registered trademark of MKS Instruments, Inc. VCR® is a registered trademark of Swagelok® Company.

Figure A.4.: Datasheet pressure sensor MKS902.

A.8. Datasheet pressure sensor MKS626B

Specifications and Ordering Information

Full Scale Ranges	1, 2, 10, 20, 100, 1000 mbar / Torr
Accuracy - % of Reading*	0.25% for 1 to 1000 mbar / Torr, optional 0.15% for 10 to 1000 mbar / Torr
Temperature Coefficients	
Zero	0.005% FS/°C for 10 to 1000 mbar / Torr ranges,
	0.010% FS/°C for 2 mbar / Torr ranges, 0.015% FS/°C for 1 mbar / Torr ranges
Span	0.04% of Reading/°C
Resolution	0.001% of Full Scale
Ambient Operating Temperature	0 to 50°C
Overpressure Limit	45 psia (310 kPa)
Materials Exposed to Gases	Inconel® 600 and 316 SS
Volume	< 7 cm³
Input Power Required for Analogue Version	20.0 – 31.5 VDC @ 100 mA max
Input Power Required for Profibus Version	20.0 – 31.5 VDC @ 200 mA max
Analogue Output Signal	Pressure: 0 to +10 VDC into >10K Ω load
Digital Output Signal (optional)	Profibus DPV1
Regulatory Approvals	CE compliant to ECD Directive 2004/108/EEC**
Restriction of Hazardous Substances	Fully compliant to RoHS Directive 2002-95-EC Fittings
Standard	½" (12.7 mm) OD tube standard
Optional	8 VCR® compatible (female), 8 VCO® compatible (female), NW16-KF, NW25-KF, NW16-CF (rotatable), NW40-CF (rotatable)

*Includes hysteresis, non-linearity, and non-repeatability.
**For CE compliance, the mating connector must be properly grounded.
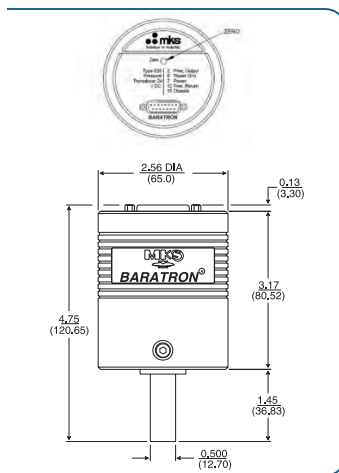
Dimensional Drawing —
Unless otherwise specified, dimensions are nominal values in inches (mm referenced).

Ordering Code Example: 626B13MDE9

	Code		Configuration
Type 626B	**626B**		626B
Full Scale Range (XXX)			
	mbar	**Torr**	
1 mbar / Torr	01M	01T	
2 mbar / Torr	02M	02T	
10 mbar / Torr	11M	11T	
20 mbar / Torr	21M	21T	13M
100 mbar / Torr	12M	12T	
1000 mbar / Torr	13M	13T	
Fittings (Y)			
½" (12.7 mm) OD tube	A		
8 VCR compatible (female)	B		
NW 16 CF, rotatable	C		
NW 16 KF	D		D
8 VCO compatible (female)	E		
NW 25 KF	Q		
NW 40 CF, rotatable	L		
Accuracy (Z)			
0.25% Reading (1 to 1000 mbar / Torr) - standard	E		
0.15% Reading (10 to 1000 mbar / Torr) - optional	D		E
Options			
Standard Configuration (only ± 15VDC input)	(NONE)		
Profibus Interface with 20.0 – 31.5 VDC input and analogue 0 – 10VDC output	4		9
20.0 – 31.5 VDC input / 0 – 10 VDC output	9		

Global Headquarters
2 Tech Drive, Suite 201
Andover, MA 01810-2449
Tel: (978) 645.5500
Tel: (800) 227.8766 within U.S. only
Web: www.mksinst.com

MKS Germany
MKS Instruments Deutschland GmbH
Schatzbogen 43, D-81829 München
Tel: +49 (0) 89 42 00 08 0
Fax: +49 (0) 89 42 41 06
Web: www.mksinst.com

Figure A.5.: Datasheet pressure sensor MKS626.

A.9. Datasheet pressure sensor MKS903

Specifications and Ordering Information

Dimensions

3.0 (76)

5.0 (127)
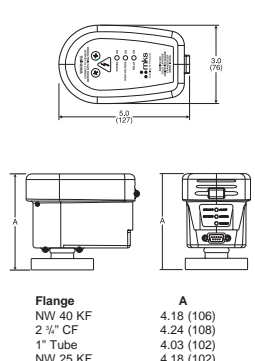
Flange	A
NW 40 KF	4.18 (106)
2 ¾" CF	4.24 (108)
1" Tube	4.03 (102)
NW 25 KF	4.18 (102)

Pinout
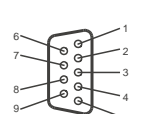
Standard	Alternate
1) Relay - NO	1) HV enable
2) Relay - NC	2) - VIN
3) + VIN	3) Analog Output (+)
4) - VIN	4) + VIN
5) Analog Output (+)	5) no conn
6) Relay - Common	6) no conn
7) Relay - Disable	7) Analog Output (-)
8) Analog Output (-)	8) no conn
9) HV enable	9) Status

Specifications

Measuring Range	3.0×10^{-10} to 5.0×10^{-3} Torr
Set Point Range (Std 903 only)	1.0×10^{-9} to 1.0×10^{-3} Torr
Repeatability	Approx. 5% of reading
Calibration Gas	Air/nitrogen
Operating Temperature Range	0° to 50° C (32° to 122° F)
Maximum Bakeout Temperature	400° C (752° F) without electronics
Relative Humidity	80% maximum for temperatures less than 31° C, decreasing linearly to 50% maximum at 40° C
Relay (Std. 903 only)	1 relay set point
Contact Rating	SPDT, 1 A @ 30 VDC, resistive
Relay Hysteresis	150 mV
Relay Response	< 50 msec (0 to 99%) for Δp from 5.0×10^{-8} to 3.0×10^{-4} Torr
Power Requirements	14 to 30 VDC, 3 Watts max
Output Voltage	30 Ω maximum output impedance
903 (Standard)	1.5 to 8.7 VDC
903 (AP)	0.5 to 7.7 VDC
Installation Orientation	Any
Internal Volume	0.9 in.³ (15.0 cm³) maximum
Materials Exposed to Vacuum	304 and 302 stainless steel, aluminum, Inconel® X-750, glass, alumina ceramic
Display LED Indications	
903 (Standard)	Set point (red), high voltage (yellow), and power (green)
903 (AP)	Vacuum (red), high voltage (yellow), and power (green)
Electronic Casing	ABS plastic, UL94-5V flame rating (with conductive coating)
Weight (with CF Flange)	2.3 lb (1.04 kg)
CE Certification	EMC Directive, General Product Safety Directive

Ordering Information

Part Number	Description
109030001	Series 903 Transducer, NW 40 KF
109030002	Series 903 Transducer, 2 ¾" CF
109030003	Series 903 Transducer, 1" Tube
109030004	Series 903 Transducer, NW 25 KF
104230101	Sensor Rebuild - KF 40
104230102	Sensor Rebuild - 2 ¾" CF
104230103	Sensor Rebuild - 1" Tube
104230104	Sensor Rebuild - KF 25
100002353	Internal Rebuild Kit

mks
Technology for Productivity
Granville-Phillips®

Figure A.6.: Datasheet pressure sensor MKS903.

A.10. Gas correction factors for the ionization vacuum gauge MKS903

Gas	Symbol	Gas Correction Factor
Air	—	1.00
Ammonia	NH3	1.30
Argon	Ar	1.29
Benzene	C6H6	5.90
Bromine	Br2	3.80
Bromomethane	CH3Br	3.70
Carbon Dioxide	CO2	1.42
Carbon Disulfide	CS2	5.00
Carbon Monoxide	CO	1.05
Carbon Tetrachloride	CCl4	6.00
Chlorine	Cl2	0.68
Deuterium	D2	0.35
Helium	He	0.18
Hydrogen	H2	0.46
Hydrogen Chloride	HCl	1.50
Hydrogen Fluoride	HF	1.40
Isobutylene	C4H8	3.60
Krypton	Kr	1.94
Methane	CH4	1.40
Neon	Ne	0.30
Nitric Oxide	NO	1.30
Nitrogen	N2	1.00
Nitrogen Oxide	NO	1.16
Nitrous Oxide	N2O	1.50
Oxygen	O2	1.01
Propane	C3H8	4.20
Sulfur Dioxide	SO2	2.10
Sulfur Hexafluoride	SF6	2.50
Xenon	Xe	2.87

A.11. Mechanical dimensions Amptek X123
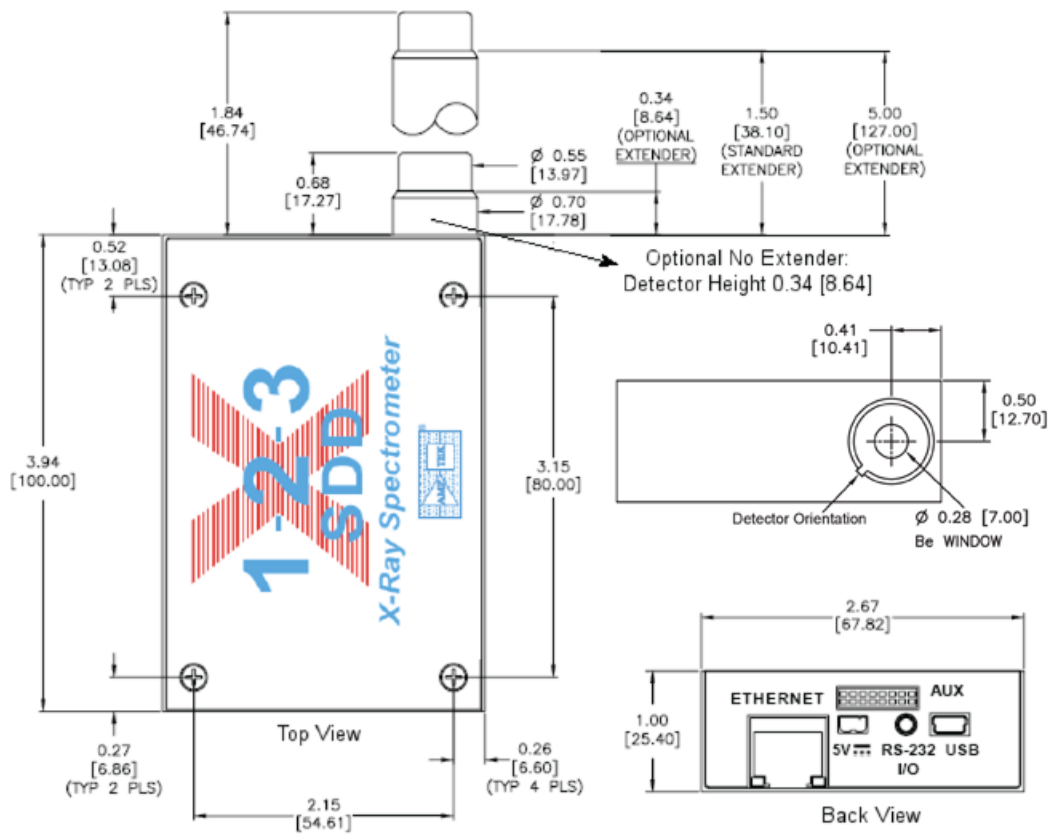
Figure A.7.: Mechanical dimensions Amptek X123. Dimensions in mm.

A.12. Detector parameters of the TRIADE X-ray detector

«DP5 CONFIGURATION»
RESC=?; Reset Configuration
CLCK=80; 20MHz/80MHz
TPEA=11.200; Peaking Time
GAIF=1.0446; Fine Gain
GAIN=69.108; Total Gain (Analog * Fine)
RESL=204; Detector Reset Lockout
TFLA=0.200; Flat Top
TPFA=100; Fast Channel Peaking Time
PURE=ON; PUR Interval On/Off
RTDE=OFF; RTD On/Off
MCAS=NORM; MCA Source
MCAC=8192; MCA/MCS Channels
SOFF=OFF; Set Spectrum Offset
AINP=POS; Analog Input Pos/Neg
INOF=822; Input Offset
GAIA=15;
CUSP=0; Non-Trapezoidal Shaping
PDMD=NORM; Peak Detect Mode (Min/Max)
THSL=0.976; Slow Threshold
TLLD=OFF; LLD Threshold
THFA=56.25; Fast Threshold
DACO=INPUT; DAC Output
DACF=0; DAC Offset
RTDS=0; RTD Sensitivity
RTDT=0.00; RTD Threshold
BLRM=1; BLR Mode
BLRD=3; BLR Down Correction
BLRU=0; BLR Up Correction
GATE=OFF; Gate Control
AUO1=PEAKH; AUX OUT Selection
PRET=OFF; Preset Time
PRER=OFF; Preset Real Time

PREC=OFF; Preset Counts
PRCL=0; Preset Counts Low Threshold
PRCH=0; Preset Counts High Threshold
HVSE=-110; HV Set
TECS=220; TEC Set
PAPS=ON; Preamp 8.5/5 (N/A)
SCOE=RI; Scope Trigger Edge
SCOT=50; Scope Trigger Position
SCOG=4; Digital Scope Gain
MCSL=1; MCS Low Threshold
MCSH=8191; MCS High Threshold
MCST=600.00; MCS Timebase
AUO2=ICR; AUX OUT2 Selection
TPMO=OFF; Test Pulser On/Off
GPED=RI; G.P. Counter Edge
GPIN=AUX1; G.P. Counter Input
GPME=ON;
GPGA=ON;
GPMC=ON;
MCAE=OFF; MCA/MCS Enable
BOOT=ON; Turn Supplies On At Power Up
«DP5 CONFIGURATION END»
«DPP STATUS»
Device Type: DP5
Serial Number: 11120
Firmware: 6.06 Build: 5
FPGA: 5.13
HV Volt: -112V
TEC Temp: 227K
Board Temp: 40°C
«DPP STATUS END»

A.13. Datasheet MKS Microvision Plus

Dimensional Drawing
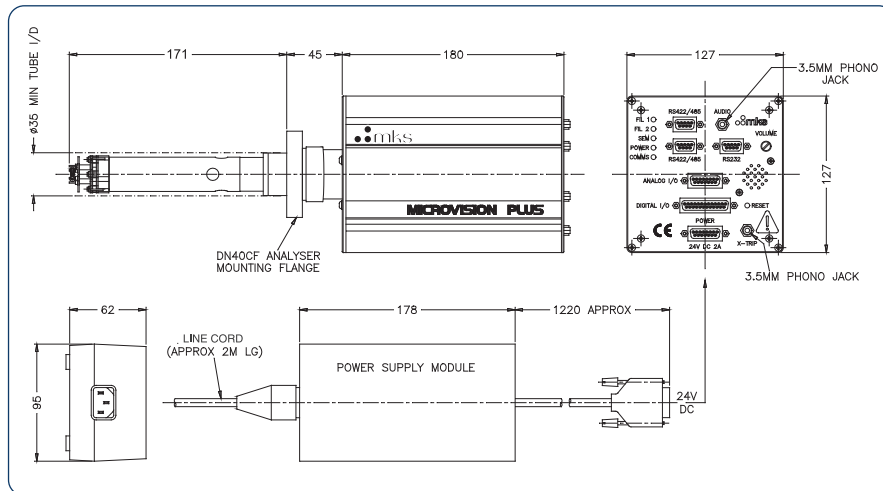
Note: Unless otherwise specified, dimensions are nominal values in millimeters.

Specifications

HARDWARE

Mass Range Options	1-100, 1-200 & 1-300 amu standard 1-6, & 1-100 amu high performance optional
Maximum Operating Pressure*	7.6×10^{-5} Torr (1×10^{-4} mbar)
Minimum Detectable Partial Pressure*	Faraday: 1.5×10^{-11} Torr (2×10^{-11} mbar) Channelplate SEM: 3.8×10^{-14} Torr (5×10^{-14} mbar) Single channel SEM: 7.6×10^{-15} Torr (1×10^{-14} mbar)
Mass Stability	Better than ±0.1 amu over 8 hours at stable ambient temperature
Resolution	Better than 10% valley between peaks of equal height, throughout mass range

ANALYZER

Bakeout Temperature	250°C (electronics dismounted)
Maximum Operating Temperature	200°C (Faraday mode only, electronics in horizontal orientation)
Mounting Flange	DN40CF (70 mm/2.75" OD) Conflat® Flange
Ion Source Options	Open, UHV, Closed and Cross-Beam
Ion Source Sensitivity	2×10^{-4} A/mbar
Ion Source Parameter Variables	Electron energy: 20-100eV. Emission current: 0-5 mA. Ion energy: 0-10V. Ion extraction potential: 0 - minus 130 V (adjustable from PC).
UHV Analyzer Outgassing Spec	Less than 1×10^{-9} mbar-l/s
Filaments	Twin tungsten (optional ThO_2/Ir or Y_2O_3/Ir)

CONTROL UNIT/PC

MicroVision Plus Electronics Module Weight	2.1 kg
Power	24 VDC, 3.4 A external supply (included)
Maximum Ambient Operating Temperature	35°C, 80% RH (non condensing)
LED Status Indication	Filament 1, filament 2, SEM, power & communications
MicroVision Plus I/O Capability	RGA for Windows: 4 analog inputs (1 for external gauge reading), 12 TTL output signals; Process Eye 2000: 4 analog inputs (0-10V, 16 bit), 1 analog output (0-10V, 16 bit), 16 digital TTL I/O, 1 opto-isolated filament control input
I/O Capability (optional PC based)	Process Eye 2000: Generic I/O card support for ISA slots, DTS300 I/O card support for PCI slots, Modbus/GEM SECS support for some product configurations
Other Facilities	Leak-check audio headset socket with volume adjustment, external filament-protect speaker and socket, instrument reset
Software	Software: RGA for Windows: Windows 3.1, 3.11, 95/98*, NT 4.0*, Millennium* and 2000* compatible; Process Eye 2000: fully network compatible control platform generating under Microsoft® Windows NT 4.0, 98, Me, 2000* or XP* (recommended) *Contact MKS for degree of functionality
MicroVision Plus Communications (baud rate & max. distance)	RGA for Windows: RS232C, 9600 baud, 15 m (50ft) maximum; Process Eye 2000: RS232C, 9600 baud, 15 m (50ft) RS422, 115000 baud, 1.2 Km (4000ft)
Recommended PC Spec	Pentium III 233 MHz, 64MB RAM, 6 GB disk drive. Multi-sensor installations may require higher specifications.

OPTIONS AND PLUG-IN MODULES

Radiation Resistant Extenders for Remote Location of Electronics	Two optional extender lengths available: 3 meters & 15 meters
Remote Vacuum Controller (RVC)	Provides interlocked PC-based control of differentially pumped vacuum system
Valve Actuator	Converts TTL logic signals to multiple 24 volt output signals
Valve Controller	Provides automated PC-based control of multi-way valve manifold

SHIPPING INFORMATION

Complete Instrument Shipping Weight	10 kg
MicroVision Plus Packaging Dimensions	430 mm x 390 mm x 330 mm

A.14. Overview of TRIADE vacuum pumps, temperature and pressure sensors

Table A.2.: Overview of the TRIADE pressure sensors.

Label	Range in mbar	Safety function	Type
RP001	$0.133 - 1333$	no	MKS 902
		detector electronics volume	
RP002	$0.133 - 1333$	no	MKS 902
		sampling port	
RP003	$10^{-2} - 20$	no	Baratron 626B
		BV061	
RP004	$0.133 - 1333$	yes	MKS 902
		BV061	
RP005	$10^{-5} - 10^{-1}$	no	Baratron 627D
		BV061	
RP006	$10^{-10} - 10^{-3}$	no	MKS 903
		BV061	
RP007	$0.133 - 1333$	no	MKS 902
		If-volume	
RP008	$0.133 - 1333$	yes	MKS 902
		BV062	
RP009	$0.133 - 1333$	yes	MKS 902
		ZTS-connection	
RP010	$0.133 - 1333$	no	MKS 902
		VA052	

Table A.3.: Overview of the TRIADE vacuum pumps.

Type	Siemens Interatom	Normetex Type 15	Pfeiffer HiPace 300	Leybold SL80	Oerlikon Divac 0.8 T
Label	VA055	VA054	VA053	VA052	VA051
Max. outlet mbar	1000	100	20	16	1000
Min. inlet mbar	100	10^{-2}	$\leqslant 5 \cdot 10^{-10}$	$< 2 \cdot 10^{-10}$	$\leqslant 10^{-1}$
Pumping speed	$3 \, \mathrm{m^3/h}$	$12 \, \mathrm{m^3/h}$	$260 \, \mathrm{l/s}$	$65 \, \mathrm{l/s}$	$0.6 \, \mathrm{m^3/h}$
Leakage rate mbar l/s	$\leqslant 10^{-9}$	$\leqslant 10^{-6}$	$\leqslant 10^{-6}$	$\leqslant 10^{-6}$	

Table A.4.: Overview of the TRIADE pressure sensor types.

Type	Series 902 piezo-electrical	Baratron 626B capacitive	Baratron 627D capacitive	Series 903 ionization
Range in mbar from	0.13	10^{-2}	10^{-5}	$4 \cdot 10^{-10}$
to	1333	20	10^{-1}	$6.7 \cdot 10^{-3}$
Input voltage in V	$12 - 30$	± 15	± 15	$14 - 30$
Output voltage in V	$0 - 10$	$0 - 10$	$0 - 10$	$1.5 - 8.5$

Table A.5.: Overview of the TRIADE temperature sensors.

Label	Range in °C	Function	Type
RT011	$-30 - 70$	temperature	PT1000
		heatsink detector electronics	
RT012	$0 - 200$	temperature	PT100
		heating coil BV061	
RT013	$0 - 200$	temperature	PT100
		heating sleeve blind flange BV061	
RT014	$0 - 200$	temperature	PT100
		inlet VA052	
RT015	$-200 - 650$	temperature	PT100
		heating coil BV062	
RT016	$-200 - 650$	temperature	PT100
		cold gas coil blind flange BV061	
RT017	$0 - 200$	temperature	PT100
		cold gas stream after flowmeter	

A.15. Tritium gas correction factor for the ionization vacuum gauge MKS903
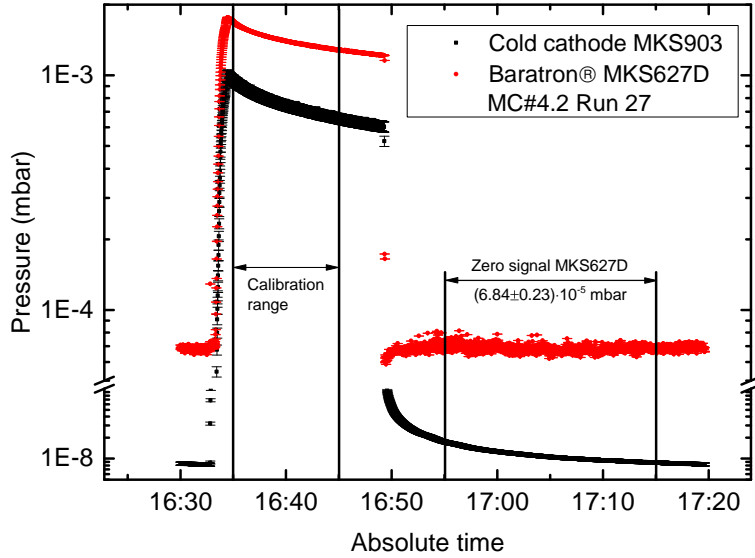
Figure A.8.: Pressure trend during run 27 of MC4.2. The pressure has been measured gas species independently with the capacitance manometer MKS627D and gas species dependent with ionization gauge MKS903. Values of the MKS903 are nitrogen calibrated.
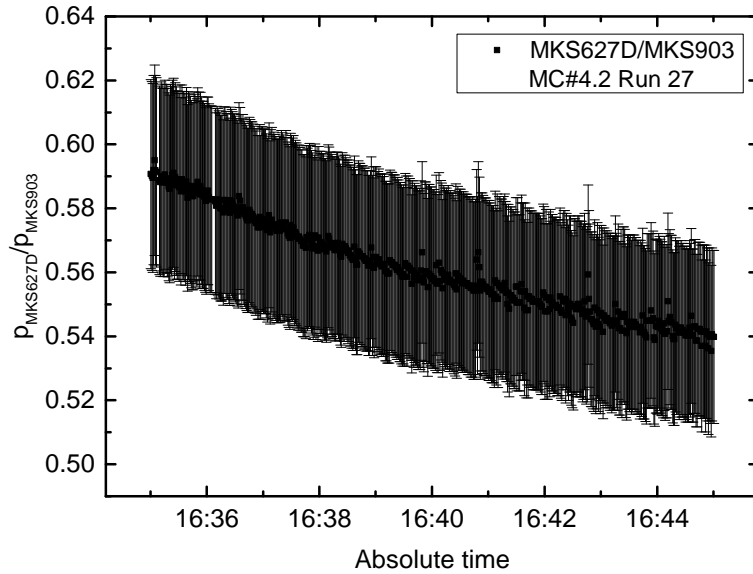
Figure A.9.: Calculated gas correction factors for tritium for the ion gauge MKS903. The pressure signal $p_{MKS627D}$ has been corrected for the zero signal as marked in figure A.8. As the tritium purity during exposure phase is decreasing with time due to outgassing effects, the first calculated value should give the best estimated value of 0.59 ± 0.03. Potential systematic effects of the MKS903 due to the large pressure increase from 10^{-9} mbar to 10^{-3} mbar within several minutes are not considered here.

A.16. Fit results of the TRIADE BIXS count rates
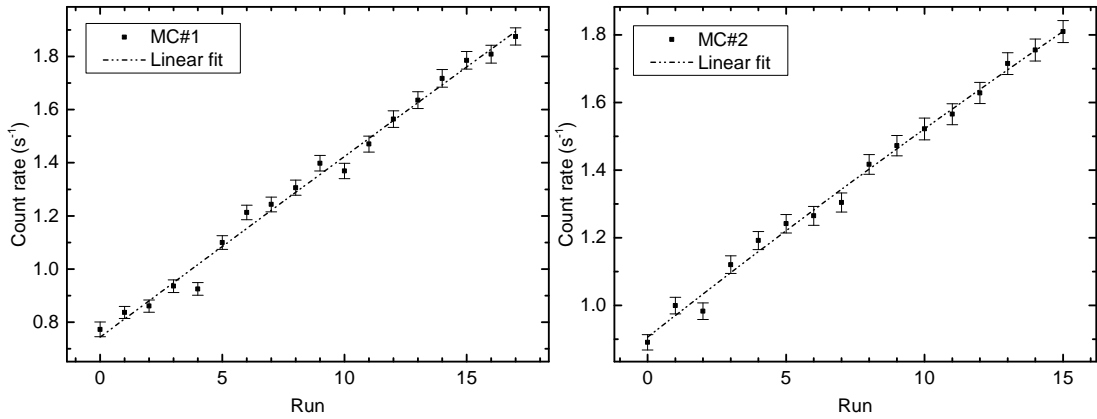
Figure A.10.: BIXS count rates of campaigns MC#1 (left) and MC#2 (right), fitted with a linear model. Error bars representing 1σ statistical uncertainties of the measured count rates.
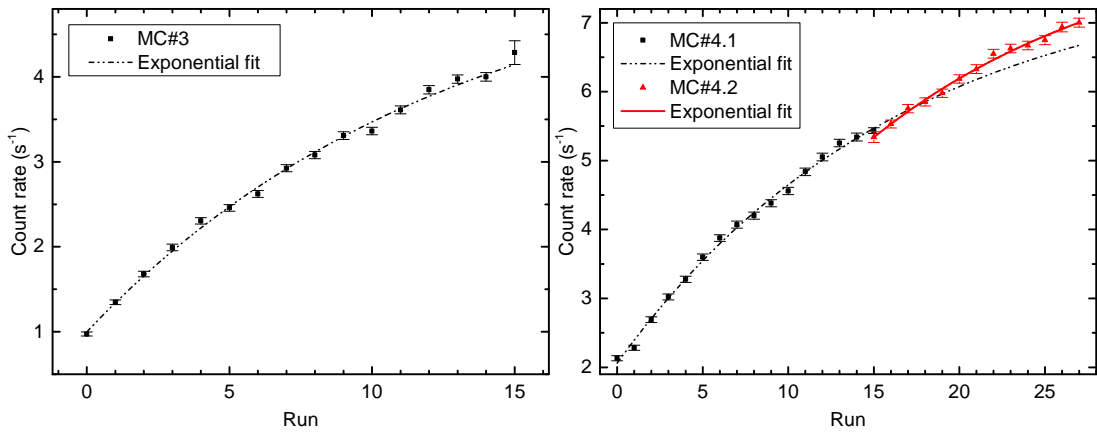
Figure A.11.: BIXS count rates of campaigns MC#3, MC#4.1 and MC#4.2, fitted with an exponential model. Error bars representing 1σ statistical uncertainties of the measured count rates.

A.17. Simulated geometry of TriReX

```
G4Material* Au_Layer = nist->FindOrBuildMaterial("G4_Au");
G4Material* Al_Layer = nist->FindOrBuildMaterial("G4_Al");
G4Material* Be_Layer = nist->FindOrBuildMaterial("G4_Be");
G4Material* Zr_Layer = nist->FindOrBuildMaterial("G4_Zr");
G4Material* SS_Layer = nist->FindOrBuildMaterial("G4_STAINLESS-STEEL");


//G4ThreeVector pos1 = G4ThreeVector(0, 0*cm, 0.0*cm); //Absorber
G4ThreeVector pos2 = G4ThreeVector(0, 0*cm, -2.099995*cm-2*mm); //
    Al_absorber
G4ThreeVector pos3 = G4ThreeVector(0, 0*cm, +1.4875*cm); //BeCF40
G4ThreeVector pos4 = G4ThreeVector(0, 0*cm, +1.50001*cm); //AuCF40
G4ThreeVector pos5 = G4ThreeVector(0, 0*cm, +0.865*cm); //SSCF40
G4ThreeVector pos6 = G4ThreeVector(0, 0*cm, +3.61*cm); //BeCF50
G4ThreeVector pos7 = G4ThreeVector(0, 0*cm, +3.54999*cm); //AuCF50
G4ThreeVector pos8 = G4ThreeVector(0, 0*cm, +4.465*cm); //SSCF50
G4ThreeVector pos9 = G4ThreeVector(0, 0*cm, -0.77*cm); //SS1Rez Flansch
G4ThreeVector pos10 = G4ThreeVector(0, 0*cm, +4.23*cm); //SS2Rez CF100
    Hülle
G4ThreeVector pos11 = G4ThreeVector(0, 0*cm, -2.074*cm-2*mm); //ZrKoll Zr
    Kollimator_Neu am 4.3.2014 in Simulation

G4Tubs* AuCF40Tube=new G4Tubs("AuCF40",0.*cm,1.95*cm,60.*nm,0.*deg,360.*
    deg);
G4LogicalVolume* logicAuCF40Tube = new G4LogicalVolume(AuCF40Tube,
    Au_Layer,"AuCF40");
G4VPhysicalVolume* physicalAuCF40Tube = new G4PVPlacement(0,pos4,
    logicAuCF40Tube,"AuCF40",fLogicWorld,false,0, true);


G4Tubs* AuCF50Tube=new G4Tubs("AuCF50",0.*cm,2.55*cm,60.*nm,0.*deg,360.*
    deg);
G4LogicalVolume* logicAuCF50Tube = new G4LogicalVolume(AuCF50Tube,
    Au_Layer,"AuCF50");
G4VPhysicalVolume* physicalAuCF50Tube = new G4PVPlacement(0,pos7,
    logicAuCF50Tube,"AuCF50",fLogicWorld,false,0, true);


G4Tubs* SSCF40Tube=new G4Tubs("SSCF40",1.95*cm,3.5*cm,6.35*mm,0.*deg
    ,360.*deg);
G4LogicalVolume* logicSSCF40Tube = new G4LogicalVolume(SSCF40Tube,
    SS_Layer,"SSCF40");
G4VPhysicalVolume* physicalSSCF40Tube = new G4PVPlacement(0,pos5,
    logicSSCF40Tube,"SSCF40",fLogicWorld,false,0, true);


G4Tubs* SSCF50Tube=new G4Tubs("SSCF50",2.55*cm,4.3*cm,8.65*mm,0.*deg
    ,360.*deg);
G4LogicalVolume* logicSSCF50Tube = new G4LogicalVolume(SSCF50Tube,
    SS_Layer,"SSCF50");
G4VPhysicalVolume* physicalSSCF50Tube = new G4PVPlacement(0,pos8,
    logicSSCF50Tube,"SSCF50",fLogicWorld,false,0, true);


G4Tubs* BeCF40Tube=new G4Tubs("BeCF40",0.*cm,1.95*cm,0.125*mm,0.*deg
    ,360.*deg);
G4LogicalVolume* logicBeCF40Tube = new G4LogicalVolume(BeCF40Tube,
    Be_Layer,"BeCF40");
G4VPhysicalVolume* physicalBeCF40Tube = new G4PVPlacement(0,pos3,
    logicBeCF40Tube,"BeCF40",fLogicWorld,false,0, true);
```

```
G4Tubs* BeCF50Tube=new G4Tubs("BeCF50",0.*cm,2.55*cm,0.1*mm,0.*deg,360.*
    deg);
G4LogicalVolume* logicBeCF50Tube = new G4LogicalVolume(BeCF50Tube,
    Be_Layer,"BeCF50");
G4VPhysicalVolume* physicalBeCF50Tube = new G4PVPlacement(0,pos6,
    logicBeCF50Tube,"BeCF50",fLogicWorld,false,0, true);

G4Tubs* AlAbsTube=new G4Tubs("AlAbs",0.0*mm,5.64*mm,50.*nm,0.*deg,360.*
    deg);
G4LogicalVolume* logicAlAbsTube = new G4LogicalVolume(AlAbsTube,Al_Layer,
    "AlAbs");
G4VPhysicalVolume* physicalAlAbsTube = new G4PVPlacement(0,pos2,
    logicAlAbsTube,"AlAbs",fLogicWorld,false,0, true);

G4Tubs* SSFlanschTube=new G4Tubs("SSFlansch",1.95*cm,5.0*cm,1.0*cm,0.*deg
    ,360.*deg);
G4LogicalVolume* logicSSFlanschTube = new G4LogicalVolume(SSFlanschTube,
    SS_Layer,"SSFlansch");
G4VPhysicalVolume* physicalSSFlanschTube = new G4PVPlacement(0,pos9,
    logicSSFlanschTube,"SSFlansch",fLogicWorld,false,0, true);

G4Tubs* SSRezTube=new G4Tubs("SSRez",5.0*cm,5.1*cm,40.0*mm,0.*deg,360.*
    deg);
G4LogicalVolume* logicSSRezTube = new G4LogicalVolume(SSRezTube,SS_Layer,
    "SSRez");
G4VPhysicalVolume* physicalSSRezTube = new G4PVPlacement(0,pos10,
    logicSSRezTube,"SSRez",fLogicWorld,false,0, true);

G4Tubs* ZrTube=new G4Tubs("ZrAbs",5.05*mm,7.5*mm,0.5*mm,0.*deg,360.*deg);
     // neu am 4.3.14 eingefügt
G4LogicalVolume* logicZrTube = new G4LogicalVolume(ZrTube,Zr_Layer,"ZrAbs
    ");
G4VPhysicalVolume* physicalZrTube = new G4PVPlacement(0,pos11,logicZrTube
    ,"ZrAbs",fLogicWorld,false,0, true);

G4VisAttributes * gold = new G4VisAttributes(G4Colour(1.,1.,0.));
logicAuCF40Tube->SetVisAttributes(gold);
logicAuCF50Tube->SetVisAttributes(gold);

G4VisAttributes * silber = new G4VisAttributes(G4Colour(0.5,0.5,0.5));
logicBeCF40Tube->SetVisAttributes(silber);
logicBeCF50Tube->SetVisAttributes(silber);

G4VisAttributes * red = new G4VisAttributes(G4Colour(1.,0.,0.));
logicAlAbsTube->SetVisAttributes(red);

G4VisAttributes * magenta = new G4VisAttributes(G4Colour(1.,0.,1.0,0.1));
logicSSRezTube->SetVisAttributes(magenta);
logicSSFlanschTube->SetVisAttributes(magenta);

G4VisAttributes * blue = new G4VisAttributes(G4Colour(0.0,0.0,1.0));
logicSSCF40Tube->SetVisAttributes(blue);
logicSSCF50Tube->SetVisAttributes(blue);
// Absorber
//
fSolidAbsorber = new G4Tubs("Absorber",
```

```
                        0.*cm, 5.64*mm, fAbsorberThickness ,0.* deg ,360.* deg ) ;


fLogicAbsorber = new  G4LogicalVolume ( fSolidAbsorber ,      //its  solid
                                        fAbsorberMaterial , //its
                                             material
                                        "Absorber" ) ;          //its  name


fPhysiAbsorber = new  G4PVPlacement ( 0 ,                      //no  rotation
                       G4ThreeVector (0. ,0. , − 2.1225∗cm−2∗mm) ,     //its
                            position
                             fLogicAbsorber ,       //its  logical  volume
                             "Absorber" ,           //its  name
                             fLogicWorld ,          //its  mother
                             false ,                //no  boulean  operat
                             0) ;                   //copy  number
```

A.18. Simulated geometry of the KATRIN BIXS system

```cpp
  G4Material* Au_Layer = nist->FindOrBuildMaterial("G4_Au");
  G4Material* Cu_Layer = nist->FindOrBuildMaterial("G4_Cu");
  G4Material* Al_Layer = nist->FindOrBuildMaterial("G4_Al");
  G4Material* Be_Layer = nist->FindOrBuildMaterial("G4_Be");
  G4Material* Si_Layer = nist->FindOrBuildMaterial("G4_Si");
  G4Material* Zr_Layer = nist->FindOrBuildMaterial("G4_Zr");
  G4Material* SS_Layer = nist->FindOrBuildMaterial("G4_STAINLESS-STEEL");


  G4Element* elH  = new G4Element("Hydrogen","H" , 1., 1.008*g/mole);
  G4Element* elO  = new G4Element("Oxygen"  ,"O" , 8., 15.999*g/mole);
  G4Element* elC  = new G4Element("Carbon"  ,"C" , 6., 12.011*g/mole);
  G4Material* PEEK = new G4Material("PEEK", 1.32*g/cm3, 3);
  PEEK->AddElement(elH, 14);
  PEEK->AddElement(elO, 3);
  PEEK->AddElement(elC, 19);

  bool checkoverlapp= true;
  //Be-Window + SS CF Flange
  G4double zPlaneBeWi[] = {-12.8*mm, -0.01*mm, 0*mm,  65.25*mm, 65.26*mm,
      66*mm};
  G4double rInnerBeWi[] = {13*mm, 13*mm, 13*mm, 13*mm, 17.5*mm, 17.5*mm};
  G4double rOuterBeWi[] = {35*mm, 35*mm, 18*mm, 18*mm, 18*mm, 18*mm};
  G4VSolid* BeWi= new G4Polycone("BeWindow",0, 360.*deg,6, zPlaneBeWi,
      rInnerBeWi, rOuterBeWi);
  G4double zPlaneBe[] = {65.26*mm, 65.51*mm};
  G4double rInnerBe[] = {0*mm, 0*mm};
  G4double rOuterBe[] = {17.49*mm, 17.49*mm};
  G4VSolid* Be= new G4Polycone("Beryllium",0, 360.*deg,2, zPlaneBe,
      rInnerBe, rOuterBe);
  G4double zPlaneBeAu[] = {65.51*mm, 65.5101*mm};
  G4double rInnerBeAu[] = {0*mm, 0*mm};
  G4double rOuterBeAu[] = {17.49*mm, 17.49*mm};
  G4VSolid* BeAu= new G4Polycone("BeAu",0, 360.*deg,2, zPlaneBeAu,
      rInnerBeAu, rOuterBeAu);

  G4LogicalVolume* logic_BeWi1 = new G4LogicalVolume(BeWi,SS_Layer,"BeWi1")
      ;
  G4LogicalVolume* logic_BeWi2 = new G4LogicalVolume(BeWi,SS_Layer,"BeWi2")
      ;
  G4LogicalVolume* logic_Be1 = new G4LogicalVolume(Be,Be_Layer,"Be1");
  G4LogicalVolume* logic_Be2 = new G4LogicalVolume(Be,Be_Layer,"Be2");
  G4LogicalVolume* logic_BeAu1 = new G4LogicalVolume(BeAu,Au_Layer,"BeAu1")
      ;
  G4LogicalVolume* logic_BeAu2 = new G4LogicalVolume(BeAu,Au_Layer,"BeAu2")
      ;

  G4VPhysicalVolume* physical_BeWi1 = new G4PVPlacement(G4Transform3D(
      G4RotationMatrix().rotateX(128*deg), G4ThreeVector(0, 175.3*mm, 232.5*
      mm)),logic_BeWi1,"BeWi1",fLogicWorld,false,0, checkoverlapp);
  G4VPhysicalVolume* physical_BeWi2 = new G4PVPlacement(G4Transform3D(
      G4RotationMatrix().rotateX(-128*deg), G4ThreeVector(0, -175.3*mm,
      232.5*mm)),logic_BeWi2,"BeWi2",fLogicWorld,false,0, checkoverlapp);
  G4VPhysicalVolume* physical_Be1 = new G4PVPlacement(G4Transform3D(
      G4RotationMatrix().rotateX(128*deg), G4ThreeVector(0, 175.3*mm, 232.5*
```

```
      mm)),logic_Be1,"Be1",fLogicWorld,false,0, checkoverlapp);
G4VPhysicalVolume* physical_Be2 = new G4PVPlacement(G4Transform3D(
      G4RotationMatrix().rotateX(−128*deg), G4ThreeVector(0, −175.3*mm,
      232.5*mm)),logic_Be2,"Be2",fLogicWorld,false,0, checkoverlapp);
G4VPhysicalVolume* physical_BeAu1 = new G4PVPlacement(G4Transform3D(
      G4RotationMatrix().rotateX(128*deg), G4ThreeVector(0, 175.3*mm, 232.5*
      mm)),logic_BeAu1,"BeAu1",fLogicWorld,false,0, checkoverlapp);
G4VPhysicalVolume* physical_BeAu2 = new G4PVPlacement(G4Transform3D(
      G4RotationMatrix().rotateX(−128*deg), G4ThreeVector(0, −175.3*mm,
      232.5*mm)),logic_BeAu2,"BeAu2",fLogicWorld,false,0, checkoverlapp);

//Rearwallvessel
G4double zPlaneD[] = {0*mm,    22*mm,    22.1*mm, 84.5*mm, 154.7*mm, 297.4*mm
      , 297.5*mm, 322.5*mm};
G4double rInnerD[] = {75*mm, 75*mm, 75*mm, 75*mm, 124*mm, 124*mm, 124*mm,
      124*mm};
G4double rOuterD[] = {250*mm, 250*mm, 250*mm, 250*mm, 250*mm, 250*mm,
      250*mm, 250*mm};
G4VSolid* RW_VesselDummy= new G4Polycone("RW␣VesselDummy",0, 360.*deg,8,
      zPlaneD, rInnerD, rOuterD);
G4double zPlane[] = {0*mm,    22*mm,    22.1*mm, 84.5*mm, 154.7*mm, 297.4*mm,
       297.5*mm, 322.5*mm};
G4double rInner[] = {75*mm, 75*mm, 75*mm, 75*mm, 124*mm, 124*mm, 124*mm,
      124*mm};
G4double rOuter[] = {101.5*mm, 101.5*mm, 77*mm, 77*mm, 127*mm, 127*mm,
      152*mm, 152*mm};
G4VSolid* RW_Vessel= new G4Polycone("RW␣Vessel",0, 360.*deg,8, zPlane,
      rInner, rOuter);

//Viewport Drehpunkt um Flanschmitelpunkt auÃŸen
G4double zPlaneVP[] = {0*mm,    13*mm,    13.1*mm, 100*mm};
G4double rInnerVP[] = {0*mm, 0*mm, 0*mm, 0*mm};
G4double rOuterVP[] = {34.5*mm, 34.5*mm, 21.2*mm, 21.2*mm};
G4VSolid* ViewportDummy= new G4Polycone("Viewport",0, 360.*deg,4,
      zPlaneVP, rInnerVP, rOuterVP);
G4VSolid* VPInner_Tube=new G4Tubs("VPInner_Tube",0*mm,19.2*mm,50.0*mm,0.*
      deg,360.*deg);
G4VSolid* ViewportComplete=new G4SubtractionSolid("Viewport␣Complete",
      ViewportDummy, VPInner_Tube,0, G4ThreeVector(0, 0*cm, 5*cm));

//Cuts fÃ¼r RW Vessel und Viewports und Placement
G4VSolid* RW_VesselCut1=new G4SubtractionSolid("RW_VesselCut1",RW_Vessel,
       ViewportDummy,G4Transform3D(G4RotationMatrix().rotateX(128*deg),
      G4ThreeVector(0, 175.3*mm, 232.5*mm)));
G4VSolid* RW_VesselCut2=new G4SubtractionSolid("RW_VesselCut2",
      RW_VesselCut1, ViewportDummy,G4Transform3D(G4RotationMatrix().rotateX
      (−128*deg), G4ThreeVector(0, −175.3*mm, 232.5*mm)));
G4LogicalVolume* logic_RW_Vessel = new G4LogicalVolume(RW_VesselCut2,
      SS_Layer,"RW_Vessel");
G4VPhysicalVolume* physical_RW_Vessel = new G4PVPlacement(0,G4ThreeVector
      (0, 0, 0*mm),logic_RW_Vessel,"RW_Vessel",fLogicWorld,false,0,
      checkoverlapp);

G4VSolid* ViewportCut1=new G4IntersectionSolid("ViewportCut1",
      RW_VesselDummy, ViewportComplete,G4Transform3D(G4RotationMatrix().
      rotateX(128*deg), G4ThreeVector(0, 175.3*mm, 232.5*mm)));
```

```
G4LogicalVolume* logic_Viewport1 = new G4LogicalVolume(ViewportCut1,
    SS_Layer,"logic_Viewport1");
G4VPhysicalVolume* physical_Viewport1 = new G4PVPlacement(0,G4ThreeVector
    (0, 0, 0*mm),logic_Viewport1,"Viewport1",fLogicWorld,false,0,
    checkoverlapp);

G4VSolid* ViewportCut2=new G4IntersectionSolid("ViewportCut2",
    RW_VesselDummy, ViewportComplete,G4Transform3D(G4RotationMatrix().
    rotateX(-128*deg), G4ThreeVector(0, -175.3*mm, 232.5*mm)));
G4LogicalVolume* logic_Viewport2 = new G4LogicalVolume(ViewportCut2,
    SS_Layer,"logic_Viewport2");
G4VPhysicalVolume* physical_Viewport2 = new G4PVPlacement(0,G4ThreeVector
    (0, 0, 0*mm),logic_Viewport2,"Viewport2",fLogicWorld,false,0,
    checkoverlapp);

//Detector Geometry
G4double zPlaneDG[] = {0*mm, 11.5*mm, 11.51*mm, 211.5*mm, 211.51*mm
    ,216.8*mm, 216.81*mm, 217.3*mm, 217.31*mm, 217.8*mm};
G4double rInnerDG[] = {11.5*mm, 11.5*mm, 11.5*mm, 11.5*mm, 10.0*mm, 10.0*
    mm, 7*mm, 7*mm, 9.1*mm, 9.1*mm};
G4double rOuterDG[] = {27*mm, 27*mm, 12.5*mm, 12.5*mm, 10.5*mm, 10.5*mm,
    10.5*mm, 10.5*mm, 10.5*mm, 10.5*mm};
G4VSolid* DetectorGeometry= new G4Polycone("DetectorGeometry",0, 360.*deg
    ,10, zPlaneDG, rInnerDG, rOuterDG);
G4LogicalVolume* logic_Detector1 = new G4LogicalVolume(DetectorGeometry,
    SS_Layer,"logic_Detector1");
G4VPhysicalVolume* physical_Detector1 = new G4PVPlacement(G4Transform3D(
    G4RotationMatrix().rotateX(128*deg), G4ThreeVector(0, +175.3*mm
    +133.42*mm, 232.5*mm+104.24*mm)),logic_Detector1,"Detector1",
    fLogicWorld,false,0, checkoverlapp);
G4LogicalVolume* logic_Detector2 = new G4LogicalVolume(DetectorGeometry,
    SS_Layer,"logic_Detector2");
G4VPhysicalVolume* physical_Detector2 = new G4PVPlacement(G4Transform3D(
    G4RotationMatrix().rotateX(-128*deg), G4ThreeVector(0, -175.3*mm
    -133.42*mm, 232.5*mm+104.24*mm)),logic_Detector2,"Detector2",
    fLogicWorld,false,0, checkoverlapp);

//Zr Collimator
G4double zPlaneZr[] = {215.5*mm, 216*mm};
G4double rInnerZr[] = {5.41*mm, 5.41*mm};
G4double rOuterZr[] = {8*mm, 8*mm};
G4VSolid* ZrCol= new G4Polycone("ZrCol",0, 360.*deg,2, zPlaneZr, rInnerZr
    , rOuterZr);
G4LogicalVolume* logic_ZrCol = new G4LogicalVolume(ZrCol,Zr_Layer,"
    logic_ZrCol");
G4VPhysicalVolume* physical_ZrCol = new G4PVPlacement(G4Transform3D(
    G4RotationMatrix().rotateX(128*deg), G4ThreeVector(0, +175.3*mm
    +133.42*mm, 232.5*mm+104.24*mm)),logic_ZrCol,"ZrCol",fLogicWorld,false
    ,0, checkoverlapp);

//Rear Wall Assembly
G4double zPlaneRWall[] = {0*mm, 1.9998*mm};
G4double rInnerRWall[] = {2.5*mm, 2.5*mm};
G4double rOuterRWall[] = {73*mm, 73*mm};
G4VSolid* RWall= new G4Polycone("RWall",0, 360.*deg,2, zPlaneRWall,
    rInnerRWall, rOuterRWall);
```

```
G4Tubs* RWallAuHole = new G4Tubs("RWallAuHole", 2.4998*mm, 2.5*mm,
    1.9998/2*mm, 0.*deg,360.*deg);
G4Tubs* RWallAu = new G4Tubs("RWallAu", 2.5*mm, 73*mm, 100/2*nm, 0.*deg
    ,360.*deg);

//G4double zPlaneRWallAu[] = {0*mm, 1.99980*mm, 1.999801*mm, 2*mm};
//G4double rInnerRWallAu[] = {2.4998*mm, 2.4998*mm, 2.5*mm, 2.5*mm};
//G4double rOuterRWallAu[] = {2.5*mm, 2.5*mm, 73*mm, 73*mm};
//G4VSolid* RWallAu= new G4Polycone("RWallAu",0, 360.*deg,4,
//    zPlaneRWallAu, rInnerRWallAu, rOuterRWallAu);
G4double zPlaneRWallHolder[] = {2*mm, 3.5*mm};
G4double rInnerRWallHolder[] = {67*mm, 67*mm};
G4double rOuterRWallHolder[] = {74.5*mm, 74.5*mm};
G4VSolid* RWallHolder= new G4Polycone("RWallHolder",0, 360.*deg,2,
    zPlaneRWallHolder, rInnerRWallHolder, rOuterRWallHolder);

G4LogicalVolume* logic_RWall = new G4LogicalVolume(RWall,SS_Layer,"
    logic_RWall");
G4LogicalVolume* logic_RWallAuHole = new G4LogicalVolume(RWallAuHole,
    Au_Layer,"logic_RWallAuHole");
G4LogicalVolume* logic_RWallAu = new G4LogicalVolume(RWallAu,Au_Layer,"
    logic_RWallAu");
G4LogicalVolume* logic_RWallHolder = new G4LogicalVolume(RWallHolder,PEEK
    ,"RWallHolder");

G4VPhysicalVolume* physical_RWall = new G4PVPlacement(0, G4ThreeVector(0,
     0, 84.372*mm),logic_RWall,"RWall",fLogicWorld,false,0, checkoverlapp)
    ;
G4VPhysicalVolume* physical_RWallAuHole = new G4PVPlacement(0,
    G4ThreeVector(0, 0, (84.372*mm+1.9998/2*mm)),logic_RWallAuHole,"
    RWallAuHole",fLogicWorld,false,0, checkoverlapp);
G4VPhysicalVolume* physical_RWallAu = new G4PVPlacement(0, G4ThreeVector
    (0, 0, (84.372*mm+2*mm)),logic_RWallAu,"RWallAu",fLogicWorld,false,0,
    checkoverlapp);
G4VPhysicalVolume* physical_RWallHolder = new G4PVPlacement(0,
    G4ThreeVector(0, 0, 84.372*mm),logic_RWallHolder,"RWallHolder",
    fLogicWorld,false,0, checkoverlapp);

fSolidAbsorber = new G4Tubs("Absorber",
                   0.*cm, 6.91*mm, 450*um ,0.*deg,360.*deg);

fLogicAbsorber = new G4LogicalVolume(fSolidAbsorber,      //its solid
                                       fAbsorberMaterial, //its
                                           material
                                      "Absorber");         //its name

fPhysiAbsorber = new G4PVPlacement(G4Transform3D(G4RotationMatrix().
    rotateX(128*deg), G4ThreeVector(0, +175.3*mm-36.406*mm+0.355*mm,
    232.5*mm-28.444*mm+0.277*mm)),
                                    fLogicAbsorber,        //its logical volume
                                    "Absorber",            //its name
                                    fLogicWorld,           //its mother
                                    false,                 //no boulean operat
                                    0);                    //copy number
```

A.19. Simulated geometry of TRIADE

```
G4Material* Au_Layer = nist->FindOrBuildMaterial("G4_Au");
G4Material* Al_Layer = nist->FindOrBuildMaterial("G4_Al");
G4Material* Be_Layer = nist->FindOrBuildMaterial("G4_Be");
G4Material* Zr_Layer = nist->FindOrBuildMaterial("G4_Zr");
G4Material* SS_Layer = nist->FindOrBuildMaterial("G4_STAINLESS-STEEL");
G4Material* Ti_Layer = nist->FindOrBuildMaterial("G4_Ti");


G4ThreeVector pos1 = G4ThreeVector(0, 0*cm, 0.94*cm); //Start
G4ThreeVector pos2 = G4ThreeVector(0, 0*cm, 7.3665*cm); //Recipient
G4ThreeVector pos3 = G4ThreeVector(0, 0*cm, 9.35*cm); //BasePlate
G4ThreeVector pos4 = G4ThreeVector(0, 0*cm, 9.9*cm); //ProbeLayer
G4ThreeVector pos5 = G4ThreeVector(0, 0*cm, 10.10001*cm); //HolderRing
G4ThreeVector pos6 = G4ThreeVector(0, 0*cm, 11.550005*cm); //AuCoating
G4ThreeVector pos7 = G4ThreeVector(0, 0*cm, 11.5500105*cm); //AdLayer
G4ThreeVector pos8 = G4ThreeVector(0, 0*cm, 11.555011*cm); //BeWindow
G4ThreeVector pos9 = G4ThreeVector(0, 0*cm, 11.7750055*cm); //BeWindowAu
G4ThreeVector pos10 = G4ThreeVector(0, 0*cm, 12.4265*cm); //Fenster
G4ThreeVector pos11 = G4ThreeVector(0, 0*cm, 15.2765*cm); //RestIf
G4ThreeVector pos12 = G4ThreeVector(0, 0*cm, 9.950005*cm); //AuCoating
    Sample
G4ThreeVector pos13 = G4ThreeVector(0, 0*cm, (12.583*cm-0.0*mm)); //SS
    Capsule
G4ThreeVector pos14 = G4ThreeVector(0, 0*cm, (12.553625*cm-0.0*mm)); //Be
    Window
G4ThreeVector pos15 = G4ThreeVector(0, 0*cm, (12.778*cm-0.0*mm)); //Zr
    Collimator


G4Tubs* StartTube=new G4Tubs("Start",0.*cm,7.5*cm,1.88/2*cm,0.*deg,360.*deg
    );
G4LogicalVolume* logicStartTube = new G4LogicalVolume(StartTube,Au_Layer,"
    Start");
G4VPhysicalVolume* physicalStartTube = new G4PVPlacement(0,pos1,
    logicStartTube,"Start",fLogicWorld,false,0, true);

G4Tubs* RecipientTube=new G4Tubs("Recipient",5.0*cm,5.2*cm,(12.853-1.88)/2*
    cm,0.*deg,360.*deg);
G4LogicalVolume* logicRecipientTube = new G4LogicalVolume(RecipientTube,
    Au_Layer,"Recipient");
G4VPhysicalVolume* physicalRecipientTube = new G4PVPlacement(0,pos2,
    logicRecipientTube,"Recipient",fLogicWorld,false,0, true);

G4Tubs* Recipient2Tube=new G4Tubs("Recipient2",(4.9*cm),5.0*cm
    ,(12.853-1.88)/2*cm,0.*deg,360.*deg);
G4LogicalVolume* logicRecipient2Tube = new G4LogicalVolume(Recipient2Tube,
    fWorldMaterial,"Recipient2");
G4VPhysicalVolume* physicalRecipient2Tube = new G4PVPlacement(0,pos2,
    logicRecipient2Tube,"Recipient2",fLogicWorld,false,0, true);

G4Tubs* BasePlateTube=new G4Tubs("BasePlate",0.0*cm,4.7*cm,(9.85-8.85)/2*cm
    ,0.*deg,360.*deg);
G4LogicalVolume* logicBasePlateTube = new G4LogicalVolume(BasePlateTube,
    Au_Layer,"BasePlate");
G4VPhysicalVolume* physicalBasePlateTube = new G4PVPlacement(0,pos3,
    logicBasePlateTube,"BasePlate",fLogicWorld,false,0, true);
```

```
G4Tubs* ProbeLayerTube=new G4Tubs("ProbeLayer",0.0*cm,3.5*cm,(9.95-9.85)/2*
    cm,0.*deg,360.*deg);
G4LogicalVolume* logicProbeLayerTube = new G4LogicalVolume(ProbeLayerTube,
    Be_Layer,"ProbeLayer");
G4VPhysicalVolume* physicalProbeLayerTube = new G4PVPlacement(0,pos4,
    logicProbeLayerTube,"ProbeLayer",fLogicWorld,false,0, true);

G4Tubs* ProbeLayer2Tube=new G4Tubs("ProbeLayer2",3.5*cm,4.7*cm,(9.95-9.85)
    /2*cm,0.*deg,360.*deg);
G4LogicalVolume* logicProbeLayer2Tube = new G4LogicalVolume(ProbeLayer2Tube
    ,Au_Layer,"ProbeLayer2");
G4VPhysicalVolume* physicalProbeLayer2Tube = new G4PVPlacement(0,pos4,
    logicProbeLayer2Tube,"ProbeLayer2",fLogicWorld,false,0, true);

G4Tubs* AuCoatingSampleTube=new G4Tubs("AuCoatingSample",0.0*cm,3.5*cm
    ,(100)/2*nm,0.*deg,360.*deg);
G4LogicalVolume* logicAuCoatingSampleTube = new G4LogicalVolume(
    AuCoatingSampleTube,Au_Layer,"AuCoatingSample");
G4VPhysicalVolume* physicalAuCoatingSampleTube = new G4PVPlacement(0,pos12,
    logicAuCoatingSampleTube,"AuCoatingSample",fLogicWorld,false,0, true);

G4Tubs* HolderRingTube=new G4Tubs("HolderRing",3.0*cm,4.7*cm,(10.25-9.95)
    /2*cm,0.*deg,360.*deg);
G4LogicalVolume* logicHolderRingTube = new G4LogicalVolume(HolderRingTube,
    Au_Layer,"HolderRing");
G4VPhysicalVolume* physicalHolderRingTube = new G4PVPlacement(0,pos5,
    logicHolderRingTube,"HolderRing",fLogicWorld,false,0, true);

G4Tubs* AuCoatingTube=new G4Tubs("AuCoating",0.0*cm,1.0*cm,(11.55001-11.55)
    /2*cm,0.*deg,360.*deg);
G4LogicalVolume* logicAuCoatingTube = new G4LogicalVolume(AuCoatingTube,
    Au_Layer,"AuCoating");
G4VPhysicalVolume* physicalAuCoatingTube = new G4PVPlacement(0,pos6,
    logicAuCoatingTube,"AuCoating",fLogicWorld,false,0, true);

G4Tubs* AdLayerTube=new G4Tubs("AdLayer",0.0*cm,1.0*cm,(11.550011-11.55001)
    /2*cm,0.*deg,360.*deg);
G4LogicalVolume* logicAdLayerTube = new G4LogicalVolume(AdLayerTube,
    Ti_Layer,"AdLayer");
G4VPhysicalVolume* physicalAdLayerTube = new G4PVPlacement(0,pos7,
    logicAdLayerTube,"AdLayer",fLogicWorld,false,0, true);

G4Tubs* BeWindowTube=new G4Tubs("BeWindow",0.0*cm,1.0*cm
    ,(11.560011-11.550011)/2*cm,0.*deg,360.*deg);
G4LogicalVolume* logicBeWindowTube = new G4LogicalVolume(BeWindowTube,
    Be_Layer,"BeWindow");
G4VPhysicalVolume* physicalBeWindowTube = new G4PVPlacement(0,pos8,
    logicBeWindowTube,"BeWindow",fLogicWorld,false,0, true);

G4Tubs* BeWindowAuTube=new G4Tubs("BeWindowAu",1.0*cm,3.5*cm
    ,(12.00-11.550011)/2*cm,0.*deg,360.*deg);
G4LogicalVolume* logicBeWindowAuTube = new G4LogicalVolume(BeWindowAuTube,
    Au_Layer,"BeWindowAu");
G4VPhysicalVolume* physicalBeWindowAuTube = new G4PVPlacement(0,pos9,
    logicBeWindowAuTube,"BeWindowAu",fLogicWorld,false,0, true);
```

```
G4Tubs* FensterTube=new G4Tubs("Fenster",1.9*cm,3.5*cm,(12.853-12.00)/2*cm
    ,0.*deg,360.*deg);
G4LogicalVolume* logicFensterTube = new G4LogicalVolume(FensterTube,
    Au_Layer,"Fenster");
G4VPhysicalVolume* physicalFensterTube = new G4PVPlacement(0,pos10,
    logicFensterTube,"Fenster",fLogicWorld,false,0, true);

G4Tubs* RestIfTube=new G4Tubs("RestIf",1.9*cm,10.10*cm,(17.7-12.853)/2*cm
    ,0.*deg,360.*deg);
G4LogicalVolume* logicRestIfTube = new G4LogicalVolume(RestIfTube,Au_Layer,
    "RestIf");
G4VPhysicalVolume* physicalRestIfTube = new G4PVPlacement(0,pos11,
    logicRestIfTube,"RestIf",fLogicWorld,false,0, true);

G4Tubs* SS_capsule=new G4Tubs("SS_capsule",7/2*mm,14/2*mm,0.6/2*mm,0.*deg
    ,360.*deg);
G4LogicalVolume* logicSS_capsule = new G4LogicalVolume(SS_capsule,SS_Layer,
    "SS_capsule");
G4VPhysicalVolume* physicalSS_capsule = new G4PVPlacement(0,pos13,
    logicSS_capsule,"SS_capsule",fLogicWorld,false,0, true);

G4Tubs* Be_window_SDD=new G4Tubs("Be_window_SDD",0.0*cm,7/2*mm,12.5/2*um
    ,0.*deg,360.*deg);
G4LogicalVolume* logicBe_window_SDD = new G4LogicalVolume(Be_window_SDD,
    Be_Layer,"Be_window_SDD");
G4VPhysicalVolume* physicalBe_window_SDD = new G4PVPlacement(0,pos14,
    logicBe_window_SDD,"Be_window_SDD",fLogicWorld,false,0, true);

G4Tubs* Zr_collimator=new G4Tubs("Zr_collimator",2.33*mm,4*mm,0.5/2*mm,0.*
    deg,360.*deg);
G4LogicalVolume* logicZr_collimator = new G4LogicalVolume(Zr_collimator,
    Zr_Layer,"Zr_collimator");
G4VPhysicalVolume* physicalZr_collimator = new G4PVPlacement(0,pos15,
    logicZr_collimator,"Zr_collimator",fLogicWorld,false,0, true);

// Absorber
fSolidAbsorber = new G4Tubs("Absorber",0.*cm, 2.82*mm, 0.5/2*mm,0.*deg
    ,360.*deg);
fLogicAbsorber = new G4LogicalVolume(fSolidAbsorber, fAbsorberMaterial,"
    Absorber");//Silicon drift detector
fPhysiAbsorber = new G4PVPlacement(0,G4ThreeVector(0.,0.,12.828*cm),
    fLogicAbsorber,"Absorber",fLogicWorld,false,0);
```

A.20. Technical drawings TRIADE

A.21. Technical drawings TRIADE

NOTES:
1. ASSEMBLY TO BE MASS SPECTROMETER LEAK TIGHT WITH NO LEAKS
   GREATER THAN 1 X 10-9 ATM CC/SEC OF He.
2. DIMENSIONS ARE TO BE INSPECTED AGAINST SEPARATE DETAIL
   DRAWINGS. DIMENSIONS SHOWN ARE FOR REFERENCE ONLY.
3. ASSEMBLY TO BE BI-DIRECTIONALLY PRESSURE TESTED AT 1 BARR.

SECTION A-A

(Ø 69.1 [2.72])
STOCK

Ø 25.0 [.98]
Ø 20.0 [.79]

ATM

(12.7 [.50])

VAC

Ø 38.0 [1.50]

1.0 [.04]

DIFFUSION BONDED
0.1mm THK IF-1 Be

INTERPRET DRAWING PER
ANSI Y14.5M-1994.

UNLESS OTHERWISE SPECIFIED:
DIMENSIONS ARE IN MM[INCH]
TOLERANCES:
ANGLES   ±0.5
.X   ±0.8
.XX   ±0.13

FINISH (Ra): 1.6

IF-1, PF-60, PS-200, IS-50M
AND TRUEXTENT ARE REGISTERED
TRADEMARKS OF
MATERION BRUSH INC.

	NAME	DATE
DRAWN	J.Protteau	4/3/12
ENG. APPR.	.	.
CUSTOMER	KIT	
MATERIAL	304L SST/IF-1 Be	

© Copyright 2012 Materion Brush Inc.
PROPRIETARY INFORMATION OF MATERION BRUSH INC.
The information included in this document may not be
disseminated without prior written authorization
of Materion Brush Inc.

Customer approval print

Signed _____

Date _____

M A T E R I O N   Electrofusion

TITLE:
70mm SSCFF DB ASSY

SIZE A	DWG. NO. 73859	REV A
SCALE: 1:1	DO NOT SCALE DRAWING	SHEET 1 OF 1

ZONE	REV.	DESCRIPTION	DATE	APPROVED
	A	INITIAL RELEASE	4/3/12	JP

REVISIONS

Diese Zeichnung ist Eigentum der VACOM Vakuum Komponenten & Messtechnik GmbH.
Sie darf nur mit ausdrücklicher Genehmigung kopiert, verwertet oder an Dritte weitergegeben werden.

Ø78

A — A

18.29 (x)

31.34 (x)

(x) Ø der Bohrungen an
Durchführung anpassen

A–A (1 : 1)

ca. 20.25
20
13.88
10
M8

1
2

1x Durchführung W-SUBD-9-DE-CE-SSG
Schweißlippe 18.29±0.05 x 31.34±0.05
Leitermaterial Edelstahl vergoldet
Leiterdurchmesser 9 x 1.0mm

vakuumseitig schweißen
flache und glatte Schweißnähte
Anlauffarben entfernt
lecktesten < 10^{-9} mbar l/s

Schweißtoleranz ISO 13920 F
Schweißtoleranz ISO 13920 B

>400..1000	± 3.0		
>120..400	± 1.5		
30..120	± 1.0		
>30..400	± 2		
2..30	± 1		
>400..1000	± 0.8		
>120..400	± 0.5		
>30..120	± 0.3		
>6..30	± 0.2		
>3..6	± 0.1		
0.5..3	± 0.1		

spanend Toleranz ISO 2768-m

Stückliste			
Pos.	Anzahl	Mat.Nr.	Mat.-Kurztext
1	1	300569	F100-316
2	1	101002	W-SUBD-9-DE-CE-SSG

10⁻ⁿ mbar VACOM®	Änderung d. Kunden	Freigabe durch Kunden	Oberflächen nach DIN EN ISO 1302	Kanten nach DIN ISO 13715
VACOM Vakuum Komponenten & Messtechnik GmbH	Name, Datum	Name, Datum	$\sqrt{}$ Ra 3,2 ($\sqrt{}$ Ra 0,8)	–0,2 +0,4

		Maßstab:	1:1 (1:3)	Werkstoff:	316L / 1.4404	2,624 kg

Vorgänger:	Freigabe durch Vacom	erstellt von: Sven Haser
Ersatz:	Name, Datum	erstellt am: 15.03.2012
		geprüft von:
		geprüft am:

SPE-10031006-20

CF-Stromdurchführung, DN100
4x M8, TK-Ø 78mm, vakuumseitig

Toleranzen:	ISO2768 mK	317910	Oberfläche in mm² 59799,2 mm²2	Blatt 1 / 1
	ISO13920 BF		J:\drawings inventor\special\CF\SPE-10031006-20\SPE-10031006-20.idw	A4

Zust. Änderungen   Datum   Name

spanend: Toleranz	0.5..3	+3..6	+6..30	+30..120	+120..400	+400..1000	Schweißtoleranz	2..30	+30..400	Schweißtoleranz	30..120	+120..400	+400..1000	Diese Zeichnung ist Eigentum der VACOM Vakuum Komponenten & Messtechnik GmbH
ISO 2768-m	±0.1	±0.1	±0.2	±0.3	±0.5	±0.8	ISO 13920 B	±1	±2	ISO 13920 F	±1.0	±15	±3.0	Sie darf nur mit ausdrücklicher Genehmigung kopiert, verwertet oder an Dritte weitergegeben werden.

53.5

85

85

B–B (1 : 2)

A–A (1 : 2)

107.2 107.2

53.5

107

X

X (1 : 1)

Ø41

(Ø38)

(Ø100)

Ø104

vakuumseitig schweißen
flache und glatte Schweißnähte
Rohre ID≥16mm vakuumseitig mechanisch poliert
atmosphärenseitig glasperlengestrahlt (außer Flansche)
Dichtflächen schützen
Lecktesten < 10⁻⁹mbar l/s

Stückliste

Pos.	Anzahl	Mat.Nr.	Mat.-Kurztext
1	2	300593	F100RB104–316
2	2	300845	F40RB41–316
3	1	100606	R14.404–41X15–11866
4	1	100603	R14.404–10.4X2.0–11866
5	2	101992	VCR–1/2M–TUBW–35.8–6LVUHPSW
6	2	100823	VCR–1/2M–NUT–316

VACOM Vakuum Komponenten
& Messtechnik GmbH

Zust. | Änderungen | Name, Datum
Ers.atz | | Änderung d. Kunden
Vorgänger: | | Freigabe durch Kunden | Name, Datum
| | Freigabe durch Vacom | Name, Datum
| | erstellt von: Sven Haer
| | erstellt am: 15.03.2012
| | geprüft von
| | geprüft am

Oberflächen nach DIN EN ISO 1302
√Ra 3.2 √Ra 0.8
Maßstab: 1:1 / 1:3
Toleranzen ISO2768 mK
ISO13920 BF

Werkstoff: 316L / 14.404
SPE–CF–Kreuz DN100, 6– fach
nach Kundenskizze

317891
SPE–1003 1006–10

Kanten nach DIN ISO 13715
3.881 kg

Blatt 1 / 1
A3

Publications

Overview of papers and proceedings published in the context of this work.

Peer-reviewed publications

Activity monitoring of a gaseous tritium source by beta induced X-ray spectrometry
M. Röllig, F. Priester, M. Babutzka, J. Bonn, B. Bornschein, G. Drexlin, S. Ebenhöch, Ernst W. Otten, M. Steidl, M. Sturm
Fusion Eng. Des., **88** 6-8, 1263–1266 (2013),

Development of a compact tritium activity monitor and first tritium measurements
M. Röllig, S. Ebenhöch, S. Niemes, F. Priester, M. Sturm
Fusion Eng. Des., (2015), *In Press, Corrected Proof,*

CAPER as central and crucial facility to support R&D with tritium at the TLK
D. Demange, E. Fanghänel, S. Fischer, T-L. Le, F. Priester, **M. Röllig**, M. Schlösser, K. Simon
Fusion Sci. Technol., **62** 2, 308–311 (2015),

Monitoring of the operating parameters of the KATRIN Windowless Gaseous Tritium Source
M. Babutzka, M. Bahr, J. Bonn, B. Bornschein, A. Dieter, G. Drexlin, K. Eitel, S. Fischer, F. Glück, S. Grohmann, M. Hötzel, T. M. James, W. Käfer, M. Leber, B. Monreal, F. Priester, **M. Röllig**, M. Schlösser, U. Schmitt, F. Sharipov, M. Steidl, M. Sturm, H. H. Telle and N. Titov
New Journal of Physics October (2012) **14** 103046 2012
doi:10.1088/1367-2630/14/10/103046, arXiv: 1205.5421v3 [physics.ins-det]

Overview of R&D at TLK for process and analytical issues on tritium management in breeder blankets of ITER and DEMO
D. Demange, C. Alecu, N. Bekris, O. Borisevich, B. Bornschein, S. Fischer, N. Gramlich, Z. Köllö, T-L. Le, R. Michling, F. Priester, **M. Röllig**, M. Schlösser, S. Stämmler, M. Sturm, R. Wagner, S. Welte
Fusion Eng. Des., **87** 7-8, 1206–1213 (2012), doi:10.1016/j.fusengdes.2012.02.105

Post Service Examination of Turbomolecular Pumps After Stress Testing with kg-Scale Tritium Throughput
Florian Priester, **Marco Röllig**
Fusion Sci. Technol., **67** 3, 539–542 (2015),

Status of the Neutrino Mass Experiment KATRIN
Lutz Bornschein, Beate Bornschein, Michael Sturm, **Marco Röllig**, Florian Priester for the KATRIN collaboration
Fusion Sci. Technol., **67** 2, 274–277 (2015),

Submitted for publication

TRIADE: A new instrument for adsorption and desorption measurements using beta-induced X-ray spectroscopy
M. Babutzka, B. Bornschein, M. Klein, F. Priester, **M. Röllig**, F. Schneck
Review of Sci. Instr., (2015)

Geant4 Monte Carlo simulations for sensitivity investigations of an experimental facility for the measurement of tritium surface contaminations by BIXS
M. Röllig, B. Bornschein, S. Ebenhöch, F. Priester
Fusion Eng. Des., (2015)

Investigations of the applicability of a new accountancy tool in a closed tritium loop
S. Ebenhöch, S. Niemes, F. Priester, **M. Röllig**
Fusion Eng. Des., (2015)

Monte Carlo Simulation for a compact gaseous tritium monitor utilizing bremsstrahlung counting (BIXS) for various process gases
S. Niemes, **M. Röllig**, S. Ebenhöch, F. Priester, M. Sturm Fusion Eng. Des., (2015)

Bibliography

[Aba11]   K. Abazajian et al., *Cosmological and astrophysical neutrino mass measure-ments*, Astroparticle Physics, **35** 4, 177 – 184 (2011).

[Aga11]   S. Agarwal and H. A. Feldman, *The effect of massive neutrinos on the matter power spectrum*, Monthly Notices of the Royal Astronomical Society, **410** 3, 1647 (2011).

[Ago03]   S. Agostinelli et al., *Geant4 - a simulation toolkit*, Nuclear Instruments and Methods in Physics Research Section A: Accelerators, Spectrometers, Detect-ors and Associated Equipment, **506** 3, 250 – 303 (2003).

[Ago13]   M. Agostini et al., *Results on neutrinoless double beta decay of 76Ge from GERDA Phase I*, Physical Review Letters, **111** 12, 122503 (2013).

[All06]   J. Allison et al., *Geant4 developments and applications*, IEEE Transactions on Nuclear Science, **53** 1, 270–278 (2006).

[Alt03]   G. H. Altarelli (Ed.), *Neutrino mass : with 10 tables*, Springer tracts in modern physics ; 190, Springer, Berlin (2003).

[Arn87]   W. D. Arnett and J. L. Rosner, *Neutrino Mass Limits From Sn1987a*, Phys. Rev. Lett., **58**, 1906 (1987).

[Ase11]   V. N. Aseev et al., *An upper limit on electron antineutrino mass from Troitsk experiment*, Physical Review D, **84** 11, 112003 (2011).

[Atk10]   P. Atkins and J. de Paula, *Atkins' Physical Chemistry*, OUP Oxford (2010).

[Aug12]   M. Auger et al., *The EXO-200 detector, part I: Detector design and construc-tion*, Journal of Instrumentation, **7** 5, 5010 (2012).

[Aym02]   R. Aymar, P. Barabaschi and Y. Shimomura, *The ITER design*, Plasma Phys-ics and Controlled Fusion, **44** 5, 519 (2002).

[Bab14]   M. Babutzka, *Design and development for the Rearsection of the KATRIN experiment*, Ph.D. thesis (2014), karlsruhe, KIT, Diss., 2014.

[Bab12]   M. Babutzka et al., *Monitoring of the operating parameters of the KATRIN Windowless Gaseous Tritium Source*, New Journal of Physics, **14** 10, 103046 (2012).

[Bae11]   O. v. Baeyer, L. Meitner and O. Hahn, *Magnetische Spektren der Beta-Strahlen des Radiums*, Physikalische Zeitschrift, **12**, 1099 – 1101 (1911).

[ESTAR]   M. J. Berger, J. S. Coursey, M. A. Zucker and J. Chang, *ESTAR, PSTAR, and ASTAR: Computer Programs for Calculating Stopping-Power and Range Tables for Electrons, Protons, and Helium Ions (version 1.2.3).*, National Institute of Standards and Technology, Gaithersburg, MD. (2005).
URL http://physics.nist.gov/Star

[XCOM]   M. J. Berger et al., *XCOM: Photon Cross Section Database (version 1.5).*, National Institute of Standards and Technology, Gaithersburg, MD. (2010).
URL http://physics.nist.gov/xcom

[Bes93]   U. Besserer, G. Jourdan and E. Hutter, *On the way to commissioning the Tritium Laboratory Karlsruhe (TLK)*, in C. FERRO, M. GASPAROTTO and H. KNOEPFEL (Eds.), *Fusion Technology 1992*, pp. 1123 – 1127, North-Holland (1993).

[Bet32]   H. Bethe, *Bremsformel für Elektronen relativistischer Geschwindigkeit*, Zeitschrift für Physik, **76** 5-6, 293–299 (1932).

[Bil15]   S. M. Bilenky and C. Giunti, *Neutrinoless Double-Beta Decay: a Probe of Physics Beyond the Standard Model*, Int. J. Mod. Phys., **A30** 04n05, 1530001 (2015).

[Bue13]   A. Bükki-Deme, C. Alecu, B. Kloppe and B. Bornschein, *First results with the upgraded TLK tritium calorimeter IGC-V0.5*, Fusion Engineering and Design, **88** 11, 2865 – 2869 (2013).

[Bor06]   B. Bornschein, *The closed tritium cycle of KATRIN*, Progress in Particle and Nuclear Physics, **57** 1, 38 – 48 (2006), international Workshop of Nuclear Physics 27th course Neutrinos in Cosmology, in Astro, Particle and Nuclear Physics Ettore Majorana Center for Scientific Culture.

[Bor07]   B. Bornschein et al., *Experimental validation of a method for performance monitoring of the impurity processing stage in the TEP system of ITER*, Fusion Engineering and Design, **82** 15–24, 2133 – 2139 (2007), proceedings of the 24th Symposium on Fusion TechnologySOFT-24.

[Bor15]   L. Bornschein et al., *Status of the Neutrino Mass Experiment KATRIN*, Fusion Science and Technology, **67** 2, 274 – 277 (2015).

[Bru38]   S. Brunauer, P. H. Emmett and E. Teller, *Adsorption of Gases in Multimolecular Layers*, J. Am. Chem. Soc., **60** 2, 309–319 (1938).

[Cab12]   A. Cabrera, *The Double Chooz Experiment*, Nuclear Physics B - Proceedings Supplements, **229–232**, 87 – 91 (2012), neutrino 2010.

[Cha14]   J. Chadwick, *Intensitätsverteilung im magnetischen Spectrum der β-Strahlen von radium B + C*, Verhandl. Dtsc. Phys. Ges., **16**, 383 (1914).

[Cha35]   J. Chadwick and M. Goldhaber, *The Nuclear Photoelectric Effect*, Proceedings of the Royal Society of London. Series A, Mathematical and Physical Sciences, **151** 873, pp. 479–493 (1935).

[Chr88]   K. Christmann, *Interaction of hydrogen with solid surfaces*, Surface Science Reports, **9** 1-3, 1 – 163 (1988).

[Chr91]   K. Christmann, *Introduction to Surface Physical Chemistry*, Berichte der Bunsengesellschaft fuer physikalische Chemie, **96** 3, 522–523 (1992).

[CUO14]   C. Collaboration et al., *Searching for neutrinoless double-beta decay of ^{130}Te with CUORE*, Adv. High Energ. Phys. (2014).

[KAT04]   K. Collaboration, *KATRIN design report 2004*, Tech. Rep., Karlsruhe (2005), wissenschaftliche Berichte / Forschungszentrum Karlsruhe in der Helmholtz-Gemeinschaft, FZKA 7090.

[Pla15]   P. Collaboration, *Planck 2015 results. XIII. Cosmological parameters* (2015).

[Com23]   A. H. Compton, *A Quantum Theory of the Scattering of X-rays by Light Elements*, Phys. Rev., **21**, 483–502 (1923).

[Cow56]   C. L. Cowan et al., *Detection of the free neutrino: A Confirmation*, Science, **124**, 103–104 (1956).

[Dan62]   G. Danby et al., *Observation of High-Energy Neutrino Reactions and the Existence of Two Kinds of Neutrinos*, Phys. Rev. Lett., **9**, 36–44 (1962).

[Dav64]   R. Davis, *Solar Neutrinos. II. Experimental*, Phys. Rev. Lett., **12**, 303–305 (1964).

[Dem10]   D. Demange et al., *Counter-current isotope swamping in a membrane reactor: The PERMCAT process and its applications in fusion technology*, Catalysis Today, **156** 3–4, 140 – 145 (2010).

[Dem12]   D. Demange et al., *Overview of R&D at TLK for process and analytical issues on tritium management in breeder blankets of ITER and DEMO*, Fusion Engineering and Design, **87** 7–8, 1206 – 1213 (2012).

[Doe02]   L. Dörr et al., *Upgrade of the Isotope Separation System at the Tritium Laboratory Karlsruhe*, Fusion Science and Technology, **41** 3P2, 1155 – 1159 (2002).

[Doe05]   L. Dörr et al., *The Closed Tritium Cycle of the Tritium Laboratory Karlsruhe*, Fusion Science and Technology, **48** 1, 262 – 267 (2005).

[Doe08]   L. Dörr et al., *A decade of tritium technology development and operation at the tritium laboratory Karlsruhe*, Fusion Science and Technology, **44** 27, 143 – 148 (2008).

[Egg04]   T. Eggert, *Die spektrale Antwort von Silizium-Röntgendetektoren*, Dissertation, Technische Universität München, München (2004).

[Fis14]   S. Fischer, *Commissioning of the KATRIN Raman system and durability studies of optical coatings in glove box and tritium atmospheres*, Ph.D. thesis (2014), karlsruhe, KIT, Diss., 2014.

[Fis11]   S. Fischer et al., *Monitoring of tritium purity during long-term circulation in the KATRIN test experiment LOOPINO using laser Raman spectroscopy*, Fusion Science and Technology, **60** 3, 925 – 930 (2011).

[Kam13]   A. Gando et al., *Limit on Neutrinoless ββ Decay of Xe-136 from the First Phase of KamLAND-Zen and Comparison with the Positive Claim in Ge-76*, Phys. Rev. Lett., **110**, 062502 (2013).

[Gat84]   E. Gatti and P. Rehak, *Semiconductor drift chamber — An application of a novel charge transport scheme*, Nuclear Instruments and Methods in Physics Research, **225** 3, 608 – 614 (1984).

[Giu07]   C. Giunti and C. W. Kim, *Fundamentals of neutrino physics and astrophysics*, Oxford Univ. Press, 1. publ. edn. (2007).

[Glu02]   M. Glugla et al., *Recovery of tritium from different sources by the ITER Tokamak exhaust processing system*, Fusion Engineering and Design, **61–62** 0, 569 – 574 (2002).

[Glu07]   M. Glugla et al., *The ITER tritium systems*, Fusion Engineering and Design, **82** 5–14, 472 – 487 (2007).

[Gre15]   M. Green et al., *The MAJORANA DEMONSTRATOR for 0νββ: Current Status and Future Plans*, Physics Procedia, **61**, 232 – 240 (2015), 13th International Conference on Topics in Astroparticle and Underground Physics, TAUP 2013.

[Gru12]   W. Grünert, *Heterogeneous Catalysis. Fundamentals and Applications. By Julian R. H. Ross.*, Angewandte Chemie International Edition, **51** 22, 5289–5289 (2012).

[Gro13]   S. Grohmann et al., *The thermal behaviour of the tritium source in KATRIN*, Cryogenics, **55–56**, 5 – 11 (2013).

[Hei54]   W. Heitler, *The quantum theory of radiation*, The international series of monographs on physics, Clarendon Pr., Oxford, 3. ed. edn. (1954).

[Hen91]   M. Henzler and W. Göpel, *Oberflächenphysik des Festkörpers*, Teubner-Studienbücher : Physik, Teubner, Stuttgart (1991).

[Hir84]   T. Hirabayashi and M. Saeki, *Sorption of gaseous tritium on the surface of type 316 stainless steel*, Journal of Nuclear Materials, **120** 2–3, 309 – 315 (1984).

[Kam87]   K. Hirata et al., *Observation of a neutrino burst from the supernova SN1987A*, Phys. Rev. Lett., **58**, 1490–1493 (1987).

[Hof13]   E. de Hoffmann and V. Stroobant, *Mass Spectrometry: Principles and Applications*, Wiley (2013).

[FFAST]   J. H. Hubbell and S. M. Seltzer, *X-Ray Form Factor, Attenuation and Scattering Tables (FFAST)*, National Institute of Standards and Technology, Gaithersburg, MD. (2004).

[Iba06]   H. Ibach, *Physics of surfaces and interfaces*, Springer, Berlin (2006).

[Jak15]   M. Jakubowski and C. Palczynski, *Handbook on the Toxicology of Metals (Fourth Edition)*, pp. 635 – 653, Academic Press, San Diego, fourth edition edn. (2015).

[Joo12]   K. Joo, *Status of the RENO Reactor Neutrino Experiment*, Nuclear Physics B - Proceedings Supplements, **229–232**, 97 – 100 (2012), neutrino 2010.

[Jou10]   K. Jousten (Ed.), *Wutz Handbuch Vakuumtechnik*, Vieweg + Teubner, Wiesbaden, 10., überarb. erw. Aufl. (2012).

[Kaz08]   O. Kazachenko et al., *TRAP—a cryo-pump for pumping tritium on precondensed argon*, Nuclear Instruments and Methods in Physics Research Section A: Accelerators, Spectrometers, Detectors and Associated Equipment, **587** 1, 136 – 144 (2008).

[Kle29]   O. Klein and Y. Nishina, *Über die Streuung von Strahlung durch freie Elektronen nach der neuen relativistischen Quantendynamik von Dirac*, Zeitschrift für Physik, **52** 11-12, 853–868 (1929).

[Koe09]   Z. Köllö et al., *Calibrating a gas chromatograph to measure tritium using calorimetry*, Fusion Engineering and Design, **84** 7–11, 1073 – 1075 (2009), proceeding of the 25th Symposium on Fusion Technology(SOFT-25).

[Kno10]   G. F. Knoll, *Radiation detection and measurement*, Wiley, Hoboken, NJ, 4th ed. edn. (2010).

[Kod01]   K. Kodama et al., *Observation of tau neutrino interactions*, Phys. Lett., **B504**, 218–224 (2001).

[Koe11]   Z. Köllö et al., *A new method to measure small volumes in tritium handling facilities, using p-V measurements*, Fus. Sci. Technol., **60** (2011) 972-975.

[Kra05]   C. Kraus et al., *Final results from phase II of the Mainz neutrino mass search in tritium β decay*, The European Physical Journal C - Particles and Fields, **40** 4, 447–468 (2005).

[Kri12]   H. Krieger, *Grundlagen der Strahlungsphysik und des Strahlenschutzes*, Studium, Springer Spektrum, Wiesbaden, 4., überarb. und erw. aufl. edn. (2012).

[Lec04]   P. Lechner, A. Pahlke and H. Soltau, *Novel high-resolution silicon drift detectors*, X-Ray Spectrometry, **33** 4, 256–261 (2004).

[Lüt97]   H. Lüth, *Surfaces and interfaces of solid materials*, Springer study edition, Springer, Berlin [u.a.], 3. ed., upd. print. edn. (1997).

[Lüt10]   H. Lüth, *Solid Surfaces, Interfaces and Thin Films*, Graduate Texts in Physics, Springer, 5. ed. edn. (2010).

[Maj06]   E. Majorana and L. Maiani, *A symmetric theory of electrons and positrons*, in G. Bassani (Ed.), *Ettore Majorana Scientific Papers*, pp. 201–233, Springer Berlin Heidelberg (2006).

[Mak62]   Z. Maki, M. Nakagawa and S. Sakata, *Remarks on the unified model of elementary particles*, Prog. Theor. Phys., **28**, 870–880 (1962).

[Mao12]   L. Mao et al., *Effect of geometrical parameter's uncertainty of BIXS experimental setup for tritium analysis*, Nuclear Instruments and Methods in Physics Research Section B: Beam Interactions with Materials and Atoms, **289** 0, 52 – 55 (2012).

[Mas96]   R. I. Masel, *Principles of adsorption and reaction on solid surfaces*, Wiley series in chemical engineeringA Wiley-Interscience publication, Wiley, New York [u.a.] (1996).

[Mat08]   M. Matsuyama, *Development of a new detection system for monitoring high-level tritiated water*, Fusion Engineering and Design, **83** 10–12, 1438 – 1441 (2008), proceedings of the Eight International Symposium of Fusion Nuclear Technology ISFNT-8 {SI}.

[Mat98]   M. Matsuyama, K. Watanabe and K. Hasegawa, *Tritium assay in materials by the bremsstrahlung counting method*, Fusion Engineering and Design, **39–40**, 929 – 936 (1998).

[Mat06]   M. Matsuyama et al., *Applicability of Beta-ray-induced X-ray spectrometry to in situ measurements of tritium retention in plasma-facing materials in ITER*, Fusion Engineering and Design, **81** 1-7, 163 – 168 (2006), proceedings of the Seventh International Symposium on Fusion Nuclear Technology ISFNT-7 Part A Proceedings of the Seventh International Symposium on Fusion Nuclear Technology.

[Mee61]   S. van der Meer, *A Directive Device for Charged Particles and Its use in an Enhanced Neutrino Beam*, Tech. Rep. (1961).

[Nag06]   S. Nagy et al., *On the Q-value of the tritium Beta-decay*, EPL (Europhysics Letters), **74** 3, 404 (2006).

[Nis89]   M. Nishikawa, T. Takeishi, Y. Matsumoto and I. Kumabe, *Ionization chamber system to eliminate the memory effect of tritium*, Nuclear Instruments and Methods in Physics Research Section A: Accelerators, Spectrometers, Detectors and Associated Equipment, **278** 2, 525 – 531 (1989).

[Aga14]   K. A. Olive et al., *Review of Particle Physics*, Chin. Phys., **C38**, 090001 (2014).

[Pat57]   L. Paty, *The pumping properties of the cold cathode ionization gauge*, Cechoslovackij fiziceskij zurnal, **7** 1, 113–115 (1957).

[Pea91]   R. N. Peacock, N. T. Peacock and D. S. Hauschulz, *Comparison of hot cathode and cold cathode ionization gauges*, Journal of Vacuum Science & Technology A, **9** 3, 1977–1985 (1991).

[Pen15]   J.-C. Peng, *Daya Bay: Results and Perspectives*, Nuclear and Particle Physics Proceedings, **265–266**, 105 – 110 (2015), proceedings of the Neutrino Oscillation WorkshopProceedings of the Neutrino Oscillation Workshop.

[Pen00]   R.-D. Penzhorn et al., *Status and research progress at the Tritium Laboratory Karlsruhe*, Fusion Engineering and Design, **49–50**, 753 – 767 (2000).

[Per09]   D. H. Perkins, *Particle astrophysics*, Oxford master series in physics ; no. 10, Oxford University Press, 2. ed. edn. (2009).

[Pri13]   F. Priester and B. Bornschein, *TriToP – A compatibility experiment with turbomolecular pumps under tritium atmosphere*, Vacuum, **98** 0, 22 – 28 (2013).

[Qia15]   X. Qian and P. Vogel, *Neutrino Mass Hierarchy*, Prog. Part. Nucl. Phys., **83**, 1–30 (2015).

[ICRU37]   I. C. on Radiation Units and Measurements, *ICRU Report*, Tech. Rep. Nr. 37 (1984).

[Roe13]   M. Röllig et al., *Activity monitoring of a gaseous tritium source by beta induced X-ray spectrometry*, Fusion Engineering and Design, **88** 6–8, 1263 – 1266 (2013), proceedings of the 27th Symposium On Fusion Technology (SOFT-27); Liège, Belgium, September 24-28, 2012.

[Roe11]   M. Röllig, *Studien zu einem Röntgendetektorsystem zur Bestimmung der Aktivität in der KATRIN Tritiumquelle*, Diplomarbeit, Institut für Experimentelle Kernphysik (IEKP), KIT (2011).

[Rut84]   D. M. Ruthven, *Principles of adsorption and adsorption processes*, A Wiley-Interscience publication, Wiley, New York [u.a.] (1984).

[Sch12]   M. Schlösser, S. Fischer, M. Hötzel and W. Käfer, *Accuracy of the Laser Raman system for KATRIN* (2012).

[Sch13a]   M. R. H. Schlösser, *Accurate calibration of the Raman system for the Karlsruhe Tritium Neutrino Experiment*, Ph.D. thesis (2013), karlsruhe, KIT, Diss., 2013.

[Sch13b]   F. Schneck, *Design and setup of the Tritium Adsorption Desorption Experiment (TRIADE)*, Diploma thesis, Institut für Experimentelle Kernphysik (IEKP), KIT (2013).

[Ste83]   S. Steward and L. L. N. Laboratory, *Review of Hydrogen Isotope Permeability Through Materials*, Lawrence Livermore National Laboratory (1983).

[Sto96]   L. Stobinski, *Molecular and atomic deuterium chemisorption on thin gold films at 78 K: an isotope effect*, Applied Surface Science, **103** 4, 503 – 508 (1996).

[Sto92]   L. Stobinski and R. Dus, *Atomic hydrogen adsorption on thin gold films*, Surface Science, **269–270** 0, 383 – 388 (1992).

[Sto94]   L. Stobinski and R. Dus, *Model of atomic hydrogen adsorption on thin gold film surface*, Vacuum, **45** 2–3, 299 – 301 (1994), special Issue Proceedings of the 16th International Seminar on Surface Physics.

[Sto99]   L. Stobinski, L. Zommer and R. Dus, *Molecular hydrogen interactions with discontinuous and continuous thin gold films*, Applied Surface Science, **141** 3–4, 319 – 325 (1999).

[Stu10]   M. Sturm, *Aufbau und Test des Inner-Loop-Systems der Tritiumquelle von KATRIN*, Ph.D. thesis (2010), karlsruhe, KIT, Diss., 2010.

[Stu10a] M. Sturm et al., *Monitoring of all hydrogen isotopologues at tritium laboratory Karlsruhe using Raman spectroscopy*, Laser Physics, **20** 2, 493 – 507 (2010).

[Sze81] S. M. Sze, *Physics of semiconductor devices*, A Wiley-Interscience publication, Wiley, New York, N.Y. [u.a.], 2. ed. edn. (1981).

[XRD09] A. Thompson et al., *X-Ray Data Booklet*, Lawrence Berkeley National Laboratory, California (2009).

[TLA15] TLA, *Technische Liefer- und Abnahmebedingungen des Tritiumlabors Karlsruhe*, internes Dokument (2015).

[Tor05] Y. Torikai et al., *Tritium distribution in JET Mark IIA type divertor tiles analysed by BIXS*, Journal of Nuclear Materials, **337** 0, 575 – 579 (2005).

[Wag11] R. Wagner et al., *Improvement and Characterization of Small Cross-Piece Ionization Chambers at the Tritium Laboratory Karlsruhe*, Fusion Science and Technology, **60** 3, 968 – 971 (2011).

[Wes60] T. Westermark, L. Devell and N. Ghanem, *On the use of bremsstrahlung for the determination of tritium in aqueous and organic systems*, Nuclear Instruments and Methods, **9** 2, 141 – 144 (1960).

[Xin11] Z.-Z. Xing and S. Zhou, *Neutrinos in particle physics, astronomy and cosmology*, Advanced topics in science and technology in China, Zhejiang Univ. Press, Hangzhou (2011).

[Zan88] A. Zangwill, *Physics at surfaces*, Cambridge Univ. Pr., Cambridge, 1. publ. edn. (1988).

[Zub98] K. Zuber, *On the physics of massive neutrinos*, Physics Reports, **305** 6, 295 – 364 (1998).

[Zub12] K. Zuber, *Neutrino physics*, Series in high energy physics, cosmology, and gravitation, CRC Press, 2. ed. edn. (2012).

Danksagung

Abschließend möchte ich allen Dank sagen, welche auf vielfältige Weise zum Gelingen dieser Arbeit beigetragen haben. Vielen Dank,

- Prof. Drexlin für die Gelegenheit an dem spannenden und vielseitigen KATRIN Projekt mitarbeiten zu dürfen.

- Prof. Noe für die Übernahme der Zweitkorrektur, das Kristberg Seminar und interessante Einblicke in die Supraleiter Forschung.

- Dr. Beate Bornschein für die fachliche Betreuung, für die Möglichkeit am TLK eigene Ideen frei umsetzen zu können und die vielfältige Förderung in allen Belangen des wissenschaftlichen Arbeitens. Ich danke auch für die immer offene Tür und all die geklauten Süssigkeiten!

- Dr. Florian Priester für die Korrektur dieser Arbeit, die wissenschaftliche Zusammenarbeit und all die Gespräche und Unternehmungen abseits des Laboralltags.

- Sylvia Ebenhöch, Manuel Klein, Florian Priester und Fabian Schneck für all die experimentellen Arbeiten und Messungen die im Rahmen dieser Arbeit und mit ihrer Hilfe stattgefunden haben.

- Meinen mit-Doktoranden und Physikstudenten für viele interessante Diskussionen, Feedback zu allen fachlichen Belangen und einer nahezu ausreichenden Versorgung mit Keksen.

- der CAPER-Crew bestehend aus Dr. David Demange, Than Long Le, Karl-Heinz Simon und Eleonore Fanghänel für das Herstellen von Gasmischungen für TRACE, TRIREX und TRIADE.

- Eva Porter und Sylvia Krieger für das Erledigen der meisten administrativen Aufgaben im Rahmen dieser Arbeit.

- Stefan Welte, Robert Michling, David Demange, Michael Sturm, Martin Babutzka, Ferenc Glück, Markus Steidl, Sebastian Fischer und Magnus Schlösser für vielfältige fachliche Tipps bezüglich Analytik und Prozessierung von Tritium und KATRIN im Allgemeinen.

- der gesamten Infrastruktur Crew des TLK, die experimentelles Arbeiten erst möglich machen.

- der Geant4 Kollaboration für das Entwickeln von Geant4.9.6p02.

- der Süssigkeiten Infrastruktur Crew Kerstin Schönung (du bist verantwortlich für 10 kg zuviel auf meinen Rippen).

- Benjamin Kehrer für viel schlechten Humor, hunderte gelaufene Kilometer, ein erinnerungswürdiges Auslandsstudium in Stockholm und viele gemeinsame Reisen.

- meinen Freunden in Karlsruhe für all die Freizeitunternehmungen.

- meinen Eltern Brigitte und Horst Röllig, sowie meinem Bruder Jan Röllig.

- der Geniesserecke Karlsruhe für die stete Kaffeeversorgung während meines Studiums in Karlsruhe.

- der Franz-Auweck Abendschule in München und den überaus motivierten Lehreren dort, die mir durch den nachträglichen Erwerb der allgemeinen Hochschulreife das Studium der Physik erst ermöglicht haben.

- meinem Physiklehrer in der Technikerschule (Johann-Vießmann-Schule) in Hof, dessen Name ich schändlicherweise vergessen habe, ohne den ich aber nie auf die Idee gekommen wäre Physik zu studieren.